

https://dspace.org/

Wind-tunnel study of cross vault structures.

Bradley, Ryan Anthony.

2011-10-11
http://hdl.handle.net/10539/10534

Downloaded from a DSpace repository. https://dspace.org/

WIND-TUNNEL STUDY OF CROSS VAULT STRUCTURES

Ryan Anthony Bradley

A research report submitted to the Faculty of Engineering and the Built Environment, University of the Witwatersrand, Johannesburg, in partial fulfilment of the requirements for the degree of Master of Science in Engineering.

Johannesburg 2011

DECLARATION

I declare that this research report is my own unaided work. It is being submitted to the Degree of Master of Science to the University of the Witwatersrand, Johannesburg. It has not been submitted before for any degree or examination to any other University.

……
Ryan Anthony Bradley

…… day of …… year 2011.

ABSTRACT

The present study examines the effects of surface roughness, flow characteristics, wind orientation and small geometrical changes of the roof apex (rise) on pressures measured at centrally located areas of the cross vault structure. The parameters noted above are assessed to shed light on their influence on pressure distributions and, ultimately, the loading on these structures.

Three cross vault models with flat, convex and concave roof apex geometries have been tested in two generic boundary-layer profiles within the BLWT at the CSIR, Pretoria, South Africa.

The study revealed that relatively small changes in roof geometry can noticeably influence the distribution of surface pressures, at certain azimuths and areas of the roof. Generally, mean and negative peak pressures over the cross vaults increased with the addition of surface roughness. Furthermore, mean pressures showed marginal sensitivity to the change of boundary-layer conditions, whereas noticeable differences were evident for the fluctuating pressures.

ACKNOWLEDGEMENTS

I would like to thank:

- My supervisor, Prof. M. Gohnert, for the support and encouragement received while undertaking this degree.

- My supervisor, Dr. A.M. Goliger, for the support received while completing the degree and for the guidance received during testing.

- Mr. T. van Wyk, for the calibration of equipment and assistance during testing.

- The Council for Scientific and Industrial Research (CSIR) for the use of the Boundary-Layer Wind-Tunnel.

- Mr. L. Wills for his assistance whilst building the models.

- My parents for their support throughout my studies.

CONTENTS **Page**

DECLARATION 2

ABSTRACT 3

ACKNOWLEDGEMENTS 4

CONTENTS 5

LIST OF FIGURES 9

LIST OF TABLES 22

LIST OF SYMBOLS 23

1	**INTRODUCTION**	**25**
1.1	**General**	**25**
1.2	**Objectives**	**26**
1.3	**Scope**	**26**
2	**LITERATURE REVIEW**	**28**
2.1	**Introduction**	**28**
2.2	**Design Information**	**28**
2.3	**Role of Wind-Tunnel Technology**	**31**
2.4	**Wind-Tunnel Testing Requirements for Pressure Measurement**	**32**
2.4.1	**Similarity requirements**	**32**
2.4.2	**Atmospheric boundary-layer requirements**	**33**
2.4.3	**Reynolds number**	**36**
2.5	**Effects of the Mean Wind Profile and Turbulence Characteristics on Sharp Edged Bluff Body Structures**	**37**
2.6	**Effects of Turbulence on the Surface Pressures over Curved Roofs**	**40**
2.6.1	**General**	**40**
2.6.2	**Effects of turbulence intensity**	**41**
2.7	**Effects of Surface Roughness on Pressures over Bluff Bodies**	**44**

2.7.1	Sharp edged structures	44
2.7.2	Curved structures	46
2.8	Simulating High Reynolds Number Flow in Wind-Tunnel Testing	50
3	EXPERIMENTAL METHODOLOGY	53
3.1	Boundary-Layer Wind-Tunnel	53
3.1.1	Wind-tunnel facility	53
3.1.2	Instrumentation	54
3.2	Boundary-Layer Modelling	55
3.2.1	Introduction	55
3.2.2	Boundary-layer simulation	56
3.3	Surface Pressure Instrumentation, Measurements and Calculation	63
3.3.1	Instrumentation	63
3.3.2	Reference dynamic pressure	63
3.3.3	Reference static pressures	64
3.3.4	Wind-tunnel models	64
3.3.5	Surface pressures	66
3.3.6	Pneumatically averaged surface pressures	68
3.3.7	Data acquisition and processing	69
3.4	Qualitative Measurements	75
3.5	Reynolds Number	76
3.6	Repeatability of Measurements	77
3.7	Chapter Summary	78
4	EFFECTS OF SURFACE ROUGHNESS / REYNOLDS NUMBER MODELLING	79
4.1	General	79
4.2	Test Procedure	79
4.3	Distributed Surface Roughness	80
4.4	Results of the ESDU- 80025 (1980) Procedures	81
4.5	Results and Discussion	83

4.5.1 Mean pressure coefficients 83
4.5.2 RMS pressure coefficient..... 87
4.5.3 Negative peak pressure coefficients..... 90
4.6 Conclusions..... 94
5 EFFECTS OF TURBULENCE 95
5.1 General..... 95
5.2 Results and Discussion..... 96
5.2.1 Mean pressure coefficients 96
5.2.2 RMS pressure coefficients 99
5.2.3 Negative peak pressure coefficients..... 103
5.3 Conclusions..... 105
6 EFFECTS OF ROOF GEOMETRY: POINT PRESSURES.....
..... 106
6.1 General..... 106
6.2 Pressure Distributions 106
6.2.1 0° wind direction 106
6.2.2 15° wind direction 111
6.2.3 30° wind direction 115
6.2.4 45° wind direction 119
6.2.5 60° wind direction 123
6.2.6 75° wind direction 126
6.2.7 90° wind direction 129
6.2.8 120° wind direction 133
6.2.9 150° wind direction 137
6.2.10 180° wind direction 141
6.3 Pressure Distribution variation with Wind Direction 145
6.3.1 15° to 45° wind directions..... 145
6.3.2 45° to 75° wind directions..... 150
6.3.3 120° to 150° wind directions..... 154
6.4 Contour Plots..... 158
6.5 Flow Visualisation..... 177

6.6 Conclusions 180

7 EFFECTS OF ROOF GEOMETRY: AVERAGED PRESSURES 181

7.1 General 181

7.2 Results, Discussion and Conclusions 184

8 COMPARASION OF EXPERIMENTAL RESULTS WITH CODIFIED DATA USED FOR THE DESIGN OF SINGLE VAULT STRUCTURES 196

8.1 Introduction 196

8.2 Minimum Pressure Coefficients at Central Locations over Cross Vault Structures 197

8.3 Design Data for Arched Roof Structures 202

8.3.1 Wind normal to curvature 202

8.3.2 Wind normal to the arch 205

8.4 Predicted Design Cefficients over Cross Vault Structures 207

8.4.1 0° wind direction 207

8.4.2 30°-60° wind directions 209

8.5 Conclusions 210

9 CONCLUSIONS AND RECOMMENDATIONS 212

9.1 Summary and Conclusions of the Present Study 212

9.2 Recommendations for Future Wind-Tunnel Studies related to the Cross Vault Structure 213

REFERENCES 215

BIBLIOGRAPHY 218

APPENDIX A C_{DO} AND Cp CALCULATION PROCEDURES OUTLINED IN ESDU- 80025 (1980) 222

APPENDIX B EXPERIMENTAL SCATTER 225

APPENDIX C PRESSURE COEFFICIENT VARIATION WITH WIND DIRECTION 227

LIST OF FIGURES

Figure 1.1 - Cross vault structure (Good Hope Centre, Cape Town) 25
Figure 2.1 - Design pressure distributions for simple vault structures 29
Figure 2.2 - Comparison of *Cp* values from codes and experimental results (Reproduced from Blackmore and Tsokri (2006)) 30
Figure 2.4 - Typical wind speed time history 34
Figure 2.5 - Pressure distribution over a circular cylinder for subcritical and supercritical Reynolds numbers (Reproduced from Holmes (2001)) 37
Figure 2.6 - Separation, reattachment and pressure coefficient distribution over flat roofs (Reproduced from Cook (1985)) 39
Figure 2.7 - Comparison of the mean pressure coefficients over the centreline of a dome with h/d = 0.5 (Reproduced form Taylor (1991)) 42
Figure 2.8 - Drag coefficient and Strouhal number for various turbulence intensities (%), aspect ratio (L/D) and blockage ratio (D/B) (Reproduced from Zdravkovich (1990)) 44
Figure 2.9 - Flow regimes around a circular cylinder in smooth flow (Produced from Cook (1985)) 44
Figure 2.10 - Effects of surface roughness on the peak and RMS pressure coefficients over the building facade (Reproduced from Maruta et al (1998)) 45
Figure 2.11 - Pressure coefficients on smooth and rough wall surfaces (Reproduced from Stathopoulos and Zhu (1988)) 46
Figure 2.12 - Influence of Reynolds number and surface roughness on the drag coefficient for square and circular cylinders (Reproduced from Scruton (1971)) 47
Figure 2.13a – Comparison of mean centreline pressure coefficient distributions for rough and smooth domes (Reproduced from Letchford and Sarkar (2000)) 49
Figure 2.13b– Comparison of peak centreline pressure coefficient distributions for rough and smooth domes (Reproduced from Letchford and Sarkar (2000)) 49
Figure 2.13c – Comparison of RMS centreline pressure coefficient distributions for rough and smooth domes (Reproduced from Letchford and Sarkar (2000)) 50
Figure 2.14 - Variation of drag coefficient with Reynolds number (Reproduced from Cook (1985)) 51
Figure 3.1 - Wind-tunnel facility 53

Figure 3.2 - Wind-tunnel test section 54
Figure 3.3 - Instrumentation panel 54
Figure 3.4 - Pitot-tube 55
Figure 3.5 - Mini-air instrumentation 55
Figure 3.6 - Simple schematic diagram of the CSIR BLWT 56
Figure 3.7 - Upwind fetch (‘smooth’ boundary-layer) 57
Figure 3.8 - Upwind fetch (‘rough’ boundary-layer) 57
Figure 3.9 - Turbulence measurement position 58
Figure 3.10 - Time Series (30 mm above wind-tunnel floor) 58
Figure 3.11 - Mean wind speed profile (‘smooth’ flow) 59
Figure 3.12 - Turbulence intensity (‘smooth’ flow) 59
Figure 3.13 - Mean wind speed profile (‘rough’ flow) 60
Figure 3.14 - Turbulence intensity (‘rough’ flow) 60
Figure 3.15 - Longitudinal turbulence spectra (‘smooth’ boundary-layer) 61
Figure 3.16 - Longitudinal turbulence spectra (‘rough’ boundary-layer) 62
Figure 3.17 - Dynamic pressure measurement at roof height 63
Figure 3.18 - Flat, convex and concave cross vaults (from left to right) 64
Figure 3.19 - Catenary profile 65
Figure 3.20 - Pressure tap positions 67
Figure 3.21 - Effective pressure tap positions 67
Figure 3.22 - Scanivalve device attached to the model 68
Figure 3.23 - Pneumatic manifold 69
Figure 3.24 - Position of taps 1 and 8 for the 0° wind direction 72
Figure 3.25 - Typical time series for the flat cross vault ($\theta = 0°$ and I= 10%) 72
Figure 3.26 - Smoke visualization 76
Figure 3.27 - Mini-flag devices 76
Figure 3.28 - Repeatability of a typical mean pressure coefficient distribution 77
Figure 4.1 - Tap location and wind direction 79
Figure 4.2 - P150(left) and P40(right) grit sandpapers attached to the model 81
Figure 4.3 - P150, P40 grit sandpapers and tap surroundings 81
Figure 4.4 - Results of the ESDU mean pressure distribution procedure 82
Figure 4.5 - Mean pressure coefficient vs. tap (0° wind direction) 84

Figure 4.6 - Mean pressure coefficient vs. tap (30° wind direction) 84
Figure 4.7 - Mean pressure coefficient vs. tap (45° wind direction) 84
Figure 4.8 - Cp_{mean} (Smooth fibreglass) vs. Cp_{mean} (P150 sandpaper) 85
Figure 4.9 - Cp_{mean} (Smooth fibreglass) vs. Cp_{mean} (P40 sandpaper) 85
Figure 4.10 - Area-averaged mean pressure coefficients 86
Figure 4.11 - RMS pressure coefficient vs. tap (0° wind direction) 88
Figure 4.12 - RMS pressure coefficient vs. tap (30° wind direction) 88
Figure 4.13 - RMS pressure coefficient vs. tap (45° wind direction) 88
Figure 4.14 - Cp_{RMS} (Smooth fibreglass) vs. Cp_{RMS} (P150 sandpaper) 89
Figure 4.15 - Cp_{RMS} (Smooth fibreglass) vs. Cp_{RMS} (P40 sandpaper) 89
Figure 4.16 - 10s peak pressure coefficients vs. tap (0° wind direction) 91
Figure 4.17- 3s peak pressure coefficients vs. tap (0° wind direction) 91
Figure 4.18 - 10s peak pressure coefficients vs. tap (30° wind direction) 91
Figure 4.19 - 3s peak pressure coefficients vs. tap (30° wind direction) 92
Figure 4.20 - 10s peak pressure coefficients vs. tap (45° wind direction) 92
Figure 4.21 - 3s peak pressure coefficients vs. tap (45° wind direction) 92
Figure 4.22 - Cp_{peak} (Smooth fibreglass) vs. Cp_{peak} (P150 sandpaper) 93
Figure 4.23 - Cp_{peak} (Smooth fibreglass) vs. Cp_{peak} (P40 sandpaper) 93
Figure 5.1 - Turbulence intensity profiles for the two boundary-layers 95
Figure 5.2 - Position of model with wind direction = 0°, 45°, 90° and 180° 96
Figure 5.3 - Mean pressure coefficient (‘smooth’ BL) versus mean pressure coefficient (‘rough’ BL), for the flat cross vault 97
Figure 5.4 - Mean pressure coefficient (‘smooth’ BL) versus mean pressure coefficient (‘rough’ BL), for the convex cross vault 98
Figure 5.5 - Mean pressure coefficient (‘smooth’ BL) versus mean pressure coefficient (‘rough’ BL), for the concave cross vault 98
Figure 5.6 - RMS pressure coefficient (‘smooth’ BL) versus RMS pressure coefficient (‘rough’ BL), for the flat cross vault 100
Figure 5.7 - RMS pressure coefficient (‘smooth’ BL) versus RMS pressure coefficient (‘rough’ BL), for the convex cross vault 100
Figure 5.8 - RMS pressure coefficient (‘smooth’ BL) versus RMS pressure coefficient (‘rough’ BL), for the concave cross vault 101

Figure 5.9 - Negative 3s peak pressure coefficient (‘smooth’ BL) versus negative 3s peak pressure coefficient (‘rough’ BL), for the flat cross vault 104
Figure 5.10 - Negative 3s peak pressure coefficient (‘smooth’ BL) versus negative 3s peak pressure coefficient (‘rough’ BL), for the convex cross vault 104
Figure 5.11 - Negative 3s peak pressure coefficient (‘smooth’ BL) versus negative 3s peak pressure coefficient (‘rough’ BL), for the concave cross vault 105
Figure 6.1 - Tap positions for the the 0° wind direction 106
Figure 6.2a - Mean pressure coefficient distribution (‘smooth’ BL, θ = 0°) 108
Figure 6.2b - RMS pressure coefficient distribution (‘smooth’ BL, θ = 0°) 108
Figure 6.2c - 3s peak pressure coefficient distribution (‘smooth’ BL, θ = 0°) 108
Figure 6.3a - Mean pressure coefficient distribution (‘rough’ BL, θ = 0°) 109
Figure 6.3b - RMS pressure coefficient distribution (‘rough’ BL, θ = 0°) 109
Figure 6.3c - 3s peak pressure coefficient distribution (‘rough’ BL, θ = 0°) 109
Figure 6.4 - Centreline mean pressure distribution over duo-pitch roofs (Reproduced from Holmes (2001)) 110
Figure 6.5 - Tap positions for the the 15° wind direction 111
Figure 6.6a - Mean pressure coefficient distribution (‘smooth’ BL, θ = 15°) 113
Figure 6.6b - RMS pressure coefficient distribution (‘smooth’ BL, θ = 15°) 113
Figure 6.6c - 3s peak pressure coefficient distribution (‘smooth’ BL, θ = 15°) 113
Figure 6.7a - Mean pressure coefficient distribution (‘rough’ BL, θ = 15°) 114
Figure 6.7b - RMS pressure coefficient distribution (‘rough’ BL, θ = 15°) 114
Figure 6.7c - 3s peak pressure coefficient distribution (‘rough’ BL, θ = 15°) 114
Figure 6.8 - Tap positions for the the 30° wind direction 115
Figure 6.9a - Mean pressure coefficient distribution (‘smooth’ BL, θ = 30°) 117
Figure 6.9b - RMS pressure coefficient distribution (‘smooth’ BL, θ = 30°) 117
Figure 6.9c - 3s peak pressure coefficient distribution (‘smooth’ BL, θ = 30°) 117
Figure 6.10a - Mean pressure coefficient distribution (‘rough’ BL, θ = 30°) 118
Figure 6.10b - RMS pressure coefficient distribution (‘rough’ BL, θ = 30°) 118
Figure 6.10c - 3s peak pressure coefficient distribution (‘rough’ BL, θ = 30°) 118
Figure 6.11 - Tap positions for the the 45° wind direction 119
Figure 6.12a - Mean pressure coefficient distribution (‘smooth’ BL, θ = 45°) 121
Figure 6.12b - RMS pressure coefficient distribution (‘smooth’ BL, θ = 45°) 121

Figure 6.12c - 3s peak pressure coefficient distribution (‘smooth’ BL, θ = 45°) 121
Figure 6.13a - Mean pressure coefficient distribution (‘rough’ BL, θ = 45°) 122
Figure 6.13b - RMS pressure coefficient distribution (‘rough’ BL, θ = 45°) 122
Figure 6.13c - 3s peak pressure coefficient distribution (‘rough’ BL, θ = 45°) 122
Figure 6.14 - Tap positions for the the 60° wind direction 123
Figure 6.15a - Mean pressure coefficient distribution (‘smooth’ BL, θ = 60°) 124
Figure 6.15b - RMS pressure coefficient distribution (‘smooth’ BL, θ = 60°) 124
Figure 6.15c - 3s peak pressure coefficient distribution (‘smooth’ BL, θ = 60°) 124
Figure 6.16a - Mean pressure coefficient distribution (‘rough’ BL, θ = 60°) 125
Figure 6.16b - RMS pressure coefficient distribution (‘rough’ BL, θ = 60°) 125
Figure 6.16c - 3s peak pressure coefficient distribution (‘rough’ BL, θ = 60°) 125
Figure 6.17 - Tap positions for the the 75° wind direction 126
Figure 6.18a - Mean pressure coefficient distribution (‘smooth’ BL, θ = 75°) 127
Figure 6.18b - RMS pressure coefficient distribution (‘smooth’ BL, θ = 75°) 127
Figure 6.18c - 3s peak pressure coefficient distribution (‘smooth’ BL, θ = 75°) 127
Figure 6.19a - Mean pressure coefficient distribution (‘rough’ BL, θ = 75°) 128
Figure 6.19b - RMS pressure coefficient distribution (‘rough’ BL, θ = 75°) 128
Figure 6.19c - 3s peak pressure coefficient distribution (‘rough’ BL, θ = 75°) 128
Figure 6.20 - Tap positions for the the 90° wind direction 129
Figure 6.21a - Mean pressure coefficient distribution (‘smooth’ BL, θ = 90°) 131
Figure 6.21b - RMS pressure coefficient distribution (‘smooth’ BL, θ = 90°) 131
Figure 6.21c - 3s peak pressure coefficient distribution (‘smooth’ BL, θ = 90°) 131
Figure 6.22a - Mean pressure coefficient distribution (‘rough’ BL, θ = 90°) 132
Figure 6.22b - RMS pressure coefficient distribution (‘rough’ BL, θ = 90°) 132
Figure 6.22c - 3s peak pressure coefficient distribution (‘rough’ BL, θ = 90°) 132
Figure 6.23 - Tap positions for the the 120° wind direction 133
Figure 6.24a - Mean pressure coefficient distribution (‘smooth’ BL, θ = 120°) 135
Figure 6.24b - RMS pressure coefficient distribution (‘smooth’ BL, θ = 120°) 135
Figure 6.24c - 3s peak pressure coefficient distribution (‘smooth’ BL, θ = 120°) 135
Figure 6.25a - Mean pressure coefficient distribution (‘rough’ BL, θ = 120°) 136
Figure 6.25b - RMS pressure coefficient distribution (‘rough’ BL, θ = 120°) 136

Figure 6.25c - 3s peak pressure coefficient distribution (‘rough’ BL, θ = 120°) 136
Figure 6.26 - Tap positions for the the 150° wind direction 137
Figure 6.27a - Mean pressure coefficient distribution (‘smooth’ BL, θ = 150°) 139
Figure 6.27b - RMS pressure coefficient distribution (‘smooth’ BL, θ = 150°) 139
Figure 6.27c - 3s peak pressure coefficient distribution (‘smooth’ BL, θ = 150°) 139
Figure 6.28a - Mean pressure coefficient distribution (‘rough’ BL, θ = 150°) 140
Figure 6.28b - RMS pressure coefficient distribution (‘rough’ BL, θ = 150°) 140
Figure 6.28c - 3s peak pressure coefficient distribution (‘rough’ BL, θ = 150°) 140
Figure 6.29 - Tap positions for the 180° wind direction 141
Figure 6.30a - Mean pressure coefficient distribution (‘smooth’ BL, θ = 180°) 143
Figure 6.30b - RMS pressure coefficient distribution (‘smooth’ BL, θ = 180°) 143
Figure 6.30c - 3s peak pressure coefficient distribution (‘smooth’ BL, θ = 180°) 143
Figure 6.31a - Mean pressure coefficient distribution (‘rough’ BL, θ = 180°) 144
Figure 6.31b - RMS pressure coefficient distribution (‘rough’ BL, θ = 180°) 144
Figure 6.31c - 3s peak pressure coefficient distribution (‘rough’ BL, θ = 180°) 144
Figure 6.32a - Mean pressure coefficient distribution for the flat vault (‘smooth’ BL, θ = 15°, 30°, 45°) 147
Figure 6.32b - RMS pressure coefficient distribution for the flat vault (‘smooth’ BL, θ = 15°, 30°, 45°) 147
Figure 6.33a - Mean pressure coefficient distribution for the flat vault (‘rough’ BL, θ = 15°, 30°, 45°) 147
Figure 6.33b - RMS pressure coefficient distribution for the flat vault (‘rough’ BL, θ = 15°, 30°, 45°) 147
Figure 6.34a - Mean pressure coefficient distribution for the concave vault (‘smooth’ BL, θ = 15°, 30°, 45°) 148
Figure 6.34b - RMS pressure coefficient distribution for the concave vault (‘smooth’ BL, θ = 15°, 30°, 45°) 148
Figure 6.35a - Mean pressure coefficient distribution for the concave vault (‘rough’ BL, θ = 15°, 30°, 45°) 148

Figure 6.35b - RMS pressure coefficient distribution for the concave vault ('rough' BL, θ = 15°, 30°, 45°) 148
Figure 6.36a - Mean pressure coefficient distribution for the convex vault ('smooth' BL, θ = 15°, 30°, 45°) 149
Figure 6.36b - RMS pressure coefficient distribution for the convex vault ('smooth' BL, θ = 15°, 30°, 45°) 149
Figure 6.37a - Mean pressure coefficient distribution for the convex vault ('rough' BL, θ = 15°, 30°, 45°) 149
Figure 6.37b - Mean pressure coefficient distribution for the convex vault ('rough' BL, θ = 15°, 30°, 45°) 149
Figure 6.38a - Mean pressure coefficient distribution for the flat cross vault ('smooth' BL, θ = 45°, 60°, 75°) 151
Figure 6.38b - RMS pressure coefficient distribution for the flat cross vault ('smooth' BL, θ = 45°, 60°, 75°) 151
Figure 6.39a - Mean pressure coefficient distribution for the flat cross vault ('rough' BL, θ = 45°, 60°, 75°) 151
Figure 6.39b - RMS pressure coefficient distribution for the flat cross vault ('rough' BL, θ = 45°, 60°, 75°) 151
Figure 6.40a - Mean pressure coefficient distribution for the concave cross vault ('smooth' BL, θ = 45°, 60°, 75°) 152
Figure 6.40b - RMS pressure coefficient distribution for the concave cross vault ('smooth' BL, θ = 45°, 60°, 75°) 152
Figure 6.41a - Mean pressure coefficient distribution for the concave cross vault ('rough' BL, θ = 45°, 60°, 75°) 152
Figure 6.41b - RMS pressure coefficient distribution for the concave cross vault ('rough' BL, θ = 45°, 60°, 75°) 152
Figure 6.42a - Mean pressure coefficient distribution for the convex cross vault ('smooth' BL, θ = 45°, 60°, 75°) 153
Figure 6.42b - RMS pressure coefficient distribution for the convex cross vault ('smooth' BL, θ = 45°, 60°, 75°) 153

Figure 6.43a - Mean pressure coefficient distribution for the convex cross vault ('rough' BL, θ = 45°, 60°, 75°) 153
Figure 6.43b - Mean pressure coefficient distribution for the convex cross vault ('rough' BL, θ = 45°, 60°, 75°) 153
Figure 6.44a - Mean pressure coefficient distribution for the flat cross vault ('smooth' BL, θ = 120° and 150°) 155
Figure 6.44b - RMS pressure coefficient distribution for the flat cross vault ('smooth' BL, θ = 120° and 150°) 155
Figure 6.45a- Mean pressure coefficient distribution for the flat cross vault ('rough' BL, θ = 120° and 150°) 155
Figure 6.45b- RMS pressure coefficient distribution for the flat cross vault ('rough' BL, θ = 120° and 150° 155
Figure 6.46a - Mean pressure coefficient distribution for the concave cross vault ('smooth' BL, θ = 120° and 150°) 156
Figure 6.46b - RMS pressure coefficient distribution for the concave cross vault ('smooth' BL, θ = 120° and 150°) 156
Figure 6.47a - Mean pressure coefficient distribution for the concave cross vault ('rough' BL, θ = 120° and 150°) 156
Figure 6.47b - RMS pressure coefficient distribution for the concave cross vault ('rough' BL, θ = 120° and 150°) 156
Figure 6.48a - Mean pressure coefficient distribution for the convex cross vault ('smooth' BL, θ = 120° and 150°) 157
Figure 6.48b - RMS pressure coefficient distribution for the convex cross vault ('smooth' BL, θ = 120° and 150°) 157
Figure 6.49a- Mean pressure coefficient distribution for the convex cross vault ('rough' BL, θ = 120° and 150°) 157
Figure 6.49b- RMS pressure coefficient distribution for the convex cross vault ('rough' BL, θ = 120° and 150°) 157
Figure 6.50 - Intrumented area for the the 0° wind direction 158
Figure 6.51a - Mean pressure distribution for θ = 0°
(Flat cross vault, 'smooth' BL) 159

Figure 6.51b - RMS pressure distribution for θ = 0°
(Flat cross vault, ‘smooth’ BL) 159
Figure 6.52a - Mean pressure distribution for θ = 0°
(Flat cross vault, ‘rough’ BL) 160
Figure 6.52b - RMS pressure distribution for θ = 0°
(Flat cross vault, ‘rough’ BL) 160
Figure 6.53a - Mean pressure distribution for θ = 0°
(Convex cross vault, ‘smooth’ BL) 161
Figure 6.53b - RMS pressure distribution for θ = 0°
(Convex cross vault, ‘smooth’ BL) 161
Figure 6.54a - Mean pressure distribution for θ = 0°
(Convex cross vault, ‘rough’ BL) 162
Figure 6.54b - RMS pressure distribution for θ = 0°
(Convex cross vault, ‘rough’ BL) 162
Figure 6.55a - Mean pressure distribution for θ = 0°
(Concave cross vault, ‘smooth’ BL) 163
Figure 6.55b - RMS pressure distribution for θ = 0°
(Concave cross vault, ‘smooth’ BL) 163
Figure 6.56a - Mean pressure distribution for θ = 0°
(Concave cross vault, ‘rough’ BL) 164
Figure 6.56b - RMS pressure distribution for θ = 0°
(Concave cross vault, ‘rough’ BL) 164
Figure 6.57a- Mean pressure distribution for θ = 30°
(Flat cross vault, ‘smooth’ BL) 165
Figure 6.57b - RMS pressure distribution for θ = 30°
(Flat cross vault, ‘smooth’ BL) 165
Figure 6.58a - Mean pressure distribution for θ = 30°
(Flat cross vault, ‘rough’ BL) 166
Figure 6.58b - RMS pressure distribution for θ = 30°
(Flat cross vault, ‘rough’ BL) 166
Figure 6.59a- Mean pressure distribution for θ = 30°
(Convex cross vault, ‘smooth’ BL) 167

Figure 6.59b - RMS pressure distribution for θ = 30°
(Convex cross vault, ‘rough’ BL) 167
Figure 6.60a - Mean pressure distribution for θ = 30°
(Convex cross vault, ‘rough’ BL) 168
Figure 6.60b - RMS pressure distribution for θ = 30°
(Convex cross vault, ‘rough’ BL) 168
Figure 6.61a - Mean pressure distribution for θ = 30°
(Concave cross vault, ‘smooth’ BL) 169
Figure 6.61b - RMS pressure distribution for θ = 30°
(Concave cross vault, ‘smooth’ BL) 169
Figure 6.62a - Mean pressure distribution for θ = 30°
(Concave cross vault, ‘rough’ BL) 170
Figure 6.62b - RMS pressure distribution for θ = 30°
(Concave cross vault, ‘rough’ BL) 170
Figure 6.63a - Mean pressure distribution for θ = 60°
(Flat cross vault, ‘smooth’ BL) 171
Figure 6.63b - RMS pressure distribution for θ = 60°
(Flat cross vault, ‘smooth’ BL) 171
Figure 6.64a - Mean pressure distribution for θ = 60°
(Flat cross vault, ‘rough’ BL) 172
Figure 6.64b - RMS pressure distribution for θ = 60°
(Flat cross vault, ‘rough’ BL) 172
Figure 6.65a - Mean pressure distribution for θ = 60°
(Convex cross vault, ‘smooth’ BL) 173
Figure 6.65b - RMS pressure distribution for θ = 60°
(Convex cross vault, ‘rough’ BL) 173
Figure 6.66a - Mean pressure distribution for θ = 60°
(Convex cross vault, ‘rough’ BL) 174
Figure 6.66b - RMS pressure distribution for θ = 60°
(Convex cross vault, ‘rough’ BL) 174
Figure 6.67a - Mean pressure distribution for θ = 60°
(Concave cross vault, ‘smooth’ BL) 175

Figure 6.67b - RMS pressure distribution for θ = 60°
(Concave cross vault, 'smooth' BL) 175
Figure 6.68a - Mean pressure distribution for θ = 60°
(Concave cross vault, 'rough' BL) 176
Figure 6.68b - RMS pressure distribution for θ = 60°
(Concave cross vault, 'rough' BL) 176
Figure 6.69 - Smoke visualization at roof edge 177
Figure 6.70 - Centreline RMS pressure coefficient distribution for θ = 0° and 180°
178
Figure 6.71 - Smoke visualization in front of the flat cross vault 178
Figure 6.72 - Flow direction devices in front and attached to a model for the 0°
wind direction 179
Figure 6.73 - Flow direction devices behind a model for the 0° wind direction 179
Figure 7.1 - Manifold attached to the flat cross vault 181
Figure 7.2 - Comparison of mean pressure coefficients (Taps 2, 3, 5 and 6) 183
Figure 7.3 - Comparison of RMS pressure coefficients (Area 2) 184
Figure 7.4 - Simple representations of the numerically averaged areas 185
Figure 7.5a - Mean pressure coefficient variation with wind direction
[Area 1 (Taps 2, 3, 5 and 6) and ('smooth' BL)] 188
Figure 7.5b - RMS pressure coefficient variation with wind direction
[Area 1 (Taps 2, 3, 5 and 6) and ('smooth' BL)] 188
Figure 7.5c - Negative 3s peak pressure coefficient variation with wind direction
[Area 1 (Taps 2, 3, 5 and 6) and ('smooth' BL)] 188
Figure 7.6a - Mean pressure coefficient variation with wind direction
[Area 1 (Taps 2, 3, 5 and 6) and ('rough' BL)] 189
Figure 7.6b - RMS pressure coefficient variation with wind direction
[Area 1 (Taps 2, 3, 5 and 6)] and ('rough' BL)] 189
Figure 7.6c - Negative 3s peak pressure coefficient variation with wind direction
[Area 1 (Taps 2, 3, 5 and 6) and ('rough' BL)] 189
Figure 7.7a - Mean pressure coefficient variation with wind direction
[Area 2 (Taps 1, 2, 3 and 4) and ('smooth' BL)] 190

Figure 7.7b - RMS pressure coefficient variation with wind direction
[Area 2 (Taps 1, 2, 3 and 4) and (‘smooth’ BL)] 190
Figure 7.7c - Negative 3s peak pressure coefficient variation with wind direction
[Area 2 (Taps 1, 2, 3 and 4) and (‘smooth’ BL)] 190
Figure 7.8a - Mean pressure coefficient variation with wind direction
[Area 2 (Taps 1, 2, 3 and 4) and (‘rough’ BL)] 191
Figure 7.8b - RMS pressure coefficient variation with wind direction
[Area 2 (Taps 1, 2, 3 and 4) and (‘rough’ BL)] 191
Figure 7.8c - Negative 3s peak pressure coefficient variation with wind direction
[Area 2 (Taps 1, 2, 3 and 4) and (‘rough’ BL)] 191
Figure 7.9a - Mean pressure coefficient variation with wind direction
[Area 3 (Taps 5, 6, 7 and 8) and (‘smooth’ BL)] 192
Figure 7.9b - RMS pressure coefficient variation with wind direction
[Area 3 (Taps 5, 6, 7 and 8) and (‘smooth’ BL)] 192
Figure 7.9c - Negative 3s peak pressure coefficient variation with wind direction
[Area 3 (Taps 5, 6, 7 and 8) and (‘smooth’ BL)] 192
Figure 7.10a - Mean pressure coefficient variation with wind direction
[Area 3 (Taps 5, 6, 7 and 8) and (‘rough’ BL)] 193
Figure 7.10b - RMS pressure coefficient variation with wind direction
[Area 3 (Taps 5, 6, 7 and 8) and (‘rough’ BL)] 193
Figure 7.10c - Negative 3s peak pressure coefficient variation with wind direction
[Area 3 (Taps 5, 6, 7 and 8) and ‘rough’ BL)] 193
Figure 7.11a - Mean pressure coefficient variation with wind direction
[Area 4 (Taps 3, 4, 6 and 7) and (‘smooth’ BL)] 194
Figure 7.11b - RMS pressure coefficient variation with wind direction
[Area 4 (Taps 3, 4, 6 and 7) and (‘smooth’ BL)] 194
Figure 7.11c - Negative 3s peak pressure coefficient variation with wind direction
[Area 4 (Taps 3, 4, 6 and 7) and (‘smooth’ BL)] 194
Figure 7.12a - Mean pressure coefficient variation with wind direction
[Area 4 (Taps 3, 4, 6 and 7) and (‘rough’ BL)] 195
Figure 7.12b - RMS pressure coefficient variation with wind direction
[Area 4 (Taps 3, 4, 6 and 7) and (‘rough’ BL)] 195

Figure 7.12c - Negative 3s peak pressure coefficient variation with wind direction [Area 4 (Taps 3, 4, 6 and 7) and 'rough' BL)] 195
Figure 8.1- Local cladding damage observed on the Good Hope Centre 197
Figure 8.2 - Design coefficients at central locations for the flat roof for any wind direction 201
Figure 8.3 - Design coefficients at central locations for the convex roof for any wind direction 201
Figure 8.4 - Design coefficients at central locations for the concave roof for any wind direction 201
Figure 8.5 - EN 1991-1-4 $Cpe10$ distribution 203
Figure 8.6 - Mean design pressure coefficients for arch-roof building (Reproduced from Paluch et al (2003)) 203
Figure 8.7 - Surface point pressure distribution for a single circular vault (Reproduced from Toy and Tahouri (1988)) 204
Figure 8.8 - Mean point pressures coefficients for θ=90° 204
Figure 8.9 - Mean design pressure coefficients for arch-roof building (f/b =0.3, h/b =0.12) (Data from Paluch et al (2003)) 205
Figure 8.10 - Surface pressure distribution for a single circular vault (L/f=2 and f/d=0.5) (Reproduced from Toy and Tahouri (1988)) 205
Figure 8.11 - Specified duo-pitch areas (Reproduced from EN 1991 -1-4) 206
Figure 8.12 - Plan view: pressure coefficient segments for the 0° direction 208
Figure 8.13 - Plan view: pressure coefficient segments for the 30°- 60° directions 210
Figure A1 – Pressure distribution parameters 224
Figure C1 - Pressure coefficient variation with wind direction (Tap 1) 227
Figure C2 - Pressure coefficient variation with wind direction (Tap 2) 228
Figure C3 - Pressure coefficient variation with wind direction (Tap 3) 229
Figure C4 - Pressure coefficient variation with wind direction (Tap 4) 230
Figure C5 - Pressure coefficient variation with wind direction (Tap 5) 231
Figure C6 - Pressure coefficient variation with wind direction (Tap 6) 232
Figure C7 - Pressure coefficient variation with wind direction (Tap 7) 233
Figure C8 - Pressure coefficient variation with wind direction (Tap 8) 234

LIST OF TABLES

Table 2.1 - Characteristic parameters of the mean pressure distributions (Data from Ribeiro (1991)) 48
Table 3.1 - Difference in model dimensions 65
Table 3.2 - Lieblein (BLUE) for Fisher Tippett Type 1 distribution (Data from Cook (1985)) 74
Table 4.1 - Relative roughness 80
Table 4.2 - Results of the ESDU drag coefficient procedure 82
Table 5.1 - Percent difference (RMS pressure coefficient, flat cross vault) 101
Table 8.1 - Lowest measured mean, 10s and 3s peak pressure coefficients ('smooth' boundary-layer) 199
Table 8.2 - Lowest measured mean, 10s and 3s peak pressure coefficients ('rough' boundary-layer) 200
Table 8.3 - Area-averaged design coefficients for any wind direction 202
Table 8.4 - Area-averaged pressure coefficients (Data from Blackmore and Tsokri (2006)) 206
Table 8.5 - Flat cross vault surface averaged pressure coefficients 207
Table 8.6 - Pressure coefficient values corresponding to the areas defined in Figure 8.12 208
Table 8.7 - Wall pressures 209
Table 8.8 – Pressure coefficient values corresponding to the areas defined in Figure 8.13 210
Table B1 - Experimental Range (Mean C*p*) 225
Table B2 - Experimental Range (RMS C*p*) 225
Table B3 - Range (Negative 10s Peak C*p*) 226
Table B4 - Range (Negative 3s Peak C*p*) 226

LIST OF SYMBOLS

Drag coefficient ..... C_D

Mean drag coefficient for a 2d circular cylinder ..... C_{D0}

Pressure coefficient ..... Cp

Area-averaged pressure coefficient ..... Cp_{av}

Mean pressure coefficient ..... Cp_{mean}

Peak pressure coefficient ..... Cp_{peak}

Root mean square pressure coefficient ..... Cp_{RMS}

Mean pressure coefficient corresponding to an area of 10m^2 or larger ..... Cpe_{10}

Vault diameter ..... d [L]

Vault height ..... f [L]

Wall height ..... h [L]

Longitudinal turbulence intensity ..... I_u

Lateral turbulence intensity ..... I_v

Vertical turbulence intensity ..... I_w

Effective roughness height ..... k [L]

Von Karmen constant ..... k

Longitudinal scale of turbulence ..... L_u [L]

Frequency ..... n [T^{-1}]

Mean pressure ..... p_{mean} [FL^{-2}]

Peak pressure ..... p_{peak} [FL^{-2}]

Probability ..... P

Rise ..... r [L]

Reynolds number ..... R$_e$

Critical Reynolds number ..... R_{ecrit}

Effective Reynolds number ..... R_{ee}

Span ..... s [L]

Power spectral density function ..... $S_v(Z,n)$[L^{2}T^{-1}]

Mean wind velocity at a predefined height ..... $\bar{V}$ [LT^{-1}]

Instantaneous longitudinal free-stream speed ..... v(t) [LT^{-1}]

Fluctuating component of the wind speed ..... v'(t) [LT^{-1}]

Height ..... z [L]

Gradient height ..... Z_G [L]

Wind speed at the gradient height ..... V_{ZG} [LT^{-1}]

Power law exponent ..... α

Angle ..... θ

Turbulence parameter ..... λ_T

Roughness parameter ..... λ_R

Kinematic viscosity of air ..... υ [L^2T^{-1}]

Free-stream air density. ..... ρ [ML^{-3}]

Standard deviation ..... σ

Shear stress at the ground surface ..... τ_0 [FL^{-2}]

Roof pitch ..... Ø

1 INTRODUCTION

1.1 General

Modern developments in construction technology and materials have led to many new trends in the architectural and engineering environments. Curved roof structures are increasingly being used as they provide better functionality and economic benefits. Of importance to structural engineers is that arched structures are aerodynamically efficient and effective in load transfer.

The cross vault is one such arched roof structure which is very efficient in the transfer of load. The cross vault comprises two intersecting arched vaults, in which loads are transferred via the four intersecting diagonals to the supports. The structure requires restraining abutments at its four corners to provide support against the thrusts noted above. The Good Hope Centre in Cape Town is an example of a large cross vault structure constructed with pre-cast concrete beams and coffers, which support the roof cladding. The structure is shown in Figure 1.1 below.



Figure 1.1 - Cross vault structure (Good Hope Centre, Cape Town)

Cross vault structures are efficient and economic, but little is known about their wind load distribution. There is, however, a wealth of information on wind loads and resulting damage done to cladding on both curved roof and sharp edged bluff body structures. Some loading codes provide design information for simple curved roof structures. However, their use when designing roofing for cross vault structures is not entirely applicable, due to the significant geometrical variations. The following sections discuss the scope and objectives of the experimental study.

1.2 Objectives

The objective of this research work was to assess various conditions which effect the wind pressure distribution over cross vault structures. This investigation provides information on the sensitivity of these types of structure to surface roughness (Reynolds number), wind direction, flow characteristics and geometrical changes of the apex (rise) of the cross vault roofs.

In order to ascertain the effects of these previously mentioned conditions, a series of wind-tunnel tests was conducted in a Boundary-Layer Wind-Tunnel (BLWT), at the Council for Scientific and Industrial Research (CSIR), located in Pretoria, South Africa. Three cross vault roof forms were tested in two different boundary-layer profiles and with differing magnitudes of model surface roughness. The three cross vault types tested were the flat, convex and concave cross vaults.

Pressure tapings on all models were positioned in the same places, and mean, root-mean-square (RMS), negative 3 second peak and 10 second peak pressure coefficients were measured. Surface averaged pressures were also derived.

1.3 Scope

Chapter 2 presents a review of previous work conducted on sharp and curved roof models, with emphasis on the effects of Reynolds number, surface roughness and flow characteristics on the pressure distributions.

Chapter 3 presents information on the model configuration, and a description of the experimental techniques, data acquisition and processing. The information on

the aerodynamic characteristics of the upstream flow and boundary-layer characteristics is also provided in this chapter.

Chapter 4 presents the experimental results of comparative tests conducted on the flat cross vault, at selected pressure taps and specific wind directions, to assess the effects of surface roughness on the mean and fluctuating pressure coefficients. These experimental results, in combination with the Engineering Science Data Item (ESDU) - 80025 (1980) procedure for simulating the pressure distribution over a circular cylinder situated in high Reynolds number flow, were assessed to ascertain whether surface roughening was required.

The effect of turbulence intensity on the measured mean, RMS and negative 3s peak pressures is discussed in Chapter 5.

Chapter 6 presents local pressure coefficients for the flat, convex and concave cross vault structures. The effect of vault type is discussed and mean and negative peak pressure coefficient distributions are identified.

Chapter 7 presents surface averaged pressure coefficients for the three forms of cross vault structure.

Chapter 8 firstly presents design coefficients at central areas of the cross vault structures. Secondly, selected design coefficients over cross vault structures are compared with codified and experimental data intended for the design of single vaults.

Conclusions and recommendations are made in Chapter 9.

2 LITERATURE REVIEW

2.1 Introduction

Generally, the work published which relates to vaulted structures, pertains to single vaults or circular cylinders and no research was found on wind effects on cross vault structures. There is, however, a wealth of information on aspects relating to bluff body structures and wind-tunnel testing procedures, which are applicable to the current investigation. Besides the research mentioned in this report, many other papers were also reviewed and are referenced in the bibliography.

2.2 Design Information

Complex curved roof structures have had little experimentation into the effects of wind on their exterior surfaces. Researchers, such as Blessmann (1996), Taylor (1991), Melbourne and Cheung (1983), have conducted numerous experimental investigations on single vaults, domes and curved roof structures to provide design coefficients. Many studies have also been conducted to assess the sensitivity of surface pressures to specific parameters, namely: the Reynolds number, surface roughness, wind speed profile and turbulence characteristics. These parameters are considered vitally important for curved roof structures and for this reason, any information given in codes of practice is only considered to be suitable for preliminary design.

Simple generic structural forms are included in international codes of practice for the design of single vault structures and domes. Codes such as SABS 0160 -1989, provide pressure coefficients for a circular cylinder normal to flow, whereas EN 1991-1-4 presents design information for simple curved roof structures such as domes, cylinders and semi- circular roofs. The design values from various codes of practice and text-books are identified and discussed in this section. Comparisons of pressure coefficient values, given in Sachs (1972), EN 1991-1-4 (2005), USSR; BC and R 2.01.07-85 and China; GB 50009 -2001, for an arched roof with rise-to-span ratio (r/s) equal to 0.5, are shown in Figure 2.1. The values

denoted Cpe_{10}, as given in EN 1991-1-4, refer to pressure coefficient values appropriate to an area of $10m^2$ or larger, corresponding to overall loading.

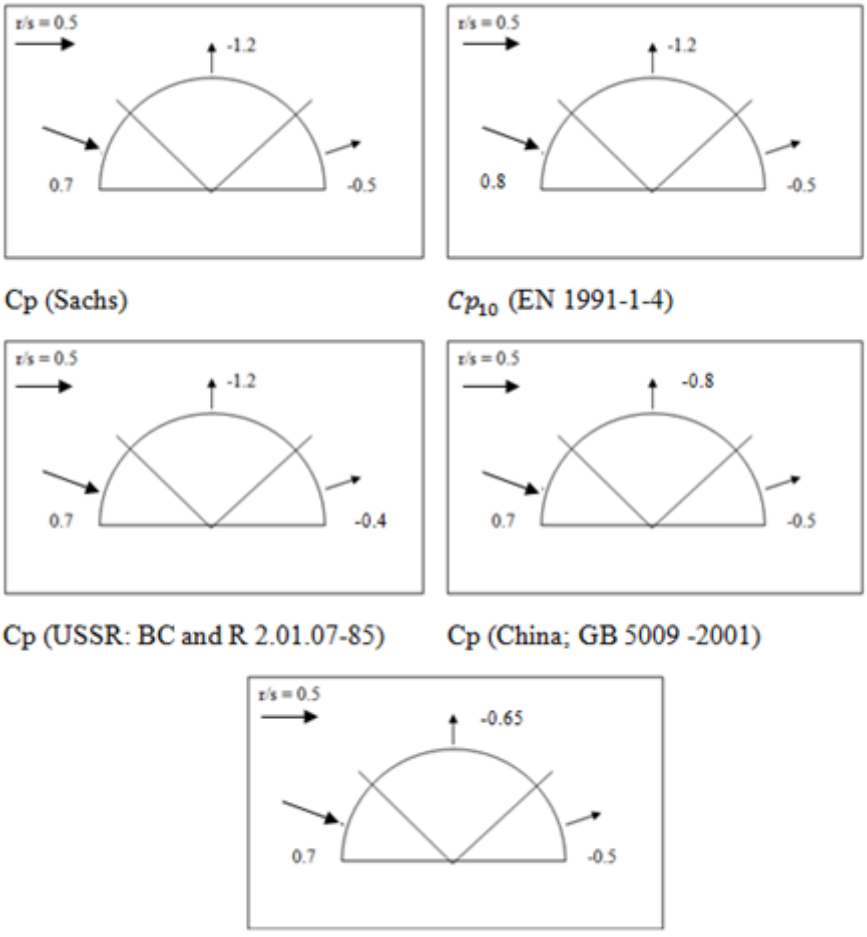


Figure 2.1 - Design pressure distributions for simple vault structures

Blackmore and Tsokri (2006) compared pressure distributions over single vault structures found in various codes with experimentally measured results. Their results indicate that codes of practice, used internationally, provide widely varying pressure coefficients, as shown in Figure 2.2. The authors indicate that in some cases, wind-tunnel testing was conducted without any simulation of natural flow conditions, which is of great importance to flow separation and ultimately pressure distributions over curved roof structures. Figure 2.2 clearly indicates the discrepancies observed and emphasizes that the correct simulation of wind-tunnel testing is crucial in attaining similitude between model and full scale structures.

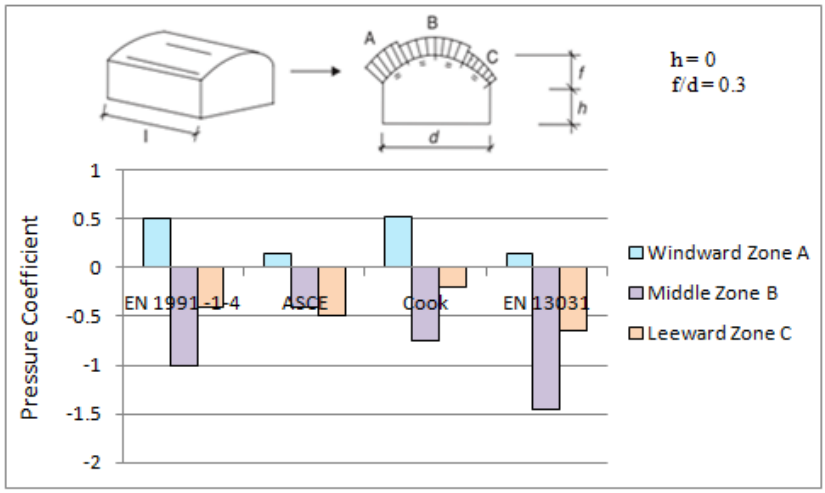


Figure 2.2 - Comparison of *Cp* values from codes and experimental results (Reproduced from Blackmore and Tsokri (2006))

The general trend in many codes of practice is that design pressure coefficients are given for the two most critical cases. These cases are defined by the direction of the wind and include wind blowing either normal or parallel to the eaves. For the wind blowing normal to the eaves (θ = 90°), there is no information given in EN 1991-1-4 or SANS 10160-1989. However, Blackmore and Tsokri (2006) conducted tests on curved roofs and compared their results with EN 1991-1-4 duo-pitch roof data. Their findings generally showed satisfactory agreement for design purposes. They also noted that their data for curved roof structures was marginally dependant on the side wall height (h), which ultimately allowed their comparison to the codified duo-pitch information. Their method requires a pitch angle to be assigned to the curved roof. The pitch angle (Ø) used to classify the curved roof is given by:

$$Ø = \tan^{-1}(f/0.5d) \qquad (2.1)$$

where f is the wall height and d is the diameter of the vault.

The results of their comparison are shown in Figure 2.3. The authors noted that there was poor agreement for the area 'G', as shown in Figure 2.3, which they

attributed to the effects of vortices shed from the ridge of the duo-pitch roofs. There was, however, satisfactory agreement found for the zones 'F', 'H' and 'I'.

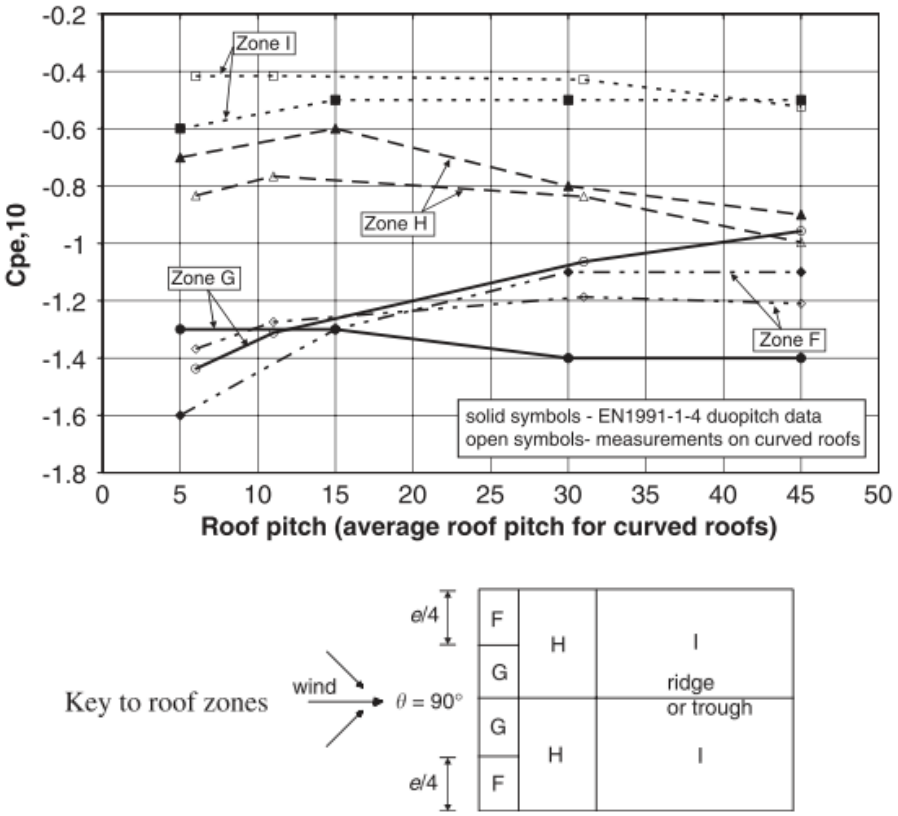


Figure 2.3 - Comparison of curved roof data with duo-pitch data for θ=90°
(Reproduced from Blackmore and Tsokri (2006))

The applicability of codes of practice and published research conducted on single vault structures for the design of cross vault structures is questionable, and is discussed in further detail in Chapter 8. It should be noted that for the eaves normal to the flow, the edge suctions and pressure distribution ahead of the vault intersection should be the same as those for single vaults, because there is no effect of the intersecting vault at these positions.

2.3 Role of Wind-Tunnel Technology

The application of wind-tunnel research to determine wind loading on buildings, or other structural elements, is generally conducted when shapes are considerably different from those given in codes of practice. The realistic evaluation of wind

loading is best achieved by the use of BLWT apparatus, which has progressed appreciably from the conventional wind-tunnel with smooth, uniform flow. The evaluation of wind loads within boundary-layer wind-tunnels has become faster and more economical, as a result of improved methodologies and technologies, and is preferred over full-scale testing, which is generally an expensive undertaking.

Boundary-layer wind-tunnel investigations provide economic solutions to a wide range of applications which include: wind loading, wind induced response of structures, dispersion of air pollutants, wind environment, wind shelter and a tool for computational fluid dynamics simulation verification. Wind-tunnel investigations generally result in loading that is more accurate than that provided in codes, since modern developments have led to more accurate testing techniques. Moreover, codes refer to generic geometrical forms, while wind-tunnel testing can model the actual situation and form of a specific building. Boggs and Lepage (2004) note that wind-tunnel loads are usually lower than those given in codes, which results in greater economy; however, in some cases, wind-tunnel loads can be greater, resulting in greater safety and reduced maintenance, which all contribute to long term economy.

2.4 Wind-Tunnel Testing Requirements for Pressure Measurement

2.4.1 Similarity requirements

The similarity requirements for the measurement of pressure coefficients over rigid models are as follows:

1) The external geometric shape and aerodynamic solidity.
2) Mean wind speed profile, longitudinal intensity of turbulence, spectral distribution of turbulence and the related length scale of turbulence.
3) Reynolds number (for structures with curved surfaces).

The geometric similarity requirement is apparent, and is not discussed in the current document. The flow characteristics and Reynolds number are, however, discussed in the following sections.

2.4.2 Atmospheric boundary-layer requirements

The atmospheric boundary-layer is a complex system in which the wind is affected by terrain roughness, the wind climate and temperature variations. Full-scale free-stream flow at low elevations is described by a large number of physical parameters. However, boundary-layer modelling principally entails developing the characteristics of strong winds in relation to the geometrical scale of the building model to be tested. The simulation of the wind speed and turbulence characteristics are considered important, as their influence may be considerable on the mean, root-mean-square (RMS) and peak pressures. Peak suction pressures usually occur at corners and leading edges for bluff body structures and are affected by the mean wind profile and turbulence of the oncoming flow. To attain the best re-creation of actual conditions, these factors should be considered in wind-tunnel testing.

The effects of ground roughness and various obstructions cause flow retardation near the surface, which causes wind speed reduction. A number of formulations are used to describe the variation of wind speed with height, which can be grouped into two generic types, namely: power and logarithmic law formulas.

The power law, as given by Stathopoulos and Baniotopoulos (2007), is an empirical equation and is expressed as:

$$\frac{\overline{V_z}}{\overline{V_{zG}}} = \left(\frac{Z}{Z_G}\right)^{\alpha} \tag{2.2}$$

where Z_G is the gradient height (i.e. the point above which the wind speed is assumed constant) and α is the appropriate power corresponding to pre-defined roughness categories. Both Z_G and α are functions of the ground roughness. The logarithmic law is based on the mechanics of approximately the bottom 30% of

the boundary-layer. Stathopoulos and Baniotopoulos (2007) express this variation of wind speed with height as:

$$\overline{V_z} = \frac{u}{k} * ln\frac{Z}{Z_0} \tag{2.3}$$

where Z_0 is the roughness length, k is the Von Karmen constant = 0.4 and

$$u = \sqrt{\frac{\tau_0}{\rho}} \tag{2.4}$$

where τ_0 is the shear stress at the ground surface and ρ is the air density.

The wind speed is comprised of both mean and fluctuating components. The instantaneous wind speed measured at a specific point is a function of time, and is expressed in the form given below:

$$v(t) = \bar{V} + v'(t), \tag{2.5}$$

where $\bar{V}$ is the mean speed and $v'(t)$ is the fluctuating component. Figure 2.4 illustrates a typical speed time history, identifying the mean and fluctuating components noted above.

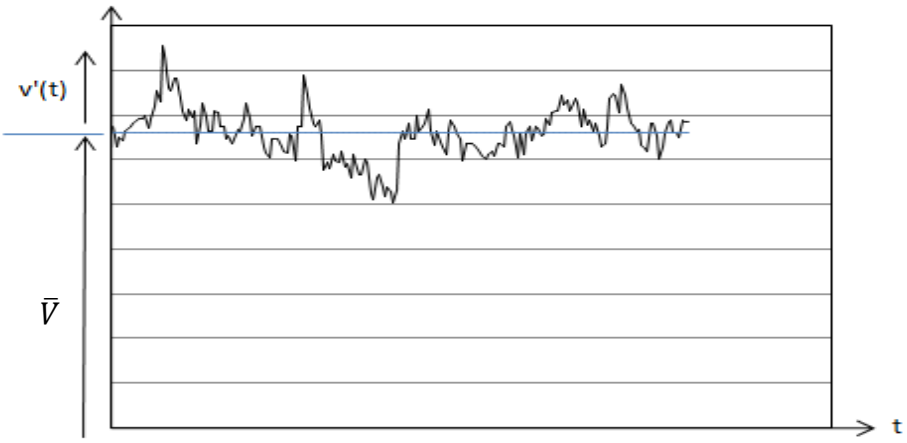


Figure 2.4 - Typical wind speed time history

The fluctuating component is produced by two different actions, which are meteorological processes and the effect of ground roughness. The turbulence characteristics of the atmospheric winds can be described in terms of the turbulence intensity and the spectral density functions.

Different structural forms are more sensitive to a particular fluctuating component. Scruton (1981) notes that structures sensitive to Reynolds number, such as vaults, are influenced by the longitudinal fluctuations, bridges are affected more severely by the vertical fluctuations and high rise structures by the lateral fluctuations. The turbulence intensities for the longitudinal, vertical and lateral directions are given below:

$$Iu = {}^{\sigma_u}/_{\bar{V}} \tag{2.6}$$

$$Iv = {}^{\sigma_v}/_{\bar{V}} \tag{2.7}$$

$$Iw = {}^{\sigma_w}/_{\bar{V}} \tag{2.8}$$

where σ_u, σ_v and σ_w are the standard deviations (root-mean-square) of the fluctuating velocities and $\bar{V}$ is the mean speed.

The size and frequency of gusts within the simulated boundary-layer need to be correctly scaled in order to achieve a reliable simulation. This is achieved by similitude of the model and full-scale longitudinal power spectral densities. The spectral density describes the distribution of turbulence with frequency and many mathematical formulations have been proposed in this regard. Holmes (2001) notes that one of the most commonly used longitudinal power spectral density equations is the non-dimensional Von Karmen-Harris equation, as given below:

$$\frac{nS_v(Z,n)}{\sigma^2} = \frac{4(\frac{nL_u}{V})}{[1+70.8(\frac{nL_u}{V})^2]^{\frac{5}{6}}} \tag{2.9}$$

where $S_v(Z,n)$ is the power spectral density function, n is the frequency, $\bar{V}$ is the mean speed, σ^2 is the variance and L_u is the longitudinal intergral length scale of turbulence.

2.4.3 Reynolds number

The Reynolds number is a dimensionless parameter expressed as the ratio of inertial to viscous forces, and is expressed as:

$$Re = \frac{\bar{V}\mathrm{d}}{\upsilon} \tag{2.10}$$

where $\bar{V}$ is the wind speed at the relevant height, d is the diameter of curvature, and υ is the kinematic viscosity of air.

A requirement in wind-tunnel testing is that the model and full scale Reynolds numbers should be similar. If this is achieved, then according to fluid mechanics principles, the flow patterns and pressure distributions will be similar between the model and the actual structure. However, it is impossible to achieve exact similarity in a low speed wind-tunnel because of the limitations of model size and wind speed.

It has been shown, through numerous tests, that Reynolds number is not critical for geometric shapes with sharp edges. This is evident in most buildings where flow separation occurs at sharp edges and corners and, ultimately, flow patterns are dependent on geometry and not the Reynolds number. The Reynolds number similarity requirement is, therefore, relaxed for sharp edged structures in wind-tunnel tests.

This relaxation is, however, not appropriate for the flow patterns and pressure distribution over curved roof structures. Tests conducted by Taylor (1992) and Cheung and Melbourne (1983) have shown that the points of flow separation and the characteristics of the wake region over curved surfaces, are dependent on the magnitude of the viscous forces in the boundary-layer and are, therefore,

Reynolds number sensitive. This aspect is of concern when testing curved roof structures, since most low speed wind-tunnels operate in the subcritical Reynolds number regime, whereas full-scale structures are almost always in the supercritical regime. Figure 2.5 compares the mean centreline pressure distribution over a circular cylinder for subcritical and supercritical flows, and indicates the effects of differing Reynolds number regime on mean surface pressures.

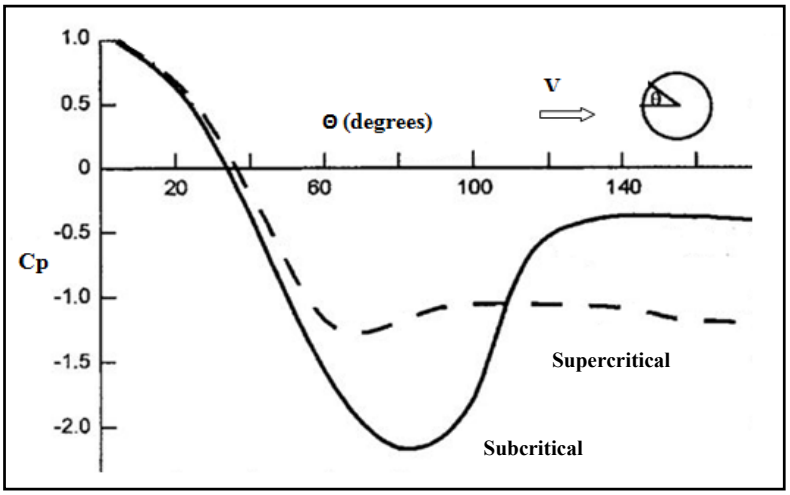


Figure 2.5 - Pressure distribution over a circular cylinder for subcritical and supercritical Reynolds numbers (Reproduced from Holmes (2001))

As indicated previously, full scale Reynolds number regimes are supercritical and wind-tunnel modelling therefore requires various artificial means to be implemented to achieve regime similitude. These means include; the use of gases and roughening of the model surface to induce higher Reynolds number flow. Furthermore, the addition of turbulence to the oncoming flow reduces the reliance of pressure distributions on Reynolds number for bodies with curved surfaces. These aspects are discussed in greater detail in the section 2.8.

2.5 Effects of the Mean Wind Profile and Turbulence Characteristics on Sharp Edged Bluff Body Structures

Recent research has confirmed the importance of the correct simulation of wind speed profile, turbulence intensities and integral scales of the incident flow on the pressure coefficients over low-rise rectangular and curved roof buildings. The

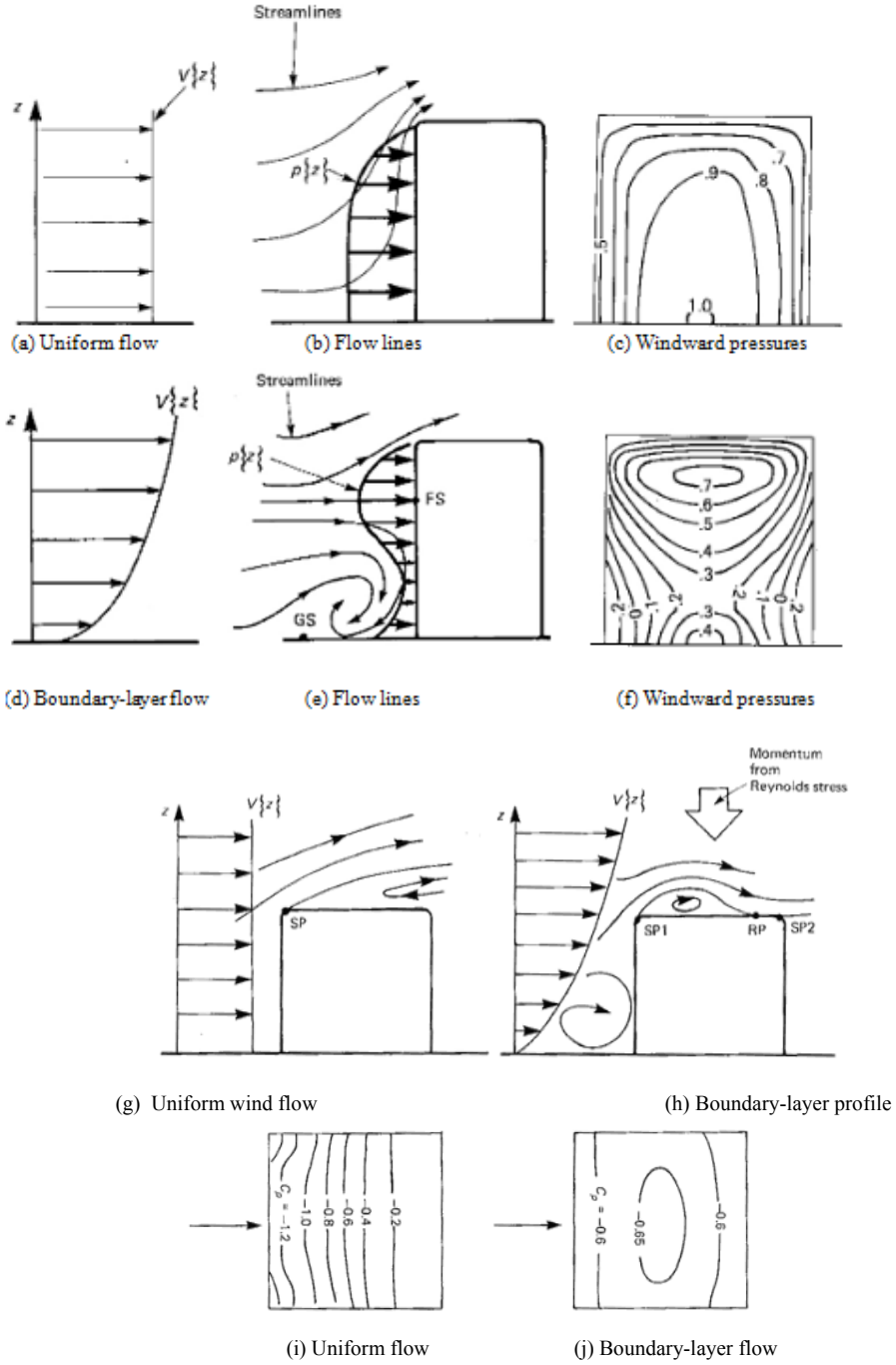
effect of the mean wind profile on the separation points, reattachment points and pressure distribution, for bluff body structures, is shown in Figure 2.6, which is reproduced from Cook (1985).

Cook (1985) shows that in uniform flow, the wind flows over the top and around the sides of the building, whereas for boundary-layer flow, there is also a tendency for flow to move down the face. In uniform wind flow, the flow from the full height of the building rises over the roof, as shown in Figure 2.6(b). However, for boundary-layer flow, the flow comes to rest at approximately two-thirds the height of the wall, as shown in Figure 2.6(e). The wind flow above this point rises over the roof, whereas flow below this point travels towards the ground. This downward flow has higher kinetic energy than the oncoming flow at this level, and therefore moves forward towards the wind. This flow slowly loses energy and forms a vortex, as shown in Figure 2.6(e). This vortex has a significant influence on the pressure distribution and flow around the sides of the structure. The flow patterns and resulting pressure distributions, on the windward face, are shown in Figure 2.6(c) and 2.6(f).

Figures 2.6(g) and 2.6(h) illustrate that there is a lower separation streamline for the boundary-layer flow, which is due to only a third of the flow rising over the roof and the displaced flow having higher kinetic energy, due to the mean wind profile. Cook (1985) notes that earlier flow re-attachment may occur for boundary-layer wind because of vorticity in the shear layer along the separation boundary-layer and the Reynolds stress of the atmospheric boundary-layer. For uniform flow, re-attachment will occur only if the building is long enough in the direction of flow.

Cook (1985) shows that, for the top third of the bluff body, flow around the sides is not dissimilar for boundary-layer and uniform flow. However, for boundary-layer flow, the flow lower down is influenced by the preceding ‘horseshoe’ vortex (as discussed previously) and is faster than the incident flow at the respective height. The pressures on the sides increase, as the distance from the leading edge

increases, as noted for the roof. However, the vortex causes vertical mixing and, ultimately, only slight vertical pressure variation.



(SP - separation, RP – reattachment and FS – stagnation point)

Figure 2.6 - Separation, reattachment and pressure coefficient distribution over flat roofs (Reproduced from Cook (1985))

The effects of turbulence characteristics on the flow patterns and pressure coefficients over sharp edged bluff body structures have been assessed by numerous researchers. "Bearman commenting on experiments performed on square prisms has suggested the possibility that turbulence, while increasing the mixing of the shear layer, may weaken the near wake instability" (Basu, 1986, 38). Basu (1986) suggests that for circular cylinders, the weakening of the near wake instability dominates for low values of turbulence intensity, whereas the mixing of the shear layers dominates at higher values.

Bienkiewicz and Sun (1992) conducted research to assess the local wind loading on a low-rise bluff building. In their investigations, they also assessed various flow effects on the mean, RMS and peak pressure coefficients. Two boundary-layer profiles were developed in the investigation, with turbulence intensities of 15% and 20%, and a 74% variation in the integral scale of turbulence at roof height. Their conclusions were that the longitudinal turbulence and integral scale of the oncoming flow affected the RMS and peak pressure distribution, especially near the roof edge, with a maximum increase of the RMS pressure coefficient by a factor of 2. However, there was no substantial change of the mean pressure coefficient distribution.

Tieleman (1993) conducted wind-tunnel tests on low-rise surface-mounted prisms in numerous boundary-layer flows. Turbulence intensity was varied considerably from 6% to 33% at roof height. The results showed that increasing turbulence intensity, for both normal and oblique wind directions, generally resulted in more positive mean and RMS pressure coefficients and the opposite for the negative peak pressures.

2.6 Effects of Turbulence on the Surface Pressures over Curved Roofs

2.6.1 General

Three major factors which affect the pressure distribution and resulting drag coefficient over circular cylinders have been identified in ESDU-80025 (1980). These factors are: the Reynolds number, turbulence characteristics of the

oncoming flow and the surface roughness, and all primarily affect the position of flow separation, which influences the subsequent wake region.

Numerous papers which discuss the effects of the turbulence characteristics of the approaching flow were reviewed. Most of the work, which discusses this factor, has been conducted on circular cylinders and domes. Some of the prominent findings on the effects of turbulence intensity on the mean pressure coefficients, fluctuating pressure coefficients and drag coefficient are discussed in the following section.

2.6.2 Effects of turbulence intensity

Tests conducted by Cheung and Melbourne (1983) were undertaken to assess the turbulence effects on some aerodynamic parameters of a circular cylinder at supercritical Reynolds number. Turbulence intensity and Reynolds number were varied to assess their effects on the drag coefficient, lift coefficient, Strouhal number and the pressure distribution. Turbulence intensity was varied from 0.4% to 9.1% at both critical and supercritical Reynolds numbers, up to $R_e = 10^6$. Two differing setups, to generate the required turbulence, were utilized. Both setups were generated with similar integral length scales of about 90mm.

Some of the findings of the investigation were:

1) Earlier transition to a supercritical regime occurred with increasing turbulence intensity.

2) The flow separation lines and zero minimum pressure coefficients shifted backwards along the cylinder with an increase in turbulence intensity.

3) The effect of turbulence in the incident flow caused a rise in Reynolds number, due to its action on the separating boundary-layers and its interaction with the separated shear layers and wake.

4) Fluctuating pressures increased with an increase of turbulence intensity.

5) Cheung and Melbourne (1983) also suggested, from comparisons with full scale data, that turbulence intensity greater than 4% and Reynolds number greater

than 2 x 10^5 should be achieved in wind-tunnel tests to simulate full scale conditions.

Taylor (1991) conducted tests on a hemispherical dome subjected to two boundary-layers and Reynolds number ranging between 1.1 x 10^5 and 3.1 x 10^5. The author compared mean centreline pressures over hemispherical domes, with differing Reynolds number and turbulence intensities, as shown in Figure 2.7. The similarity of the pressure distributions, illustrated in Figure 2.7, shows that increased turbulence resulted in an apparent increase of Reynolds number. The investigation also showed that mean pressures coefficients were not significantly affected by increased turbulence intensity, whereas the fluctuating component generally increased, which is in accordance with Cheung and Melbourne (1983).

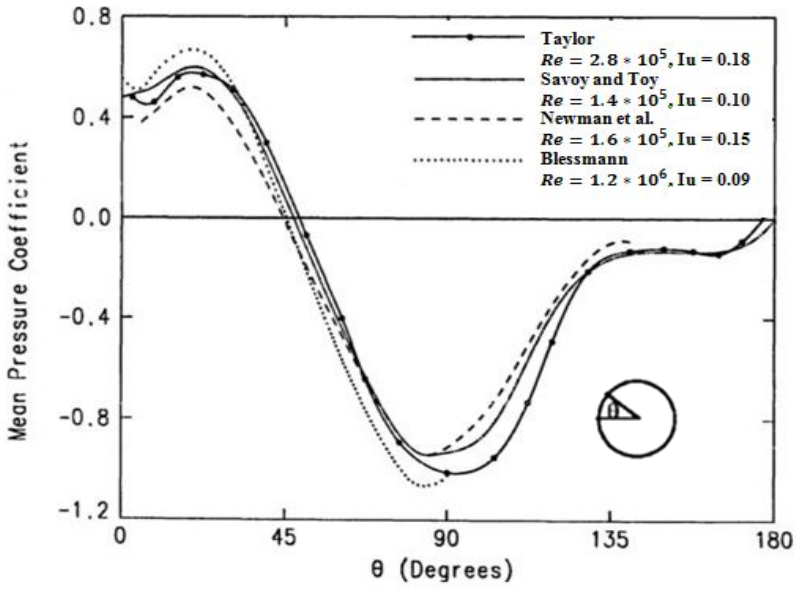


Figure 2.7 - Comparison of the mean pressure coefficients over the centreline of a dome with h/d = 0.5 (Reproduced form Taylor (1991))

Toy, Moss and Savory (1983) conducted tests on rough hemispherical domes to assess the effect of turbulence intensity on the mean surface pressure distribution. These tests were conducted with variations of turbulence intensity and speed profile, but the Reynolds number was kept constant at 1.6 x 10^5. Their findings were that an increase in turbulence intensity produced lower pressures in the

positive pressure region and slightly higher pressures in the negative pressure region. The authors also noted the position of transition from positive pressure to negative pressure and the position of flow separation over the dome moved downstream with increased turbulence in the boundary-layer, which is in accordance with Cheung and Melbourne (1983).

Ogawa et al. (1991) conducted tests on spherical and cylindrical domes, in differing boundary-layers, with turbulence intensity ranging between 10 and 30 % at roof height. They observed that the characteristics of the oncoming flow did not noticeably influence the time-averaged (mean) pressure coefficients, even with large variations in turbulence intensity. The authors also compared the RMS pressure coefficients and turbulence intensity at the model apex height and found an approximately linear relationship. Their conclusions were that different fully developed boundary-layers had little effect on the mean pressure coefficients on the surface of domes and that RMS pressure coefficients were proportional to the turbulence intensity of the oncoming flow.

An overview of work conducted by numerous researchers on the effects of turbulence intensity on circular cylinders was produced by Zdravkovich (1990). Figure 2.8 shows a trend in which the effect of increasing turbulence intensity, within the free-stream flow, results in a shift to turbulent flow on the cylinder at a lower Reynolds number. The drop of drag coefficient indicated in Figure 2.8 is due to the narrowing of the wake as a result of the downwind movement of the flow separation point associated with the boundary-layer laminar to turbulent regime transition. Figure 2.9 shows this backward procession of the flow separation points and the change from laminar to turbulent flow separation for the subcritical to supercritical Reynolds number regime change. Although not indicated in Figure 2.8, the ESDU – 80025 (1980) report notes that at a very high Reynolds number, the influence of free-stream turbulence on the R_e - C_D variation is negligible.

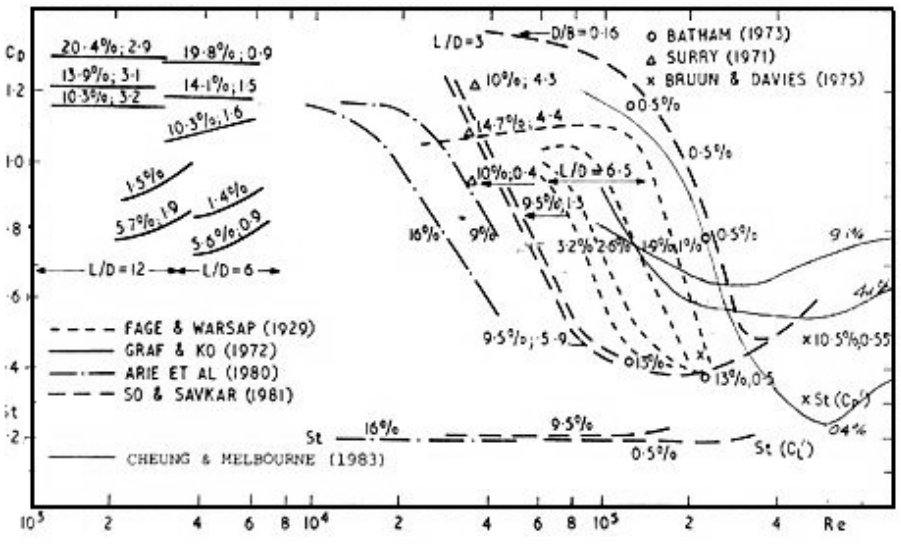


Figure 2.8 - Drag coefficient and Strouhal number for various turbulence intensities (%), aspect ratio (L/D) and blockage ratio (D/B) (Reproduced from Zdravkovich (1990))

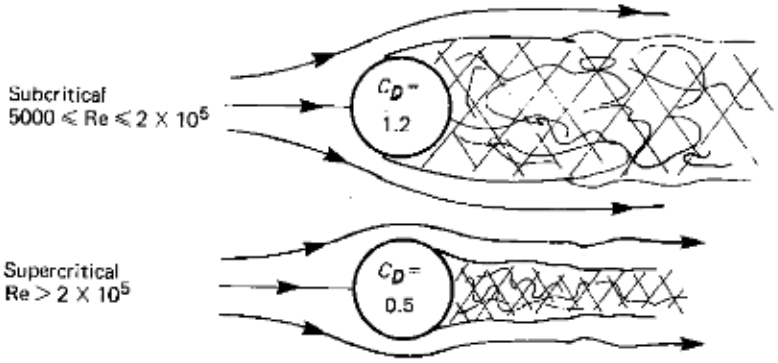


Figure 2.9 - Flow regimes around a circular cylinder in smooth flow (Produced from Cook (1985))

2.7 Effects of Surface Roughness on Pressures over Bluff Bodies

2.7.1 Sharp edged structures

Stathopoulos and Zhu (1988) and Maruta et al. (1998) investigated the effects of surface roughness on the cladding of buildings. Wind- tunnel tests were conducted on multi-storey rectangular structures, with differing forms of surface roughness. Their findings indicate that the maximum positive pressure coefficients on the windward faces were generally not affected, but variations were evident on the

side walls. Mean and minimum peak surface pressures became more positive, whilst the RMS pressures were reduced with increased surface roughness.

Maruta et al. (1998) conducted their investigations in both uniform and turbulent flow. Selected results, related to the turbulent boundary-layer, are shown in Figure 2.10. The RMS and minimum pressure coefficients were largest and lowest for the smallest magnitude of surface roughness (Type O), respectively. The opposite was evident for the largest roughness (Type B3), as shown in Figure 2.10. The authors' explanation for these phenomena was that the increase in surface roughness restrained the pressure fluctuations induced by the separation bubbles, as indicated by the decreasing RMS pressure coefficients.

Stathopoulos and Zhu (1988) conducted their tests with both open-country and sub-urban boundary-layer simulations. Two differing sandpaper sizes (80 GAR and 40 ALO) were attached to the rectangular models. Their experimental results reveal the same trends as those of Maruta et al. (1998), as shown in Figure 2.11. The authors noted, however, that the addition of surface roughness only changed pressure coefficients marginally and found almost no difference between the two sandpaper sizes.

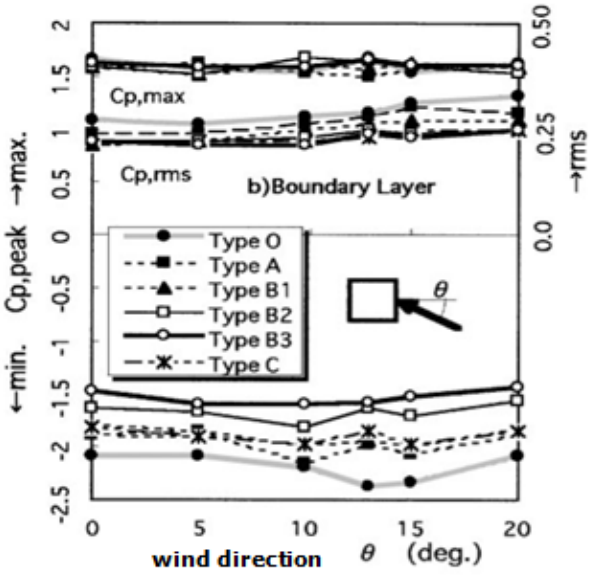


Figure 2.10 - Effects of surface roughness on the peak and RMS pressure coefficients over the building facade (Reproduced from Maruta et al (1998))

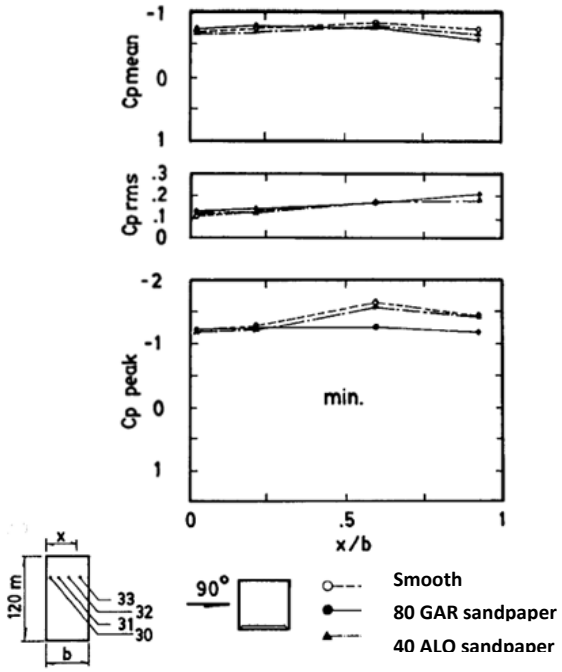
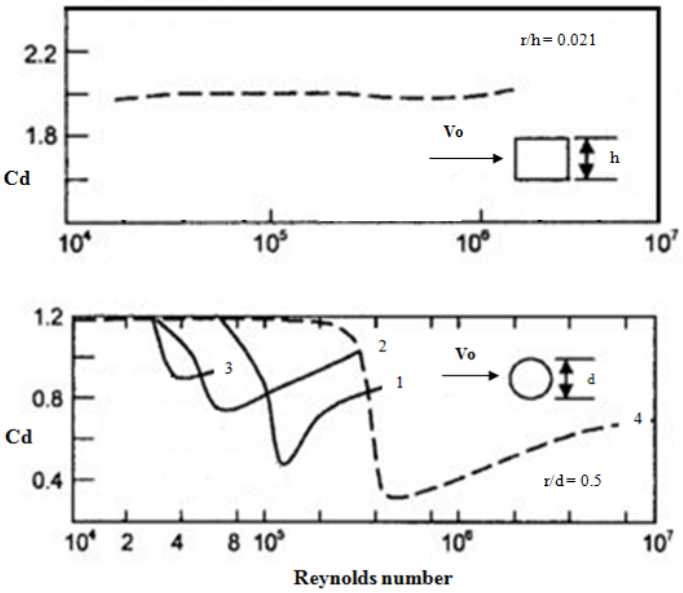


Figure 2.11 - Pressure coefficients on smooth and rough wall surfaces
(Reproduced from Stathopoulos and Zhu (1988))

2.7.2 Curved structures

Research on the effects of surface roughness on various flow parameters over circular cylinders have been conducted for about a hundred years. The first study was undertaken by Fage and Warsap (1929), in which drag coefficients over circular cylinders, in both the critical and supercritical Reynolds number regimes, were measured. Similar studies have been conducted by numerous researchers, such as Scruton (1971), Achenbach (1971), Guven, Patel and Farrel (1975) and Ribeiro (1991), and all confirm the same trend observed by Fage and Warsap (1929).

All these studies revealed that increasing surface roughness causes increased (i.e. more positive) 'minimum' drag and a shift in the critical Reynolds number. Figure 2.12 shows the relationship between drag coefficient and Reynolds number for square and circular cylinders, with differing surface roughness (k/d).



(1. $\frac{k}{d} * 10^{3} = 2$, 2. $\frac{k}{d} * 10^{3} = 7$, 3. $\frac{k}{d} * 10^{3} = 20$, 4. Smooth)

Figure 2.12 - Influence of Reynolds number and surface roughness on the drag coefficient for square and circular cylinders (Reproduced from Scruton (1971))

From the set of curves shown in Figure 2.12, it is evident that there is minimal drag coefficient variation for a square cylinder as separation occurs at the edge; however, for a smooth circular cylinder, there is a sudden drop in drag coefficient at about $R_e = 2 \times 10^5$. It is noted in ESDU-80025 (1980) that the earlier drop of the drag coefficient corresponding to increased surface roughness height is a result of increased boundary-layer thickness over the cylinder, which causes transition to turbulent flow on the rear of the cylinder to occur at progressively lower Reynolds numbers. Figure 2.12 reveals that the addition of surface roughness promotes supercritical flow at a Reynolds number at which flow is subcritical.

The effect of surface roughness on the centreline pressure distribution has been observed by numerous researchers (Maher (1965), Ribeiro (1991), Guven et al (1975) and Letchford and Sarkar (2000)). Maher (1965) conducted tests on domes within near uniform flow, at $R_e = 1.8 \times 10^6$, and with both a smooth and a roughened surface (i.e. attached sand grain roughness ($k/d \times 10^3 = 1$)). Ribeiro (1991) and Guven et al (1975) assessed the effects of surface roughness on the mean pressure coefficient distribution, with differing types of surface roughness,

such as sandpaper, wire mesh and ribs. All studies indicate an identical effect of surface roughness on the centreline pressure distribution over circular structures.

Table 2.1, which is reproduced from Ribeiro (1991), shows the results of testing conducted on circular cylinders with varying sandpaper grain sizes, at R_e = 3.8 x 10^5 , I_u = 0.5% and L_u = 11 cm. The results of the investigation revealed that mean pressure coefficients increased ahead of the point of flow separation, but an overall decrease in the wake was observed. The author notes that the mean pressures increased near the point of flow separation because surface roughness promotes formation of a turbulent boundary-layer over the surface, resulting in earlier flow separation. Because suctions are reduced near the point of flow separation and are larger in the wake, there is ultimately an overall reduction in uplift and an increase in drag. Table 2.1 also shows that for increased surface roughness, the points of flow separation (θs) and minimum pressure (θm) move forward along the cylindrical surface.

Table 2.1 - Characteristic parameters of the mean pressure distributions (Data from Ribeiro (1991))

Roughness	k/d x10^3	θo (°)	θm (°)	θs (°)	*Cp* min	C_D
Sandpaper	1.8	33	75	99	-1.63	0.94
Sandpaper	4.14	33	73	97	-1.53	0.94
Sandpaper	6.99	34	73	95	-1.48	0.97
Sandpaper	12.22	34	73	95	-1.39	0.99

θo, θm, θs - angles at which zero pressure, minimum pressure and separation occurred

Letchford and Sarkar (2000) conducted wind-tunnel tests, which focused partially on the effects of surface roughness on the mean, RMS and peak pressure coefficients over hemispherical domes, within a turbulent boundary-layer similar to ASCE7-98 Exposure C. The smooth surface was a fibreglass gel coat and the rough surface was fly screen mesh, with a relative roughness of k/d x 10^3 = 1. Mean and peak pressure results corroborate those discussed earlier, as shown in Figure 2.13a and 2.13b. The RMS pressure coefficient, for the differing surfaces, was similar up to θ = 45°, at which point the rough finish resulted in lower RMS

pressures until about θ = 135°, after which the smooth finish had lower RMS pressures. This result is shown in Figure 2.13c.

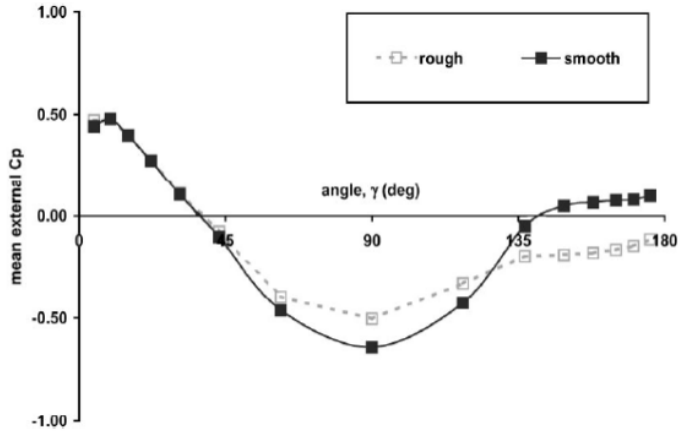


Figure 2.13a – Comparison of mean centreline pressure coefficient distributions for rough and smooth domes (Reproduced from Letchford and Sarkar (2000))

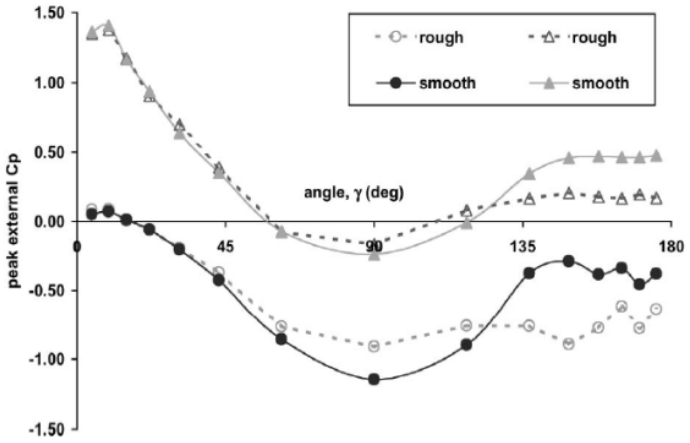


Figure 2.13b– Comparison of peak centreline pressure coefficient distributions for rough and smooth domes (Reproduced from Letchford and Sarkar (2000))

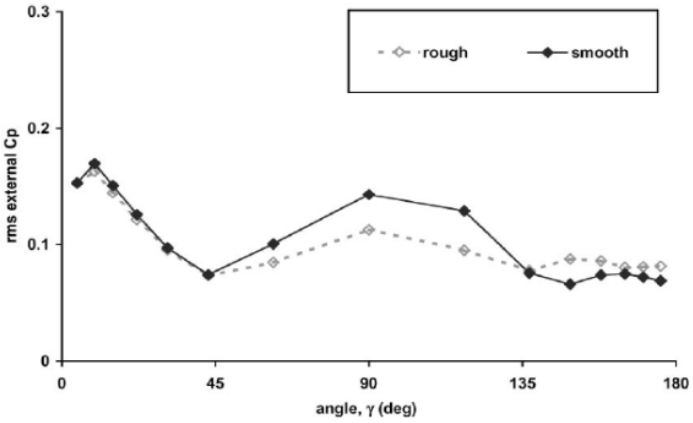


Figure 2.13c – Comparison of RMS centreline pressure coefficient distributions for rough and smooth domes (Reproduced from Letchford and Sarkar (2000))

2.8 Simulating High Reynolds Number Flow in Wind-Tunnel Testing

The sensitivity of curved structures to Reynolds number has been discussed previously in this literature review. Due to constraints on model size and Reynolds number regime, equality cannot be achieved in a traditional low speed boundary-layer wind-tunnel. There has, however, been work conducted by numerous researchers which indicates that the pressure distribution over rounded surfaces at high values of Reynolds number can be reproduced at lower values of Reynolds by using various artificial mechanisms.

The Engineering Science Data Item (ESDU) - 80025 (1980) outlines a procedure for simulating the pressure distribution over a circular cylinder situated in high Reynolds number flow by a scaled model tested at a lower Reynolds number. Ultimately, supercritical flow conditions can be promoted at a lower Reynolds number by the addition of moderate surface roughness and an increase of the turbulence intensity. This regime change is shown in Figure 2.14, in which a smooth cylinder in low turbulence is compared with a rough cylinder in turbulent flow.

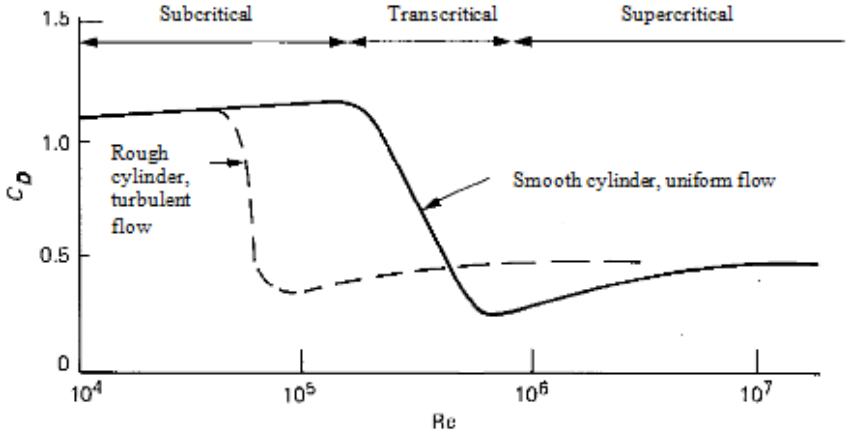


Figure 2.14 - Variation of drag coefficient with Reynolds number (Reproduced from Cook (1985))

The similarity of the pressure distribution over circular cylinders at different scales and Reynolds number regime, as given in ESDU-80025 (1980), is achieved through equality of the two-dimensional drag coefficient for an isolated cylinder normal to the flow. This procedure allows for the selection of turbulence characteristics and an equivalent sand grain roughness size, which must be applied to the model during the wind-tunnel simulation, to achieve model-prototype drag coefficient similitude. The drag coefficient and pressure distribution calculation procedures, outlined in ESDU-80025 (1980), are summarized below.

The report states that the drag coefficient of a two-dimensional cylinder can be expressed as a function of an effective Reynolds number and the surface roughness parameter, in the following form:

$$C_{D0} = f\left[R_{e_e}, {}^{k}/_{d}\right] \tag{2.11}$$

where R_{e_e} is the effective Reynolds number and k/d is the relative roughness. This effective Reynolds number is a modified Reynolds number which accounts for the effects of surface roughness and turbulence, and is expressed as:

$$R_{e_e} = \lambda_T \lambda_R R_e \tag{2.12}$$

where λ_T is the turbulence factor, λ_R is the roughness factor and R_e is the Reynolds number.

An increase in surface roughness of the model results in the decrease of Reynolds number at which flow transition occurs. The roughness factor is used to describe this effect, and is given in ESDU-80025 (1980) as:

$$\lambda_R = \frac{R_{e1}}{R_{e2}} \tag{2.13}$$

where R_{e1} is the Reynolds number for a smooth cylinder giving a specific drag coefficient and R_{e2} is the Reynolds number for a rough cylinder providing the same drag coefficient.

An increase in turbulence has the same effect as that of surface roughness, which is to promote earlier transition from subcritical to supercritical flow. The λ_T parameter is dependent on numerous factors, which are indicated in Appendix A.

The equations used to calculate λ_R, λ_T, R_{e_e} and C_{D0} have been included in Appendix A. As noted previously, if the drag coefficient (C_{D0}) is equivalent for the model and full-scale structures, then the pressures distributions will also be similar.

A simple method for calculating the mean centreline pressure distribution around the surface of a circular cylinder is given in ESDU-80025 (1980). The procedure is based on the theoretical inviscid potential flow solution (i.e. $Cp = 1 - (1-Cp_m).\sin^2\theta$ and $Cp_m = -3$), which has been modified to fit the known (or estimated) values of the pressure coefficient at $\theta = 0$, θ_m (the angle at which minimum pressure occurs), and θ_b (the angle at which the base pressure occurs). The equations included in Appendix A, which the ESDU-80025 (1980) report has identified to represent data from both wind-tunnel and full scale measurements extremely well, are then used to calculate the pressure distribution.

3 EXPERIMENTAL METHODOLOGY

3.1 Boundary-Layer Wind-Tunnel

3.1.1 Wind-tunnel facility

The present study was conducted at the Council for Scientific and Industrial Research (CSIR) Boundary-Layer Wind-Tunnel (BLWT). The wind-tunnel is an open circuit type with a centrifugal fan powered by a 75 kW thryristor-controlled motor capable of producing a maximum wind speed of 22m/s. The boundary-layer wind-tunnel facility is shown in Figure 3.1 and 3.2, and has dimensions of 1 m high x 2m wide with an 18m long boundary-layer development length.

The wind direction variation is achieved by a 'turn table' situated in test section, which is shown in Figure 3.2. The wind-tunnel is equipped with an adjustable roof in order to minimise the blockage effects due to the size of the model in relation to the tunnel cross-section. Boundary-layer characteristics are developed through the introduction of flow-processing devices. Specific information relating to the boundary-layer simulation is discussed in section 3.2.



Figure 3.1 - Wind-tunnel facility

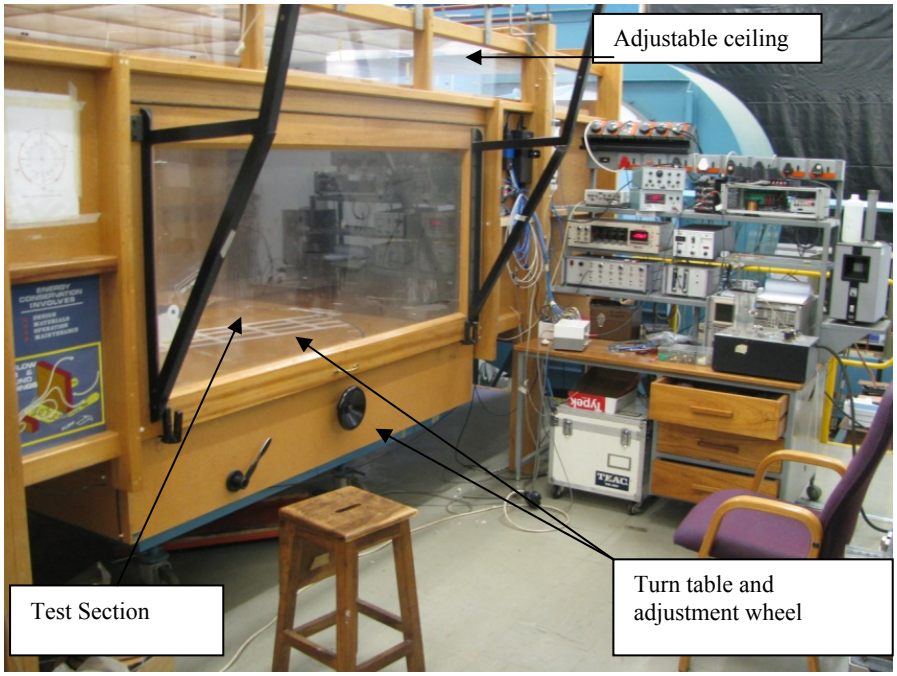


Figure 3.2 - Wind-tunnel test section

3.1.2 Instrumentation

Data acquisition was done using a PC, with an A/D system developed on the basis of the I-Otech Daqbook technology. The control panel, with instrumentation, is shown in Figure 3.3.

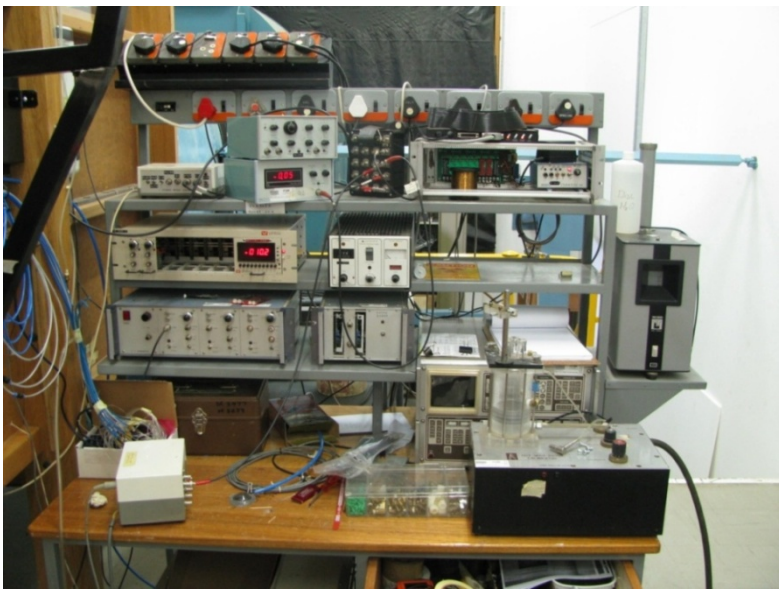


Figure 3.3 - Instrumentation panel

In the current experiment, the reference wind speed of the approach flow was monitored and measured using a Pitot-static tube placed above the model. The Pitot-static tube was positioned 740 mm above the wind-tunnel floor and was well clear of the model, so as not to influence pressure readings. The Pitot-static tube is shown in Figure 3.4. Reference wind speed was also monitored in front of the models with a mini-air anemometer type air-1, 1-40 (Schiltknecht Messtechnik) placed 300 mm above the wind-tunnel floor. The mini-air instrumentation is shown in Figure 3.5.



Figure 3.4 - Pitot-tube

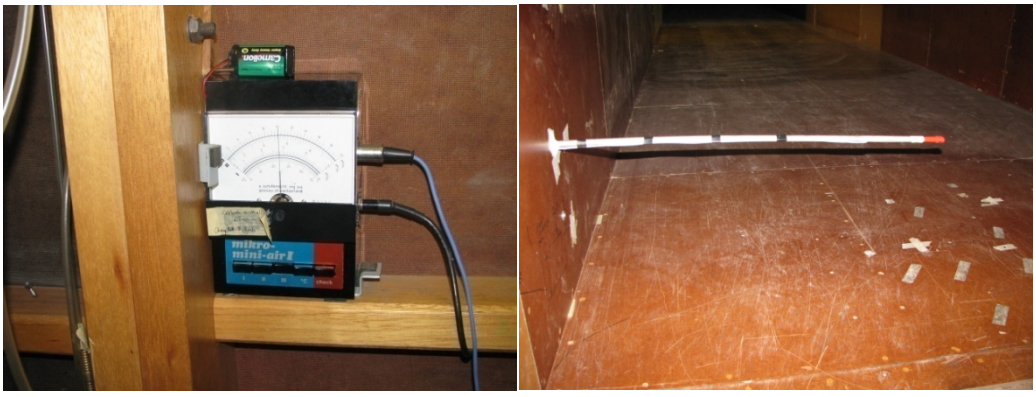


Figure 3.5 - Mini-air instrumentation

3.2 Boundary-Layer Modelling

3.2.1 Introduction

As indicated in Chapter 2, there are three important characteristics which describe boundary-layer flow. These characteristics are: the mean wind speed profile, turbulence intensity profile and the longitudinal turbulence spectra.

An aspect of this investigation was aimed at assessing the effects of turbulence on the external mean, RMS and peak wind pressure coefficients. Two generic boundary-layer profiles were developed. The smoother boundary-layer simulated in the investigations corresponds to an open sea profile, whereas the rougher boundary-layer profile had both turbulence characteristics and a power-law exponent of $\alpha = 0.16$, similar to that of the general open country terrain.

3.2.2 Boundary-layer simulation

The CSIR BLWT used for the current investigation has been discussed earlier in this report, and details on the simulation of boundary-layers are provided in this section. Figure 3.6 illustrates a diagrammatic representation of the wind-tunnel.

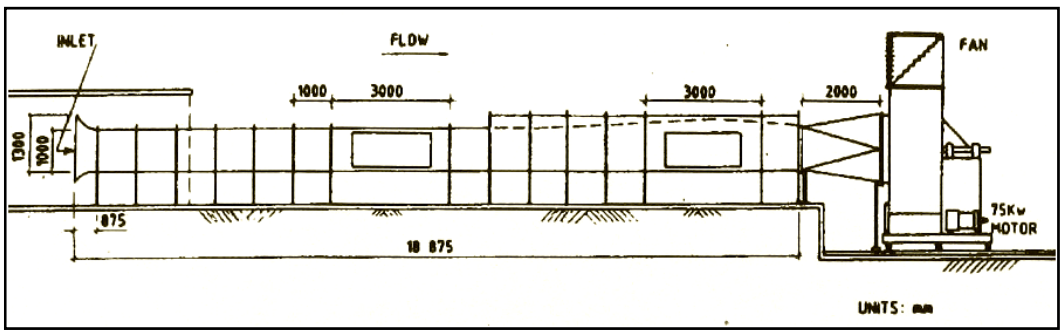


Figure 3.6 - Simple schematic diagram of the CSIR BLWT

The boundary-layer simulation was achieved by a honeycomb mesh screen at the entrance to introduce the initial small scale turbulence, four 250 mm high and 100mm wide triangular spires, followed by a 50 mm high tripping wall to achieve an initial speed deficit in the lower section of the profile. The following 16 m fetch was either left bare or covered with roughness elements to allow for gradual profile generation.

The first boundary-layer, which is denoted ‘smooth’ boundary-layer in this report, was developed with the wind-tunnel floor in its smooth state. Figure 3.7 illustrates the smooth boundary-layer setup. The second boundary-layer, which is denoted ‘rough’ boundary-layer, was developed by 16 m of attached corrugated cardboard

with uniform a roughness height of about 2.5mm. Figure 3.8 shows the 'rough' boundary-layer setup.



Figure 3.7 - Upwind fetch ('smooth' boundary-layer)



Figure 3.8 - Upwind fetch ('rough' boundary-layer)

Mean and fluctuating speed measurements were captured using a hot-wire probe, connected to the data acquisition system. The hot-wire probe was attached to a vertical traverse mechanism placed 1 metre from the face of the model, as shown in Figure 3.9. Data was captured at heights of 30, 60, 90, 120, 150, and 180 mm above the wind-tunnel floor. Figure 3.10 illustrates 1 second of the wind speed-time series, for the 'smooth' boundary-layer, measured at 30 mm above the wind-

tunnel floor. Figures 3.11 through 3.14 provide the mean speed and turbulence intensity profiles for the 'smooth' and 'rough' boundary-layers.

The blockage introduced by the model was approximately 1.5 % of the tunnel cross-section, which is well below a value of 5% noted in the literature. Therefore, the blockage effects were considered negligible in the current investigations.

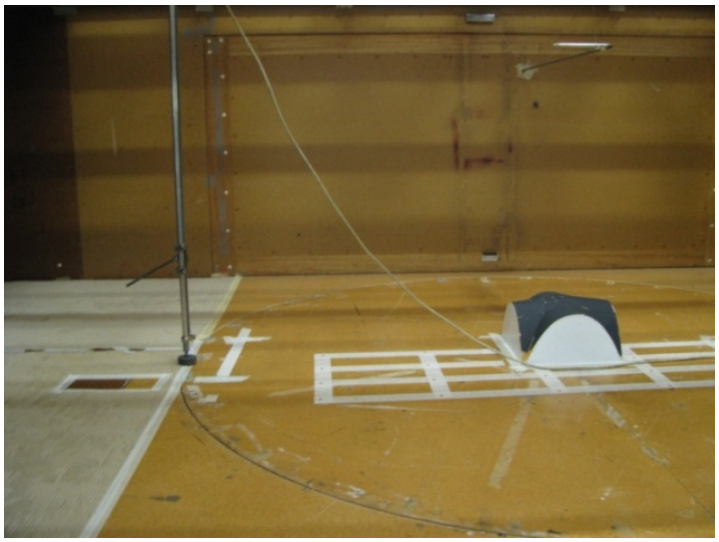


Figure 3.9 - Turbulence measurement position

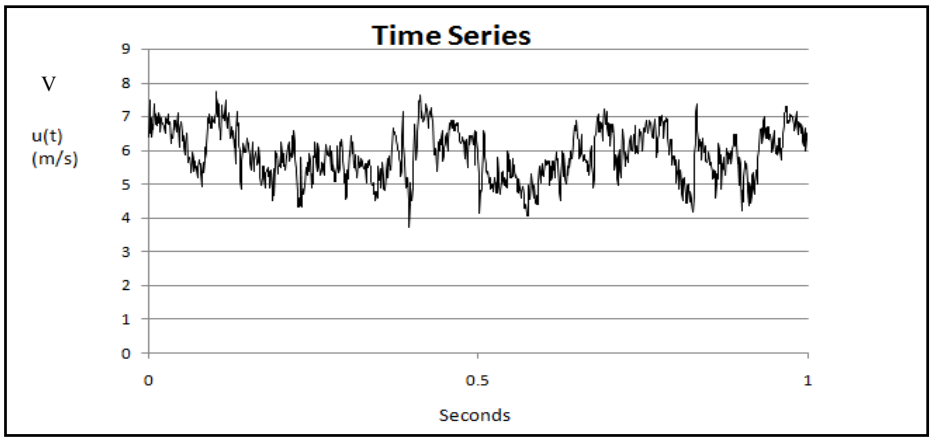


Figure 3.10 - Time Series (30 mm above wind-tunnel floor)

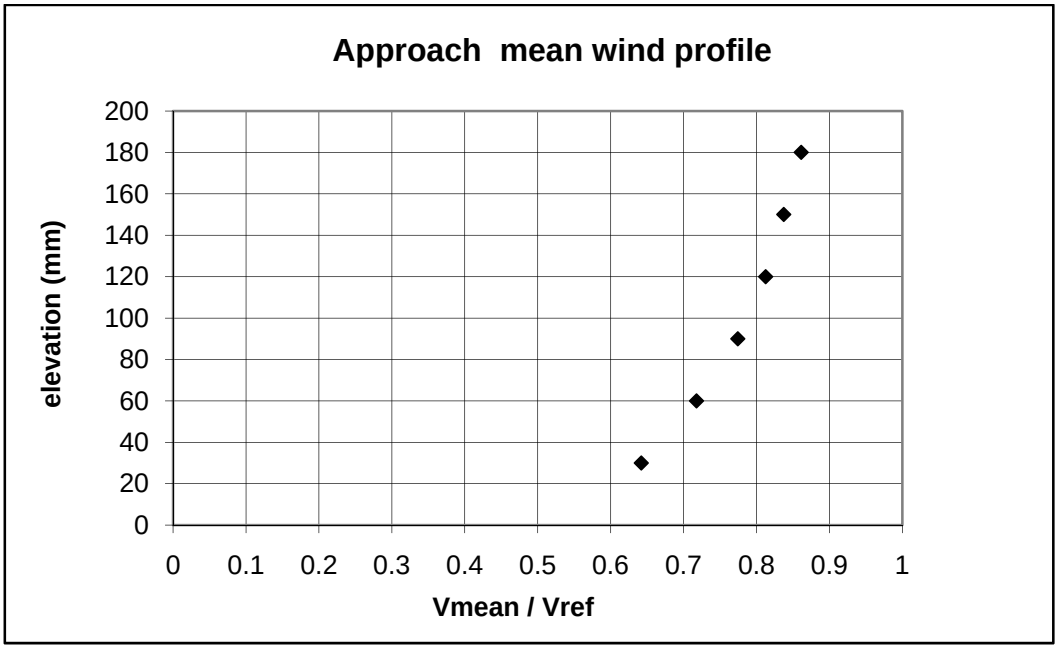


Figure 3.11 - Mean wind speed profile ('smooth' flow)

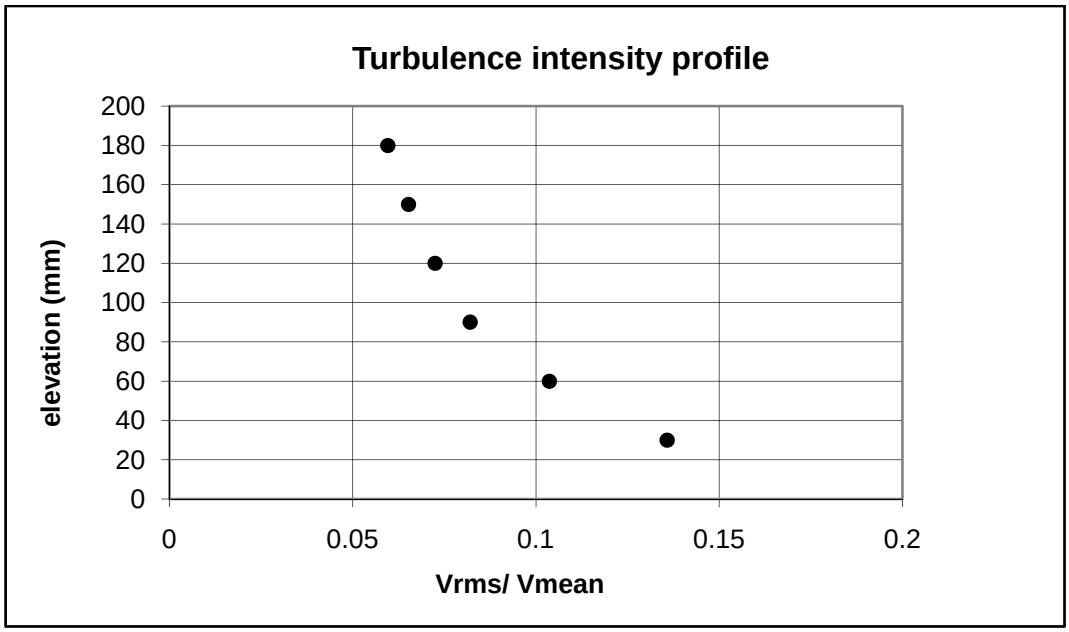


Figure 3.12 - Turbulence intensity ('smooth' flow)

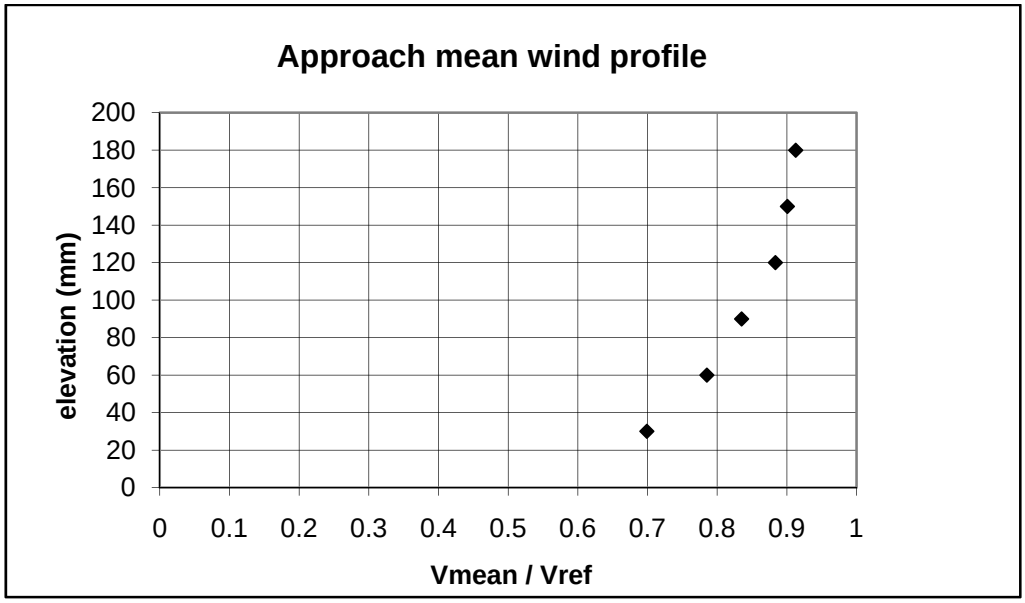


Figure 3.13 - Mean wind speed profile ('rough' flow)

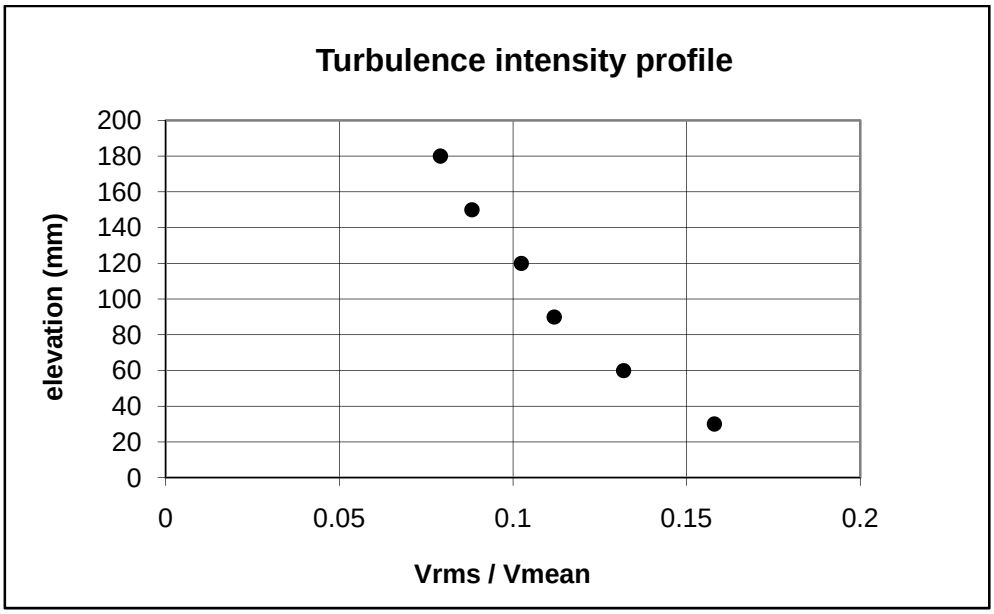


Figure 3.14 - Turbulence intensity ('rough' flow)

Longitudinal turbulence spectra were measured at 15, 30 and 50 mm for the 'rough' and 'smooth' boundary-layer profiles. These are shown in Figures 3.15 and 3.16. The spectrum $S_u(n)$ is calculated from the experimental wind speed, in the wind-tunnel.

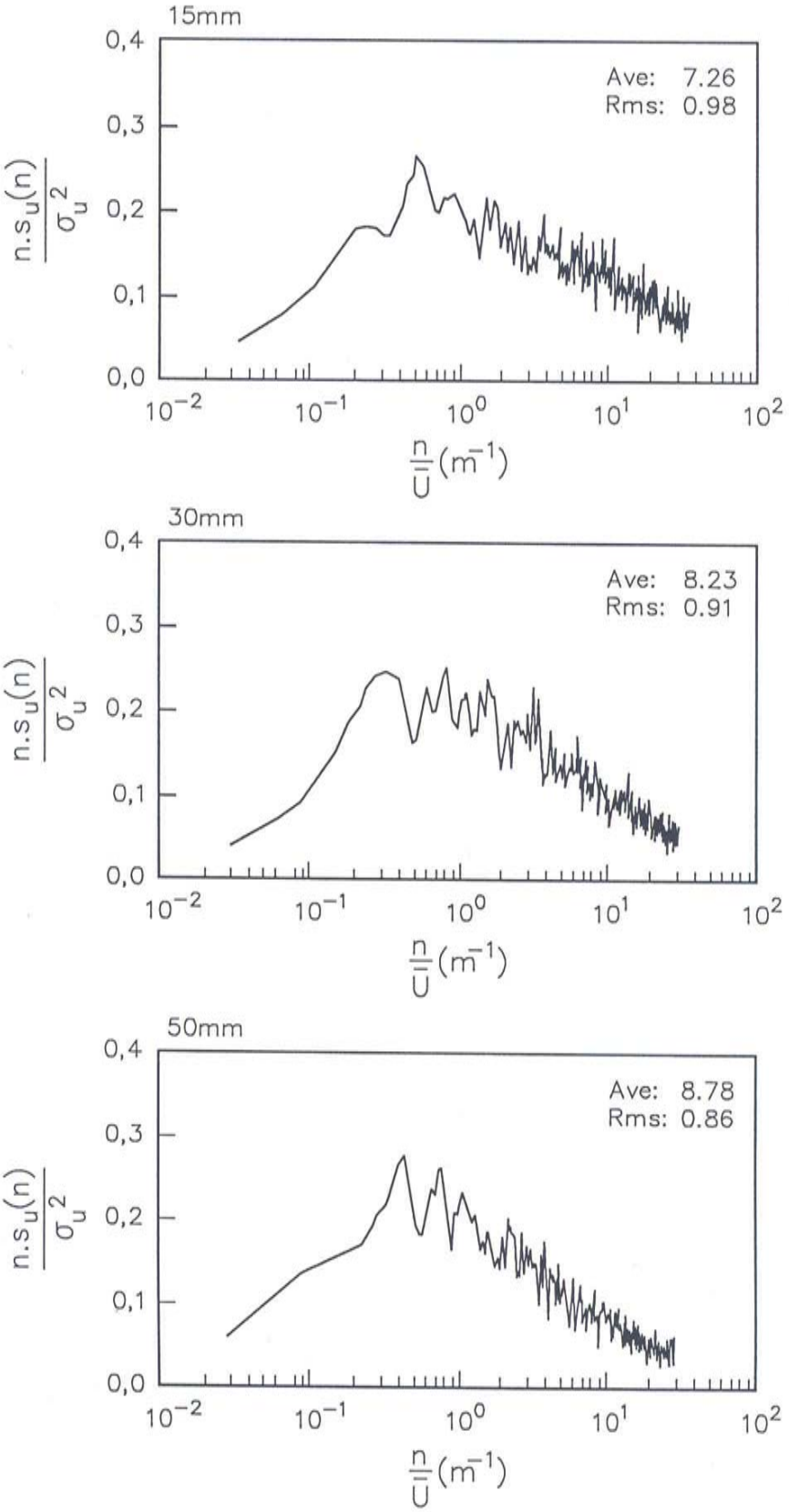


Figure 3.15 - Longitudinal turbulence spectra (‘smooth’ boundary-layer)

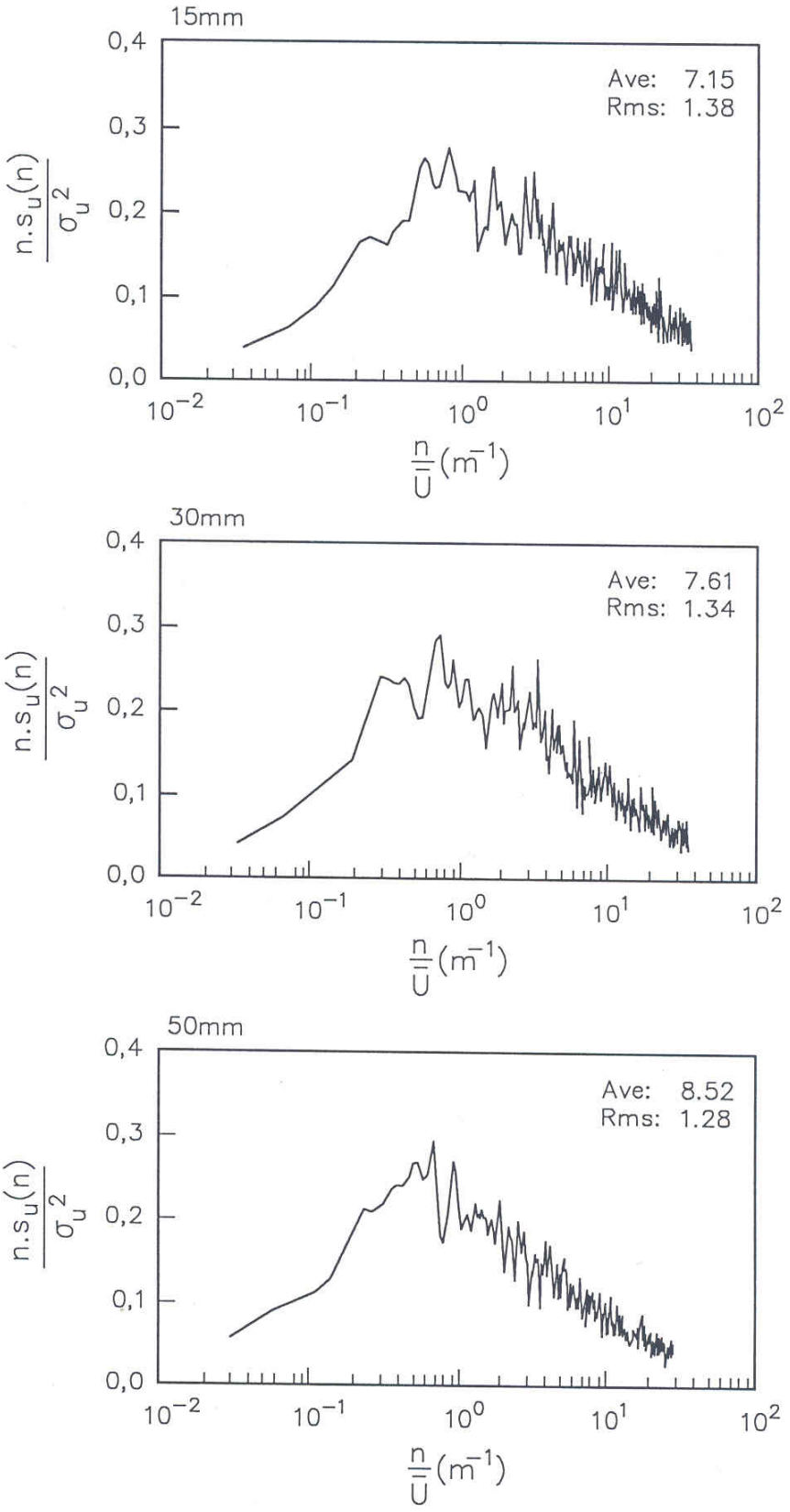


Figure 3.16 - Longitudinal turbulence spectra (‘rough’ boundary-layer)

3.3 Surface Pressure Instrumentation, Measurements and Calculation

3.3.1 Instrumentation

Measurement of the mean and fluctuating pressures over the various model surfaces was conducted using a pressure switch scanning valve (Scanivalve, Model 24D3 -2/25), fitted with a Setra pressure transducer (Model 237), allowing each tapping to be read in turn. The data acquisition system recorded the digitized signals from the pressure transducers and stored the data in the form of a time - series.

3.3.2 Reference dynamic pressure

Wind-tunnel measurements were normalised by the free-stream dynamic pressure at the model roof height. The measurement instrumentation positioned at this height would, however, influence the pressure measurements, so the reference dynamic pressures were measured with a Pitot-tube positioned 740mm above the wind-tunnel floor. These pressure results were then factored by a ratio of the free-stream speed at roof height (120 mm) to that at 740mm above the model. The free-stream dynamic pressure at roof height was measured separately with a hot-wire probe, as shown in Figure 3.17.

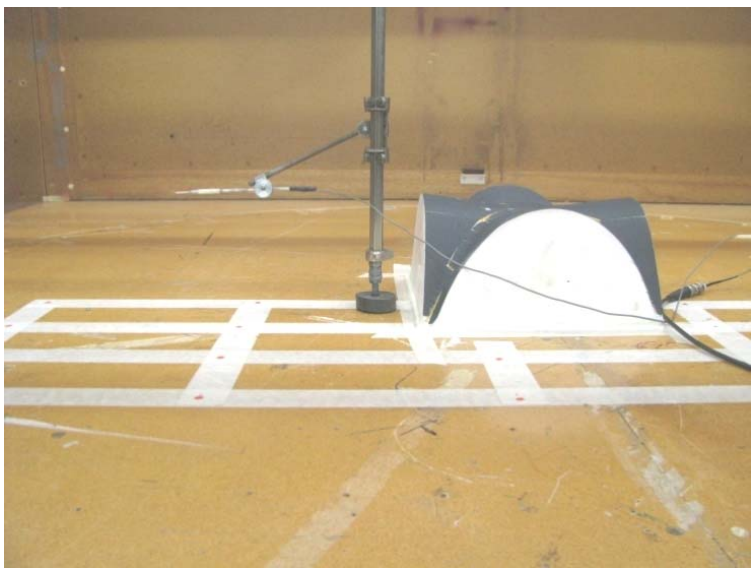


Figure 3.17 - Dynamic pressure measurement at roof height

3.3.3 Reference static pressures

Reference static pressure was measured from a tapping positioned in the roof of the wind-tunnel well above the influence of the model.

3.3.4 Wind-tunnel models

Scale

The geometric scale of the wind-tunnel model is controlled by the dimensions, and ultimately the flow conditions generated in the wind-tunnel. The BLWT at the CSIR is setup to simulate the flow characteristics providing a length scale of between 1:400 and 1:600. This present study is aimed at assessing the effects of roof geometry on surface pressures, but due to the boundary-layer characteristics and model scale (1:500), the full scale cross vault structures are fairly large (i.e. 60m high).

Model configuration

Three cross vault models (i.e. flat, convex and concave) were tested in the current investigation. Figure 3.18 shows the form of these wind-tunnel models, and the geometrical parameters are given in Table 3.1.

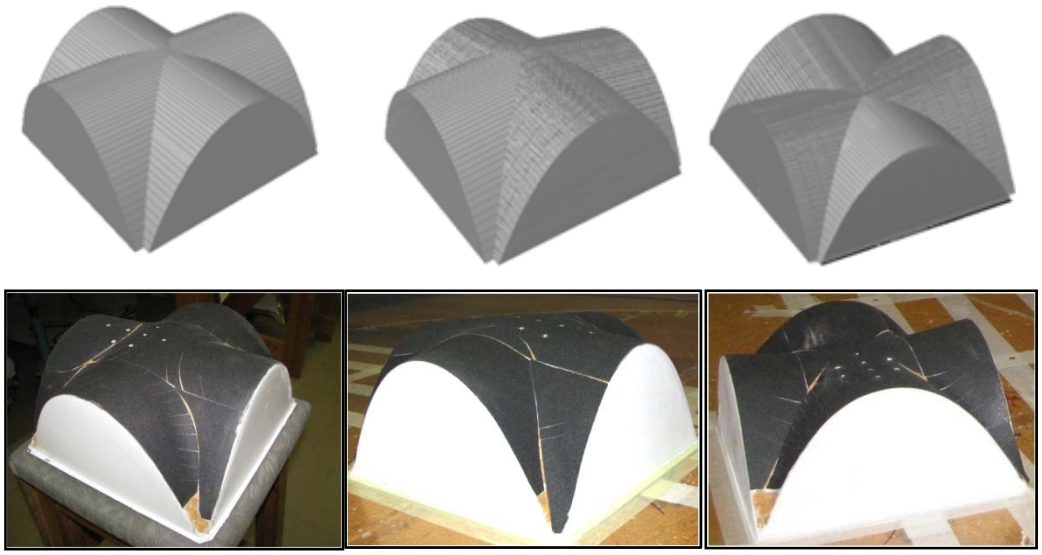


Figure 3.18 - Flat, convex and concave cross vaults (from left to right)

Table 3.1 - Difference in model dimensions

cross vault type	width (mm)	breadth (mm)	roof edge height (mm)	apex height (mm)	average slope (degrees)
flat	240	240	120	120	0
convex	240	240	120	145	12
concave	240	240	120	95	-12

The profile of the barrels was based on an inverted catenary. The catenary shape is acquired when a chain is allowed to hang freely between two supported ends. When the only force acting is self weight, then tension alone will exist within the chain (i.e. no compression). Inverting this shape will produce a structure in perfect compression. As no tension exists in the structure, the inverted catenary is an ideal shape for a single vault structure. The shape of the inverted catenary is given by the following equation:

$$y = -a.\cosh(x/a) + c \tag{3.1}$$

A width to depth ratio of two was defined for all models, requiring specific values for the constants ‘a’ and ‘c’. The following equation was used to define the right hand side of the profile, which is shown in Figure 3.19.

$$y = -6.96\cosh(x/6.96) + 6.96 \tag{3.2}$$

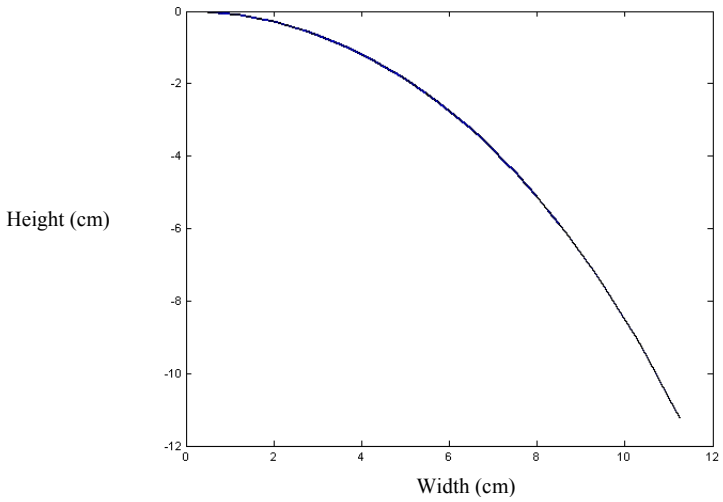


Figure 3.19 - Catenary profile

Model construction

The wind-tunnel models were constructed from fibreglass and were approximately 4 mm thick. Moulds were constructed from thin steel sheet into which the fibreglass was cast. This allowed for a fairly even external surface. After removal of the fibreglass models from the moulds, the surfaces were sanded to remove any inconsistencies and a gelcoat was applied to achieve a very smooth finish, with a relative roughness (k/d) of the order of 10^{-6}.

3.3.5 Surface pressures

Eight pressure taps were mounted to each of the cross vault models. The pressure taps were numbered 1 through 8, starting at the apex, and ordered in the manner indicated in Figure 3.20. The taps were each positioned 25mm apart with tap 8, 30mm from tap 6. Due to the symmetry of the model, there were effectively 29 pressure locations. The 29 pressure tap locations are shown schematically in Figure 3.21.

Pressures from the model surface were transferred via flexible plastic tubing, with an internal diameter of 1.5mm, to the Scanivalve device. Stainless steel tubing connectors, with an external diameter of 1.6mm, were mounted to the models, which provided the point of attachment for the flexible plastic tubing.

Flow restrictors were attached to the flexible plastic tubes, at mid-length, to account for the effects of resonance. The plastic tubing and volume within the tubing leading to the transducer form a resonant system, which requires some form of damping in order to limit the induced rise in output response. A flat frequency response up to 120Hz was obtained for the restrictors. The positions of these restrictors are shown in Figure 3.22.

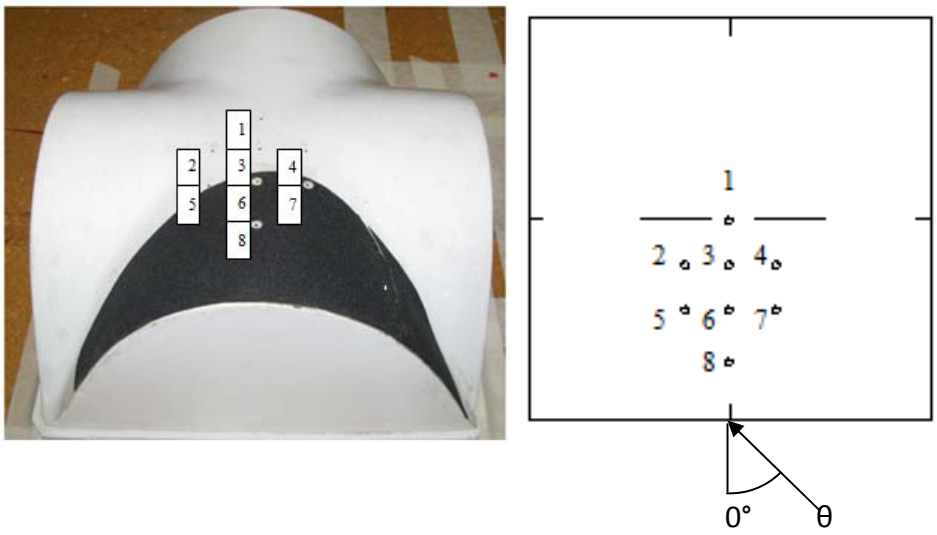


Figure 3.20 - Pressure tap positions

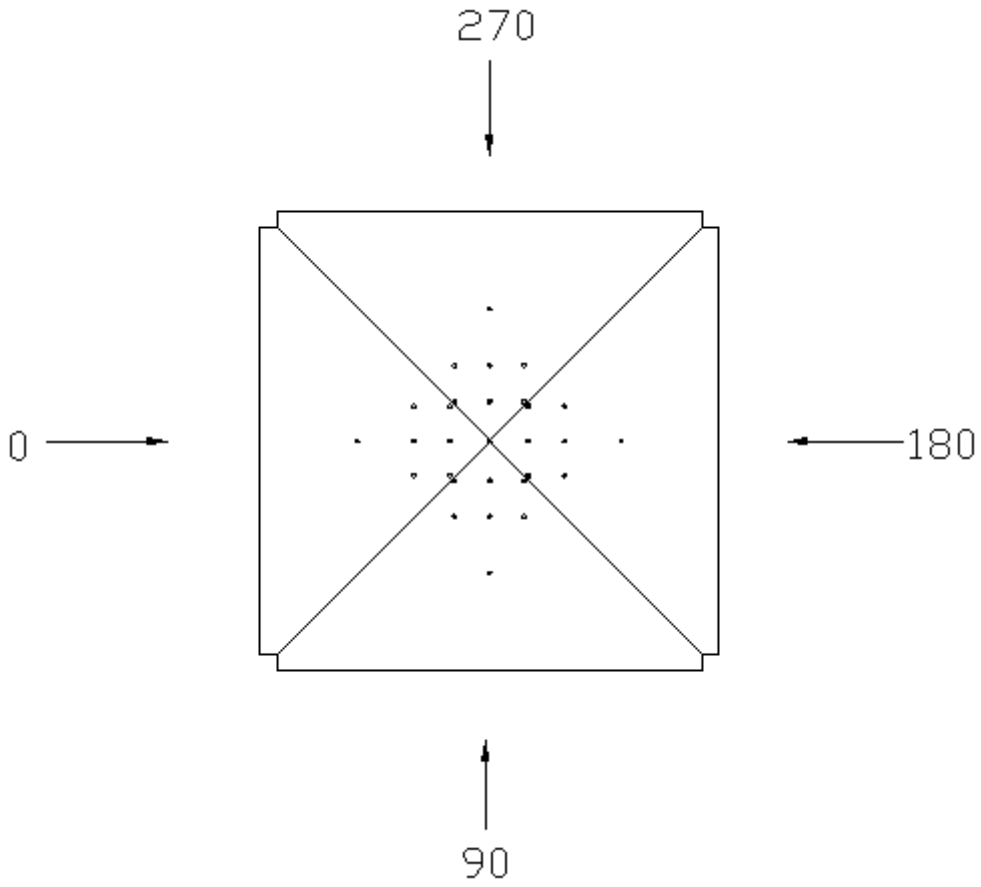


Figure 3.21 - Effective pressure tap positions

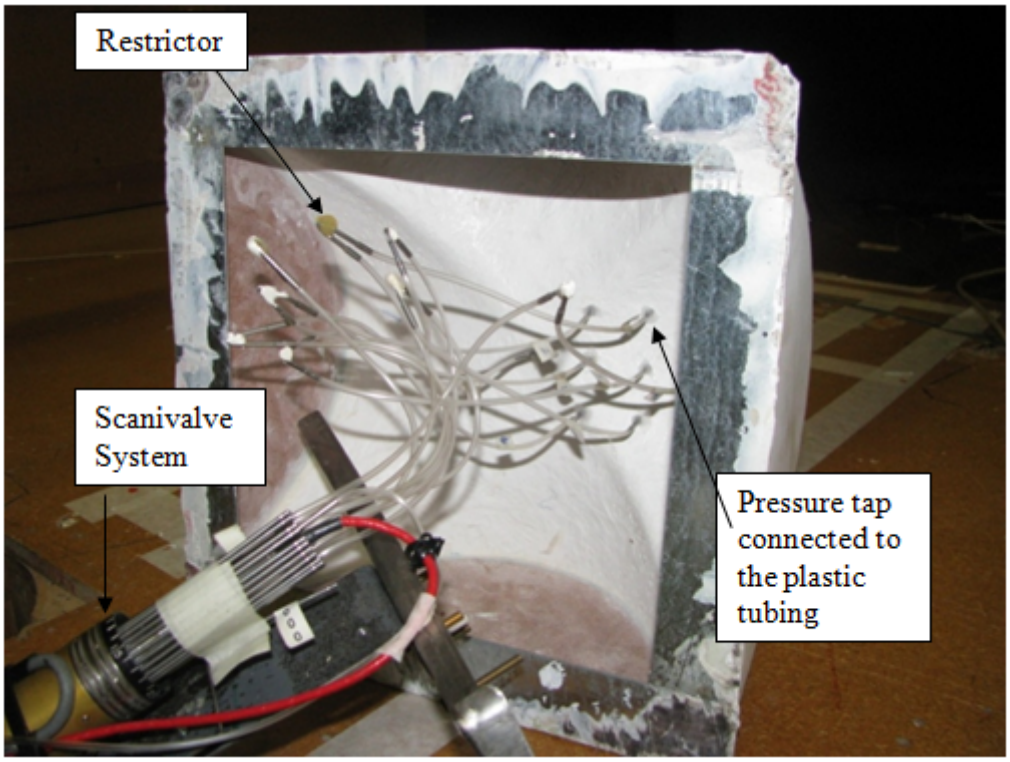


Figure 3.22 - Scanivalve device attached to the model

3.3.6 Pneumatically averaged surface pressures

The use of manifolds to average pressure fluctuations was introduced by Surry and Stathopoulos (1977). The authors studied the performance of an averager by measuring wind pressures over a sharp edged, flat roof model within separated turbulent flow. They used an eight tube pneumatic manifold and compared the mean pressure obtained from the averager with the mean of the corresponding eight individual pressures, and noted that the difference in spatial mean pressure was, in all cases, below 2%.

Holmes (2001) indicates that if the inlet tubes are identical in length and diameter, then the system should provide a true average of the fluctuating pressures at the entry of the inlet tubes (assuming laminar flow exists within them). “Usually, flatter frequency response curves to higher frequencies can be obtained with multi-tube manifold systems compared with single-point measurement using the same tube length, due to the reinforcement of the higher frequencies in the input tubes” Holmes (2001, 149).

In the present study, it was aimed at maintaining the overall volume of the averaging system as close as possible to the volume of a single tube. It is also relevant to mention that Holmes (2001) notes that the frequency response is not greatly influenced by the volume within the manifold. An eight tube manifold was used for the area-averaged pressure measurements. The device is shown in Figure 3.23. The plastic tube lengths, between the surface taps and manifold, were kept small (to avoid resonant oscillations), so that a restrictor was only required between the manifold and Scanivalve device. Only four pressure taps were attached to the manifold at any time, the other four connections were sealed off. The length of the four tubes connected to the surface pressure taps were each 40 mm long, followed by an 80 mm length of tube connecting the manifold to the restrictor, while a 240mm tube was used between the manifold and Scanivalve device.

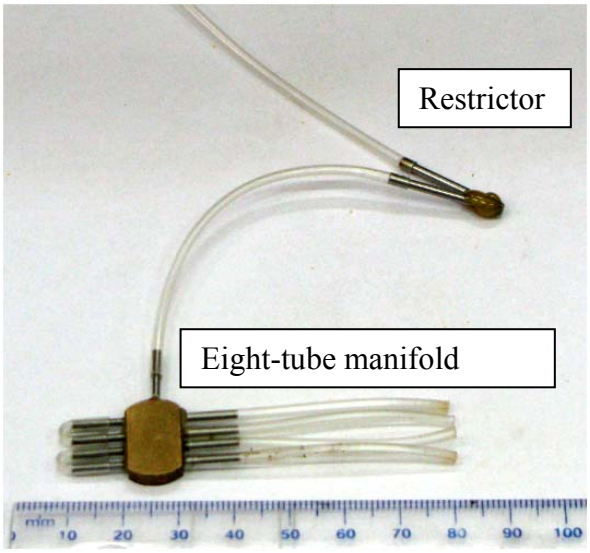


Figure 3.23 - Pneumatic manifold

3.3.7 Data acquisition and processing

Data acquisition

The correct scaling of wind-tunnel models is dependent on the simulation of specified similarity criteria. Of importance is the correct scaling of frequency, time, length and wind speed with respect to the determination of the length of samples and sample frequency in the wind-tunnel.

The similarity requirement is given by:

$$\frac{1}{\lambda_f} = \lambda_T = \frac{\lambda_L}{\lambda_V} \tag{3.3}$$

where $\lambda_f, \lambda_T, \lambda_L, \lambda_V$ are the frequency, time, geometric and speed scales, respectively.

The sampling frequency adopted for these investigations was 500Hz (500 samples per second), as used by the BLWT facility for similarly scaled models and flow conditions. This frequency is dependent on both the consideration of the energy distribution of the approach flow and the Nyquist recommendation regarding the minimum sampling rate. The minimum sampling rate suggested for these considerations was about 300Hz - 400Hz. The number of blocks used was 16 with 1024 samples per block providing a record, containing 16384 samples. The above mentioned scanning rate and number of samples result in a sampling period of 32 seconds.

The sampling period used for the measurement of surface pressures over rigid models must be chosen to achieve certain requirements. The following requirements are given by Davenport (2007). The first requirement is that the sampling period should be sufficiently long to provide stable estimates of the mean and RMS pressures. The second requirement is that the maximum and minimum measured peaks should provide representative estimates of peaks encountered during a full scale interval of about 60 minutes, because the mean hourly wind speed statistics are used in conjunction with estimated peak pressure coefficients to calculate full scale peak pressures.

Testing was conducted with a wind speed of approximately 10m/s, measured 300mm above wind-tunnel floor. A full scale wind speed of 35m/s (50-year hourly mean wind speed), corresponding to 150 m full scale was selected, providing a wind speed ratio of 3.5. The experimental wind speed, geometric and time scales are indicated below:

$$\lambda_V = \frac{1}{3.5} \tag{3.4}$$

$$\lambda_L = \frac{1}{500} \tag{3.5}$$

$$\lambda_T = \frac{\lambda_L}{\lambda_V} = \frac{\frac{1}{500}}{\frac{1}{3.5}} = \frac{1}{140} \tag{3.6}$$

The time scale used in the experimental investigations was 1:140, which indicates that 1 minute in the wind-tunnel is equivalent to a 140 minutes full scale. A time scale of 1:140 provides a full scale interval of 70 minutes (corresponding to a 32s second sampling period).

Data processing

Pressure signals were recorded in the form of time series, as indicated in the previous section. These time series were used to calculate the various pressure coefficients. The mean, RMS and peak pressure coefficients were normalised using the dynamic pressure at roof edge height. A data processing program developed in VBA was used to calculate the following coefficients.

The equations used for the calculation of the mean and RMS coefficients are defined as follows:

Mean - $$Cp_{mean} = \frac{1}{N}\sum_{i=1}^{N}\frac{Pi}{Q_{Ref}} \tag{3.7}$$

Root Mean Square - $$Cp_{RMS} = \frac{\sqrt{\frac{1}{N}\sum_{i=1}^{N}(Pi-Pmean)^2}}{Q_{Ref}} \tag{3.8}$$

where

p_i	i^{th} pressure measured at a tap on the roof
p_{mean}	mean pressure
Q_{Ref}	free-stream dynamic reference pressure at roof level
N	number of Samples (16384)

Figures 3.24 illustrates the position of taps 1 and 8, and Figure 3.25 shows a typical time series for these taps, at a wind direction and turbulence intensity of 0° and 10% (at roof height), respectively.

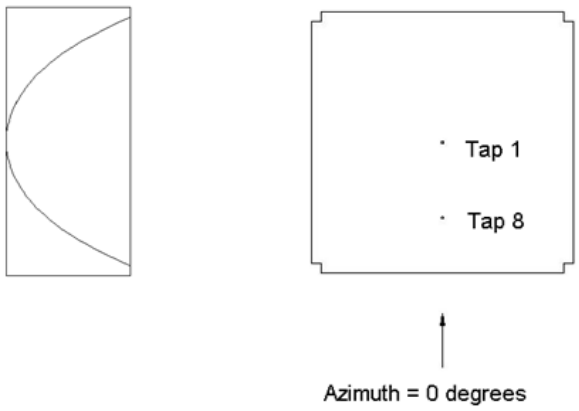


Figure 3.24 - Position of taps 1 and 8 for the 0° wind direction

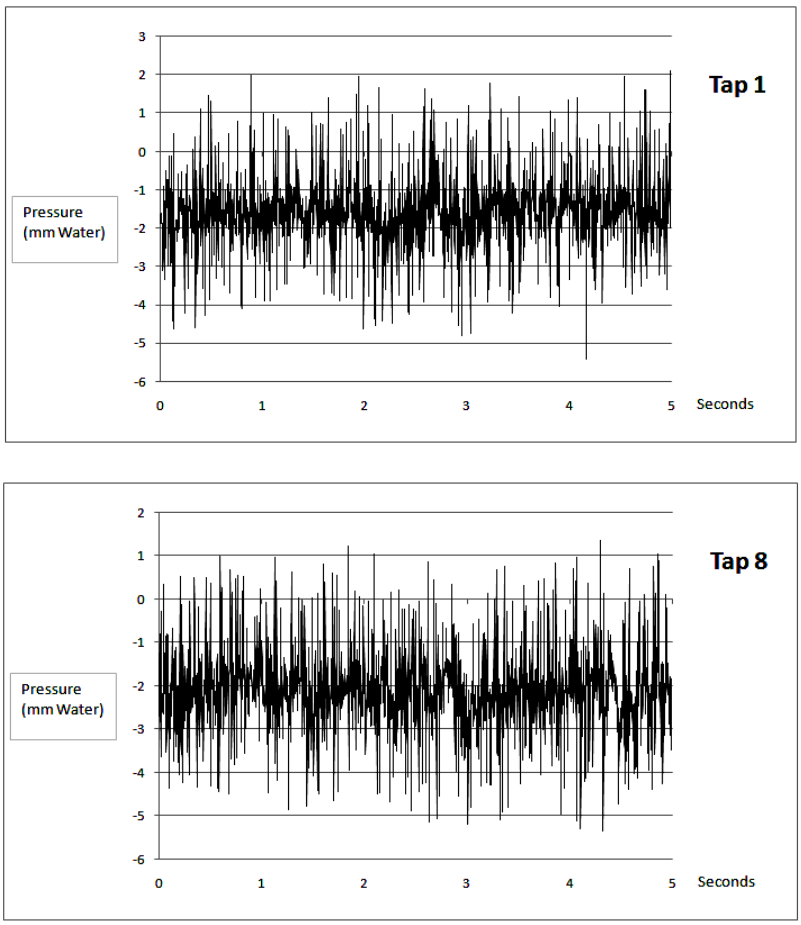


Figure 3.25 - Typical time series for the flat cross vault (θ = 0° and I= 10%)

The mean and RMS pressure coefficients are statistical quantities calculated directly from the time series. However, the peak pressure coefficient is not a statistical value, but rather the highest recorded peak. Therefore, to improve their reliability, extreme value analysis was applied. The extreme values are important in determining peak wind pressures and ultimately design loads.

Gumbel's method may be applied to a set of peak pressure values, which occur in a certain period. The periods must not overlap so that each peak is independent of any other. The peak pressures are fitted to a Fisher-Tippett Type 1 (Gumbel) distribution.

The Fisher-Tippet Type 1 asymptotic cumulative distribution function is given by:

$$P_y = e^{-e^{-y}} \tag{3.9}$$

where y is the standard measure or reduced variate and is given by:

$$y = a*(\hat{x} - U) \tag{3.10}$$

where U is the mode and (1/a) is the dispersion. A straight line (Gumbel plot) is required to calculate U and (1/a), which are the intercept and slope, respectively. This straight line plot is achieved by plotting the extreme value against 'y', which is calculated by taking twice the logarithm on both sides of the equation.

$$y = -\mathrm{Ln}(-\mathrm{LnP}) , \tag{3.11}$$

The probability term P is determined by ranking the peaks ($\hat{x}$) in ascending order of magnitude. The smallest is given the rank 1 to the largest having rank N. The estimated continuous distribution function (P) is then given by:

$$P_{\hat{x}\{m\}} = \frac{m}{N+1} \tag{3.12}$$

There is, however, an issue with this method as the estimated continuous distribution function ($P_{\hat{x}\{m\}}$) introduces bias, because of unequal confidence in the ranks. The calculation of the peak pressures was, therefore, conducted using a numerical approach to the Gumbel Method.

The Lieblein "Best Linear Unbiased Estimators" (BLUE) method was used as it is an improvement on the reliability of extreme peaks. The method correctly weights the extreme values and provides an unbiased result. This weighting is achieved by using BLUE estimators for a Fisher Tippett Type 1 distribution. The estimators comprise estimator A{m} for the mode U, and B{m} for the dispersion (1/a).

The approach comprises selecting 10 independent peaks from the time series to determine the parameters of the extreme value distribution. The data from 16 blocks (the entire time series) was sorted into 10 sets, which resulted in 10 independent peaks. Table 3.2 below shows the estimators used for N = 10.

Table 3.2 - Lieblein (BLUE) for Fisher Tippett Type 1 distribution (Data from Cook (1985))

N	M	A{m}	B{m}
10	1	0.223	-0.348
	2	0.162	-0.091
	3	0.134	-0.019
	4	0.113	0.022
	5	0.096	0.049
	6	0.081	0.066
	7	0.067	0.077
	8	0.054	0.083
	9	0.042	0.084
	10	0.029	0.078
Checksum		1.001	0.001

The mode *U* and the dispersion 1/a are then determined by multiplying the ranked extreme by the corresponding estimator and summing the products. The following equations show the calculation procedure for these two parameters:

$$U = \sum_{m=1}^{N} (A\{m\} * \hat{x}\{m\}) \tag{3.13}$$

$$1/a = \sum_{m=1}^{N}(B\{m\} * \hat{x}\{m\}) \quad (3.14)$$

Using the above mentioned parameters, the expected maximum and minimum pressure coefficients were calculated. Following the approach of SANS 10160-1989, a 3-second averaging time is appropriate to the design of cladding and fixing elements and a 10-second averaging time is appropriate to larger elements and overall loads. The expected peak pressure coefficients are defined below:

Cp_{peak}(3s) Expected negative peak pressure coefficient (3s averaging time)
Cp_{peak}(10s) Expected negative peak pressure coefficient (10s averaging time)

It should be noted that the wind specification included in SANS 10160 - 1989 is based on a 3-second gust wind speed; however, the new code, which is in development, is based on a 10-minute mean wind speed. The relationship between 3-second peak, mean hourly and 10-minute mean wind speeds are given in numerous text books (e.g. Simiu and Scanlan (1978)).

3.4 Qualitative Measurements

Two types of qualitative flow measurements were employed, which included smoke tests and mini-flag directional devices, as shown in Figures 3.26 and 3.27. Both techniques are aimed at visualization of the flow in order to get an understanding of the reasons for specific phenomenon observed in the wind-tunnel.

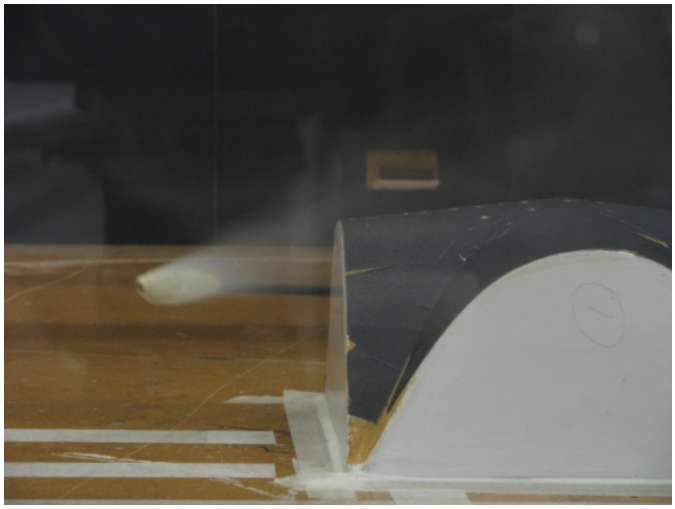


Figure 3.26 - Smoke visualization

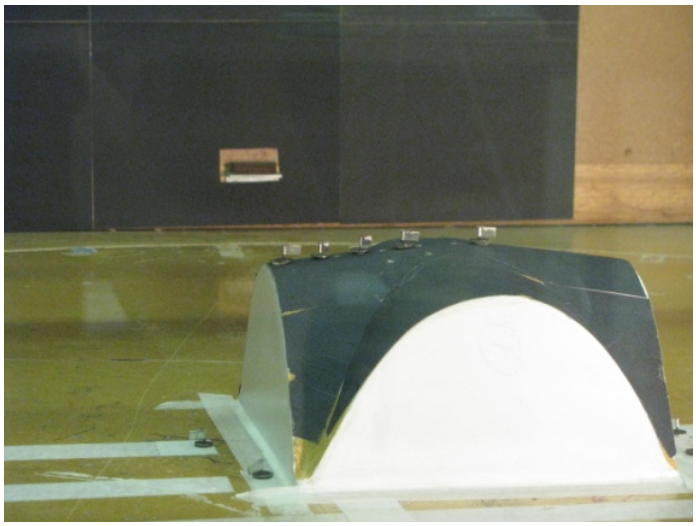


Figure 3.27 - Mini-flag devices

3.5 Reynolds Number

The model cross vault structures had a diameter of 240 mm, with a full scale/model ratio of 500. This model scale provides a full scale Reynolds number of the order 10^8 to 10^9, which corresponds to the supercritical Reynolds number regime. However, the current wind-tunnel tests were conducted at a free-stream wind speed of approximately 10 m/s (at 300mm above wind-tunnel floor) and a Reynolds number of 1.2×10^5 (based on the diameter of a single vault and wind speed at roof height). It has been indicated in the literature review that Reynolds number regime similitude is crucial when testing curved roof structures. In order to correct for this inability to model the correct range of Reynolds number, the

methodology proposed by the ESDU – 80025 (1980), as discussed in Chapter 2, was employed.

3.6 Repeatability of Measurements

The overall accuracy of the testing process can be assessed by evaluating the repeatability of the measured data. This was done by comparing the mean pressure distribution measured approximately 30 days apart. Figure 3.28 shows the test repeatability; for the flat cross vault, at taps 1 through 8, and at the 45° wind direction.

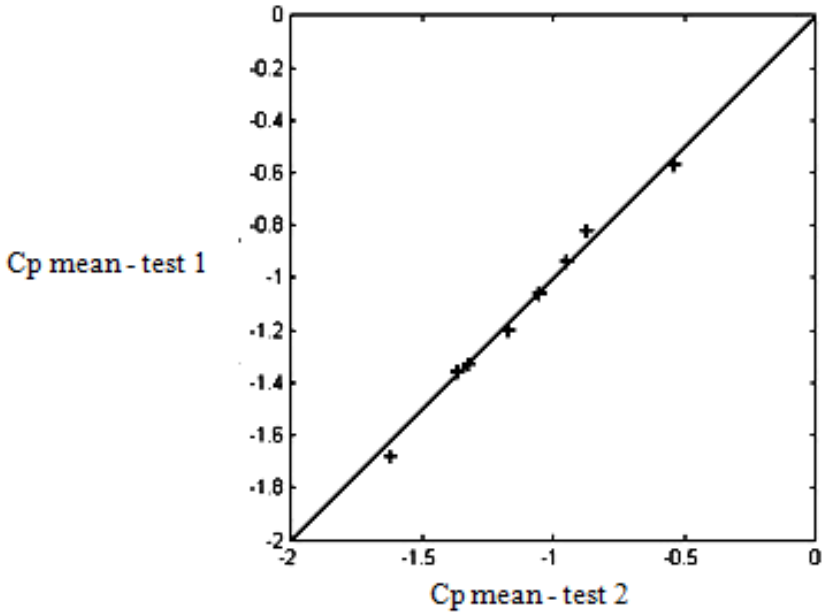


Figure 3.28 - Repeatability of a typical mean pressure coefficient distribution

Three separate tests were also carried out on the smooth flat cross vault model, to ascertain the extent of the experimental scatter. These tests were carried out in the wind-tunnel, with no attached floor roughness. Taps 6, 7 and 8 were attached to the Scanivalve device and were sampled at 500 Hz, 16 blocks and 1024 samples per block. The typical observed percentage difference (i.e. range) for the mean and RMS pressure coefficients were approximately 6% and 4%, respectively. (The maximum observed percentage range corresponding to the mean and RMS

pressure coefficients were 10% and 7%, respectively). These measurements are provided in Appendix B.

Extreme value analysis was carried out to improve the reliability of peak pressures, which are random by nature and may vary considerably from record to record. Considerable scatter was evident at some positions for both the 3 and 10 second peak pressure coefficients, with typical and maximum percentage difference of approximately 12% and 20%, respectively. The reasons for the large peak pressure discrepancies could be attributed to the spurious nature of peaks. The results of these measurements are provided in Appendix B.

3.7 Chapter Summary

This chapter described the tools and experimental procedures used to meet the objectives and accomplish the goals discussed in Chapter 1. The CSIR BLWT and instrumentation have been described. The techniques applied to the measurement of velocities and pressures were introduced. The methods for the interpretation and calculation of pressure coefficients were briefly discussed. Further experimental conditions are elaborated upon in subsequent chapters, where additional detail is applicable.

4 EFFECTS OF SURFACE ROUGHNESS / REYNOLDS NUMBER MODELLING

4.1 General

Numerous researchers have noted the sensitivity of surface pressures to surface roughness (Reynolds number). The distribution of loads over curved surfaces is largely affected by the separation point of the wind flow. Wind-tunnel scale modelling and testing is not able to reliably recreate the positions of flow separation, and artificial roughening of surfaces, as that recommended by the ESDU, is typically introduced. An initial investigation was carried out to assess the effects of surface roughness on surface pressures over cross vault structures and to establish whether surface roughening was required.

4.2 Test Procedure

These initial tests were carried out using the flat cross vault model, in the 'smooth' boundary-layer, and with surface roughness corresponding to either smooth fibreglass or attached sandpaper. The pressures were recorded at taps 6, 7 and 8, aligned at angles of 0°, 30° and 45° to the approach flow, as shown in Figure 4.1.

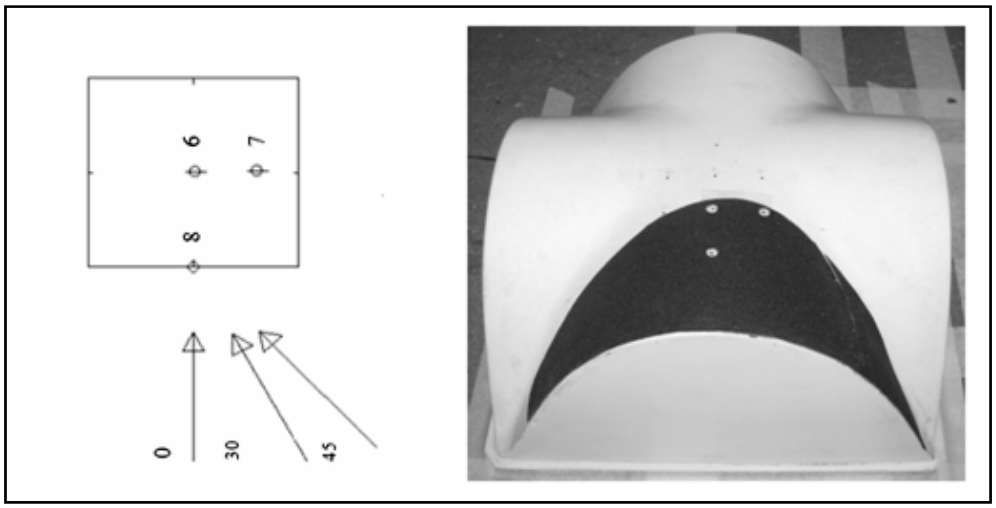


Figure 4.1 - Tap location and wind direction

4.3 Distributed Surface Roughness

The uniformly distributed surface roughness used in the current investigation was provided by means of commercially available sandpapers. The standard used for coated abrasives was that of the Federation of European Producers of Abrasives (FEPA). The FEPA standard defines the grade by the average and range of grain sizes. The particle sizes used in the current investigation are summarized in Table 4.1. The mean diameter of the smooth barrel vault was used to calculate the relative roughness, since the change in diameter, due to the addition of sandpaper, was negligible. The ESDU-80025 (1980) report suggests, from experimental evidence, that the mean quoted equivalent uniform sand grain roughness size should be increased by 50%, because the grit size varies about the manufacturers mean and is not evenly distributed over the surface.

Table 4.1 - Relative roughness

Grit	Effective Roughness ε(mm)	Relative Roughness (ε/D) $*10^3$
P40	0.64	2.66
P150	0.15	0.63

The sandpaper was cut into two sections and wrapped around the model in the manner shown in Figure 4.2. It was attached with double-sided tape, with care taken to ensure a tight fit between the paper and model. The two sandpapers attached to the flat cross vault are shown in Figures 4.2 and 4.3. Approximately 4mm diameter holes were cut into the sandpaper surrounding the pressure tappings, and wood glue was applied to the edges to achieve a smooth transition, as shown in Figure 4.3.



Figure 4.2 - P150(left) and P40(right) grit sandpapers attached to the model

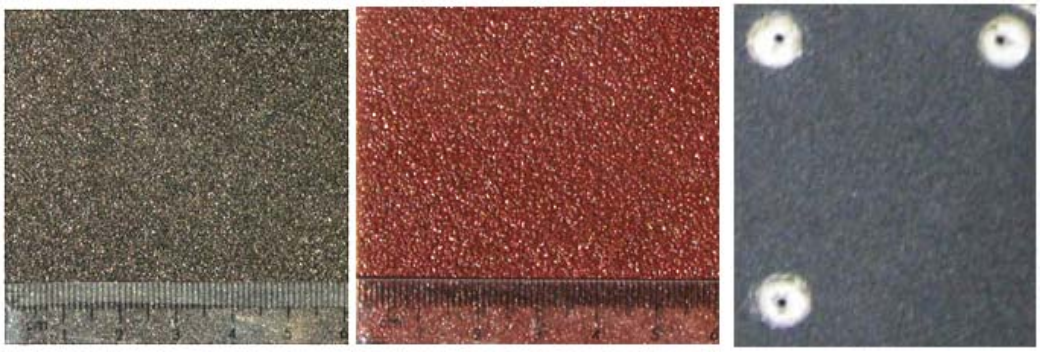


Figure 4.3 - P150, P40 grit sandpapers and tap surroundings

4.4 Results of the ESDU- 80025 (1980) Procedures

The results of the ESDU-80025 (1980) procedure discussed in Chapter 2, for two differing sandpaper sizes and four different full-scale surface finishes, are shown in Table 4.2. If the drag coefficient similarity is achieved, then the pressure distributions over a circular cylinder with differing surface roughness and scale will be similar. This similarity is indicated in Figure 4.4, which has been produced using the ESDU-80025 centreline pressure coefficient procedure. Due to the drag coefficient and pressure distribution similarity corresponding to the P150 sandpaper and full-scale surfaces, as illustrated in Table 4.2 and Figure 4.4, the P150 sandpaper was identified as the most suitable.

Table 4.2 - Results of the ESDU drag coefficient procedure

	R_e	$(\varepsilon/d)^* 10^3$	C_{D0}
Model (Smooth fibreglass)	1.2E+05	0.02	0.31
Model (P40 grit sandpaper)	1.2E+05	2.66	0.90
Model (P150 grit sandpaper)	1.2E+05	0.63	0.55
Full scale (Smooth Concrete)	2.6E+08	0.55E-03	0.52
Full scale (Rough Concrete)	2.6E+08	9.09E-03	0.54
Full scale (Painted Metal)	2.6E+08	7.27E-05	0.51
Full scale (Sheet Metal)	2.6E+08	1.82E-05	0.51

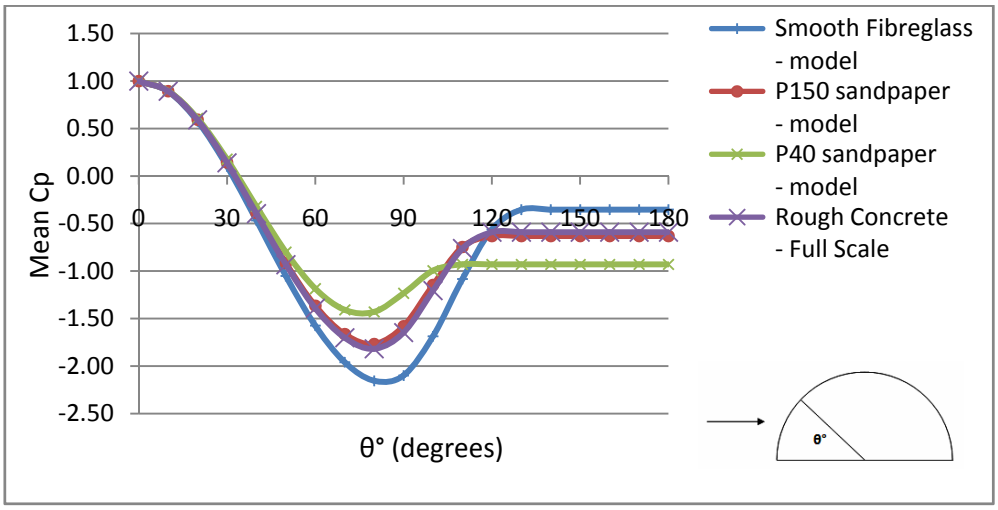


Figure 4.4 - Results of the ESDU mean pressure distribution procedure

4.5 Results and Discussion

4.5.1 Mean pressure coefficients

Work conducted by Ribeiro (1991), Taylor (1992) and Letchford and Sarkar (2000) on circular domes and cylinders indicates that increasing roughness promotes earlier flow separation, larger (i.e. more positive) mean pressure near the point of separation and lower mean pressures in the wake. Work conducted on bluff body structures by Maruta et al. (1998), on roughened rectangular structures, shows that the mean pressures were most negative for the smoothest finish and least negative for the largest roughness size.

The trend observed in Figures 4.5 through 4.7 is that the mean pressure coefficients corresponding to the P40 surface were generally more positive than those over the P150 surface, which, in turn, were larger than the pressures over the smooth surface. There are, however, inconsistencies at some pressure taps and wind directions, which may be accounted for by the experimental scatter and possible local affects at the sandpaper attachment points. The results follow those of Matura et al. (1998), and Letchford and Sakar (2000), in the vicinity of flow separation, for which increased surface roughness caused larger mean pressure coefficients. Figures 4.8 and 4.9 present comparisons between the mean pressure coefficients corresponding to the three roughness types, to further highlight the sensitivity of the mean surface pressures to surface roughness. These plots are produced from three separate experimental runs, in which pressures were measured at taps 6, 7 and 8, for the cross vault oriented at the 0°, 30° and 45° wind directions.

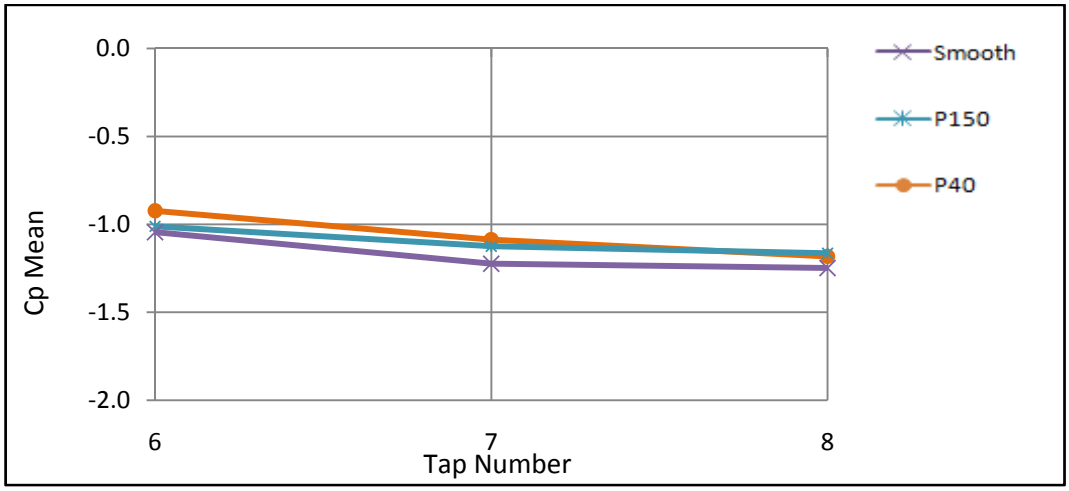


Figure 4.5 - Mean pressure coefficient vs. tap (0° wind direction)

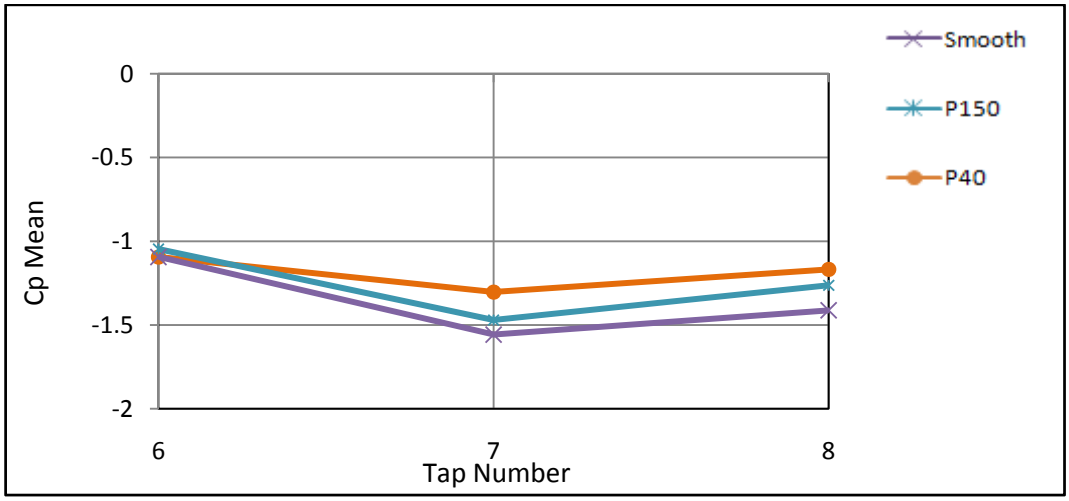


Figure 4.6 - Mean pressure coefficient vs. tap (30° wind direction)

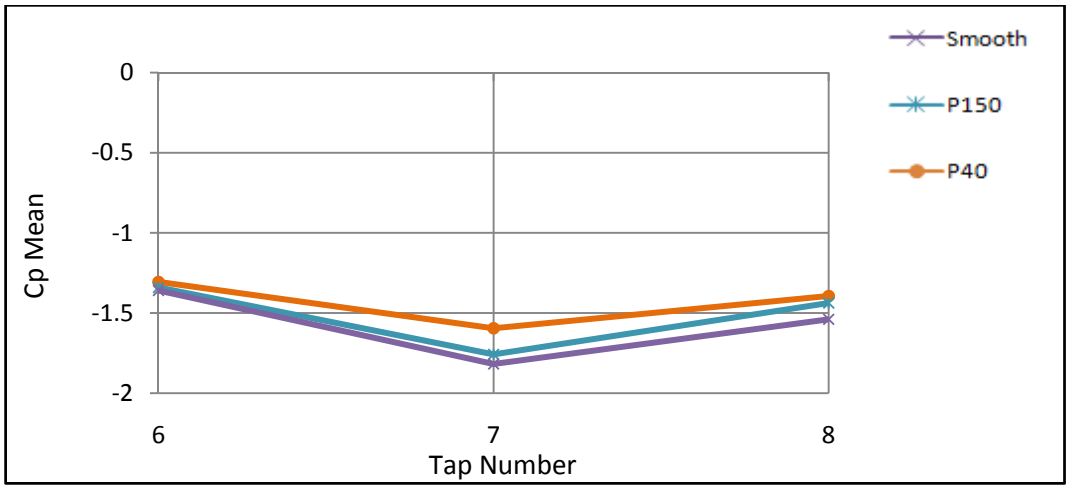


Figure 4.7 - Mean pressure coefficient vs. tap (45° wind direction)

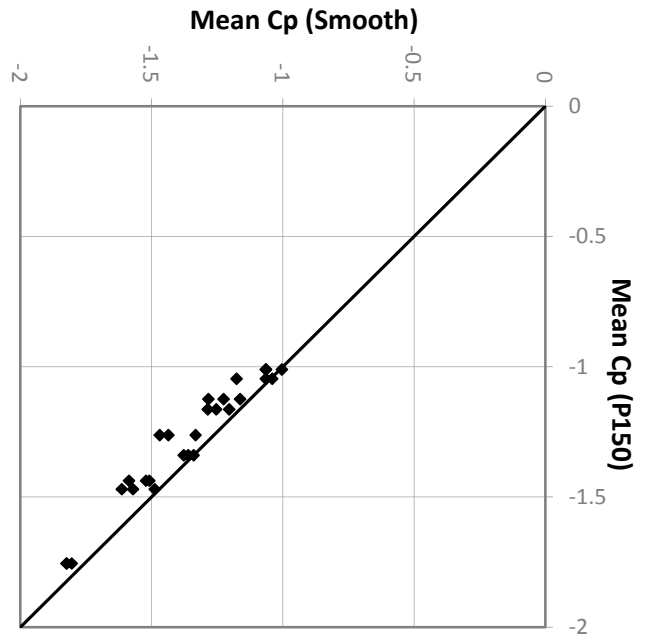


Figure 4.8 - Cp_{mean} (Smooth fibreglass) vs. Cp_{mean} (P150 sandpaper)

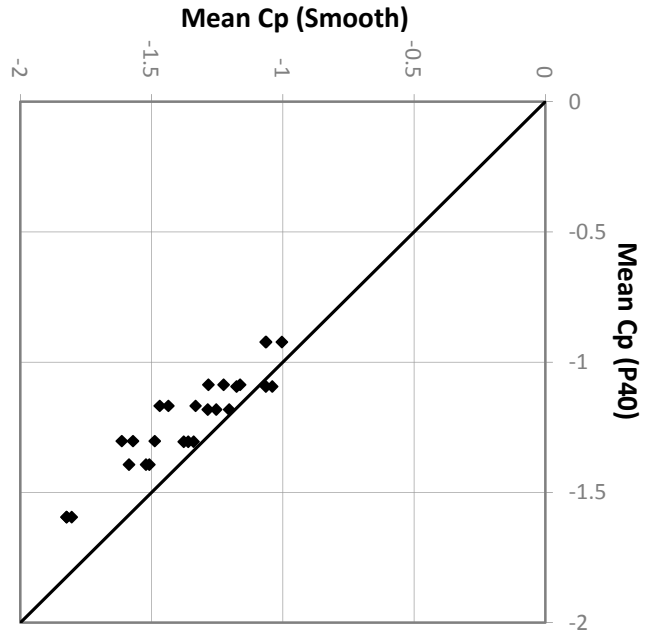


Figure 4.9 - Cp_{mean} (Smooth fibreglass) vs. Cp_{mean} (P40 sandpaper)

Numerically area-averaged pressures for taps 6, 7 and 8 further emphasize the effects of surface roughness on the mean pressure coefficients. Areas were assigned depending on the spatial distribution of the taps. Due to the positioning of the taps, each was assigned an equal tributary area. The equation used to calculate the averaged pressures is shown below:

$$Cp_{av} = \left(C_{p(tap6)} + C_{p(tap7)} + C_{p(tap8)}\right)\Big/_{3} \qquad (4.1)$$

where $Cp_{(tap6)}$, $Cp_{(tap7)}$ and $Cp_{(tap8)}$ are the point pressures at taps 6, 7 and 8, respectively. The numerically area-averaged pressures are shown in Figure 4.10.

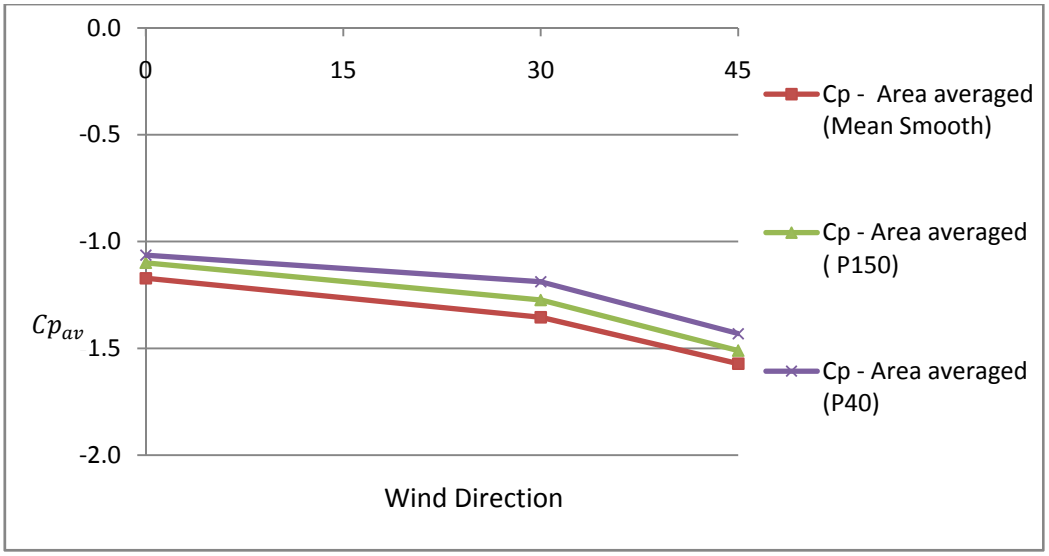


Figure 4.10 - Area-averaged mean pressure coefficients

4.5.2 RMS pressure coefficient

Maruta et al. (1998) and Stathopoulos et al. (1988) conducted tests on rectangular buildings with various forms of attached roughness. Both studies concluded that increasing surface roughness generally resulted in lower RMS pressure coefficients. Letchford and Sakar (2000) investigated centreline pressure distributions over rough and smooth domes. The authors noted that with increased surface roughness, the RMS pressure coefficients decreased near of the point of flow separation, but an overall increase was observed in the wake.

The RMS pressure coefficients measured at taps 6 through 8, for the 0° wind direction, are predominantly controlled by flow separation at the vault edge. As shown in Figure 4.11, the RMS pressure coefficients corresponding to the smooth fibreglass surface and 0° wind direction are larger than those corresponding to both rough surfaces. This trend is similar to that observed by Maruta et al (1998), with flow separation at sharp edges.

The RMS pressure coefficients for the 30° and 45° wind directions are shown in Figures 4.12 and 4.13. These results do not show any apparent trend and are generally within the experimental scatter. This result is further emphasized by Figures 4.14 and 4.15.

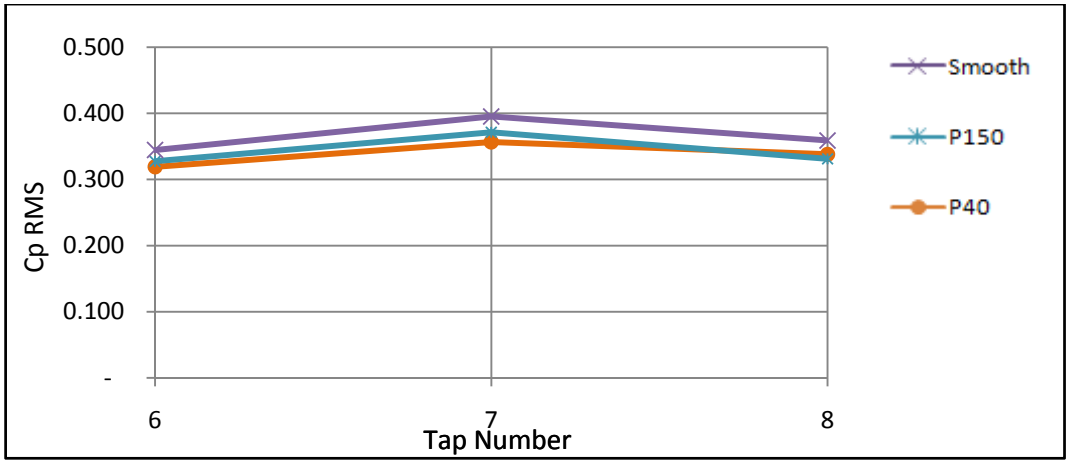


Figure 4.11 - RMS pressure coefficient vs. tap (0° wind direction)

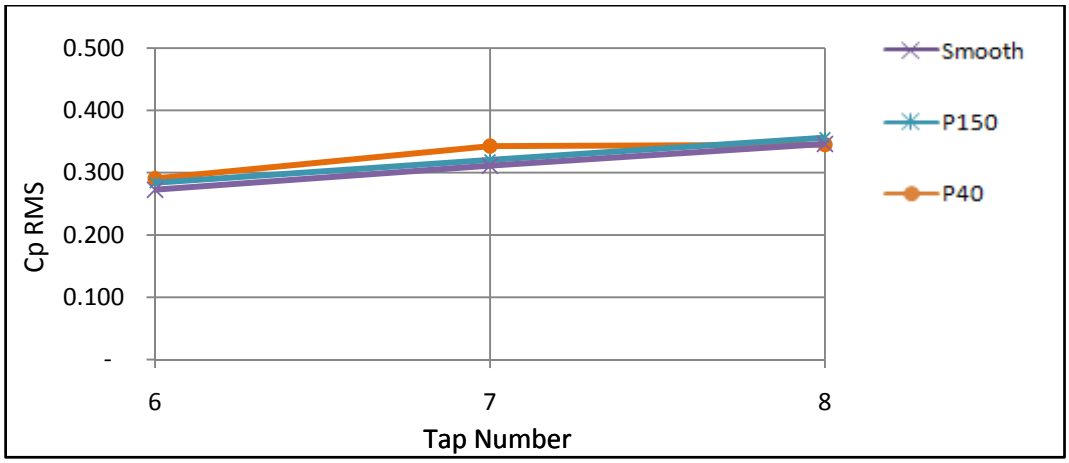


Figure 4.12 - RMS pressure coefficient vs. tap (30° wind direction)

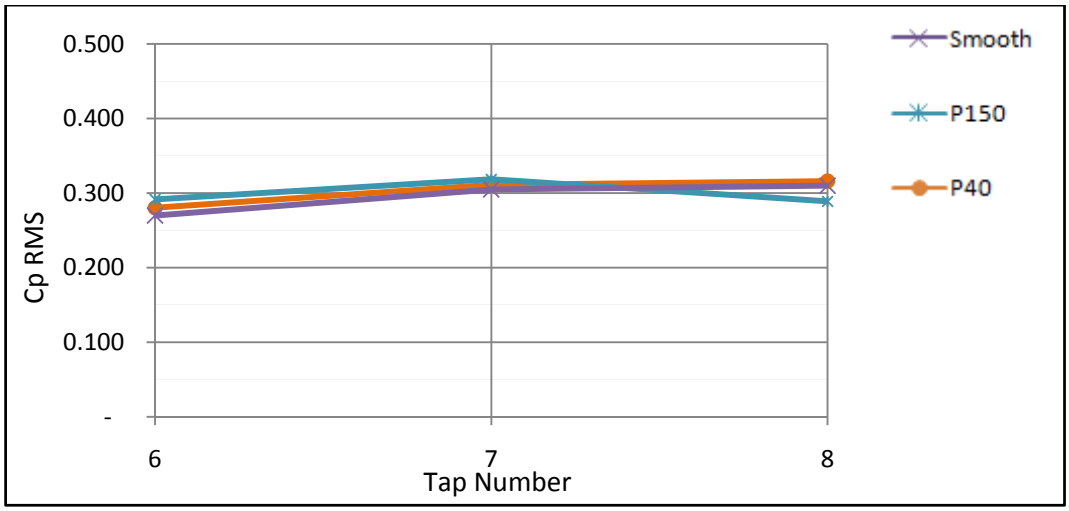


Figure 4.13 - RMS pressure coefficient vs. tap (45° wind direction)

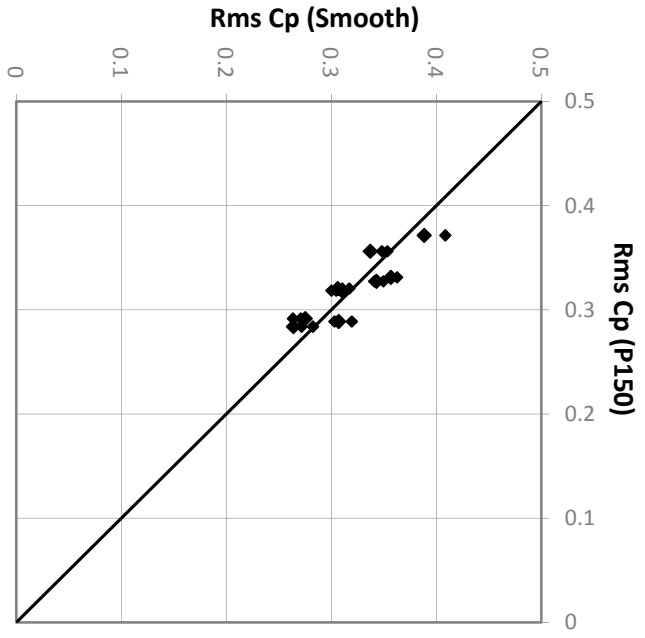


Figure 4.14 - Cp_{RMS} (Smooth fibreglass) vs. Cp_{RMS} (P150 sandpaper)

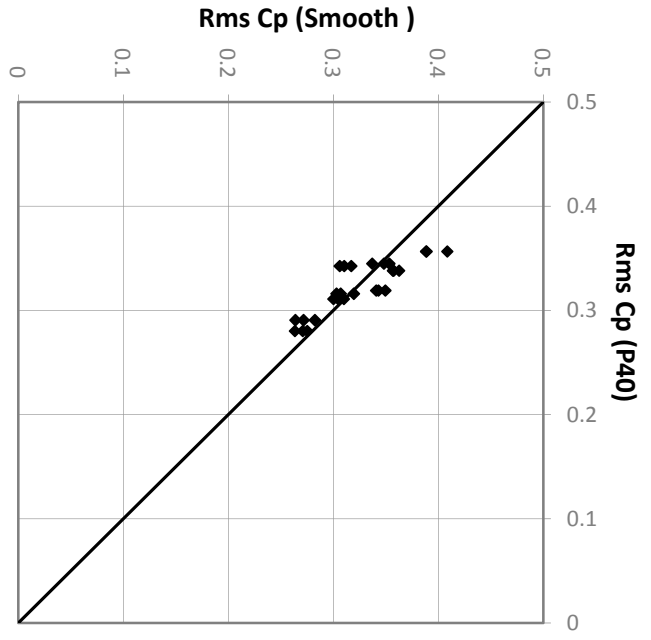


Figure 4.15 - Cp_{RMS} (Smooth fibreglass) vs. Cp_{RMS} (P40 sandpaper)

4.5.3 Negative peak pressure coefficients

Maruta et al. (1998) and Stathopoulos et al. (1988) revealed that negative peak pressures increased slightly, on side walls of rectangular wind-tunnel models, with increased surface roughness. As noted previously, the effect of surface roughening on negative peak pressures over curved structures (i.e. domes and arches), is an increase near the point of flow separation and a decrease in the wake.

In the current study, the attachment of the P150 sandpaper generally showed no noticeable peak pressure coefficient variation (refer to Figures 4.16 through 4.23). However, increased (i.e. more positive) negative peak pressures were evident for the P40 sandpaper, which also indicates that further increases in roughness magnitude may well result in more noticeable pressure reductions. It should also be noted that a sizeable reduction in magnitude of the peak suction at tap 7 is evident, which is not supported by the mean and RMS pressures. The reasons for the large discrepancy may be attributed to the spurious nature of peaks, or possibly the inadequate smoothing of the sandpaper surrounding the tapping. Figure 4.22 and 4.23 further emphasizes those trends noted in Figures 4.17 through 4.21.

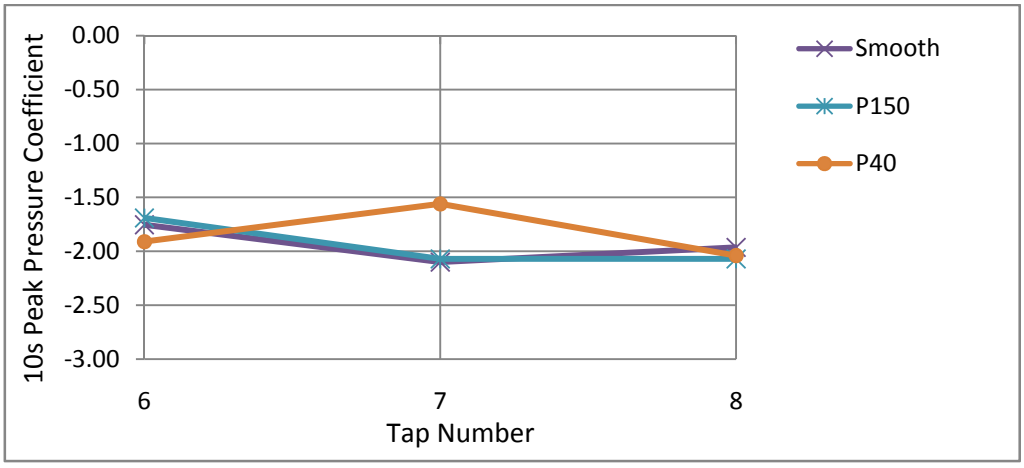


Figure 4.16 - 10s peak pressure coefficients vs. tap (0° wind direction)

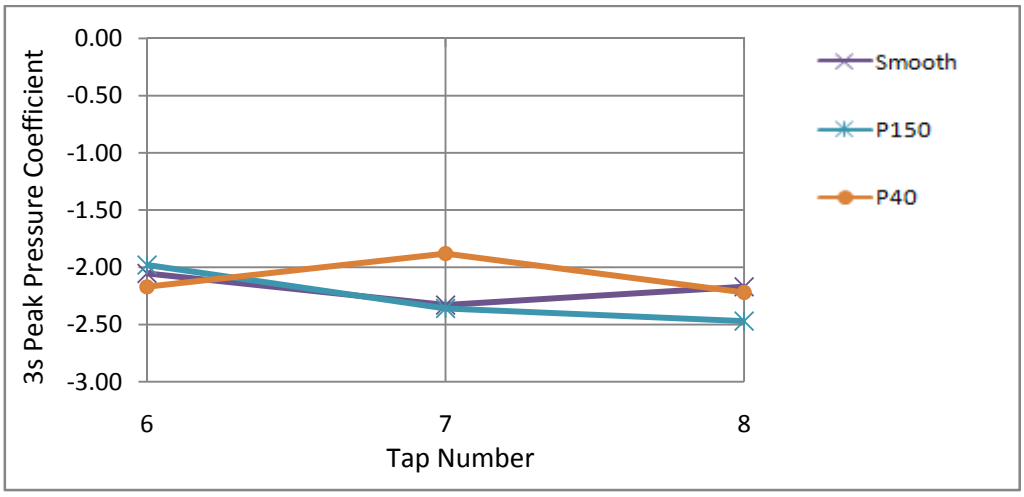


Figure 4.17- 3s peak pressure coefficients vs. tap (0° wind direction)

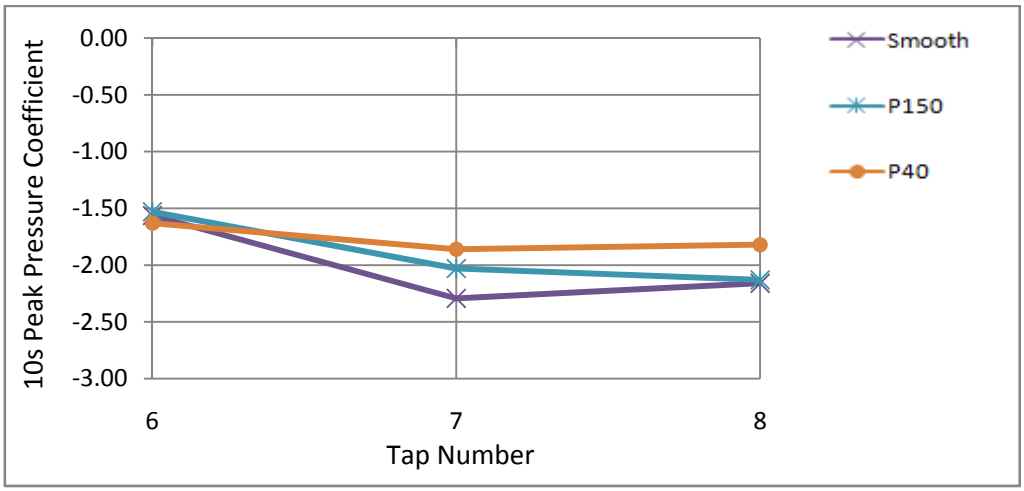


Figure 4.18 - 10s peak pressure coefficients vs. tap (30° wind direction)

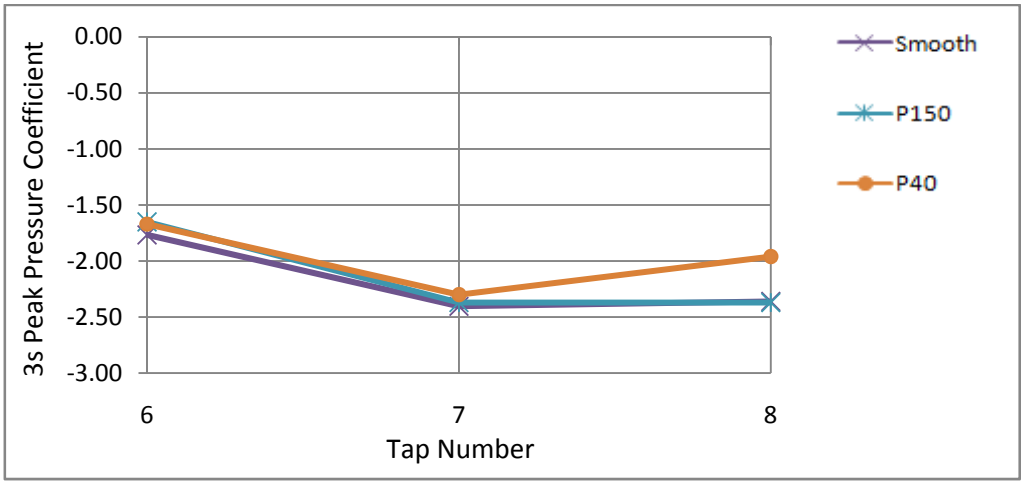


Figure 4.19 - 3s peak pressure coefficients vs. tap (30° wind direction)

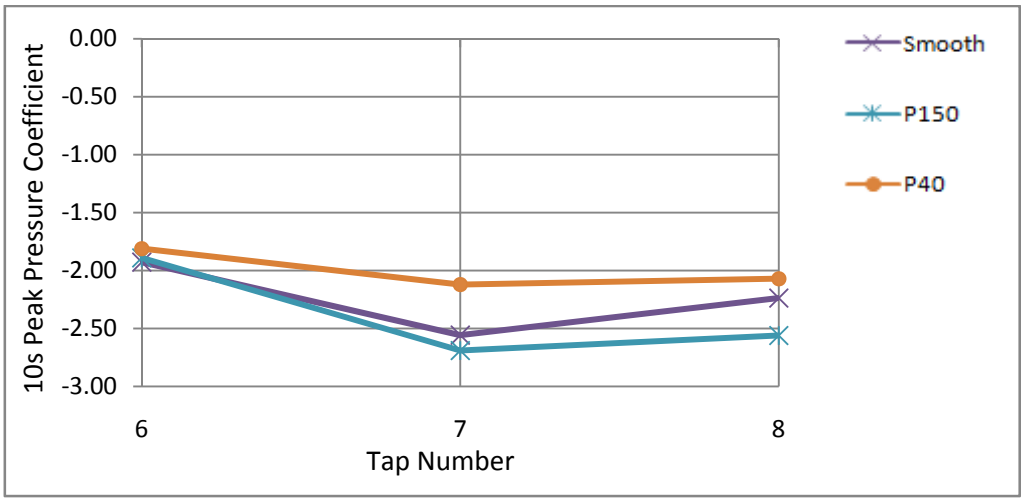


Figure 4.20 - 10s peak pressure coefficients vs. tap (45° wind direction)

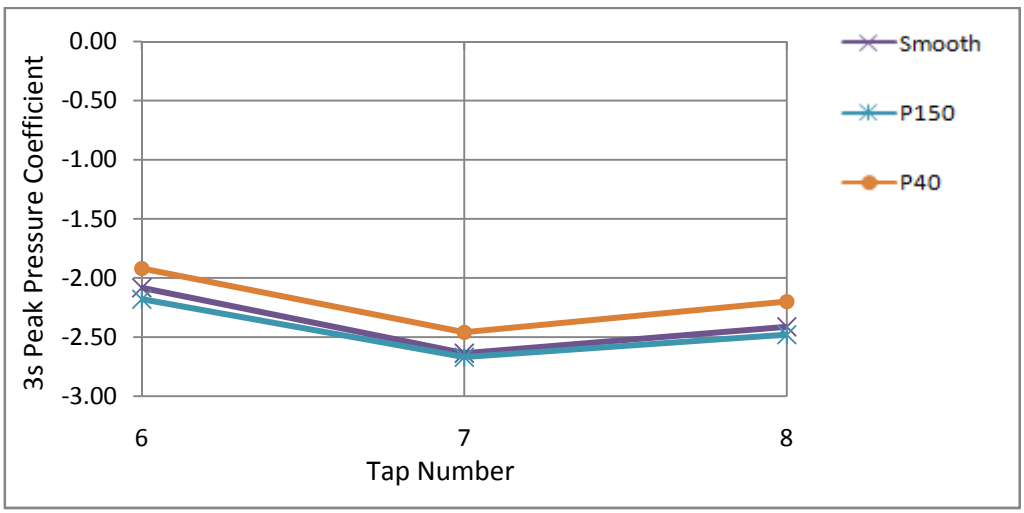


Figure 4.21 - 3s peak pressure coefficients vs. tap (45° wind direction)

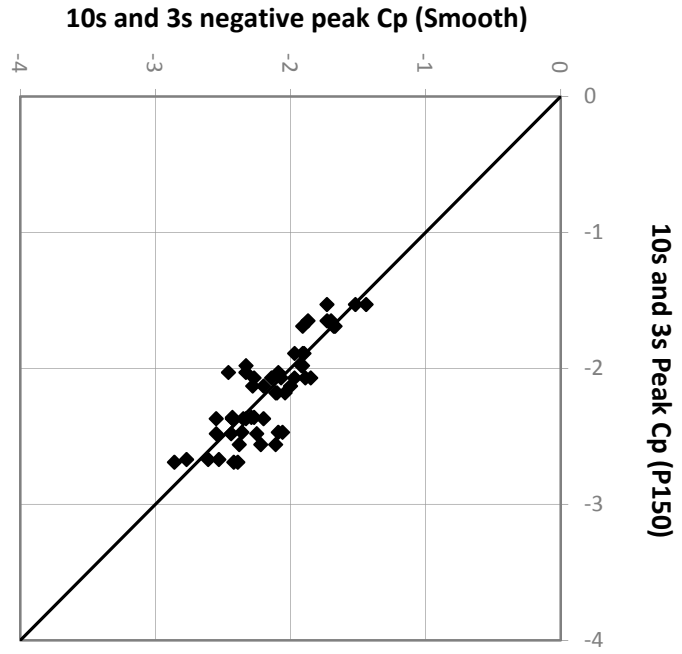


Figure 4.22 - Cp_{peak} (Smooth fibreglass) vs. Cp_{peak} (P150 sandpaper)

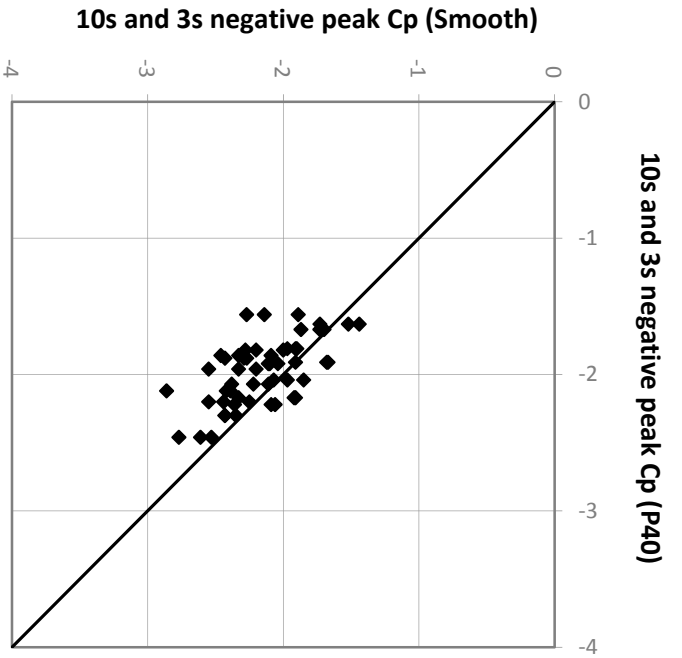


Figure 4.23 - Cp_{peak} (Smooth fibreglass) vs. Cp_{peak} (P40 sandpaper)

4.6 Conclusions

The experimental results reveal that the attached P150 and P40 uniform roughness reduced the mean suctions over the flat cross vault. A maximum reduction of approximately 15% was observed for the attached P40 sandpaper. These results coincide with results quoted in the literature, for single vaults and bluff body structures, in which mean pressures increase with increased surface roughness magnitude.

The RMS pressure coefficients were most notably affected at the 0° wind direction, for which the maximum observed difference was approximately 10 %. The results for the other wind directions showed little influence of surface roughness, as results were practically identical. Visible negative peak pressure increases were observed at several tap positions, most notably for the roughest attached sandpaper. The smooth surface did, however, generally experience slightly lower pressure coefficients.

The results of the ESDU-80025 (1980) procedure and the initial experimental investigations emphasized a need for surface roughening to achieve model and full-scale pressure distribution similitude. A roughness of $k/d \times 10^3 = 0.63$ (P150), in accordance with the ESDU procedure, was selected for all further tests.

5 EFFECTS OF TURBULENCE

5.1 General

As is the case with the addition of distributed surface roughness, the turbulence of the incident flow affects the relationship between negative surface pressures and Reynolds number for curved roof structures. For curved structures, such as domes and cylinders, the drag coefficient drops at a lower Reynolds number in turbulent flow than in smooth flow, which indicates that there is a direct shift in the effective transitional Reynolds number due to turbulence. Cheung and Melbourne (1983) indicate that turbulence intensity affects the separating boundary-layer and interacts with both the separated shear layers and the wake.

Figure 5.1 illustrates the turbulence intensity variation for the two different boundary-layers. The less turbulent boundary-layer is denoted as ‘smooth’ and the more turbulent as ‘rough’.

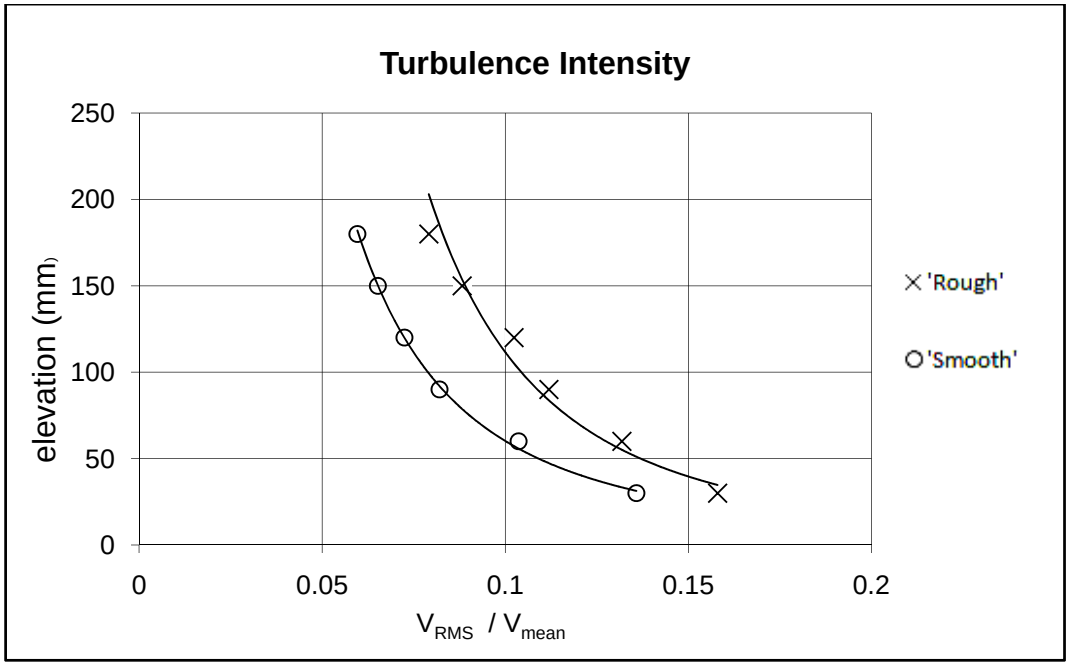


Figure 5.1 - Turbulence intensity profiles for the two boundary-layers

5.2 Results and Discussion

The effects of turbulence intensity on the mean, RMS and negative 3s peak pressure coefficients, for all vault types, are discussed in the following section. The wind direction was adjusted from 0° to 180°, with data captured at 0°, 15°, 30°, 45°, 60°, 75°, 90°, 120°, 150° and 180°. The general adjustment pattern is shown in Figure 5.2 below.

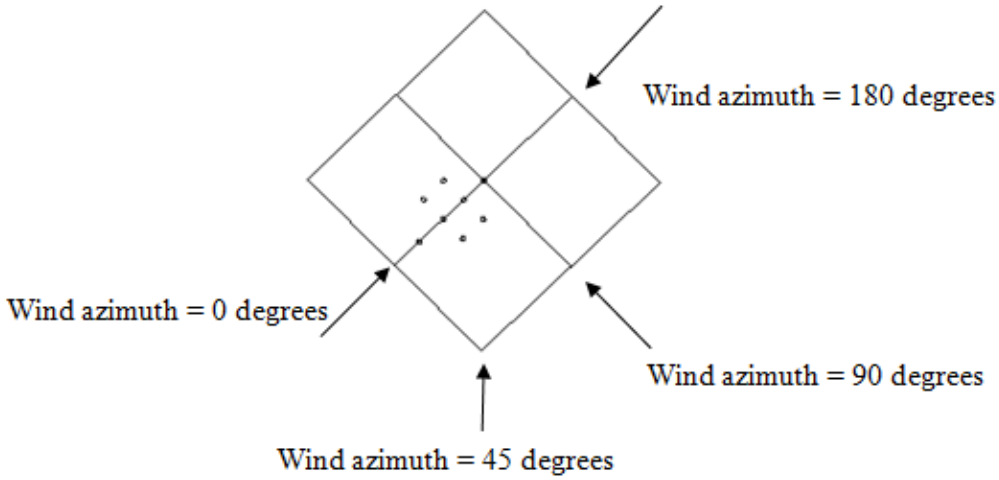


Figure 5.2 - Position of model with wind direction = 0°, 45°, 90° and 180°

5.2.1 Mean pressure coefficients

Work conducted on rectangular structures indicates that there is minimal effect of relatively small variations of turbulence intensity on mean pressure coefficient distributions. However, experimental investigations such as those by Tieleman (1993) and Saathof and Melbourne (1986), show mean pressure sensitivity to turbulence intensity. Tieleman (1993) noted that mean pressure coefficients become more positive with increased turbulence intensity. Saathof and Melbourne (1986) measured surface pressures within a separation bubble and noted that mean pressure coefficients are affected by turbulence intensity, but not turbulence scale near the leading edge.

In the case of circular cylinders and domes, the effects of turbulence observed by Cheung and Melbourne (1983) and Taylor(1991) were that the zero and minimum

mean pressure coefficients all moved slightly rearwards (further along the surface) with an increase in the turbulence intensity.

Figures 5.3 to 5.5 compare the relationship between the current experimental mean pressures, for all cross vaults, within the two boundary-layers simulated in this study. The pressures shown in these figures are those measured at all tap positions and wind directions investigated. It is evident in these figures that mean pressure coefficients were not significantly affected by the turbulence intensity variation. In most cases, the differences are negligible and well within observed experimental scatter. However, there are several cases where larger variations are observed. Generally, the mean pressure coefficients for the 'smooth' boundary-layer were either similar or slightly lower in magnitude than those measured for the 'rough' boundary-layer. The results of this investigation are consistent with trends observed in tests conducted on rectangular and curved roof bluff bodies.

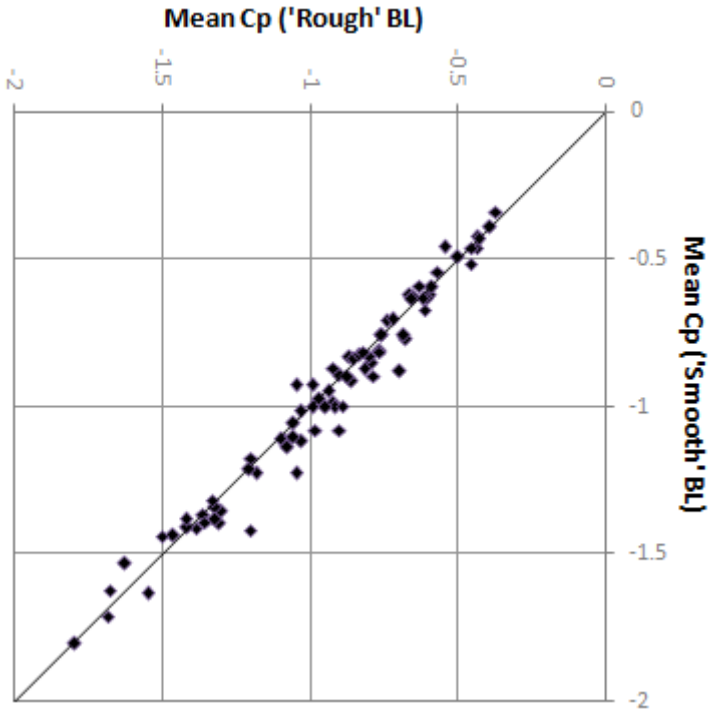


Figure 5.3 - Mean pressure coefficient ('smooth' BL) versus mean pressure coefficient ('rough' BL), for the flat cross vault

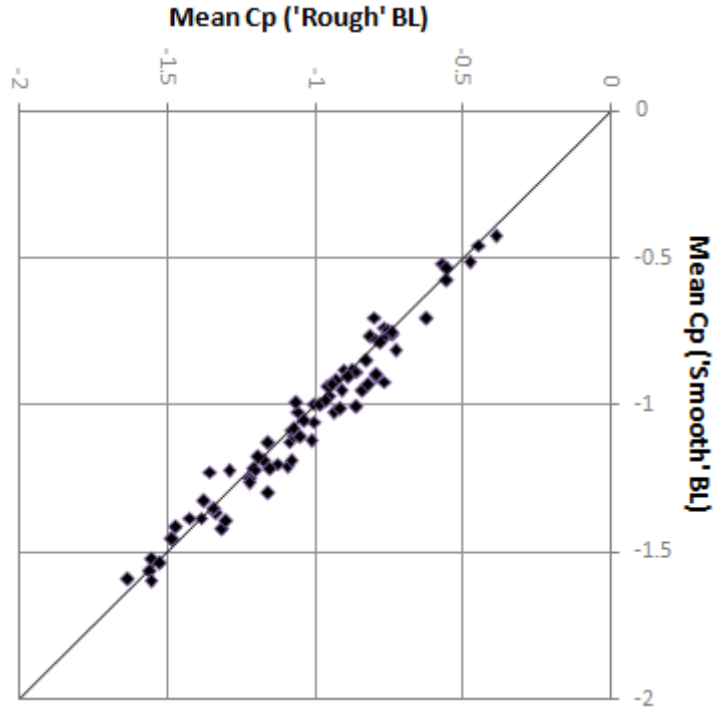


Figure 5.4 - Mean pressure coefficient (‘smooth’ BL) versus mean pressure coefficient (‘rough’ BL), for the convex cross vault

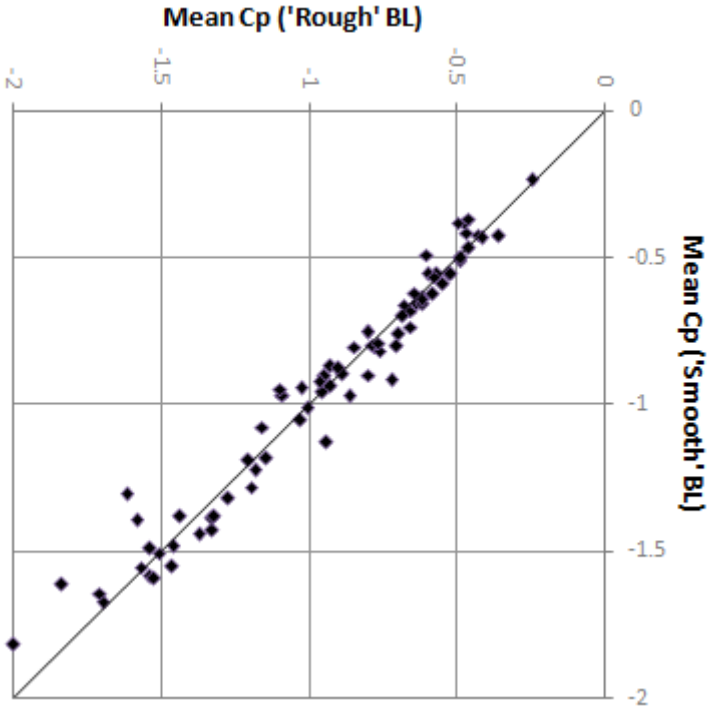


Figure 5.5 - Mean pressure coefficient (‘smooth’ BL) versus mean pressure coefficient (‘rough’ BL), for the concave cross vault

5.2.2 RMS pressure coefficients

The fluctuating pressures over sharp edged and curved roof structures are the result of two major actions. The first source of surface pressure fluctuation is produced by the velocity fluctuations of the oncoming flow, and the second source is fluctuations induced by vortex shedding and wake turbulence, which are dependent on the geometry of the structure.

RMS pressure coefficient increase with increased turbulence intensity has been observed in numerous tests on rectangular and curved structures, such as those of Tieleman (1993) on rectangular prisms, Cheung and Melbourne (1983) on circular cylinders, in both subcritical and supercritical flows, and by Taylor (1991) and Letchford and Sakar (2000) on hemispherical domes.

The results of the current investigations show that the RMS pressure coefficients increased with an increase in turbulence intensity. Figures 5.6 through 5.8 show the RMS pressure coefficient variation for all three model types and the two boundary-layer profiles. The 'rough' boundary-layer RMS pressure coefficients, for all cross vault forms, were almost entirely larger than those measured within the 'smooth' boundary-layer.

Table 5.1 shows the RMS pressure coefficient percent difference for the flat cross vault and two boundary-layers only. The observed percentage difference between the RMS pressure coefficients for the differing flows was generally between 15% and 25%. The results show that a 3% difference in turbulence intensity, at roof height, resulted in a visible increase in the magnitude of the RMS pressure coefficient, with a maximum difference of 28%.

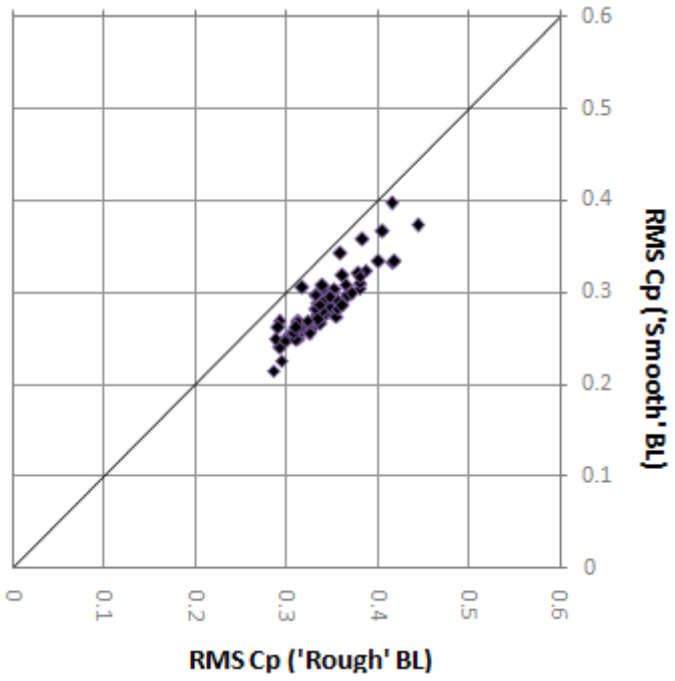


Figure 5.6 - RMS pressure coefficient (‘smooth’ BL) versus RMS pressure coefficient (‘rough’ BL), for the flat cross vault

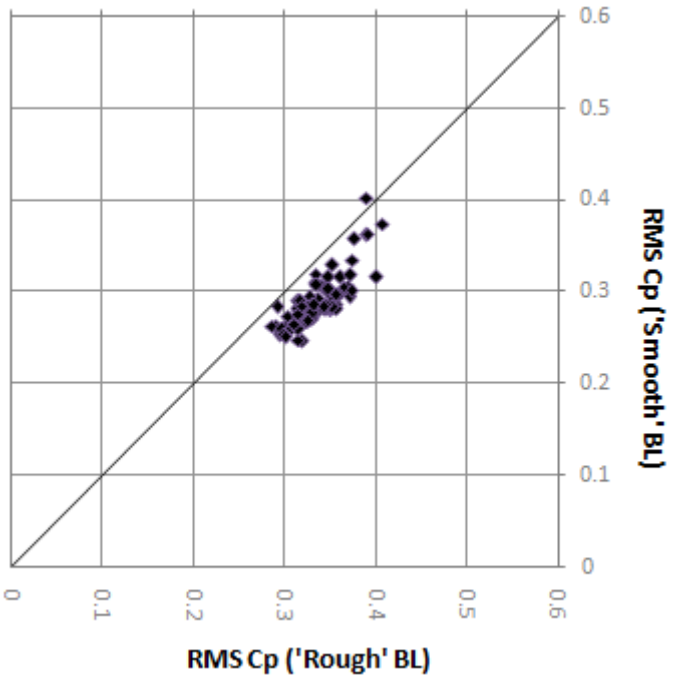


Figure 5.7 - RMS pressure coefficient (‘smooth’ BL) versus RMS pressure coefficient (‘rough’ BL), for the convex cross vault

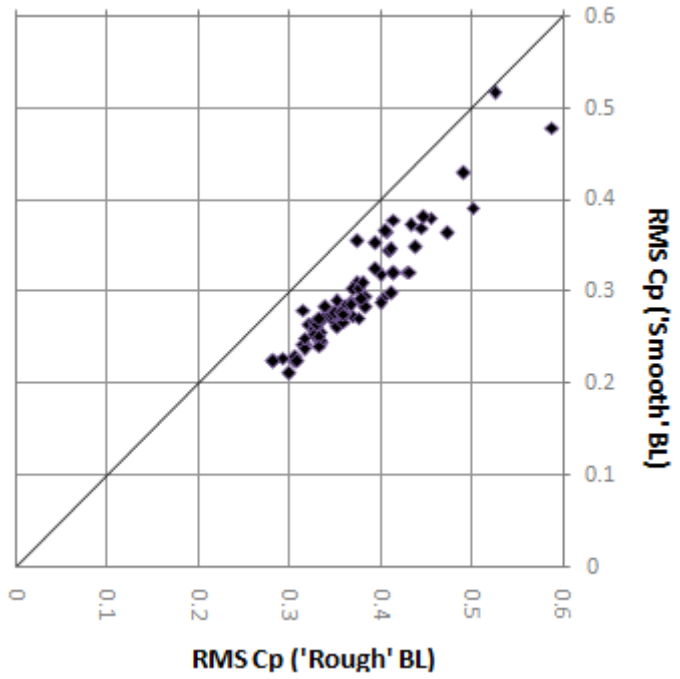


Figure 5.8 - RMS pressure coefficient ('smooth' BL) versus RMS pressure coefficient ('rough' BL), for the concave cross vault

Table 5.1 - Percent difference (RMS pressure coefficient, flat cross vault)

Θ =0°	% Difference	Θ =15°	% Difference
Tap 1	4	**Tap 1**	19
Tap2	18	**Tap2**	18
Tap 3	15	**Tap 3**	16
Tap 4	18	**Tap 4**	17
Tap 5	22	**Tap 5**	21
Tap 6	10	**Tap 6**	5
Tap 7	22	**Tap 7**	10
Tap 8	17	**Tap 8**	22

Θ =30°	% Difference	Θ =45°	% Difference
Tap 1	28	**Tap 1**	20
Tap2	18	**Tap2**	19
Tap 3	22	**Tap 3**	20
Tap 4	21	**Tap 4**	20
Tap 5	11	**Tap 5**	19
Tap 6	18	**Tap 6**	24
Tap 7	20	**Tap 7**	26
Tap 8	16	**Tap 8**	21

Θ =60°	% Difference	Θ =75°	% Difference
Tap 1	15	**Tap 1**	26
Tap2	20	**Tap2**	22
Tap 3	23	**Tap 3**	23
Tap 4	22	**Tap 4**	23
Tap 5	16	**Tap 5**	21
Tap 6	22	**Tap 6**	20
Tap 7	22	**Tap 7**	20
Tap 8	23	**Tap 8**	23

Θ =90°	% Difference	Θ =120°	% Difference
Tap 1	8	**Tap 1**	11
Tap2	12	**Tap2**	16
Tap 3	15	**Tap 3**	18
Tap 4	7	**Tap 4**	18
Tap 5	22	**Tap 5**	21
Tap 6	17	**Tap 6**	13
Tap 7	17	**Tap 7**	11
Tap 8	21	**Tap 8**	18

Θ =150°	% Difference	Θ =180°	% Difference
Tap 1	19	**Tap 1**	23
Tap2	22	**Tap2**	20
Tap 3	20	**Tap 3**	20
Tap 4	15	**Tap 4**	20
Tap 5	20	**Tap 5**	17
Tap 6	20	**Tap 6**	16
Tap 7	17	**Tap 7**	17
Tap 8	19	**Tap 8**	18

5.2.3 Negative peak pressure coefficients

Tieleman (1993) conducted tests on surface mounted prisms, in numerous boundary-layers, and noted that negative peak pressures decreased with increased turbulence intensity. Similar results have also been observed for curved roof structures, as discussed in Chapter 2.

The effects of turbulence intensity on the negative 3s peak pressure distribution is illustrated in Figures 5.9 through 5.11. Only the negative 3s peak pressure coefficients are compared here. However, the same trend is observed for the negative 10s peak pressures. The maximum calculated expected negative 3s peak pressure coefficient difference for the flat cross vault with no attached roughness was approximately 20%. Generally, differences fell within this maximum scatter. However, an apparent trend was still evident, as shown in Figures 5.9 through 5.11.

The expected negative 3second peak pressure coefficients were generally slightly lower (more negative) for the higher level of turbulence, which is in accordance with research on bluff body structures. Large variations were observed, with a maximum percent difference of 40% for the flat cross vault, which is well above the general trend. These large discrepancies may be accounted for by a combination of both the effects of turbulence and the spurious nature of peaks.

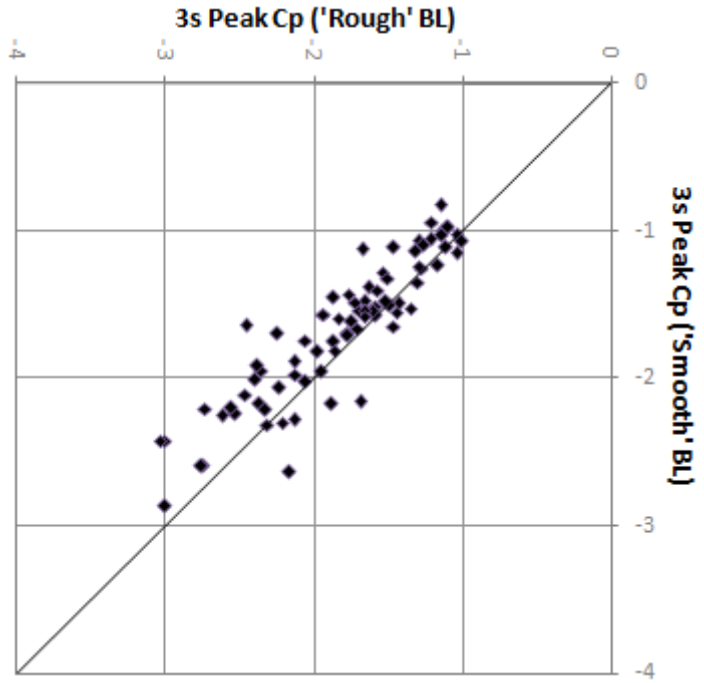


Figure 5.9 - Negative 3s peak pressure coefficient (‘smooth’ BL) versus negative 3s peak pressure coefficient (‘rough’ BL), for the flat cross vault

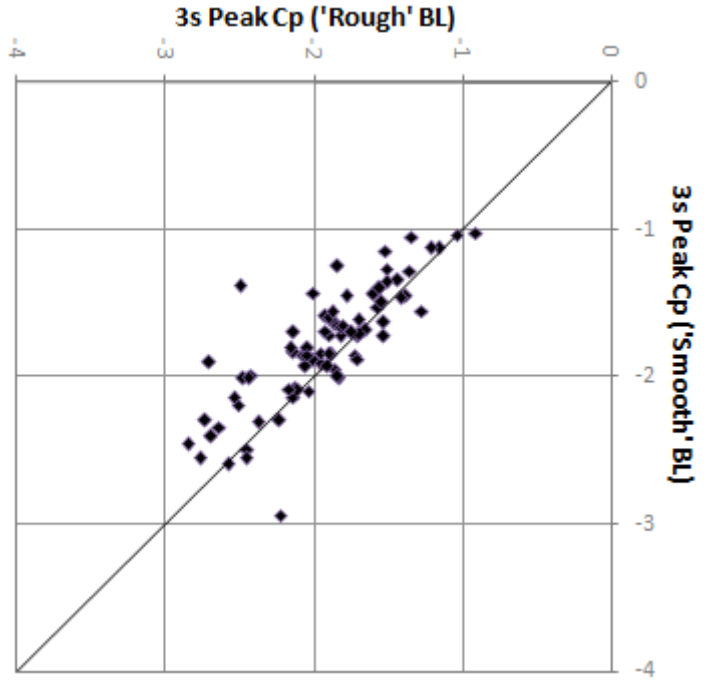


Figure 5.10 - Negative 3s peak pressure coefficient (‘smooth’ BL) versus negative 3s peak pressure coefficient (‘rough’ BL), for the convex cross vault

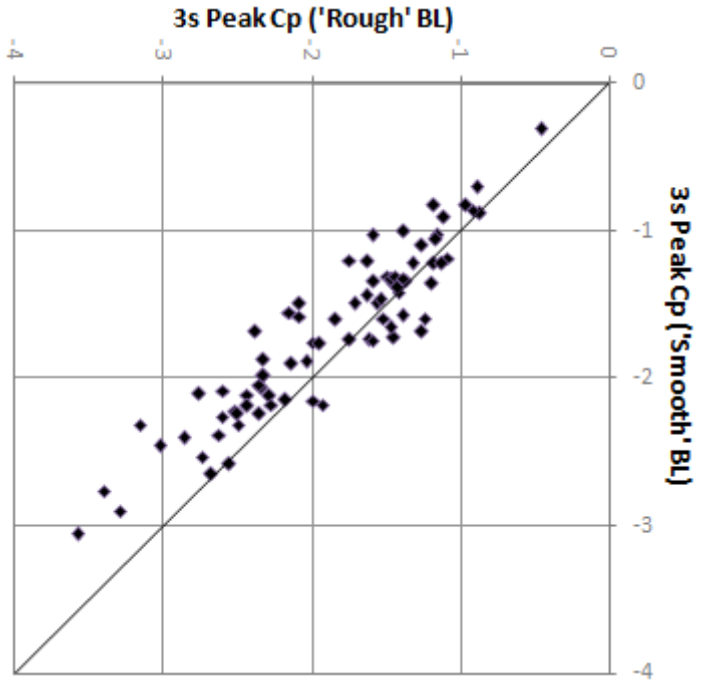


Figure 5.11 - Negative 3s peak pressure coefficient (‘smooth’ BL) versus negative 3s peak pressure coefficient (‘rough’ BL), for the concave cross vault

5.3 Conclusions

The mean, RMS and negative peak pressure coefficients measured in two generic boundary-layers were investigated. Mean pressure coefficients were not notably affected by the changes of the approach flow. It is apparent, however, that the boundary-layer characteristics affected the RMS and negative peak pressures. RMS pressures increased, whereas negative peak pressures generally decreased with the increased turbulence intensity. This trend is consistent with findings of previous measurements over sharp edged and curved bluff body structures, such as Bienkiewicz and Sun (1992) and Cheung and Melbourne (1983).

6 EFFECTS OF ROOF GEOMETRY: POINT PRESSURES

6.1 General

Roofing components, such as cladding and their fixings, are exposed to local wind forces. For this reason, point pressure coefficients are typically applicable to the design of these external elements. In this chapter, research findings on the effects of relatively small geometrical changes of the apex (rise) of the cross vault roof on the external point pressure distribution, within the central portion of such structures, are discussed.

6.2 Pressure Distributions

In this section, point mean, RMS and negative 3s peak pressure coefficient distributions over the three cross vault models, for the 0°, 15°, 30°, 45°, 60°, 75°, 90°, 120°, 150° and 180° wind directions, are compared.

6.2.1 0° wind direction

The tap positions for the 0° wind direction are shown in Figure 6.1.

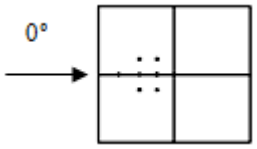


Figure 6.1 - Tap positions for the the 0° wind direction

The mean pressure coefficient distributions corresponding to all cross vault types and the 'smooth' and 'rough' boundary-layers are shown in Figures 6.2a and 6.3a, respectively. As can be seen from these figures, the mean pressures corresponding to the concave and flat cross vault show good consistency, especially for the 'smooth' boundary-layer. However, this is not the case for the convex cross vault, which experienced slightly lower mean pressure coefficients at taps 1 through 4.

It is also evident that the mean pressure coefficients decrease noticeably from line (tap 2, 3 and 4) to line (tap 5, 6 and 7) for the flat and concave cross vaults,

whereas a marginal increase is observed for the convex cross vault. This result reveals that flow accelerates over the convex apex. It is believed that the reason for this variation, at the convex roof apex, is most likely due to the effect of roof pitch and curved apex on the pressure distribution. Design codes of practice indicate large suctions near the ridge of sharp edged duo pitched roofs. Holmes (2001) noted that a second separation can occur at the roof ridge for rectangular duo-pitch roofs, with slope between 10° and 20°. This separation results in higher suctions near the ridge, as shown in Figure 6.4. The results of the current investigations show a similar trend; however, the convex cross vault roof ridge is curved and a second separation was not evident.

The RMS pressure coefficient distributions corresponding to the three vault types are shown in Figures 6.2b and 6.3b. For the 'smooth' boundary-layer, the RMS pressure distributions show similarity for all vault types, with differences almost entirely within the observed experimental scatter. For the 'rough' boundary-layer, the RMS pressures corresponding to the flat, concave and convex cross vaults differ slightly, with the concave and convex types experiencing the maximum and minimum, respectively.

The negative 3 second peak pressure distributions, presented in Figures 6.2c and 6.3c, generally show consistency with the mean pressure distributions discussed previously. Small differences at some positions are observed, which could be attributed to the spurious nature of peaks.

It should be noted that some of the pressure readings do not correlate exactly for symmetrically placed taps, as shown in Figures 6.2a through 6.3c. Postulates for these, generally, small discrepancies include; effects of the surrounding taps, variation of the surface roughness surrounding the taps, slight geometrical variations of the model and the experimental scatter discussed in section 3.6.

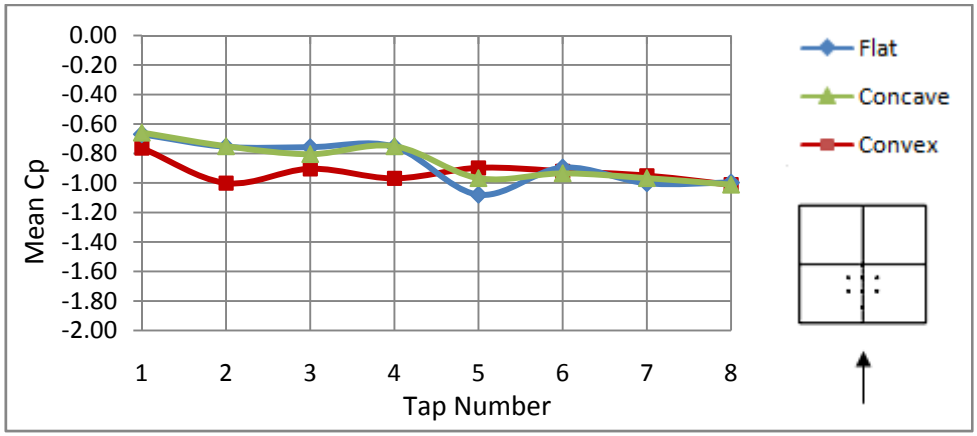


Figure 6.2a - Mean pressure coefficient distribution ('smooth' BL, θ = 0°)

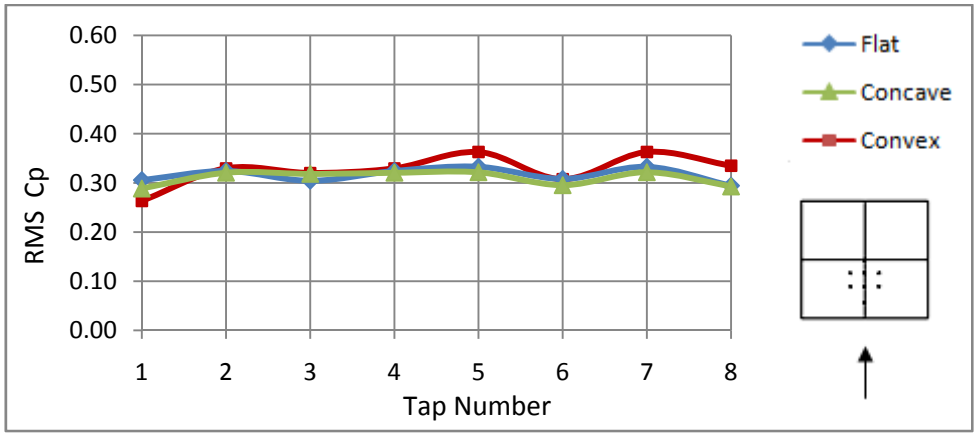


Figure 6.2b - RMS pressure coefficient distribution ('smooth' BL, θ = 0°)

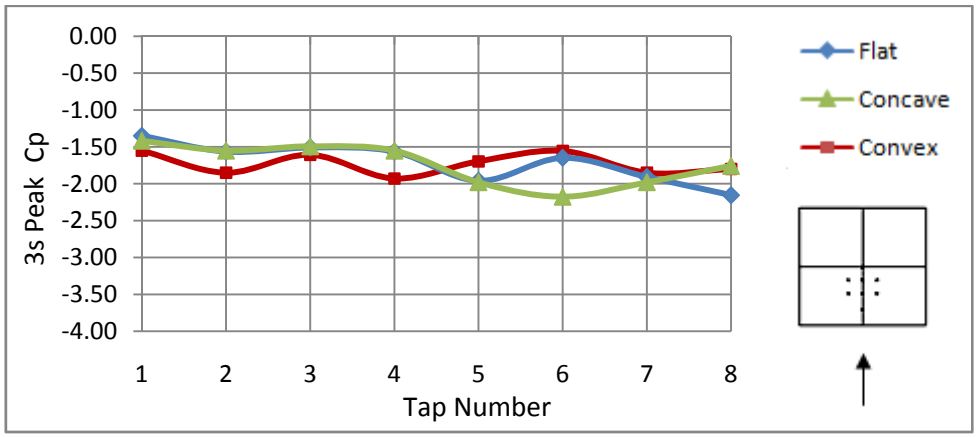


Figure 6.2c - 3s peak pressure coefficient distribution ('smooth' BL, θ = 0°)

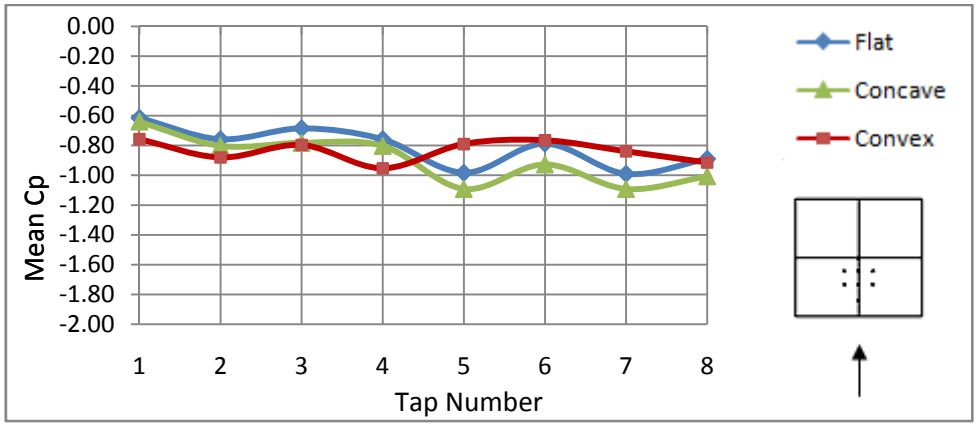


Figure 6.3a - Mean pressure coefficient distribution ('rough' BL, θ = 0°)

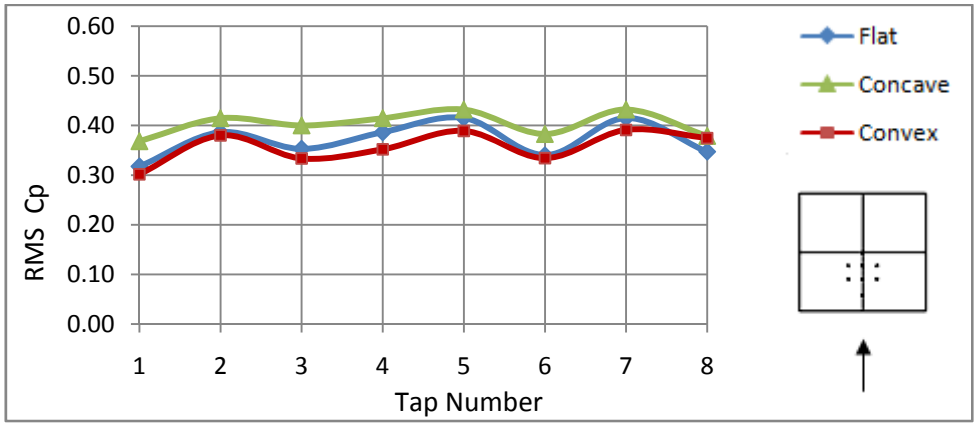


Figure 6.3b - RMS pressure coefficient distribution ('rough' BL, θ = 0°)

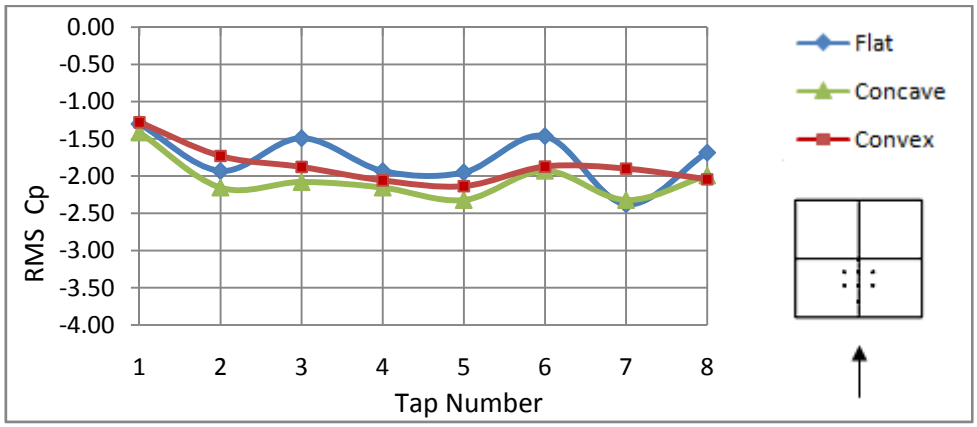


Figure 6.3c - 3s peak pressure coefficient distribution ('rough' BL, θ = 0°)

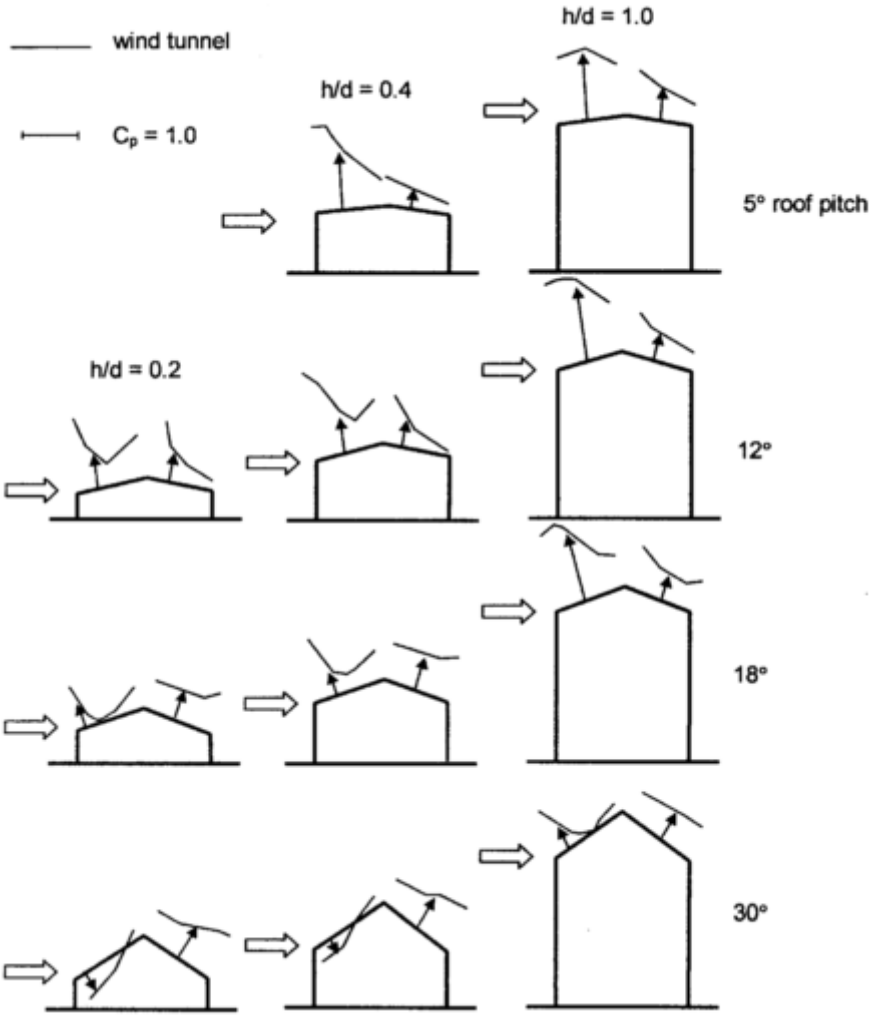


Figure 6.4 - Centreline mean pressure distribution over duo-pitch roofs (Reproduced from Holmes (2001))

6.2.2 15° wind direction

The tap positions for the 15° wind direction are shown in Figure 6.5.

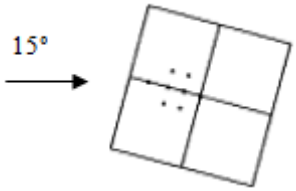


Figure 6.5 - Tap positions for the the 15° wind direction

The mean, RMS and negative 3s peak pressure coefficient distributions show considerable variation for all vault types, as shown in Figures 6.6a through 6.7c. The mean pressure distributions corresponding to the flat and concave cross vaults show a similar trend, for both boundary-layer profiles, as illustrated in Figures 6.6a and 6.7a. This is consistent with pressures observed at the 0° wind direction for the concave and flat vault forms. However, the concave cross vault generally experienced visibly lower mean pressures at the 15° wind direction.

The mean pressure distributions corresponding to the convex cross vault reveal significant variation from those for the flat and concave cross vaults, as shown in Figures 6.6a and 6.7a. Mean pressures over the convex cross vault are generally lower than those for the flat cross vault at taps 1 through 4. Considerable mean pressure coefficient variation, for all cross vault types, is also evident at taps 5 through 8.

RMS pressure coefficients over the concave cross vault are visibly larger than those for the flat cross vault, which, in turn, are larger than those for the convex cross vault. Generally, the negative 3 second peak pressure distributions, shown in Figures 6.6c and 6.7c, signify consistency with the mean pressure distributions. The negative peak pressure discrepancy observed at tap 4 corresponding to the convex cross vault and 'rough' boundary-layer may be attributed to the spurious nature of peaks, since it is not supported by any irregularities in the RMS or mean pressures.

The comparisons presented in Figures 6.6a through 6.7c clearly show noticeable effects of vault geometry on the mean, RMS and negative peak pressure coefficient distributions. The reasons for the discrepancies observed at taps 5 through 8 are believed to be due to the pitch of the roof.

Wang (1998) conducted a series of wind-tunnel tests on gable roofs, with intermediate slope, to assess the suitability of the National Building Code of Canada. The study showed that, at the 0° wind direction, the RMS pressures generally decreased with increased roof pitch. Wang (1998) also showed that mean pressures near the leading edge increased with increased roof pitch. Furthermore, the design pressures corresponding to the area ahead of the ridge/trough for duo-pitched roofs, as given in EN 1991-1-4, shows a trend in which mean pressures are largest for roofs with positive pitch and lowest for roofs with negative pitch. For these reasons, the inconsistent mean, RMS and negative peak distributions are believed to be attributed to the roof pitch.

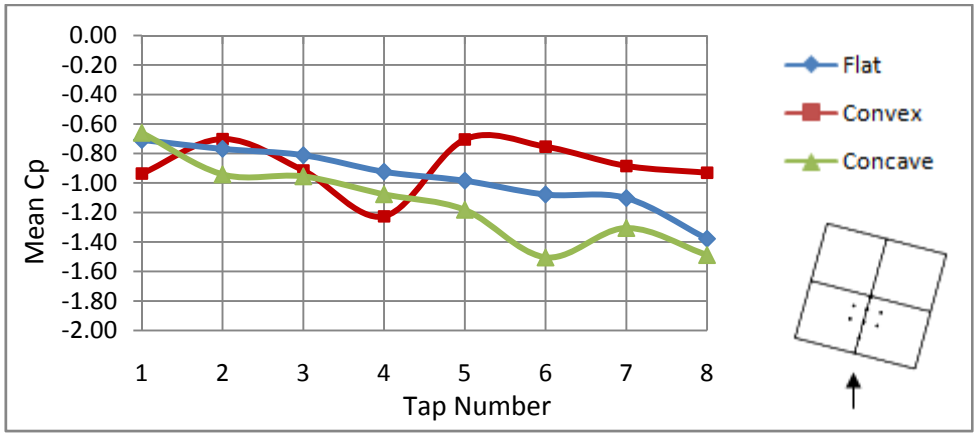


Figure 6.6a - Mean pressure coefficient distribution ('smooth' BL, θ = 15°)

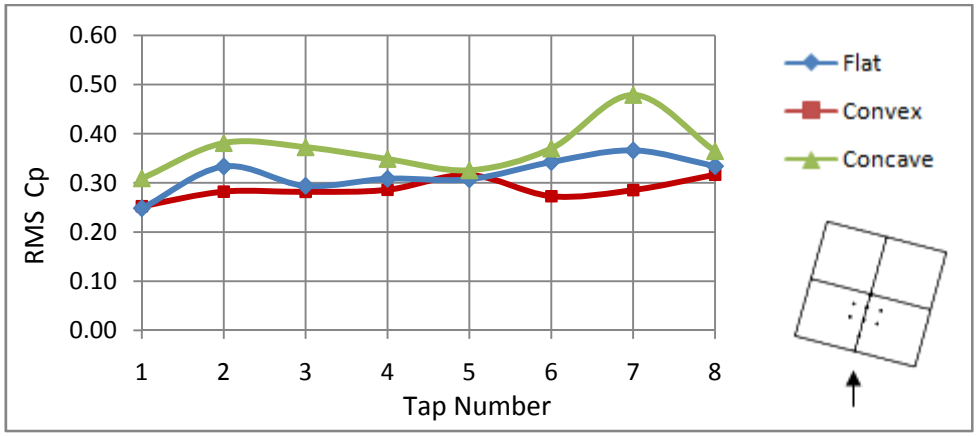


Figure 6.6b - RMS pressure coefficient distribution ('smooth' BL, θ = 15°)

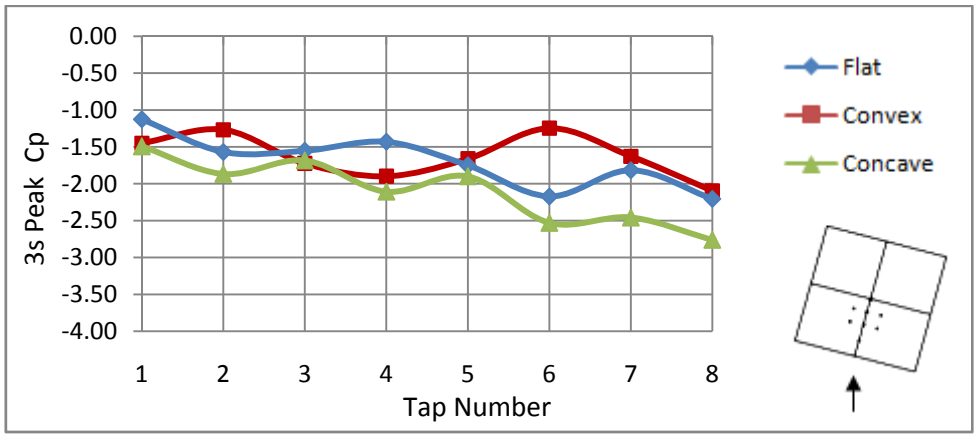


Figure 6.6c - 3s peak pressure coefficient distribution ('smooth' BL, θ = 15°)

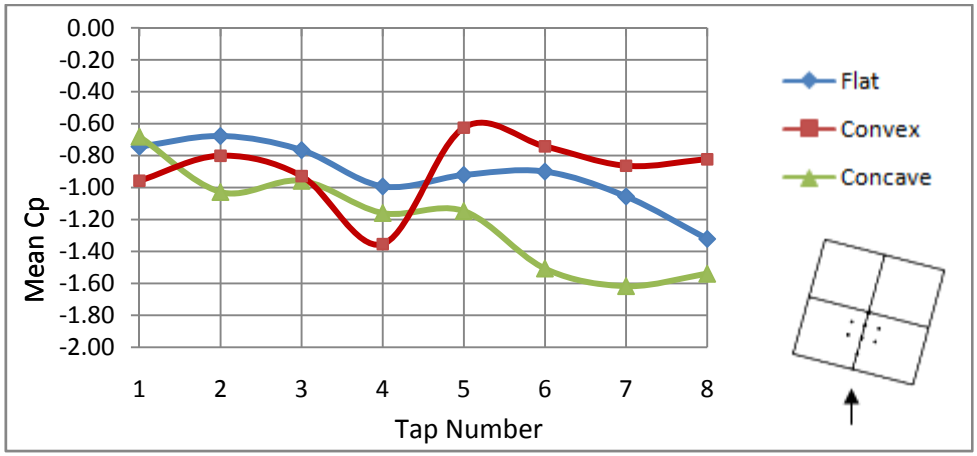


Figure 6.7a - Mean pressure coefficient distribution ('rough' BL, θ = 15°)

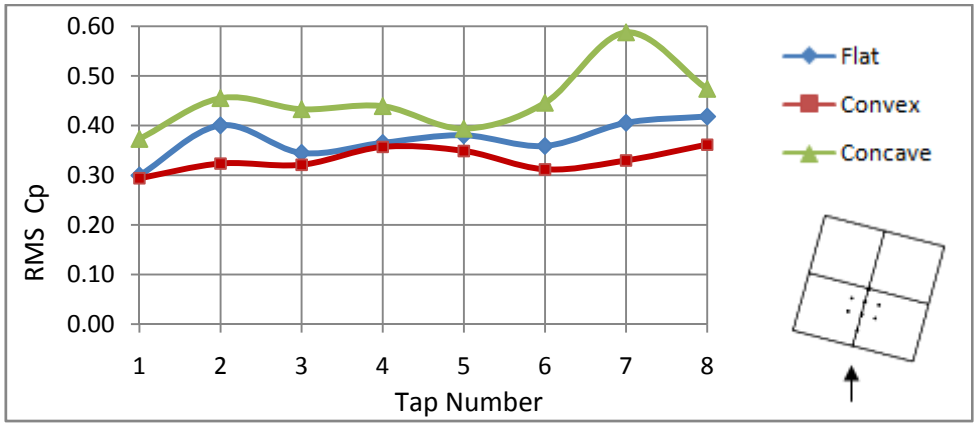


Figure 6.7b - RMS pressure coefficient distribution ('rough' BL, θ = 15°)

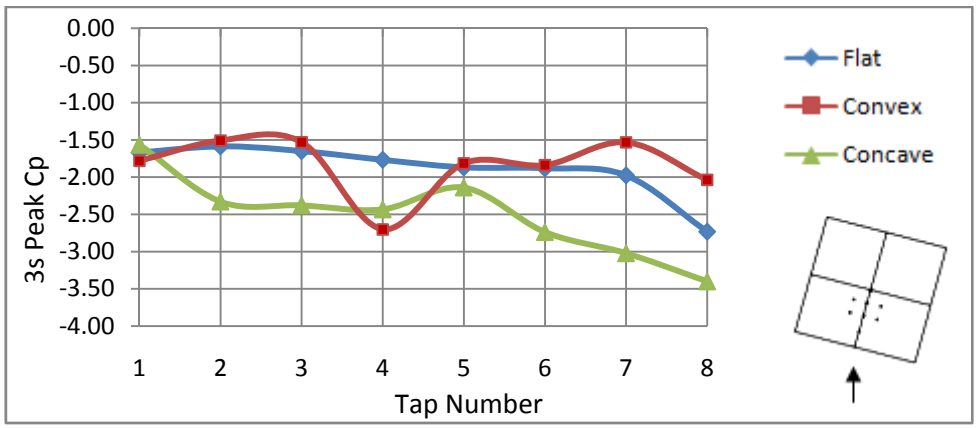


Figure 6.7c - 3s peak pressure coefficient distribution ('rough' BL, θ = 15°)

6.2.3 30° wind direction

The tap positions for the 30° wind direction are shown in Figure 6.8.

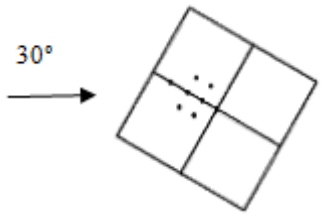


Figure 6.8 - Tap positions for the the 30° wind direction

The mean, RMS and negative 3s peak pressure coefficient distributions, at the 30° wind direction, are shown in Figures 6.9a through 6.10c. The mean pressures at taps 1 through 4 over the convex cross vault are once again lower than those corresponding to the other cross vault types. Consistency in the mean pressure coefficients over the flat and convex cross vaults, in both boundary-layer profiles, is evident at taps 5 through 8. However, the concave cross vault experiences lower mean values at these tap positions, which is consistent with results observed at the 15° wind direction.

It is to be noted that RMS pressures over the concave vault were generally larger than those corresponding to the flat and convex cross vaults at the 0°, 15° wind directions, especially within the 'rough' boundary-layer. At these wind orientations, the edge geometry plays a significant role on flow separation, however, it is apparent that roof pitch and apex geometry appear to influence the RMS pressures. A continuation of this trend is observed in Figures 6.9b and 6.10b. Conversely, the RMS pressures measured over the flat and convex cross vaults were practically identical.

As shown in Figures 6.9c and 6.10c, the negative peak pressure coefficient distributions, for all vault types and boundary-layer profiles, generally show similar distribution patterns to the corresponding mean pressures. The negative peak pressure coefficient measured at tap 3 on the convex cross vault and in the 'smooth' boundary-layer shows significant disparity from trends observed for the

mean pressure distribution. This discrepancy is believed to be due to an error, attributed to the spurious nature of peaks, since it is not supported by either the mean or RMS pressures.

Noticeable mean, RMS and negative peak pressure discrepancy is generally observed at taps 5 through 8, for both the ‘smooth’ and ‘rough’ boundary-layers, as noted at the 15° wind direction. The concave cross vault generally experienced larger RMS and lower mean and peak pressures, most notably at tap 8. This mean, RMS and negative peak pressure inconsistency is believed to be due to the effects of vault pitch on the wake, although there is a possibility that the large discrepancy may be attributed to effects of the surrounding sandpaper.

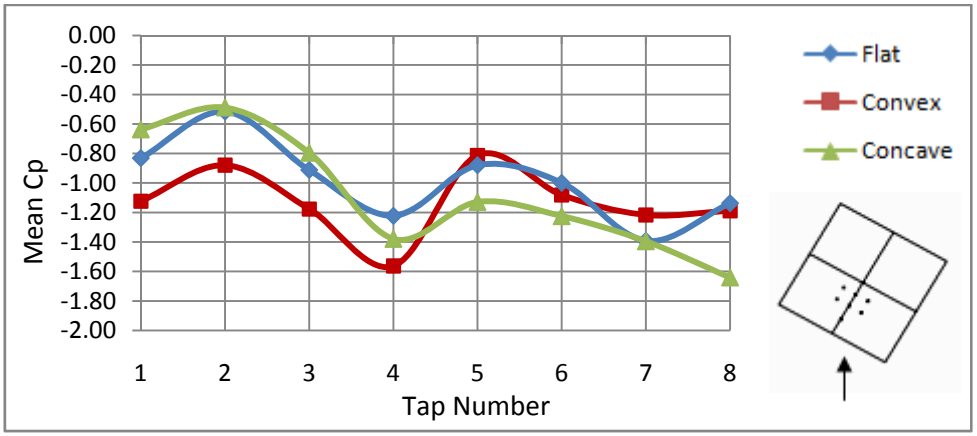


Figure 6.9a - Mean pressure coefficient distribution ('smooth' BL, θ = 30°)

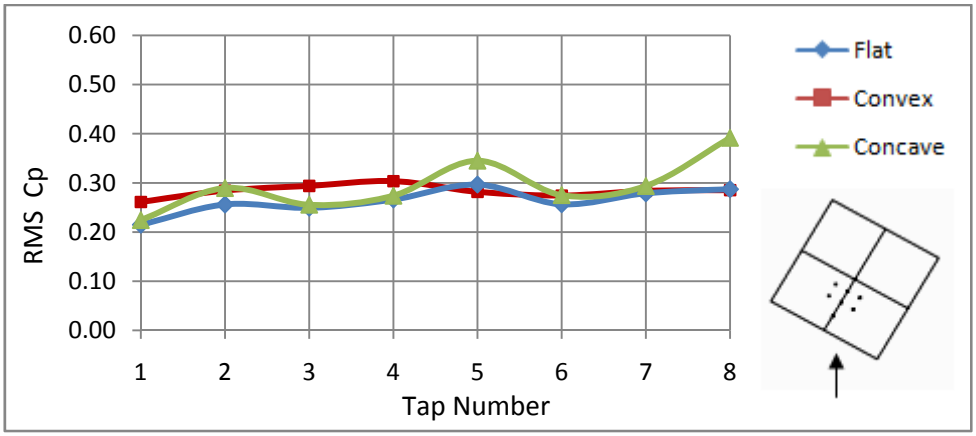


Figure 6.9b - RMS pressure coefficient distribution ('smooth' BL, θ = 30°)

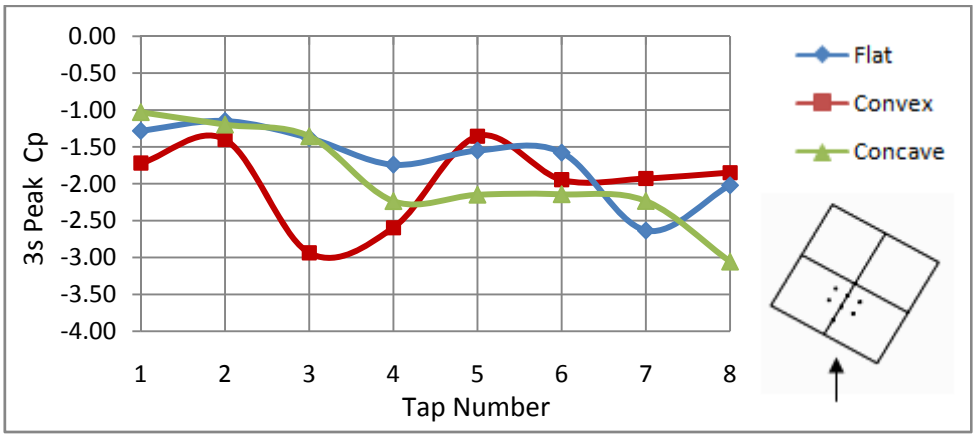


Figure 6.9c - 3s peak pressure coefficient distribution ('smooth' BL, θ = 30°)

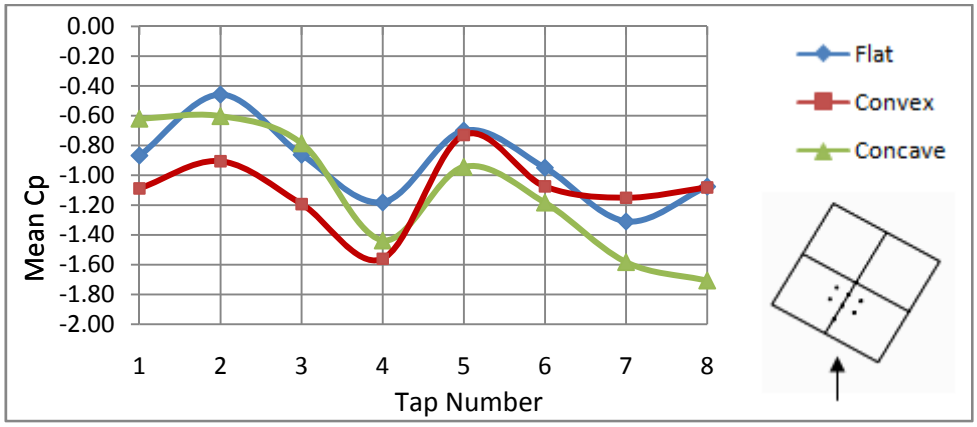


Figure 6.10a - Mean pressure coefficient distribution ('rough' BL, θ = 30°)

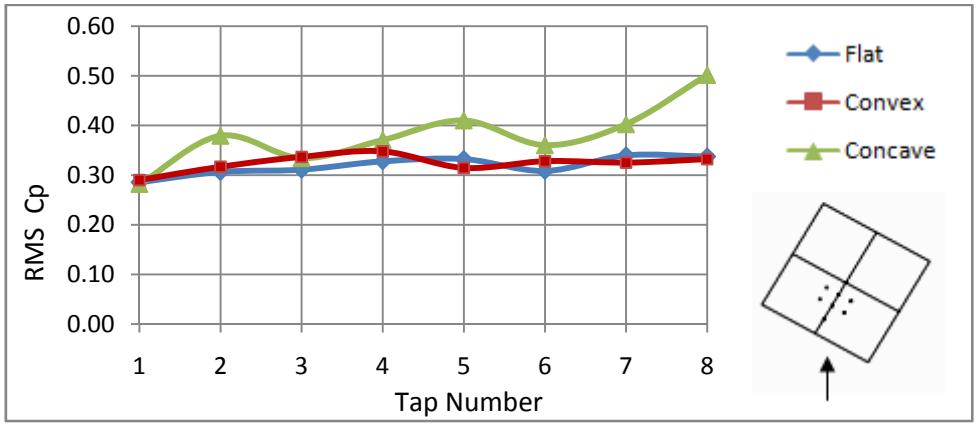


Figure 6.10b - RMS pressure coefficient distribution ('rough' BL, θ = 30°)

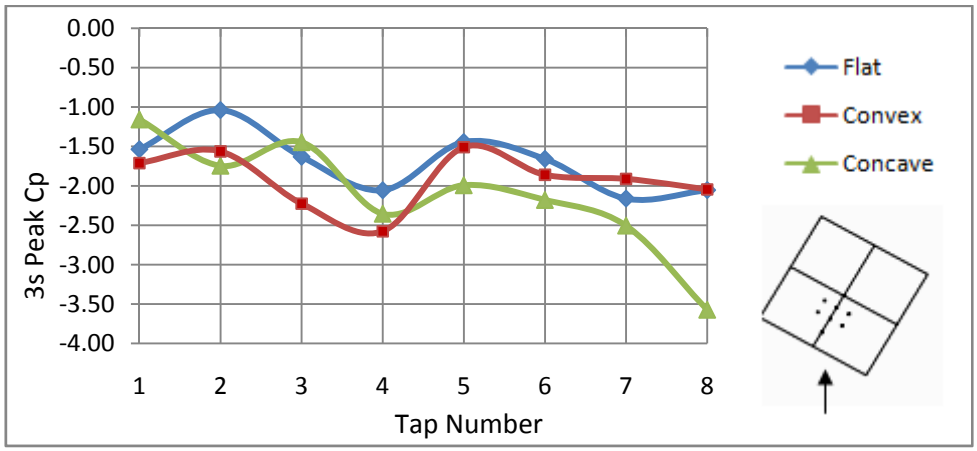


Figure 6.10c - 3s peak pressure coefficient distribution ('rough' BL, θ = 30°)

6.2.4 45° wind direction

The tap positions for the 45° wind direction are shown in Figure 6.11.

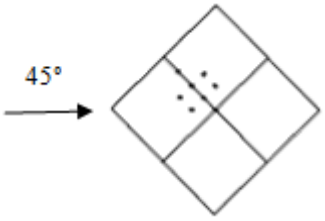


Figure 6.11 - Tap positions for the the 45° wind direction

The mean, RMS and negative 3s peak pressure coefficient distributions at the 45° wind direction, for both boundary-layer profiles, are shown in Figures 6.12a through 6.13c**.** The consistency in the mean pressure coefficient distribution for the concave and flat cross vault, within both boundary-layers, is illustrated in Figures 6.12a through 6.13a. Mean pressure coefficients at taps 5 through 8 are practically identical (which is opposed to distributions observed at the 15° and 30° wind directions), whereas slight differences are apparent at taps 1 through 4.

However, the negative mean pressures are generally lower for the convex cross vault. This result is believed to be due to the effects of the apex geometry. The mean pressure measured at tap 7 shows significant variation from the observed pressure distribution trend. Time histories were checked for any indication of tap blockage or electronic interference; however, nothing was identified. Furthermore, pressure coefficients measured at this tap 7 were consistent with tap 4, at the 0° and 180° wind directions, which may signify effects of vault geometry. This inconsistency may also be attributed to local effects of the sandpaper surrounding tap 7; however, the RMS pressures are practically identical for all cross vault types.

RMS pressure coefficients for all cross vaults are practically identical, which is in contrast to distributions for the 15° and 30° directions, discussed previously. As shown in Figures 6.12c and 6.13c, the negative 3 second peak pressure

distributions illustrate consistency with mean pressures for all vault types, most notably within the ‘smooth’ boundary-layer setup. However, a discrepancy is evident at tap 3 for the flat cross vault and ‘rough’ boundary-layer. This variation is not supported by the mean and RMS pressures, shown in Figures 6.13a and 6.13b, and may be accounted for by the spurious nature of peaks.

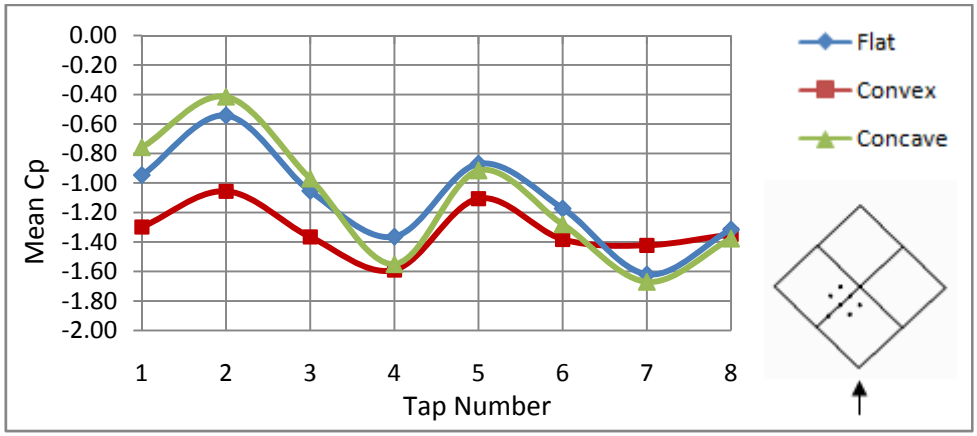


Figure 6.12a - Mean pressure coefficient distribution ('smooth' BL, θ = 45°)

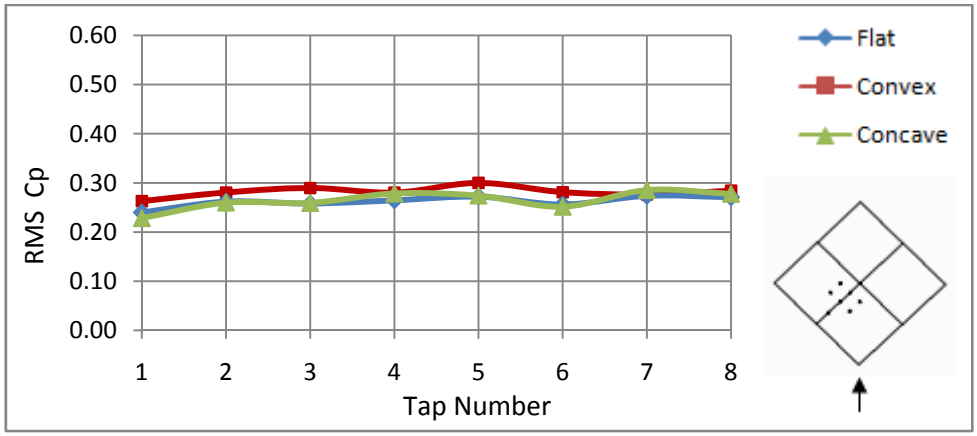


Figure 6.12b - RMS pressure coefficient distribution ('smooth' BL, θ = 45°)

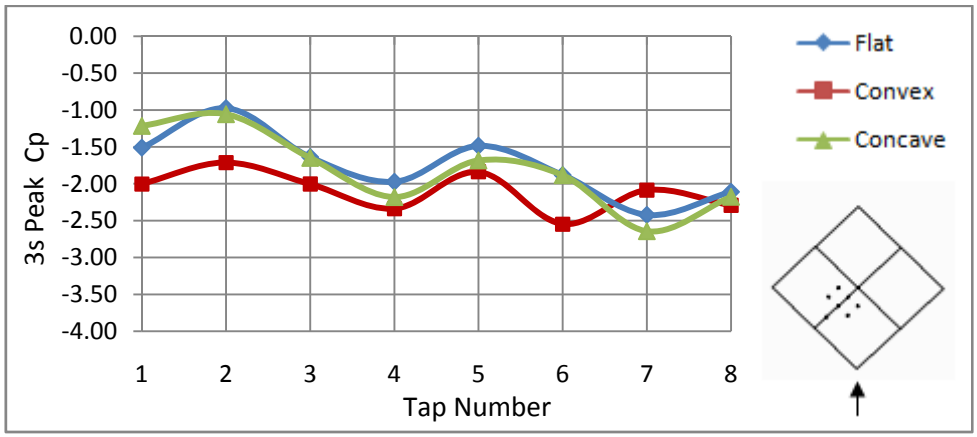


Figure 6.12c - 3s peak pressure coefficient distribution ('smooth' BL, θ = 45°)

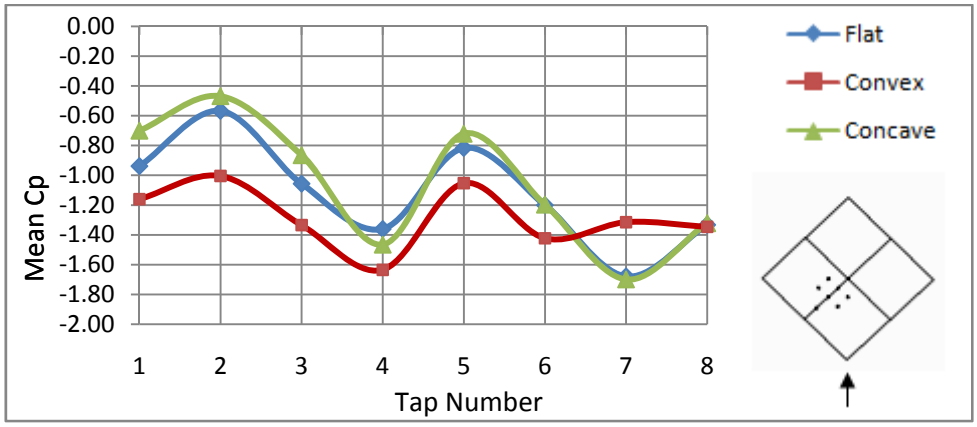


Figure 6.13a - Mean pressure coefficient distribution ('rough' BL, θ = 45°)

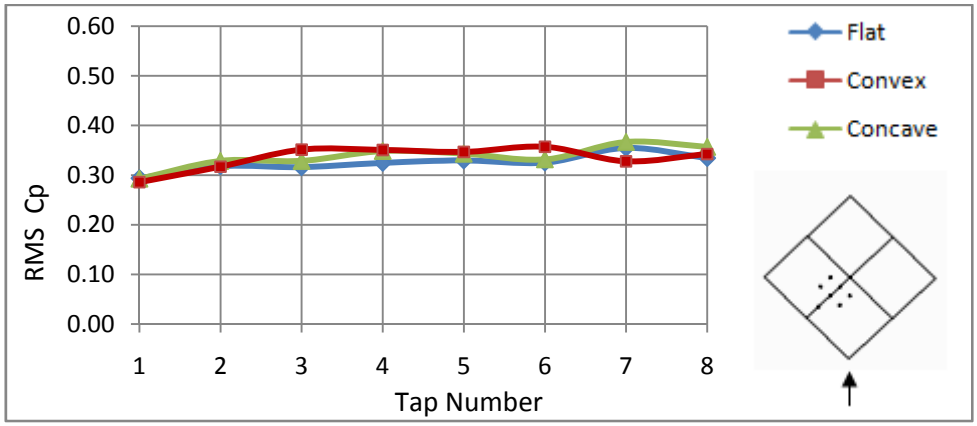


Figure 6.13b - RMS pressure coefficient distribution ('rough' BL, θ = 45°)

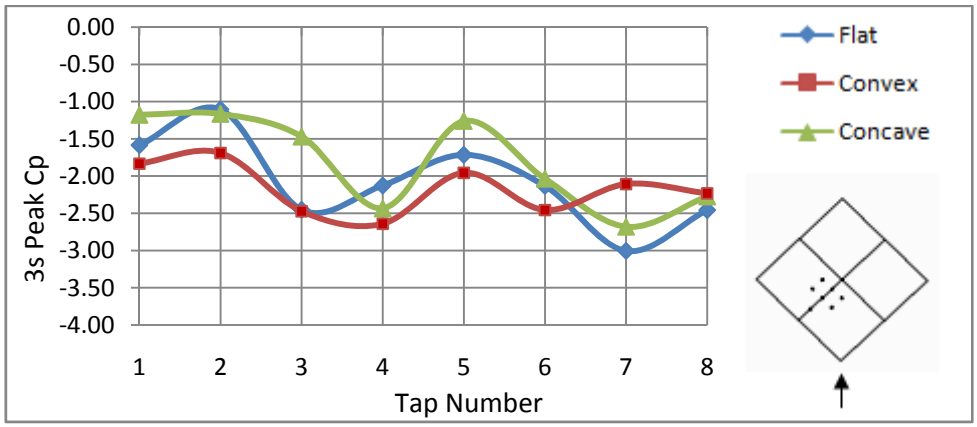


Figure 6.13c - 3s peak pressure coefficient distribution ('rough' BL, θ = 45°)

6.2.5 60° wind direction

The tap positions for the 60° wind direction is shown in Figure 6.14.

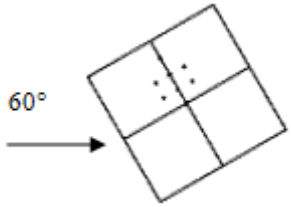


Figure 6.14 - Tap positions for the the 60° wind direction

The mean, RMS and negative 3s peak pressure coefficient distributions, at the 60° wind direction, are shown in Figures 6.15a through 6.16c. The flat, concave and convex cross vault pressure distributions are similar to those noted at the 45° wind direction.

For the 'smooth' and 'rough' boundary-layer, the RMS pressure coefficients corresponding to all vaults are practically identical. Noticeable RMS variation is evident at tap 7, within the 'rough' boundary-layer. This discrepancy may be attributed to the attached sandpaper around the tap, as discussed previously. As can be seen in Figures 6.15c and 6.16c, the negative peak pressure distributions are similar to the corresponding mean pressure distributions.

As can be seen from Figures 6.15a through 6.16c, the mean, RMS and negative peak pressures at tap 4 are practically identical for all vault types. This similarity is believed to be due the influence of the vault intersection (i.e. groove) on the flow, and resulting pressures. It was evident during testing that flow moved along this 'groove', which is fairly similar for all vault types, and may account for the observed pressure similarity.

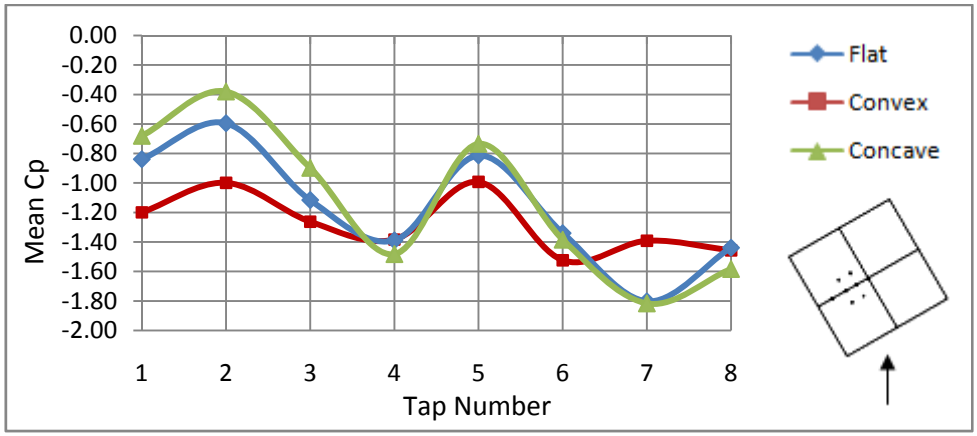


Figure 6.15a - Mean pressure coefficient distribution ('smooth' BL, θ = 60°)

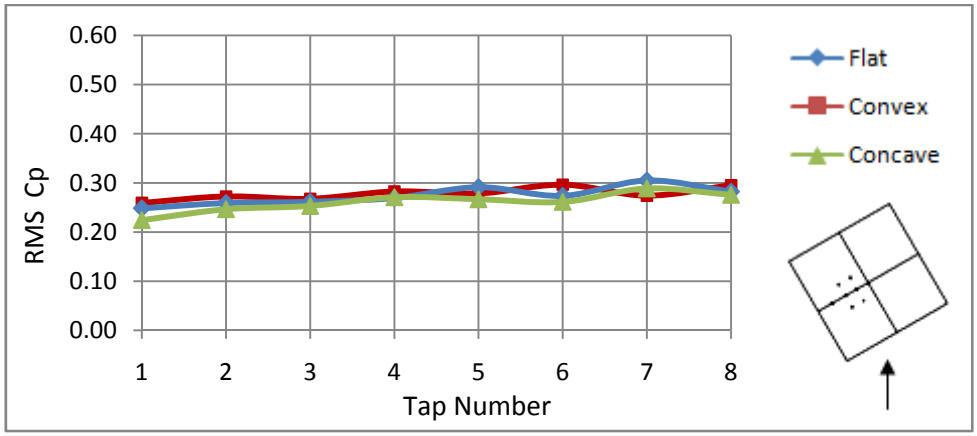


Figure 6.15b - RMS pressure coefficient distribution ('smooth' BL, θ = 60°)

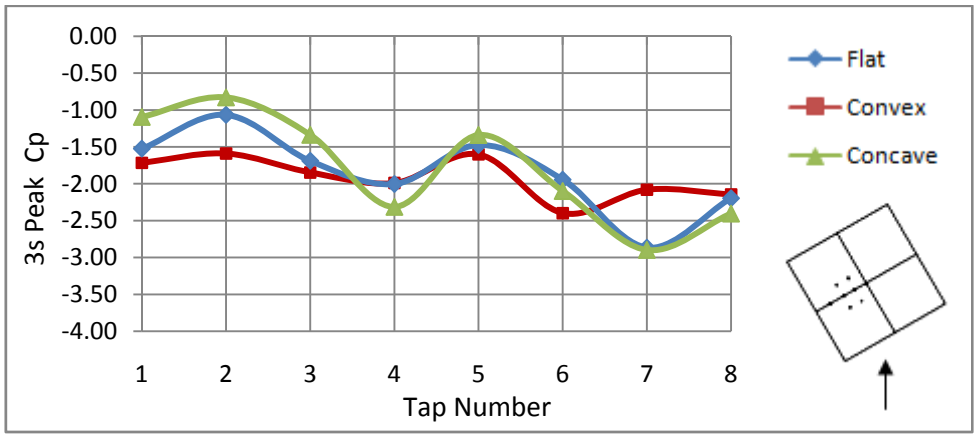


Figure 6.15c - 3s peak pressure coefficient distribution ('smooth' BL, θ = 60°)

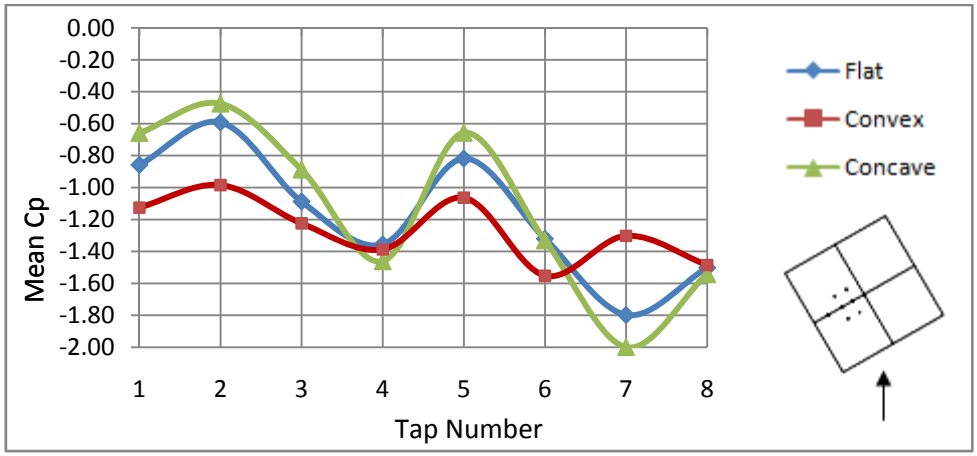


Figure 6.16a - Mean pressure coefficient distribution ('rough' BL, θ = 60°)

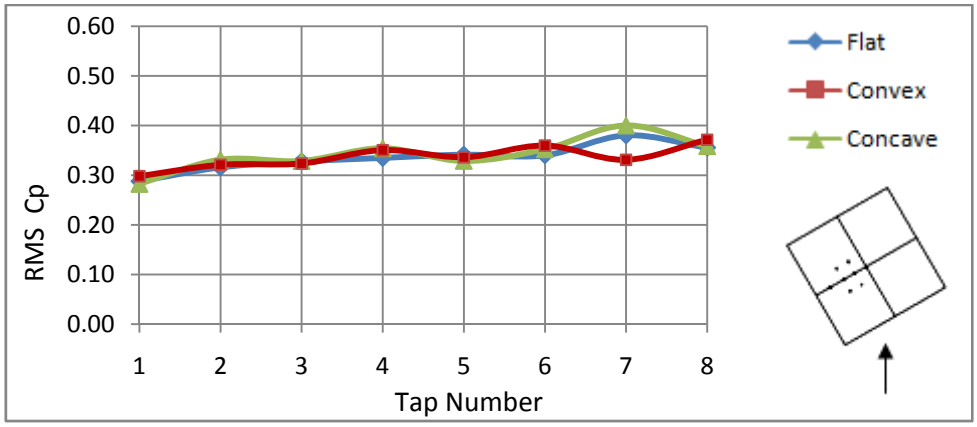


Figure 6.16b - RMS pressure coefficient distribution ('rough' BL, θ = 60°)

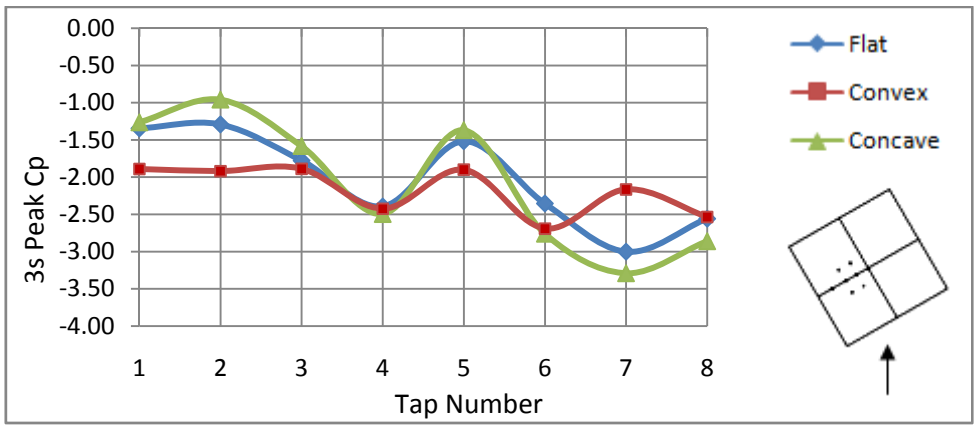


Figure 6.16c - 3s peak pressure coefficient distribution ('rough' BL, θ = 60°)

6.2.6 75° wind direction

The tap positions for the 75° wind direction is shown in Figure 6.17.

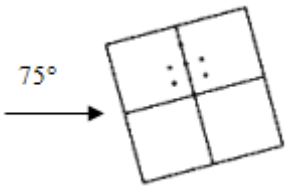


Figure 6.17 - Tap positions for the the 75° wind direction

The mean, RMS and negative 3s peak pressure coefficient distributions, at the 75° wind direction, are shown in Figures 6.18a through 6.19c. The flat and concave cross vault pressure distributions are similar to those noted at the 60° wind direction. However, mean and negative peak pressures over the convex cross vault are generally slightly larger than those observed at the 60° wind direction. It is also evident that differences between the convex and other vault types are becoming less significant, as the leading edge influences separation more heavily. This point is further emphasized at the 90° wind direction, discussed in section 6.2.7.

It should also be mentioned that the noticeable discrepancy at tap 7 is still evident. This divergence to the expected (or generally observed) trend, is now evident from 30° to 75°, which may point to a an effect of vault geometry, rather than a consequence of local roughness around the tapping.

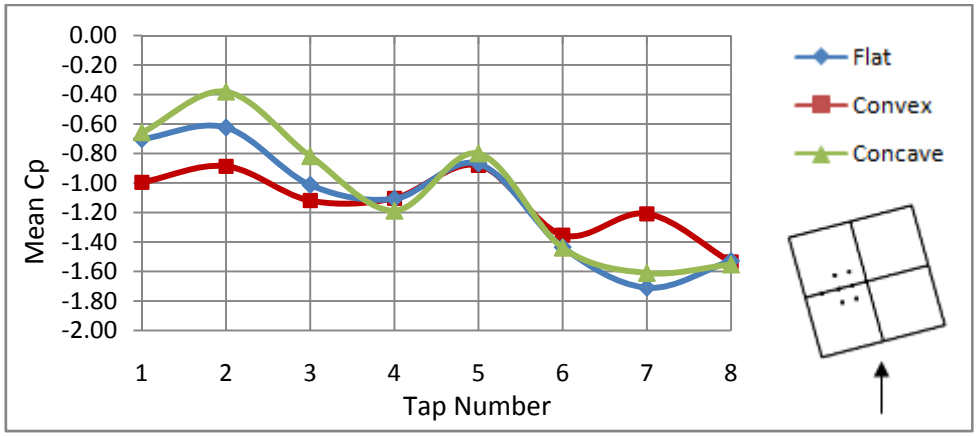


Figure 6.18a - Mean pressure coefficient distribution ('smooth' BL, θ = 75°)

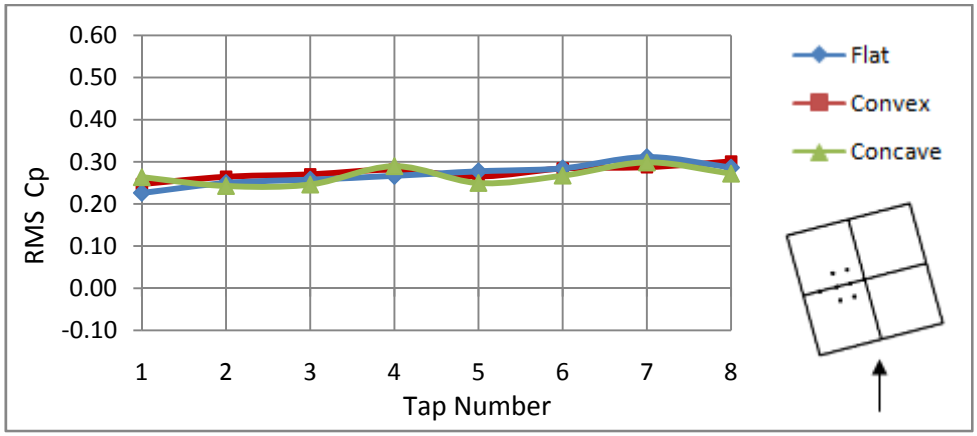


Figure 6.18b - RMS pressure coefficient distribution ('smooth' BL, θ = 75°)

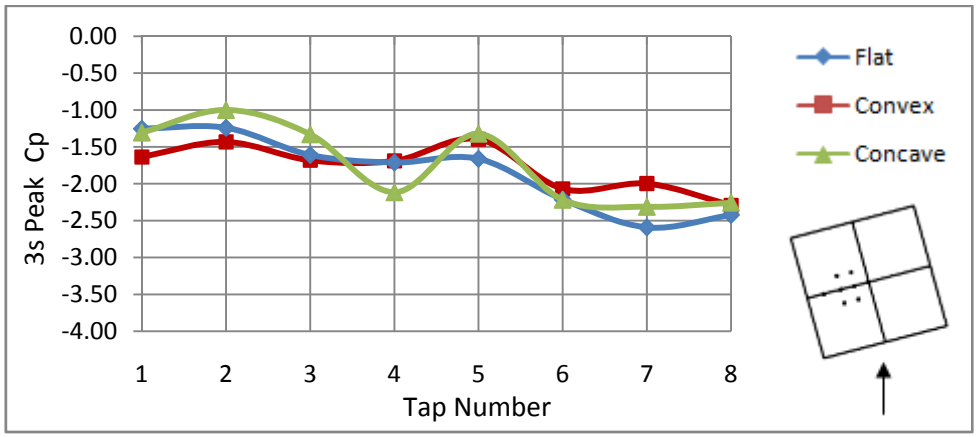


Figure 6.18c - 3s peak pressure coefficient distribution ('smooth' BL, θ = 75°)

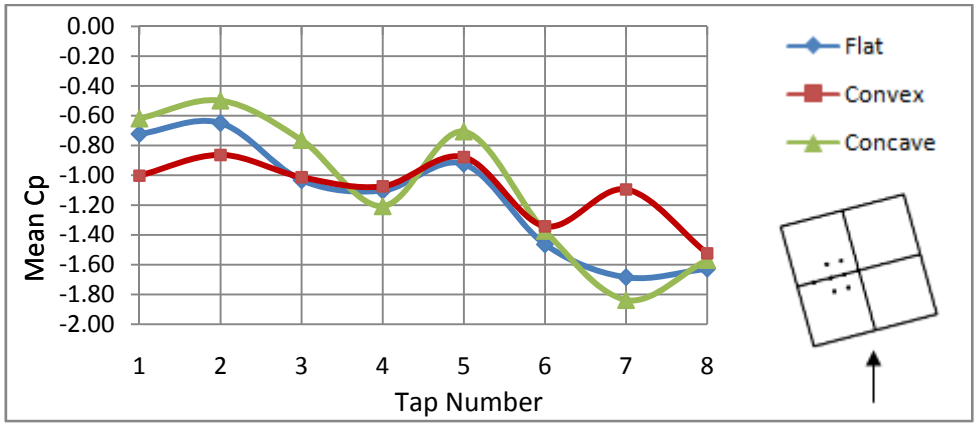


Figure 6.19a - Mean pressure coefficient distribution ('rough' BL, θ = 75°)

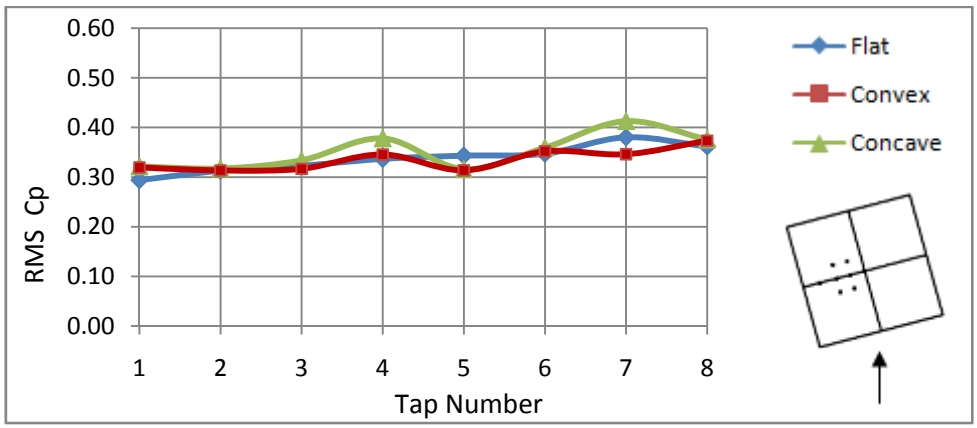


Figure 6.19b - RMS pressure coefficient distribution ('rough' BL, θ = 75°)

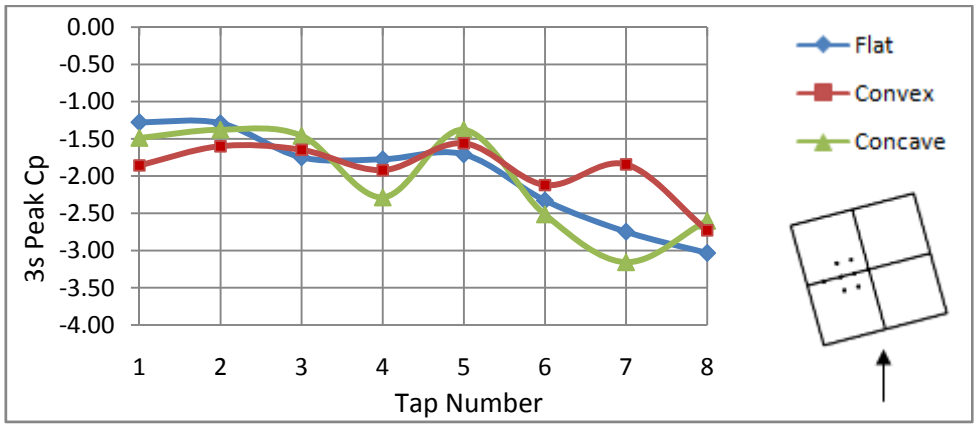


Figure 6.19c - 3s peak pressure coefficient distribution ('rough' BL, θ = 75°)

6.2.7 90° wind direction

The tap positions for the 90° wind direction are shown in Figure 6.20.

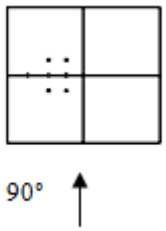


Figure 6.20 - Tap positions for the the 90° wind direction

The mean, RMS and negative peak pressures are shown in Figures 6.21a through 6.22c. Mean pressure coefficients corresponding to the concave and flat cross vaults compare fairly well for most tap positions, as shown in Figures 6.21a and 6.22a. The mean pressure coefficients observed at taps 1 through 4 further emphasise the lower mean pressures near the centre of the convex cross vault, which were observed at most wind directions investigated.

Mean pressure coefficients measured at taps 6 and 7, within the 'smooth' boundary layer, and over the flat cross vault show considerable variation from results observed for the other cross vault types and boundary-layer, as shown in Figures 6.21a and 6.22a. It should also be noted that the pressures measured at taps 6 and 7 corresponding to the flat cross vault showed noticeable sensitivity to the magnitude of the turbulence intensity. Most taps experienced differences well within the maximum observed experimental scatter (10%). However, taps 6 and 7 varied by 17% and 15%, respectively. The mean pressure coefficients for the concave and convex vaults, however, showed good consistency at these tap positions. The pressures at tap 8 show similarity for all vault types and are somewhat lower than pressures measured at the other tap positions. This result may reveal that flow re-attached at some position on the vault, with curvature normal to the flow.

The RMS pressures coefficient distributions for the three cross vaults, within both boundary-layer profiles, are shown in Figures 6.21b and 6.22b. The flat and

convex cross vaults show consistency within both boundary-layer simulations. However, the RMS pressure coefficients for the concave cross vault were, generally, noticeably larger in magnitude than those over the other cross vault forms. The largest RMS pressure coefficient variation between the flat and concave cross vaults was approximately 30%. This discrepancy is believed to be a result of the cross vault geometry, since it was evident for both the 'smooth' and 'rough' boundary-layer profiles. The negative 3 second peak surface pressure coefficients for the flat, concave and convex cross vaults, shown in Figures 6.21c and 6.22c, illustrate distribution consistency with the mean pressure coefficients. However, there are slight discrepancies at some tap positions, especially in the 'rough' boundary layer, which are believed to be attributed to the spurious nature of peaks, since the mean and RMS pressures do not show irregularity.

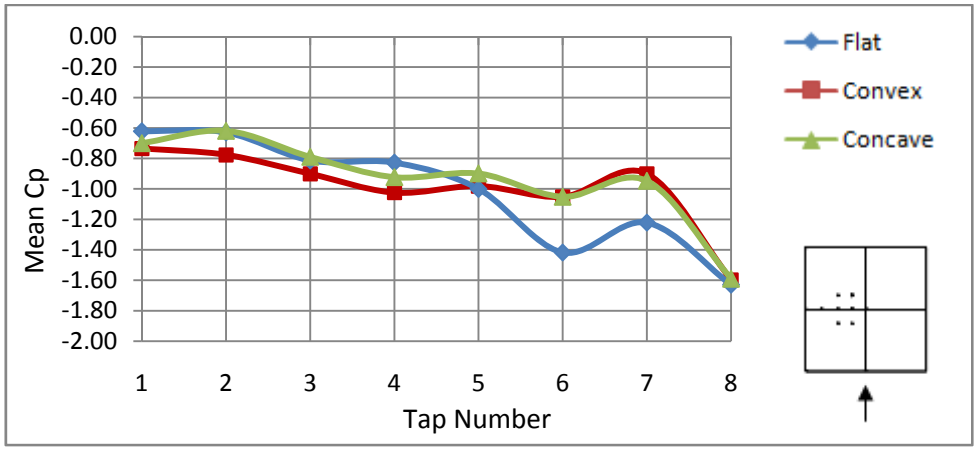


Figure 6.21a - Mean pressure coefficient distribution ('smooth' BL, θ = 90°)

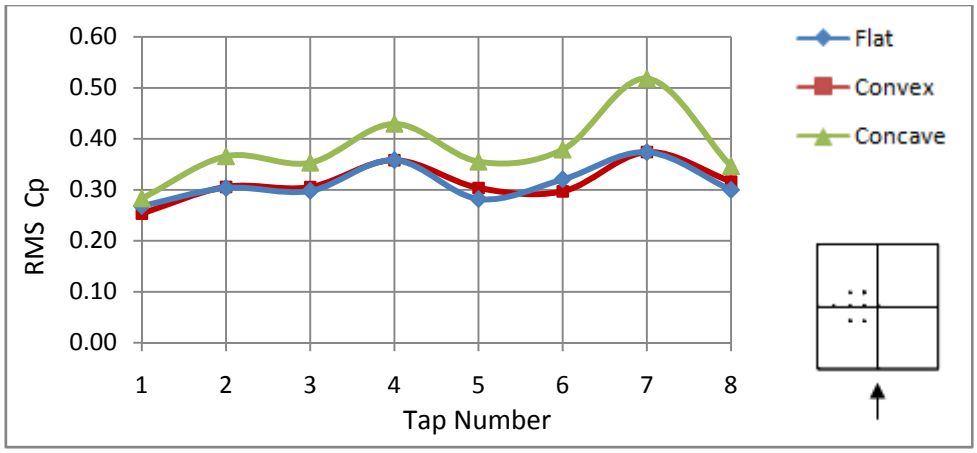


Figure 6.21b - RMS pressure coefficient distribution ('smooth' BL, θ = 90°)

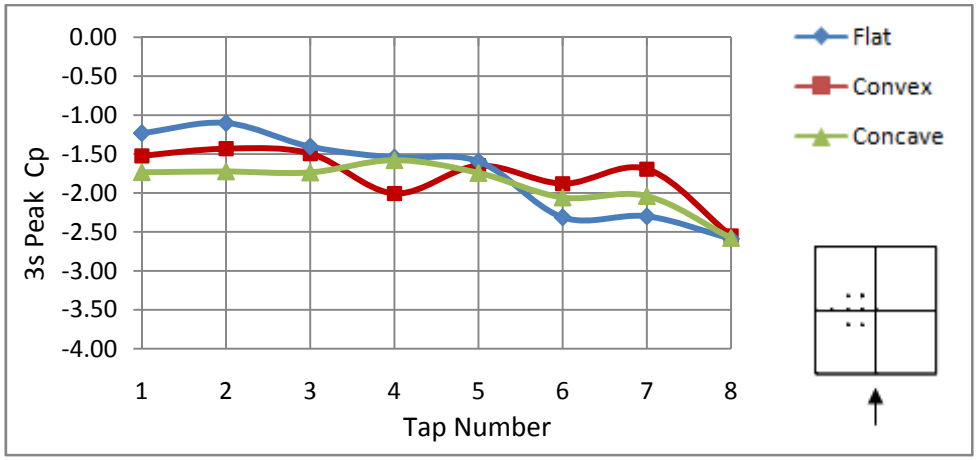


Figure 6.21c - 3s peak pressure coefficient distribution ('smooth' BL, θ = 90°)

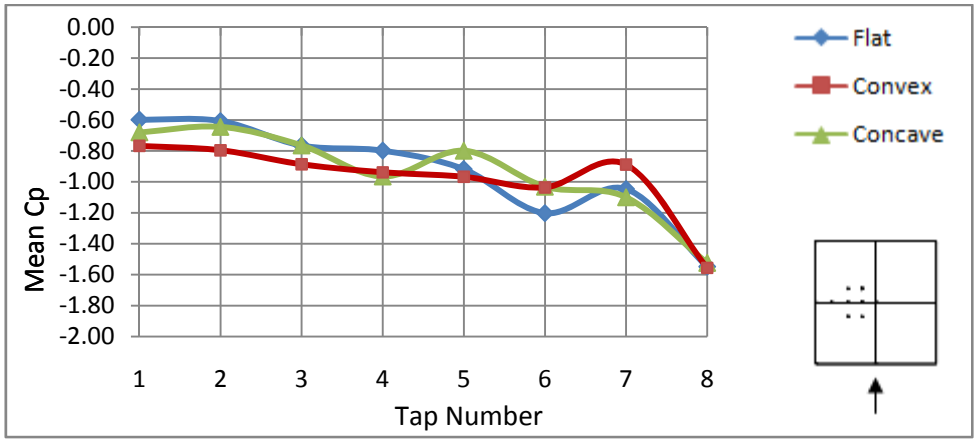


Figure 6.22a - Mean pressure coefficient distribution ('rough' BL, θ = 90°)

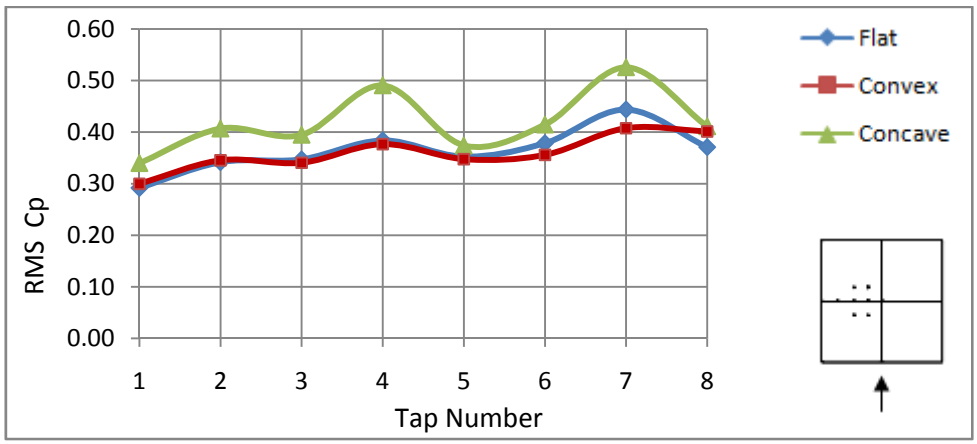


Figure 6.22b - RMS pressure coefficient distribution ('rough' BL, θ = 90°)

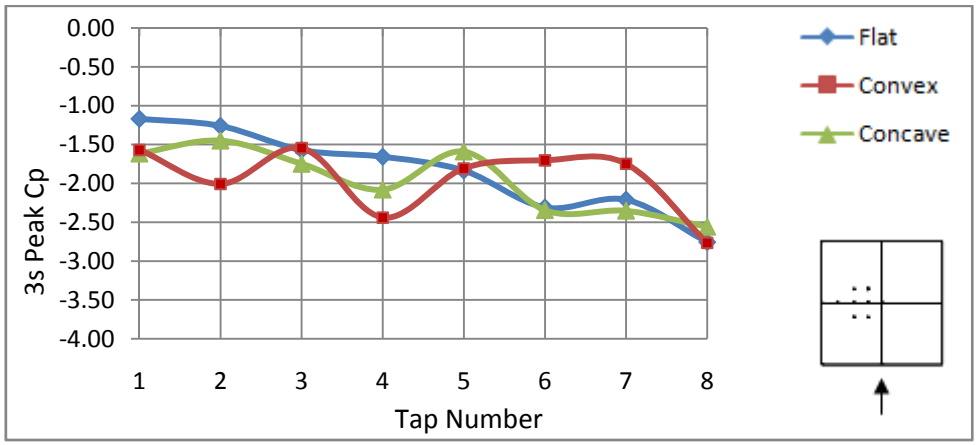


Figure 6.22c - 3s peak pressure coefficient distribution ('rough' BL, θ = 90°)

6.2.8 120° wind direction

The tap positions for the 120° wind direction are shown in Figure 6.23.

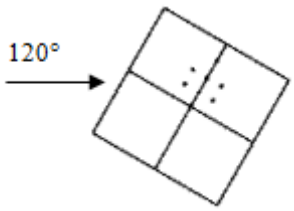


Figure 6.23 - Tap positions for the the 120° wind direction

The mean, RMS and negative peak pressures generally show significant variation at most tap positions over the flat, concave and convex cross vaults. As can be seen from Figrues 6.24a through 6.25c, the comparison of the convex cross vault pressure distribution with those for the flat cross vault confirm trends observed previously. Most notably, the mean pressures at taps 1 through 4, nearest the roof apex, are lowest for the convex cross vault, which is consistent with most other wind directions.

However, considerable mean pressure variations are evident between the concave and flat cross vault, which is in opposition to the general similarity evident at the 0°, 45°, 60°, 75°, 90° and 180° wind directions. The mean and peak pressures along the centreline (taps 1-3-6-8) are largest for the concave cross vault, with significant variation at taps 3 and 6. The pressure coefficients measured at this wind direction show slowed local velocity in comparison with pressures over other vault forms. The reasons for the lower local velocities and suctions over the concave cross vault, at most tap positions, is believed to be due to the apex geometry and the approximately 12° negative pitch of the lee-ward roof.

However, it is also evident that the mean pressures at taps 4 and 7 are similar in magnitude for the flat and concave cross vault. The similarities at taps 4 and 7 are possibly attributed to their position on the windward side of the vault. Furthermore, similarities are evident at tap 5 for all vault types. Reasons for the

similarity at this position are not clear; however, it is to be noted that this tap is positioned furthest from the cross vault apex.

As can be seen in Figures 6.24b and 6.25b, the RMS pressures are practically identical for all vault types, but a notable discrepancy is evident at tap 7 for the concave cross vault. This inconsistency is likely due to geometry, since it is observed for both boundary-layer simulations. However, the effects of the sandpaper surrounding the tap may also be a reason for this inconsistency. The negative 3 second peak surface pressure coefficients corresponding to the flat, concave and convex cross vaults illustrate distribution consistency with mean pressure distributions, as shown in Figures 6.24c and 6.25c.

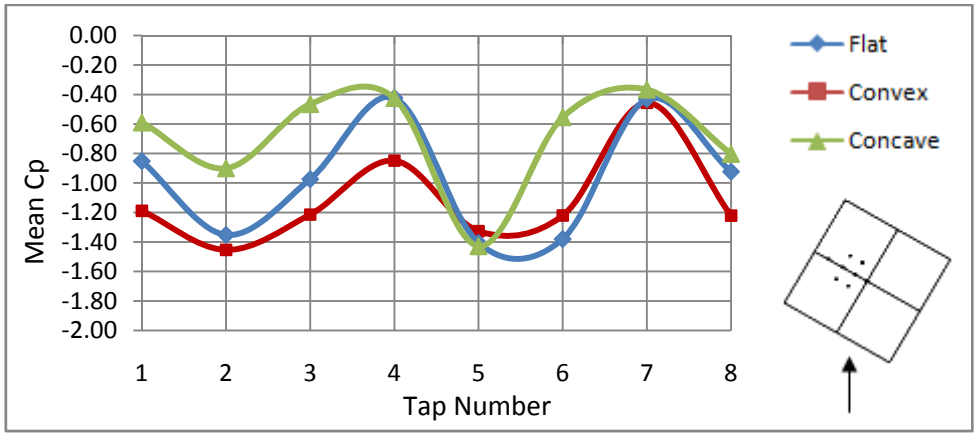


Figure 6.24a - Mean pressure coefficient distribution ('smooth' BL, θ = 120°)

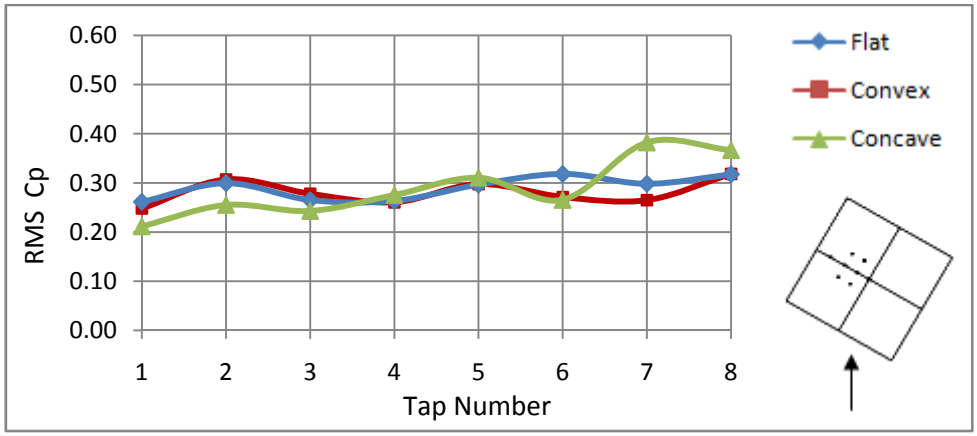


Figure 6.24b - RMS pressure coefficient distribution ('smooth' BL, θ = 120°)

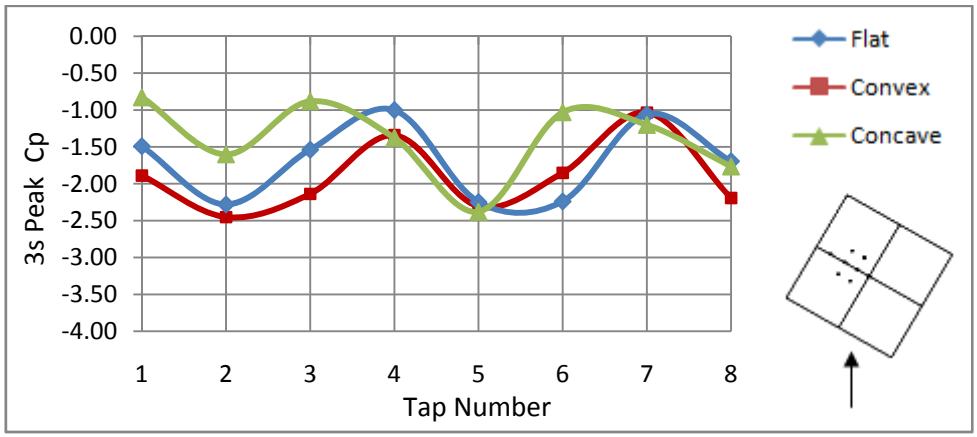


Figure 6.24c - 3s peak pressure coefficient distribution ('smooth' BL, θ = 120°)

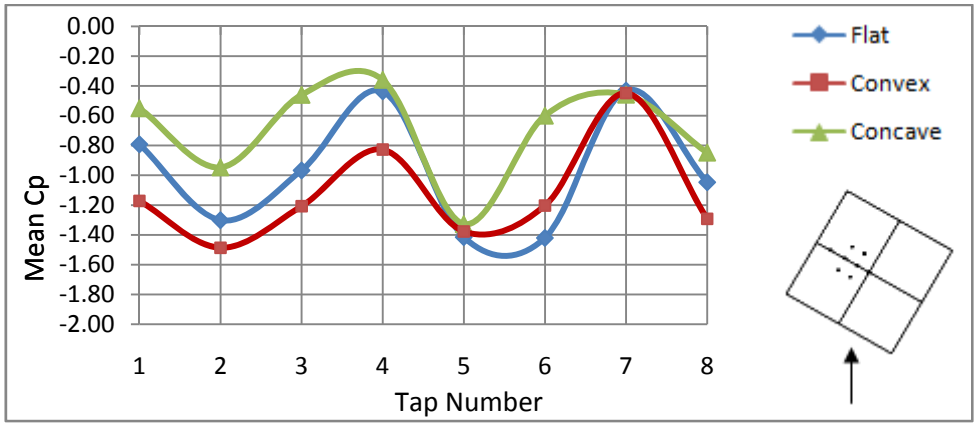


Figure 6.25a - Mean pressure coefficient distribution ('rough' BL, θ = 120°)

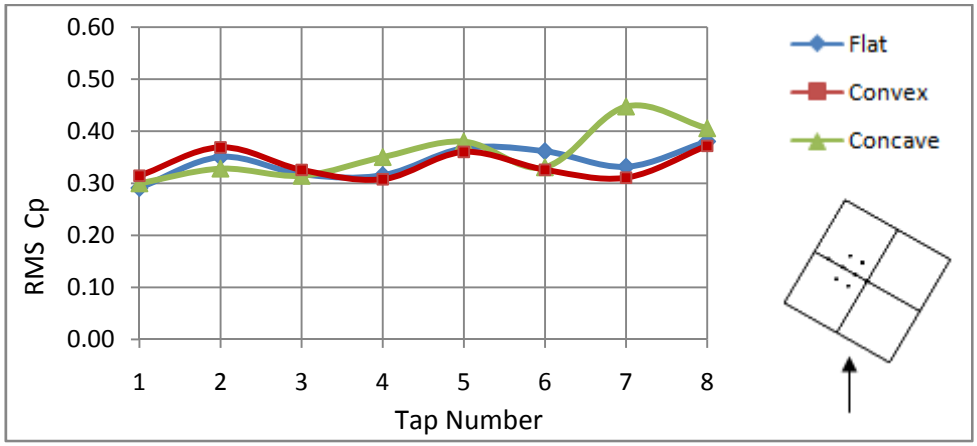


Figure 6.25b - RMS pressure coefficient distribution ('rough' BL, θ = 120°)

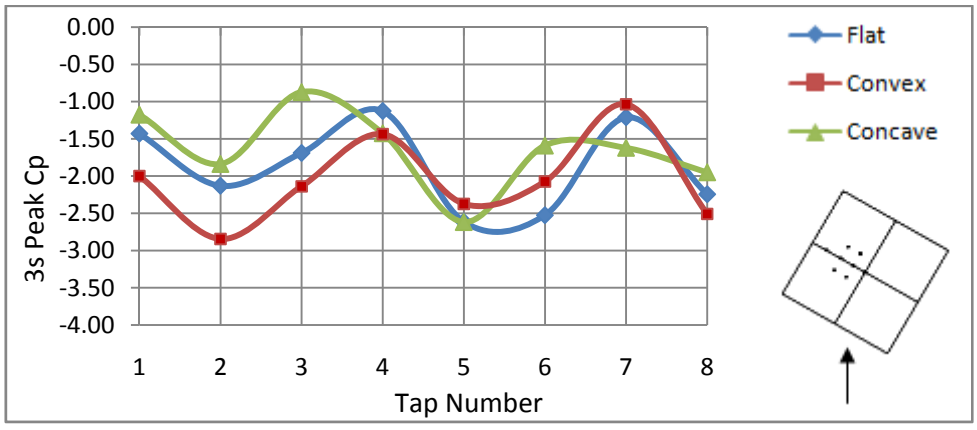


Figure 6.25c - 3s peak pressure coefficient distribution ('rough' BL, θ = 120°)

6.2.9 150° wind direction

The tap positions for the 150° wind direction is shown in Figure 6.26.

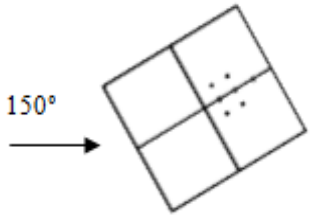


Figure 6.26 - Tap positions for the the 150° wind direction

The mean, RMS and negative peak pressures are shown in Figures 6.27a through 6.28c. The concave cross vault generally experiences larger mean and peak pressures, whereas the opposite is evident for the convex cross vault. However, similarity is evident at taps 5 and 8, for all vault types. The reasons for these similarities are unknown, but it is relevant to mention that these taps are the hindmost at the 150° wind direction (i.e. furthest from the roof apex).

The results presented in Figures 6.27a and 6.28a yet again show the large variation in the mean pressure coefficients at taps 1 through 4. In fact, mean pressure coefficients at tap 4 over the convex cross vault were approximately four times lower than the corresponding pressure over the concave cross vault. The pressure coefficients measured at this wind direction signify slowed local velocity in comparison with pressures over the other vault forms. This point is clearly emphasized by a positive mean pressure recorded at tap 7, within both boundary-layer profiles. The reasons for the lower local velocities and suctions observed over the concave cross vault, at most tap positions, is believed to be due to the apex geometry and the approximately 12° negative pitch of the leeward roof. The mean and peak pressure distributions corresponding to the convex and flat cross vaults signify similar variations to those noted at the 120° wind direction.

RMS pressures shown in Figure 6.27b indicate that the concave vault generally experienced lower RMS pressure coefficients within the ‘smooth’ boundary-layer. However, RMS pressure coefficients were practically identical for the ‘rough’

boundary-layer, as shown in Figure 6.28b. The negative 3 second peak surface pressure coefficients for the flat, concave and convex cross vaults illustrate distribution consistency with mean pressure coefficients, as shown in Figures 6.27c and 6.28c.

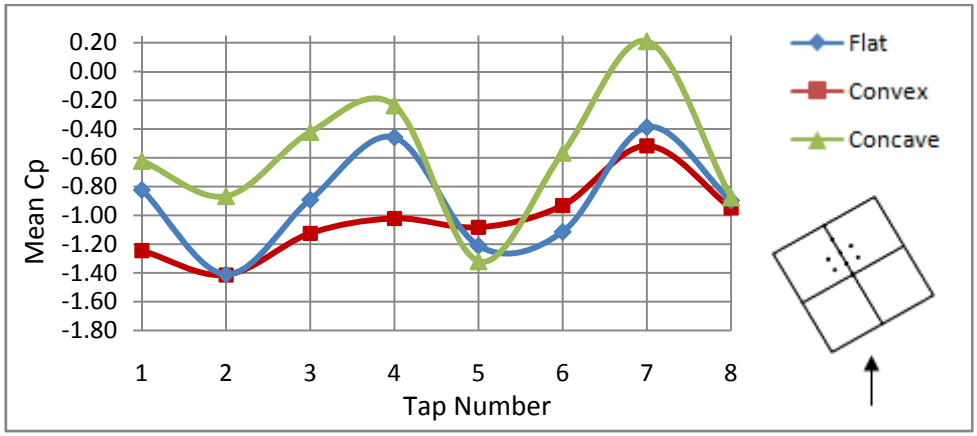


Figure 6.27a - Mean pressure coefficient distribution ('smooth' BL, θ = 150°)

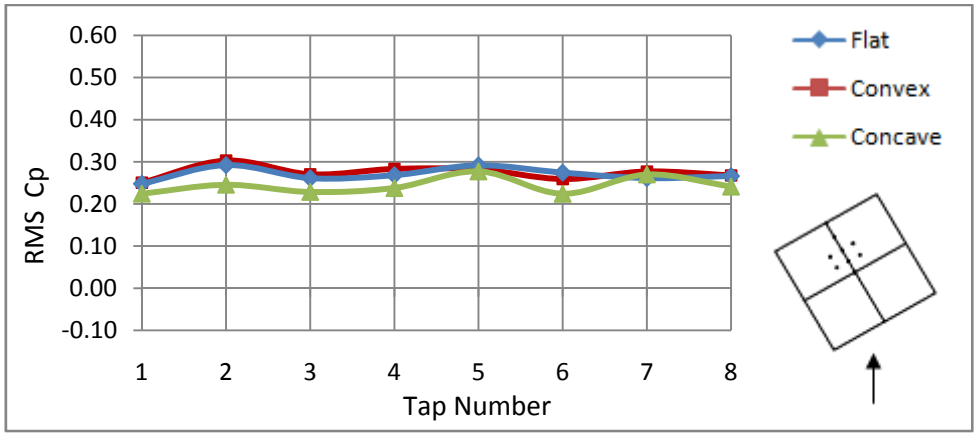


Figure 6.27b - RMS pressure coefficient distribution ('smooth' BL, θ = 150°)

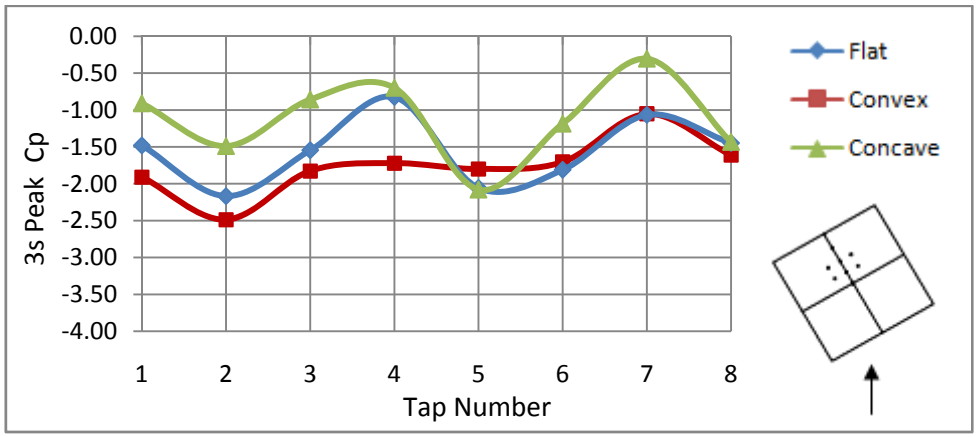


Figure 6.27c - 3s peak pressure coefficient distribution ('smooth' BL, θ = 150°)

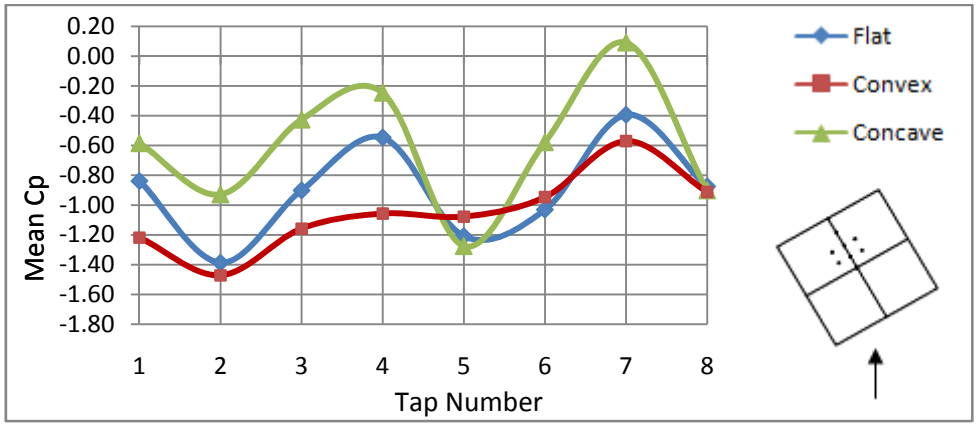


Figure 6.28a - Mean pressure coefficient distribution ('rough' BL, θ = 150°)

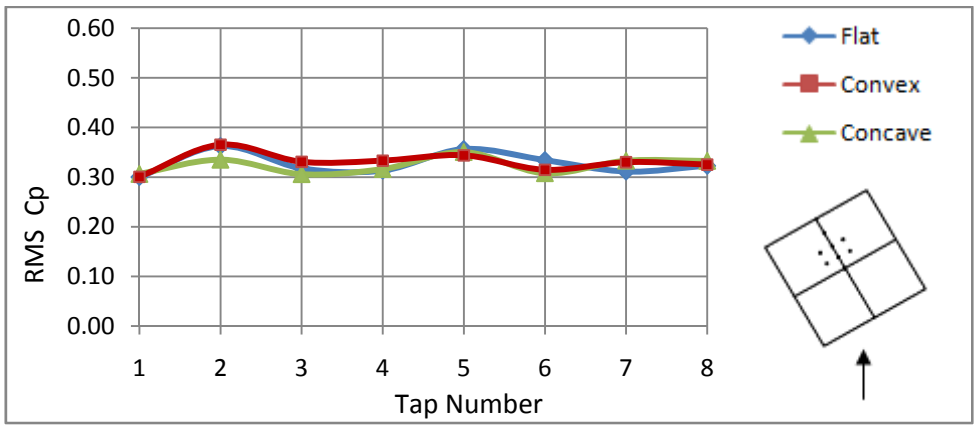


Figure 6.28b - RMS pressure coefficient distribution ('rough' BL, θ = 150°)

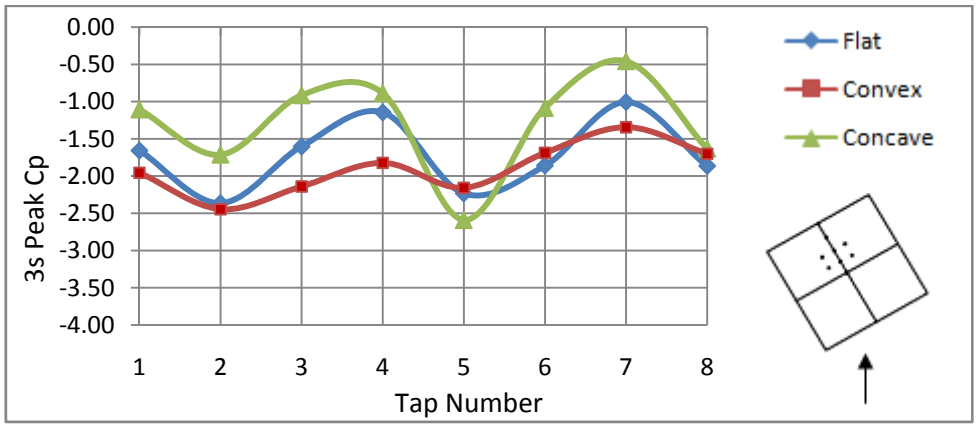


Figure 6.28c - 3s peak pressure coefficient distribution ('rough' BL, θ = 150°)

6.2.10 180° wind direction

The tap positions for the 180° wind direction are shown in Figure 6.29.

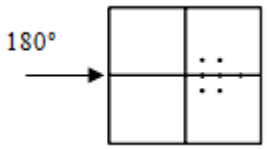


Figure 6.29 - Tap positions for the 180° wind direction

The mean, RMS and negative peak pressures are shown in Figures 6.30a through 6.31c. The consistency in the mean pressure coefficient distribution for the concave and flat cross vaults is shown in Figures 6.30a and 6.31a. The magnitude of the mean pressures nearest the roof apex (at taps 1 through 4) for the convex cross vault vary visibly with those corresponding to the concave and flat cross vaults. These results are consistent with centrally located mean pressure distributions, at numerous wind directions, discussed earlier in this chapter. However, the mean pressures at taps 5 through 8 are basically identical for all cross vault types.

For the 'smooth' boundary-layer, the RMS pressure coefficients are practically identical. For the 'rough' boundary-layer, the RMS pressure coefficients corresponding to the concave roof are slightly larger than those for the flat and convex roofs. These results are consistent with RMS distributions observed at the 0° and 90° wind directions, with separation at the leading edge. Also, the discrepancies are only noted for the 'rough' boundary layer, which may indicate that the concave cross vault is more sensitive to the increased turbulence intensity of the approaching flow.

The negative 3s peak pressures, shown in Figures 6.30c and 6.31c, illustrate similar distribution patterns to the mean pressures shown in Figures 6.30a and 6.31a. Negative 3s peak pressures for the concave cross vault are slightly larger than those for the flat cross vault by way of the larger RMS pressure coefficients.

The large variation observed at tap 2 for the convex cross vault and 'rough' boundary-layer is believed to be due to an error, as this trend was not measured at tap 4. Furthermore, the discrepancy is not supported by the mean and RMS pressures measured at this tap. This error can be attributed to the spurious nature of peaks.

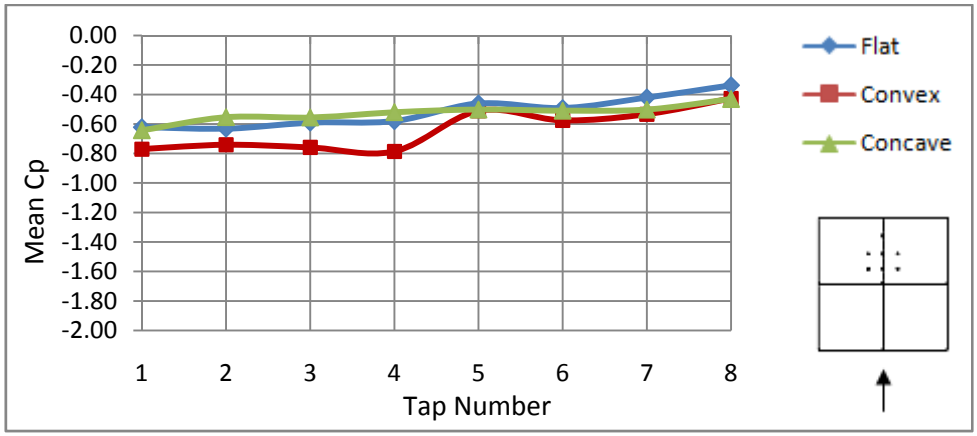


Figure 6.30a - Mean pressure coefficient distribution ('smooth' BL, θ = 180°)

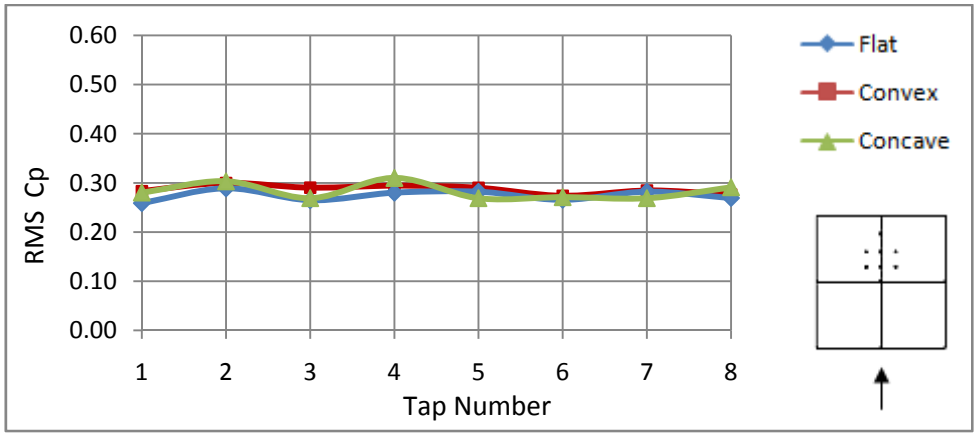


Figure 6.30b - RMS pressure coefficient distribution ('smooth' BL, θ = 180°)

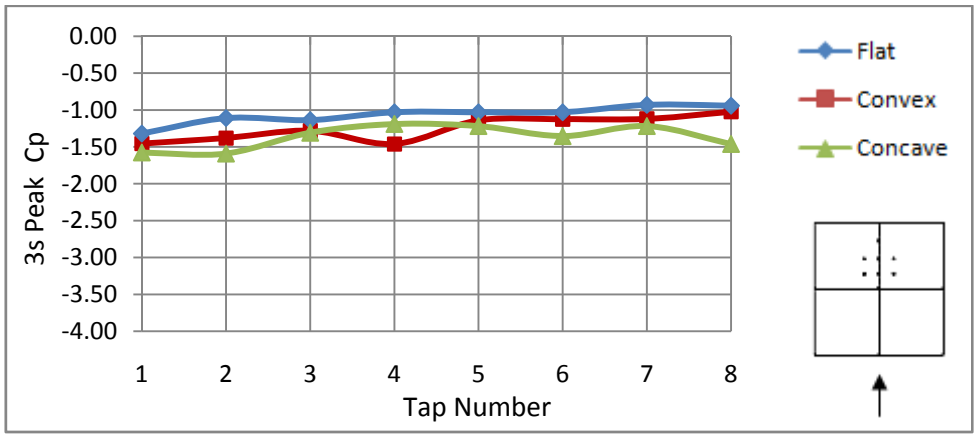


Figure 6.30c - 3s peak pressure coefficient distribution ('smooth' BL, θ = 180°)

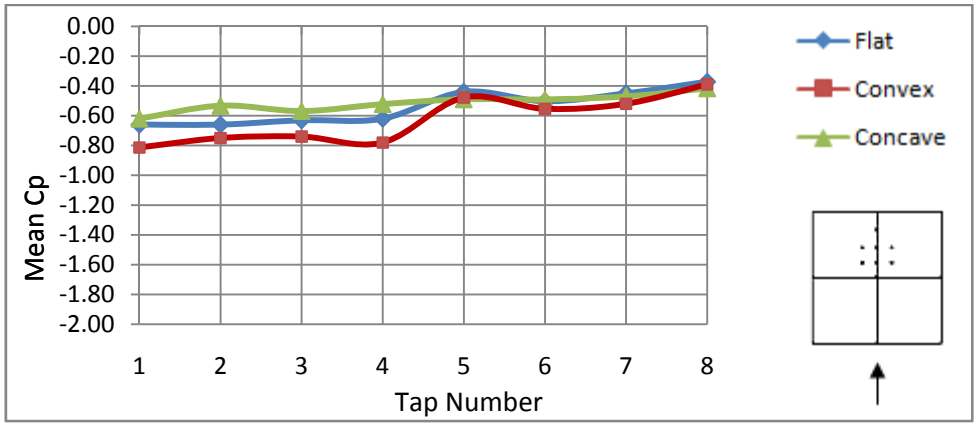


Figure 6.31a - Mean pressure coefficient distribution ('rough' BL, θ = 180°)

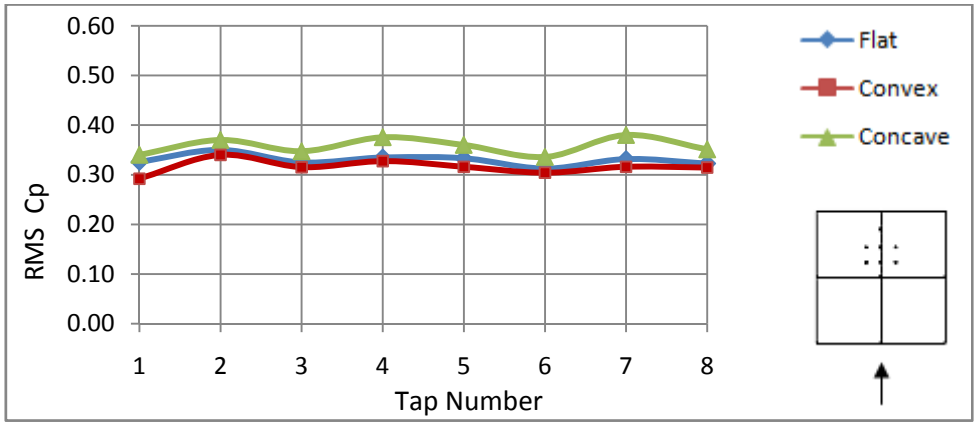


Figure 6.31b - RMS pressure coefficient distribution ('rough' BL, θ = 180°)

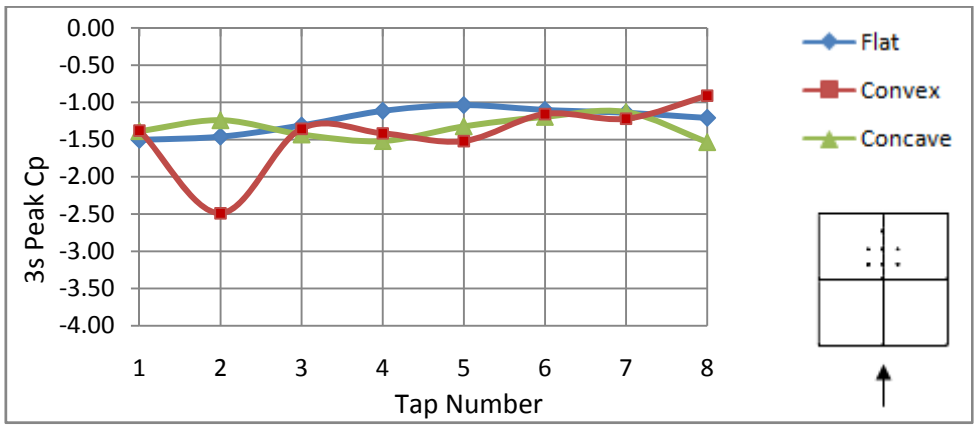


Figure 6.31c - 3s peak pressure coefficient distribution ('rough' BL, θ = 180°)

6.3 Pressure Distribution variation with Wind Direction

In this section, the variation of surface pressure coefficient distributions (comprising taps 1 through 8) with wind direction, for all vault types and boundary-layer profiles, are discussed. The pressure distributions were grouped into three segments, namely: 15° to 45°, 45° to 75° and 120° to 150°, which were selected on the basis of cross vault geometry and distribution similarities. It should be noted that the pressure distributions at the 0°, 90° and 180° degree wind directions were not included in these comparisons, since flow separation was controlled entirely by the wall-roof intersection, and only marginal differences were evident between all vault types.

6.3.1 15° to 45° wind directions

The variation of the mean and RMS pressure coefficient distributions with wind direction, ranging from 15° to 45°, are shown in Figures 6.32a through 6.37b. The mean and RMS pressure distribution patterns for the flat and concave vaults show a degree of similitude; however, this is not the case for the convex cross vault.

The most noticeable difference between the convex and other cross vault forms is shown through the noticeable variation in distribution development, as the wind direction changes from 15° to 45°. The development of the mean pressures over the convex cross vault reveals a clear pattern, in which mean pressures decrease as the wind direction increases (refer to Figures 6.36a and 6.37a). However, at the 15° wind direction, the mean pressure distributions over the other cross vault forms are generally opposed to this trend (refer to Figures 6.32a, 6.33a, 6.34a and 6.35a).

It is apparent that pressures at taps 4 and 7, which are at the most windward position, over the flat and concave cross vaults, are consistent with pressures over the convex cross vault. It is also to be noted that at the 15° wind direction, the RMS pressures over the flat and concave cross vaults are noticeably larger than those at 30° and 45°. The reasons for these discrepancies at the 15° wind directions have been discussed previously in section 6.2. Furthermore, RMS

pressure coefficients are practically identical at all three wind directions over the convex cross vault.

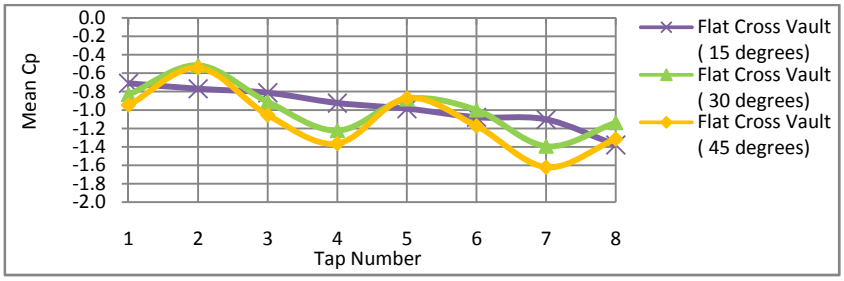


Figure 6.32a - Mean pressure coefficient distribution for the flat vault ('smooth' BL, θ = 15°, 30°, 45°)

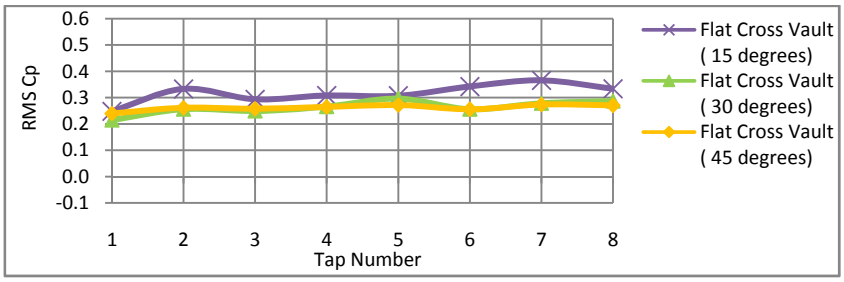


Figure 6.32b - RMS pressure coefficient distribution for the flat vault ('smooth' BL, θ = 15°, 30°, 45°)

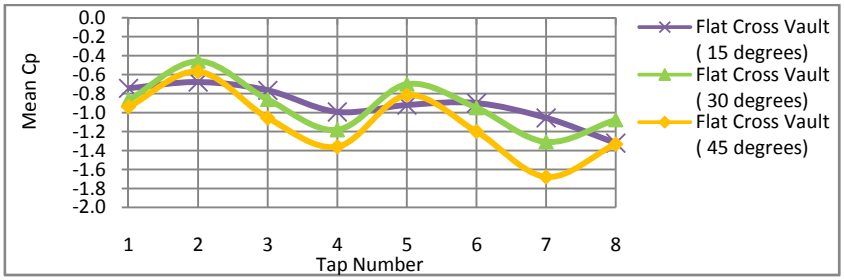


Figure 6.33a - Mean pressure coefficient distribution for the flat vault ('rough' BL, θ = 15°, 30°, 45°)

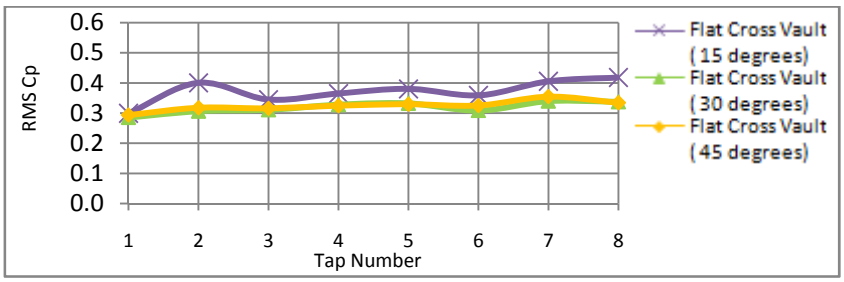


Figure 6.33b - RMS pressure coefficient distribution for the flat vault ('rough' BL, θ = 15°, 30°, 45°)

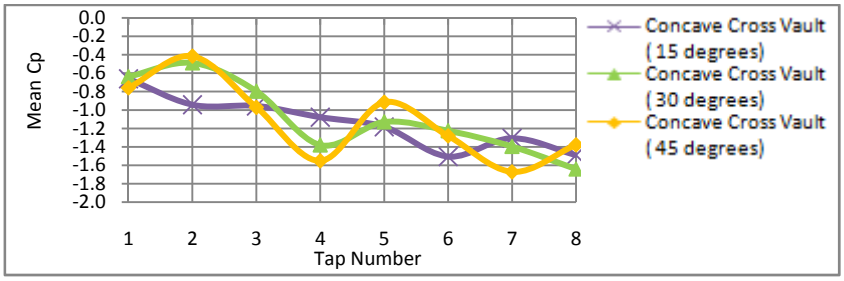


Figure 6.34a - Mean pressure coefficient distribution for the concave vault ('smooth' BL, θ = 15°, 30°, 45°)

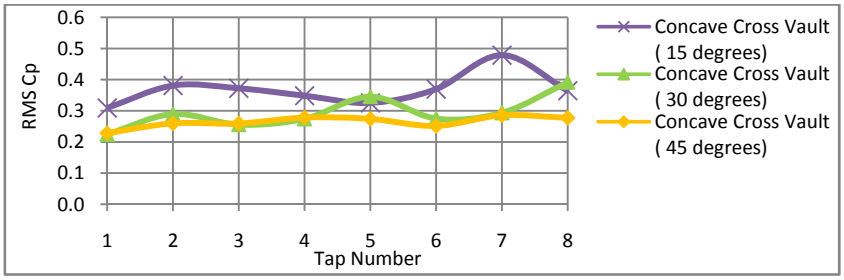


Figure 6.34b - RMS pressure coefficient distribution for the concave vault ('smooth' BL, θ = 15°, 30°, 45°)

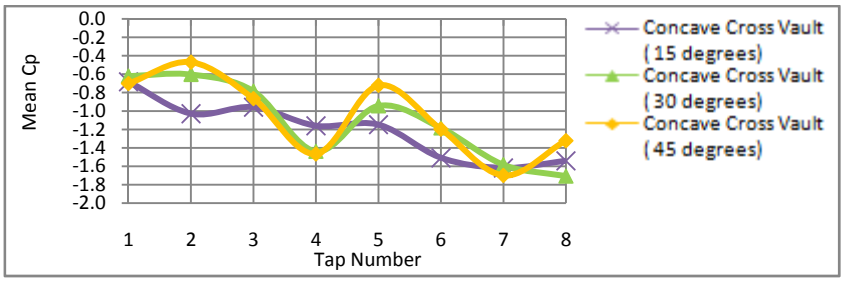


Figure 6.35a - Mean pressure coefficient distribution for the concave vault ('rough' BL, θ = 15°, 30°, 45°)

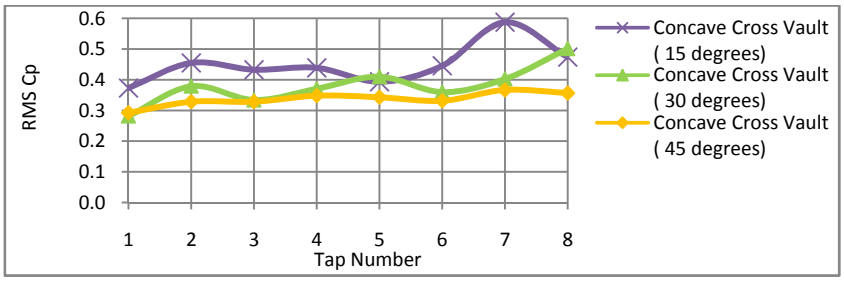


Figure 6.35b - RMS pressure coefficient distribution for the concave vault ('rough' BL, θ = 15°, 30°, 45°)

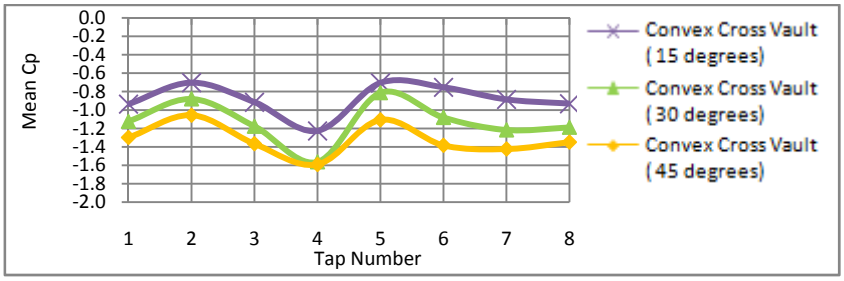


Figure 6.36a - Mean pressure coefficient distribution for the convex vault ('smooth' BL, θ = 15°, 30°, 45°)

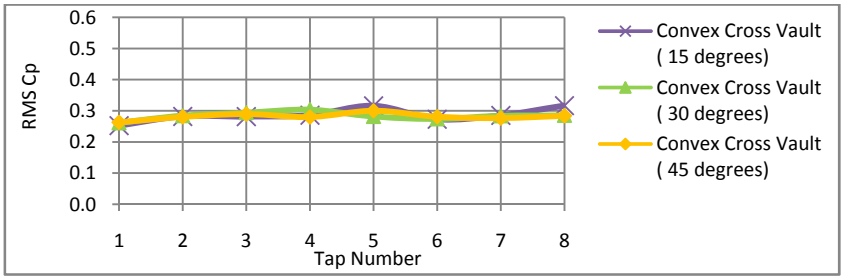


Figure 6.36b - RMS pressure coefficient distribution for the convex vault ('smooth' BL, θ = 15°, 30°, 45°)

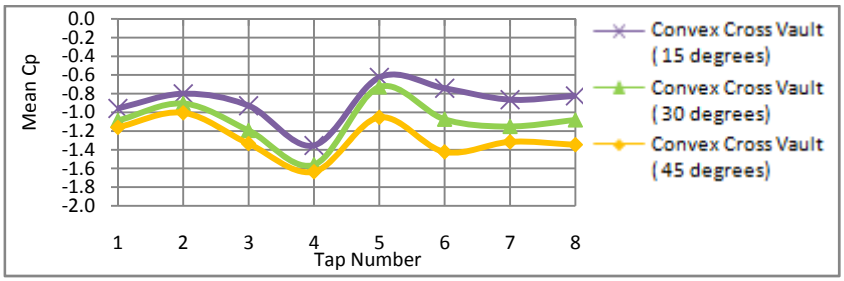


Figure 6.37a - Mean pressure coefficient distribution for the convex vault ('rough' BL, θ = 15°, 30°, 45°)

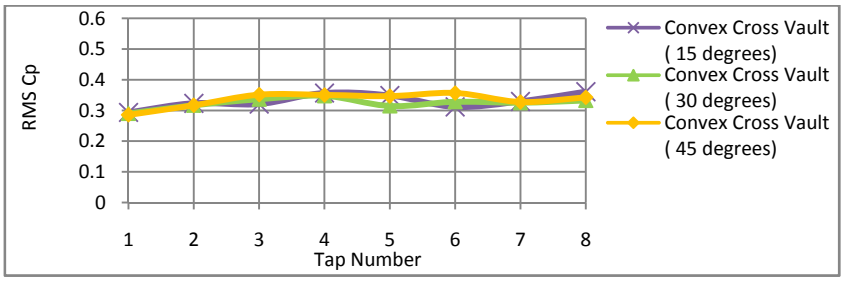


Figure 6.37b - Mean pressure coefficient distribution for the convex vault ('rough' BL, θ = 15°, 30°, 45°)

6.3.2 45° to 75° wind directions

The mean and RMS pressure coefficient distribution variation with wind direction, for all vault types and boundary-layer profiles, ranging between 45° to 75°, are shown in Figures 6.38a through 6.43b. The consistency in the pressure distribution development with wind direction for the flat and concave cross vaults is once again evident. A visible mean pressure difference between the convex and other cross vault forms is also apparent.

For the wind direction adjustment from 45° to 60°, the concave and flat cross vaults show no noticeable mean and RMS pressure coefficient variation at taps 1 through 5. However, taps 6, 7 and 8 show slight mean and RMS pressure reductions and increases, respectively. Slight pressure variations are also apparent over the convex cross vault corresponding to the direction adjustment from 45° to 60°.

As can be seen from the figures, the mean pressures at taps 4 and 7 (i.e. on the windward side), over all cross vaults, experience an increase in magnitude with direction adjustment from 60° to 75°. The reason for these pressure increases is believed to be due to a combination of the increased action of the leading edge and decreased influence of the vault intersection (groove) on the flow pattern. It is to be noted that tap 4 (for all three cross vault models), which is nearest the intersection, shows the largest mean pressure increase.

It should also be noted that mean pressure distributions, for all cross vaults, within both boundary layers, generally show marginal variation with direction adjustment from 45° to 75°, as shown in 6.38a, 6.39a, 6.40a, 6.41a, 6.42a and 6.43a. Generally speaking, pressures reach a minimum between 45° and 60°, after which pressures increase, as observed at the 75° wind direction. However, RMS pressures are practically identical, as shown in Figures 6.38b, 6.39b, 6.40b, 6.41b, 6.42b and 6.43b.

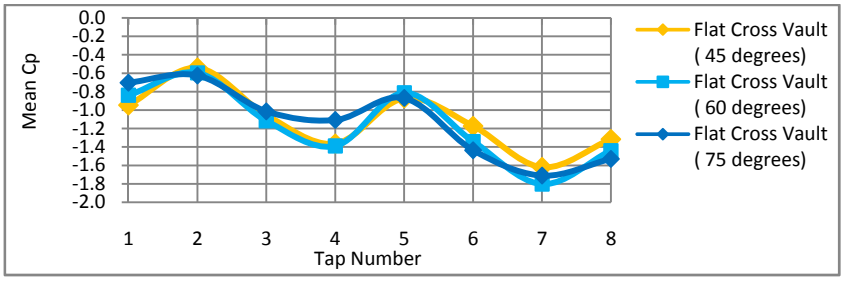


Figure 6.38a - Mean pressure coefficient distribution for the flat cross vault ('smooth' BL, θ = 45°, 60°, 75°)

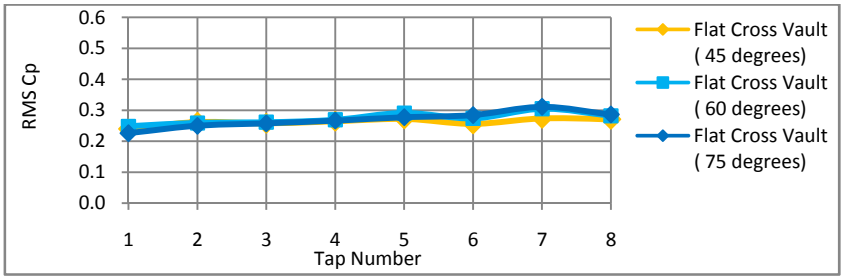


Figure 6.38b - RMS pressure coefficient distribution for the flat cross vault ('smooth' BL, θ = 45°, 60°, 75°)

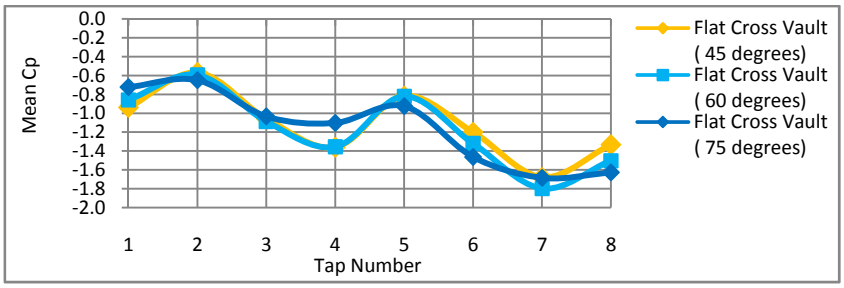


Figure 6.39a - Mean pressure coefficient distribution for the flat cross vault ('rough' BL, θ = 45°, 60°, 75°)

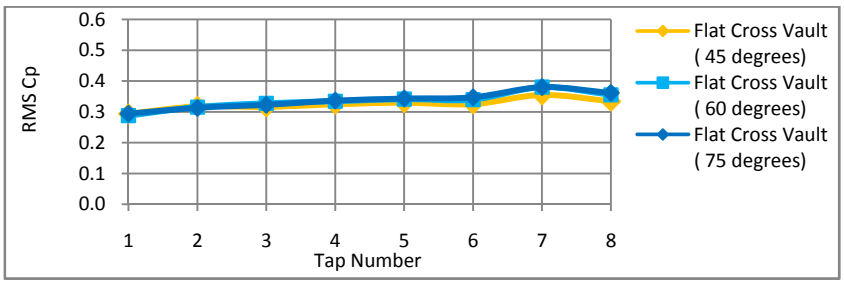


Figure 6.39b - RMS pressure coefficient distribution for the flat cross vault ('rough' BL, θ = 45°, 60°, 75°)

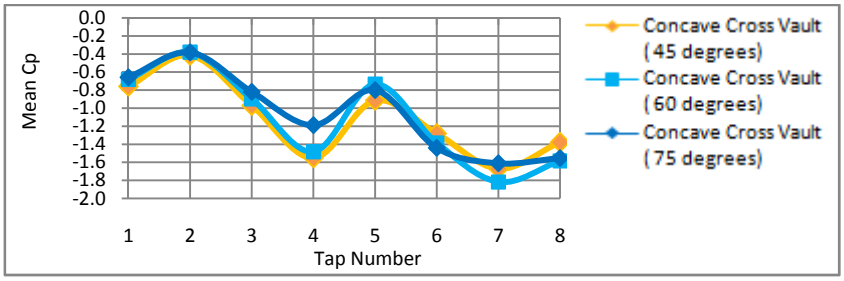


Figure 6.40a - Mean pressure coefficient distribution for the concave cross vault ('smooth' BL, θ = 45°, 60°, 75°)

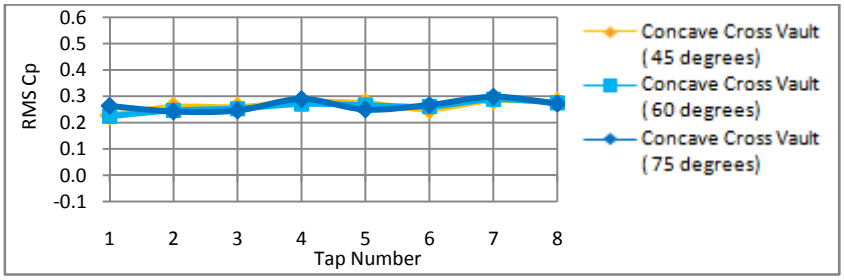


Figure 6.40b - RMS pressure coefficient distribution for the concave cross vault ('smooth' BL, θ = 45°, 60°, 75°)

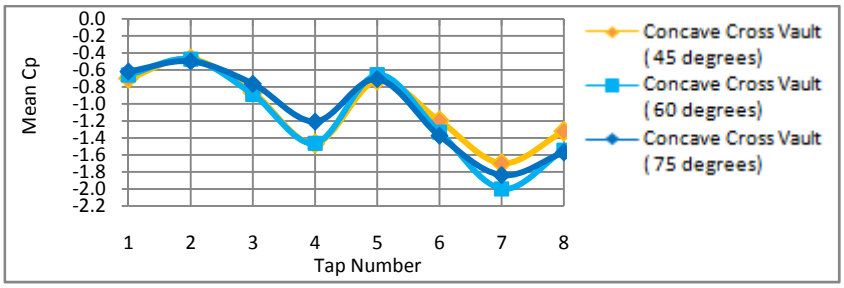


Figure 6.41a - Mean pressure coefficient distribution for the concave cross vault ('rough' BL, θ = 45°, 60°, 75°)

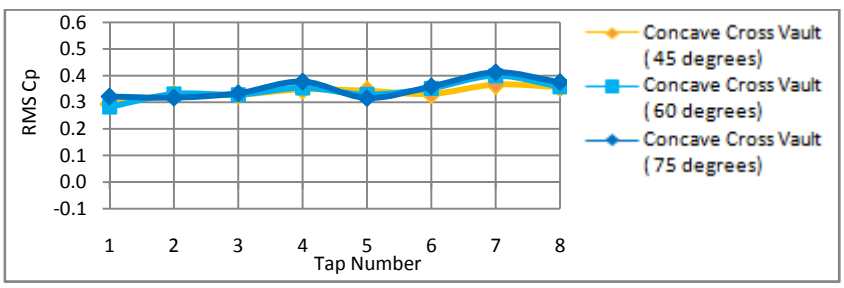


Figure 6.41b - RMS pressure coefficient distribution for the concave cross vault ('rough' BL, θ = 45°, 60°, 75°)

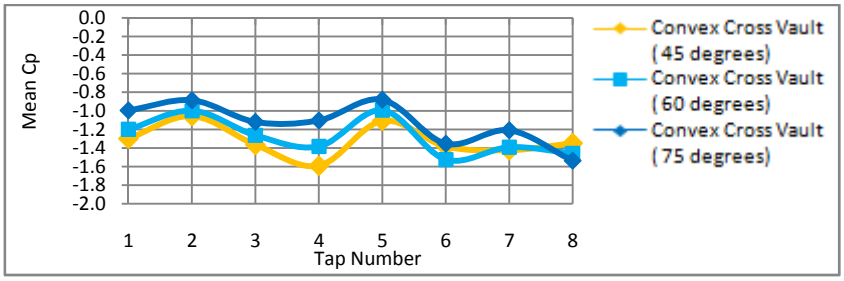


Figure 6.42a - Mean pressure coefficient distribution for the convex cross vault ('smooth' BL, θ = 45°, 60°, 75°)

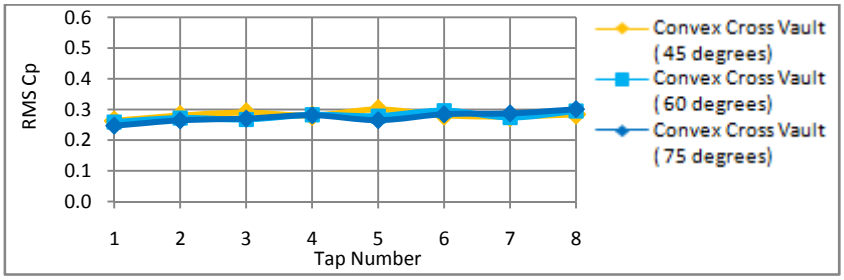


Figure 6.42b - RMS pressure coefficient distribution for the convex cross vault ('smooth' BL, θ = 45°, 60°, 75°)

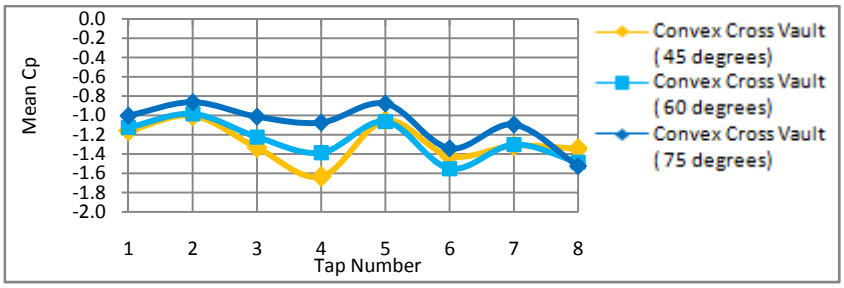


Figure 6.43a - Mean pressure coefficient distribution for the convex cross vault ('rough' BL, θ = 45°, 60°, 75°)

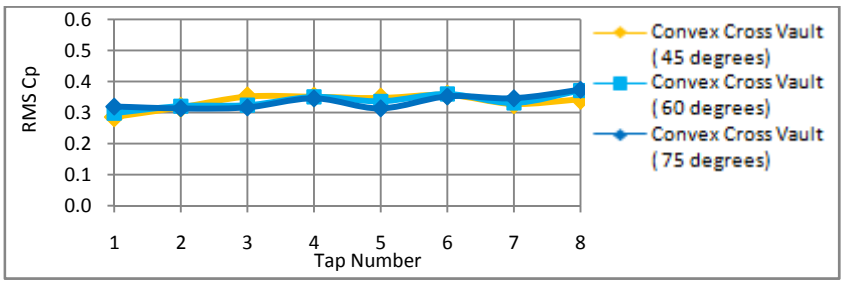


Figure 6.43b - Mean pressure coefficient distribution for the convex cross vault ('rough' BL, θ = 45°, 60°, 75°)

6.3.3 120° to 150° wind directions

The mean and RMS pressure coefficient distribution variation with wind directions, for all vault types and boundary-layer profiles, ranging between 120° to 150°, are shown in Figures 6.44a through 6.49b. Mean pressures coefficient distributions for the flat cross vault, shown in Figures 6.44a and 6.45a, call attention to the visible variations at taps 5 and 6 corresponding to the two wind directions. Negligible variations are also evident at taps 2, 3, 4 and 8, especially for the 'rough' boundary-layer setup.

Considerable dissimilarity is evident between the flat and concave cross vault pressure coefficient development with wind direction. This result is opposed to the similarity noted in sections 6.3.1 and 6.3.2. As can be seen from Figures 6.46a and 6.47a, the only noticeable mean pressure differences, between the 120° and 150° wind directions, are observed at taps 4 and 7. This result, in combination with the visible RMS pressure variation (refer to Figures 6.46b and 6.47b), may reveal an influence of the cross vault intersection on the flow and, ultimately, the adjacent pressures.

As shown in Figures 6.48a and 6.49a, the pressure distribution development with wind direction, for the convex cross vault, illustrates several similarities with the corresponding results for the flat cross vault, as shown in Figures 6.44a and 6.45a. The most notable similarity is apparent at taps 5 and 6. Mean pressure reductions are also apparent at taps 4 and 7, which is opposed to results for the concave cross vault. These variations are believed to be due to the effect of apex geometry and roof slope on the wind flow.

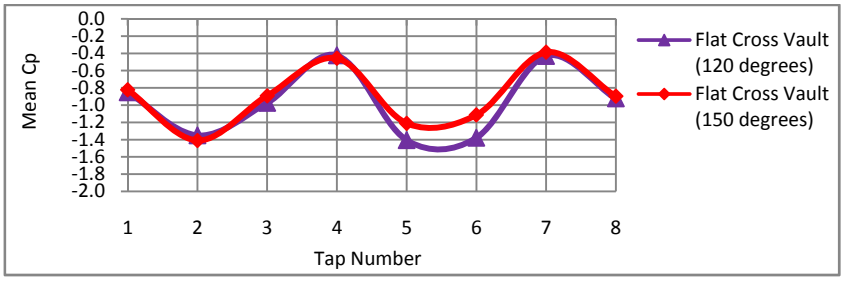


Figure 6.44a - Mean pressure coefficient distribution for the flat cross vault ('smooth' BL, θ = 120° and 150°)

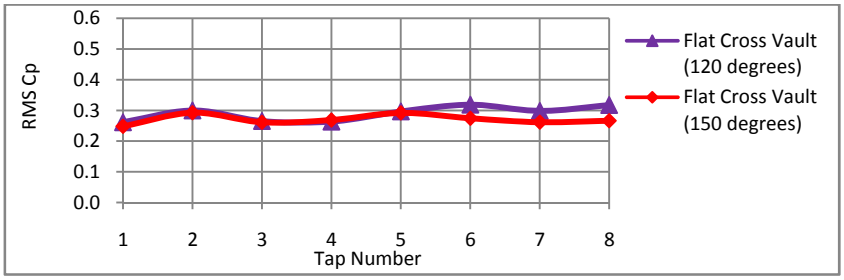


Figure 6.44b - RMS pressure coefficient distribution for the flat cross vault ('smooth' BL, θ = 120° and 150°)

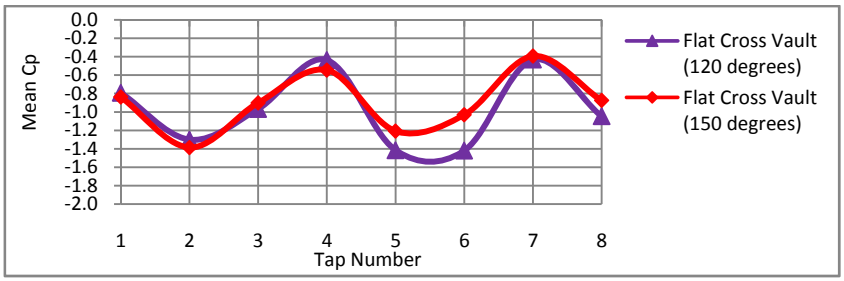


Figure 6.45a- Mean pressure coefficient distribution for the flat cross vault ('rough' BL, θ = 120° and 150°)

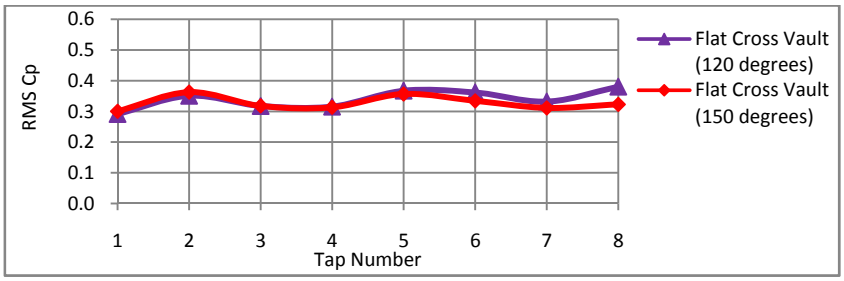


Figure 6.45b- RMS pressure coefficient distribution for the flat cross vault ('rough' BL, θ = 120° and 150°

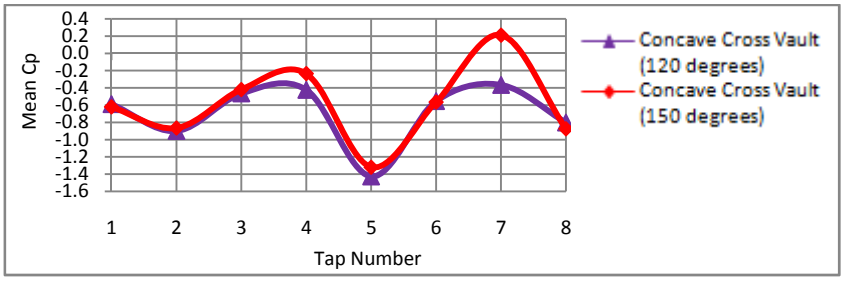


Figure 6.46a - Mean pressure coefficient distribution for the concave cross vault ('smooth' BL, θ = 120° and 150°)

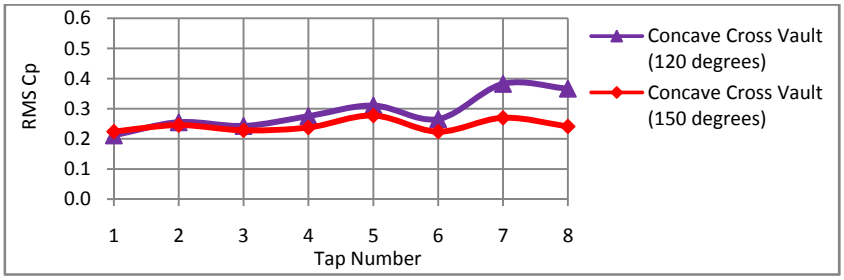


Figure 6.46b - RMS pressure coefficient distribution for the concave cross vault ('smooth' BL, θ = 120° and 150°)

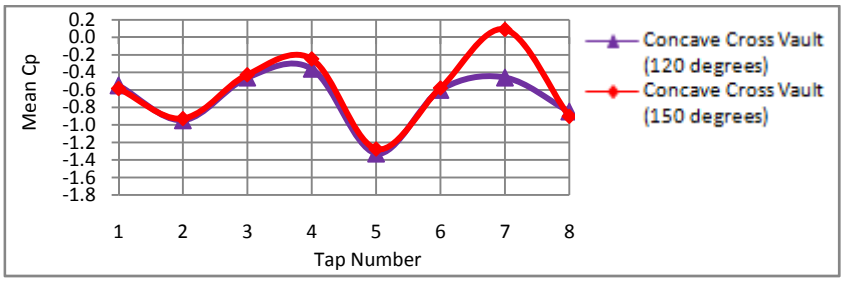


Figure 6.47a - Mean pressure coefficient distribution for the concave cross vault ('rough' BL, θ = 120° and 150°)

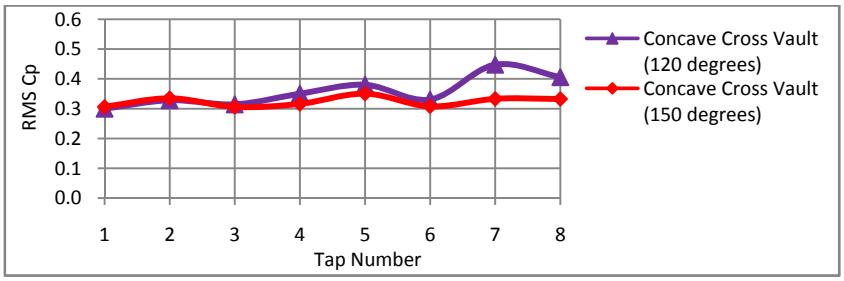


Figure 6.47b - RMS pressure coefficient distribution for the concave cross vault ('rough' BL, θ = 120° and 150°)

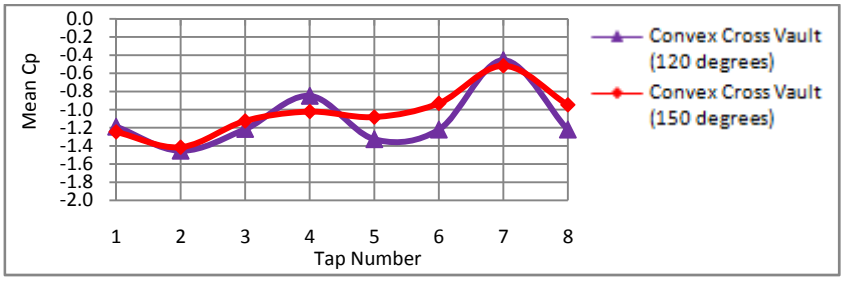


Figure 6.48a - Mean pressure coefficient distribution for the convex cross vault ('smooth' BL, θ = 120° and 150°)

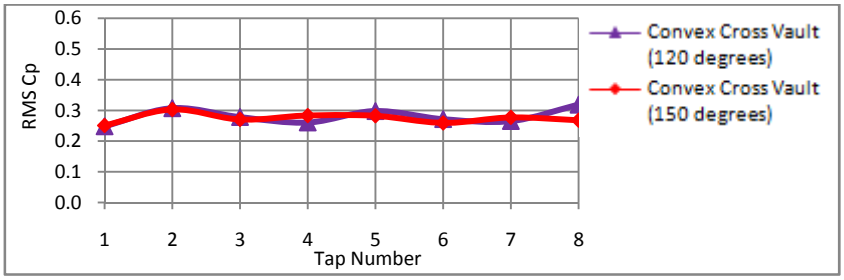


Figure 6.48b - RMS pressure coefficient distribution for the convex cross vault ('smooth' BL, θ = 120° and 150°)

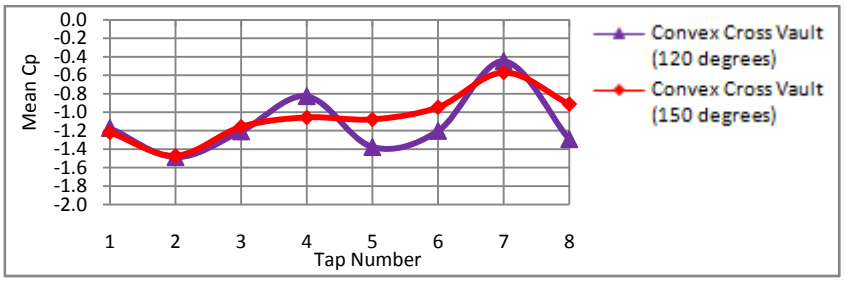


Figure 6.49a- Mean pressure coefficient distribution for the convex cross vault ('rough' BL, θ = 120° and 150°)

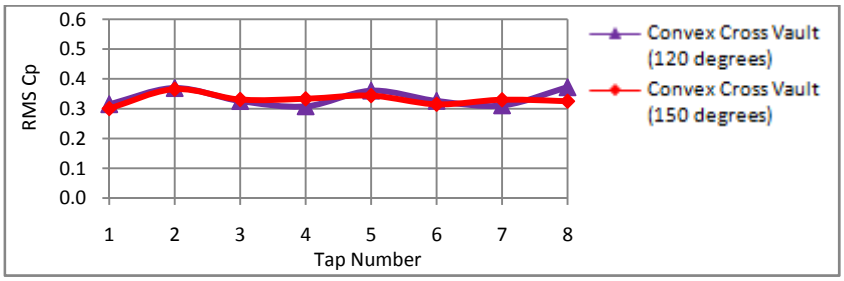


Figure 6.49b- RMS pressure coefficient distribution for the convex cross vault ('rough' BL, θ = 120° and 150°)

6.4 Contour Plots

Figures 6.51a through 6.68b show the mean and RMS pressure contour plots for the instrumented area, over all vault types and within both boundary-layers. These plots were developed by utilising the symmetry of the models and are produced from the 0°, 30°, 60°, 90°, 120°, 150° and 180° pressure coefficient measurements. The tap positions and wind direction are shown in Figure 6.50.

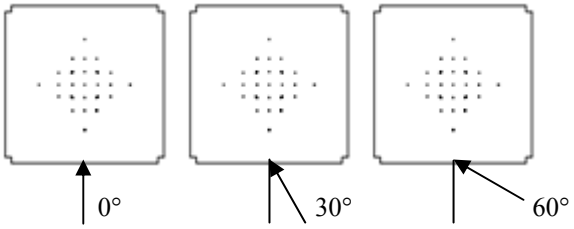


Figure 6.50 - Intrumented area for the the 0° wind direction

The consistency in the mean pressure distributions for the flat and concave cross vaults at the 0° wind direction, for both boundary-layers, is shown in Figures 6.51a, 6.52a, 6.55a and 6.56a. This general similarity is somewhat expected, since flow separates at the sharp edge. However, the mean pressure coefficients measured over the convex roof apex are slightly more negative than those over the other cross vault types, as shown in Figures 6.53a and 6.54a. This result clearly shows an influence of the convex apex on the local wind speed and pressures, even though the edge geometry, at which separation occurs, is identical for all cross vault types.

The distribution of surface pressures over the three models, in the form of contour plots, at the 30° and 60° wind flow directions are shown in Figures 6.57a through 6.68b. Comparing the pressure distributions shows that the mean pressure coefficients vary visibly for each type of geometry, most notably on the lee-side of the buildings. Separation at the 0° wind direction is controlled by the leading edge; however, for the oblique wind angles, the roof pitch and apex geometry appear to influence the positions of separation, the resulting wake and, ultimately, the surface pressures.

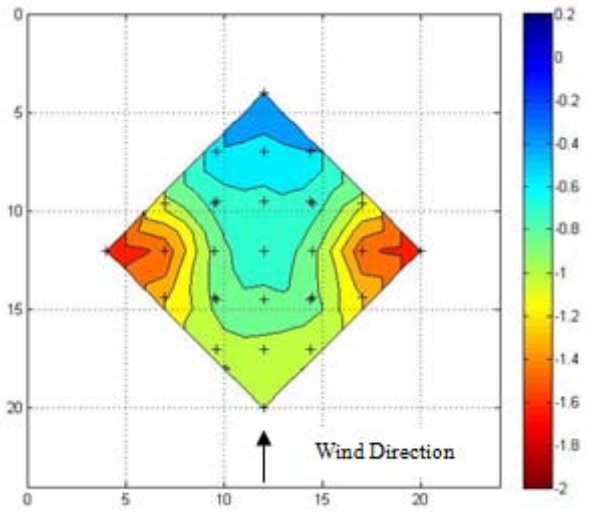


Figure 6.51a - Mean pressure distribution for θ = 0°

(Flat cross vault, 'smooth' BL)

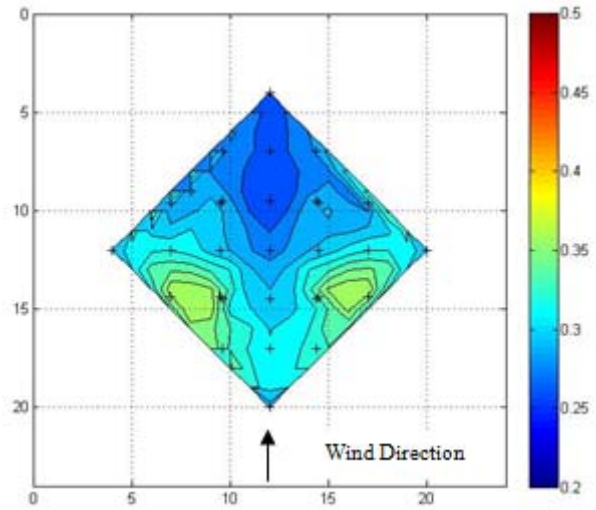


Figure 6.51b - RMS pressure distribution for θ = 0°

(Flat cross vault, 'smooth' BL)

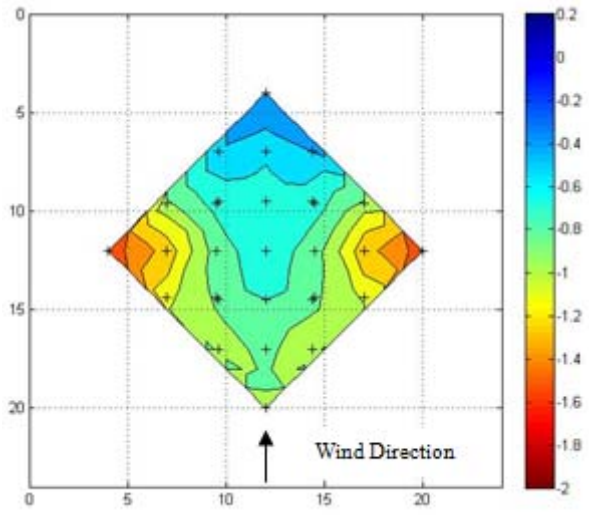


Figure 6.52a - Mean pressure distribution for θ = 0°

(Flat cross vault, 'rough' BL)

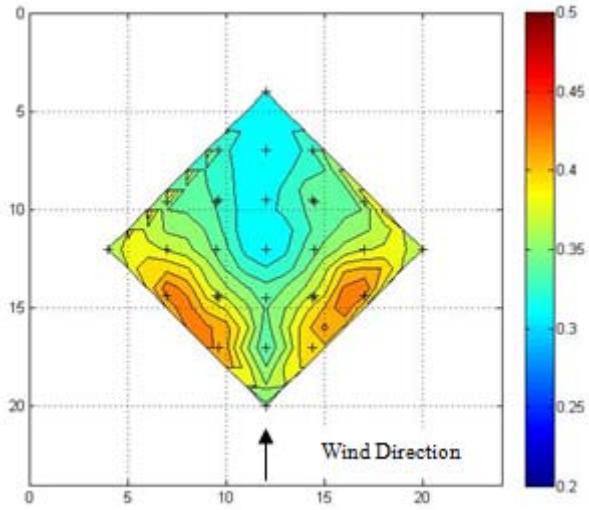


Figure 6.52b - RMS pressure distribution for θ = 0°

(Flat cross vault, 'rough' BL)

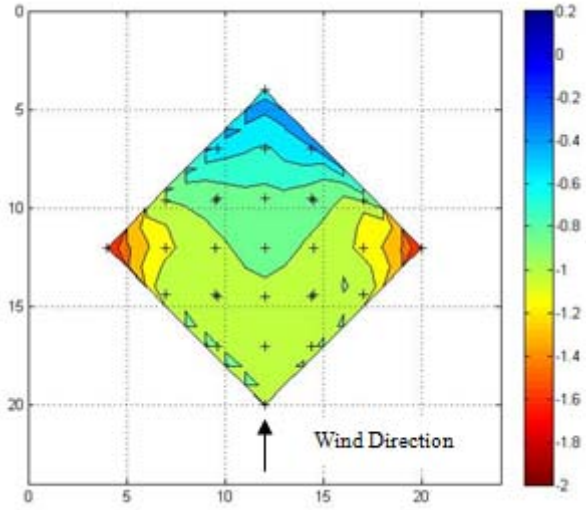


Figure 6.53a - Mean pressure distribution for θ = 0°

(Convex cross vault, 'smooth' BL)

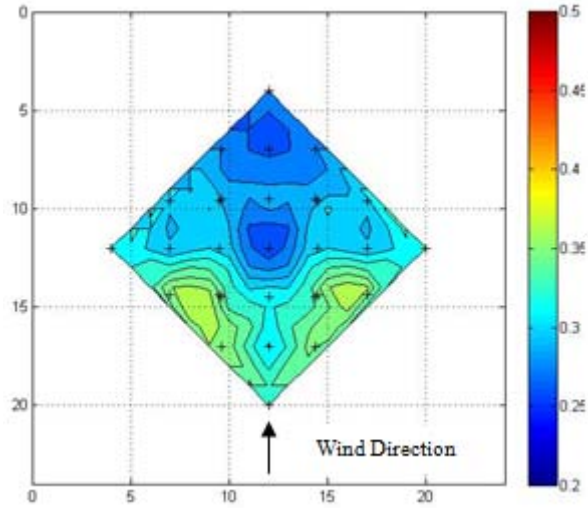


Figure 6.53b - RMS pressure distribution for θ = 0°

(Convex cross vault, 'smooth' BL)

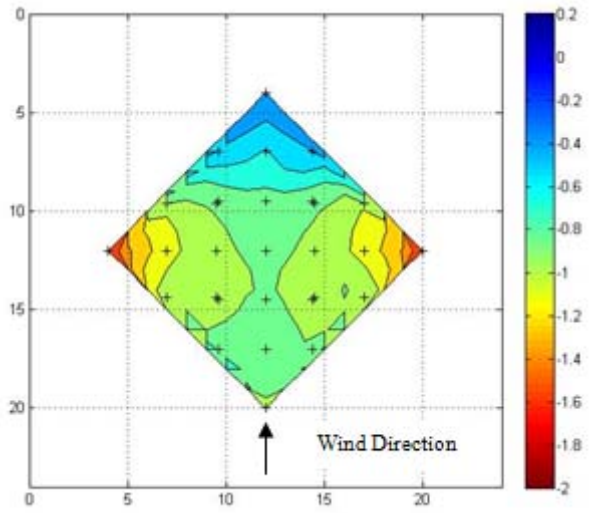


Figure 6.54a - Mean pressure distribution for θ = 0°

(Convex cross vault, 'rough' BL)

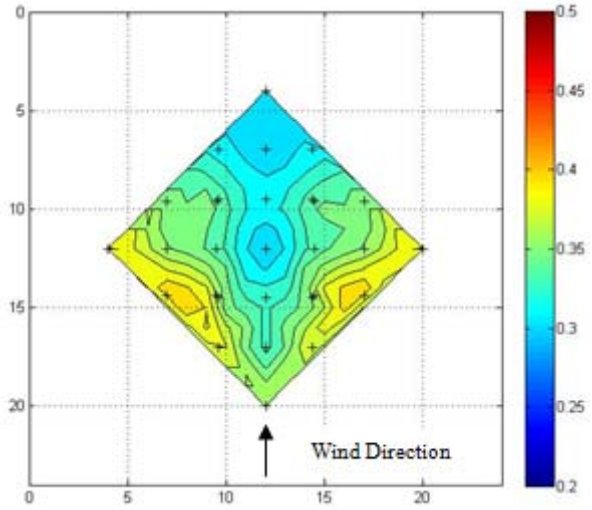


Figure 6.54b - RMS pressure distribution for θ = 0°

(Convex cross vault, 'rough' BL)

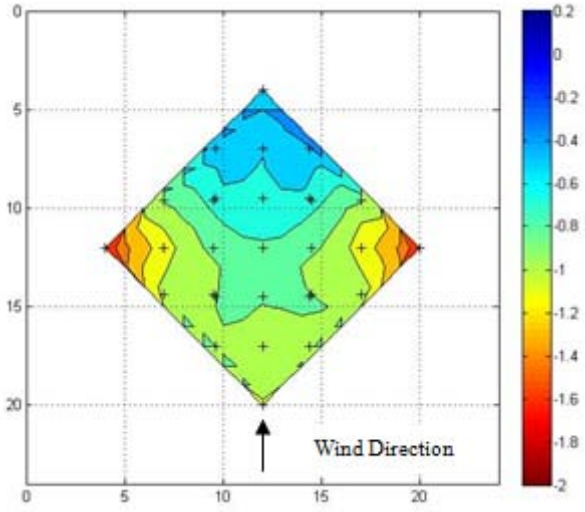


Figure 6.55a - Mean pressure distribution for θ = 0°

(Concave cross vault, 'smooth' BL)

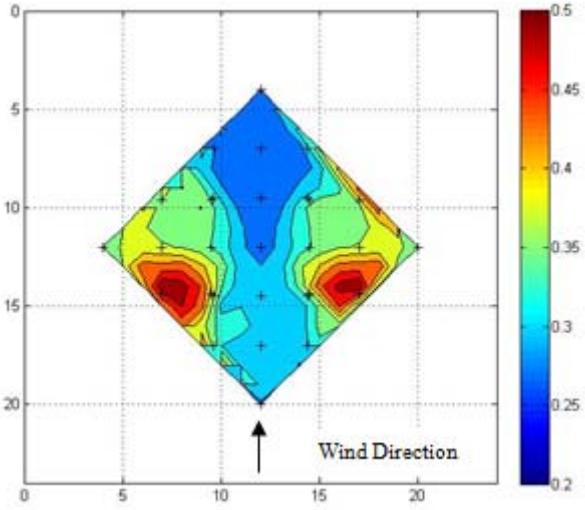


Figure 6.55b - RMS pressure distribution for θ = 0°

(Concave cross vault, 'smooth' BL)

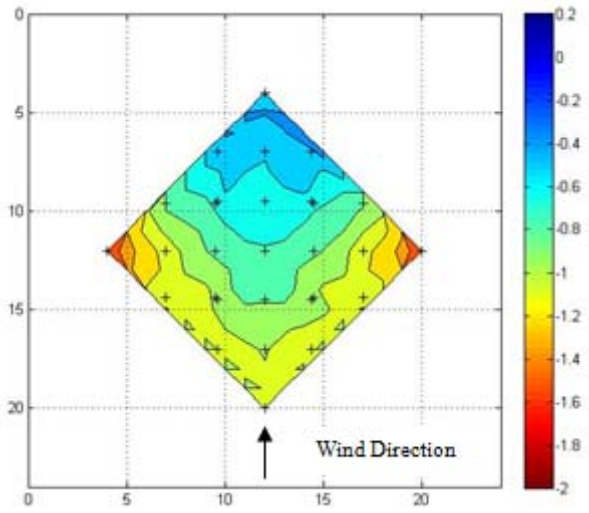


Figure 6.56a - Mean pressure distribution for θ = 0°

(Concave cross vault, 'rough' BL)

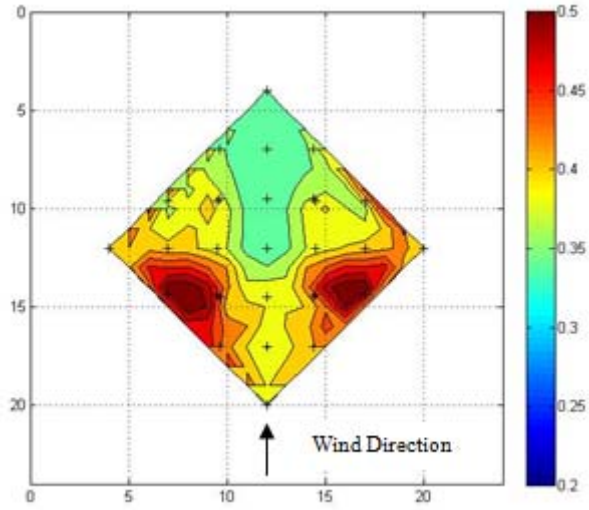


Figure 6.56b - RMS pressure distribution for θ = 0°

(Concave cross vault, 'rough' BL)

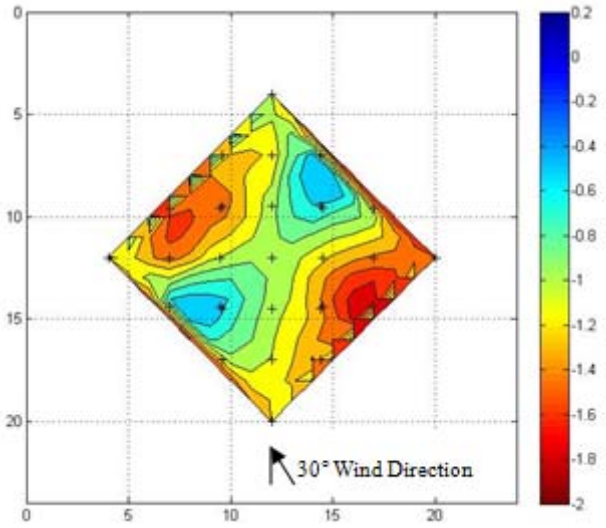


Figure 6.57a- Mean pressure distribution for θ = 30°
(Flat cross vault, 'smooth' BL)

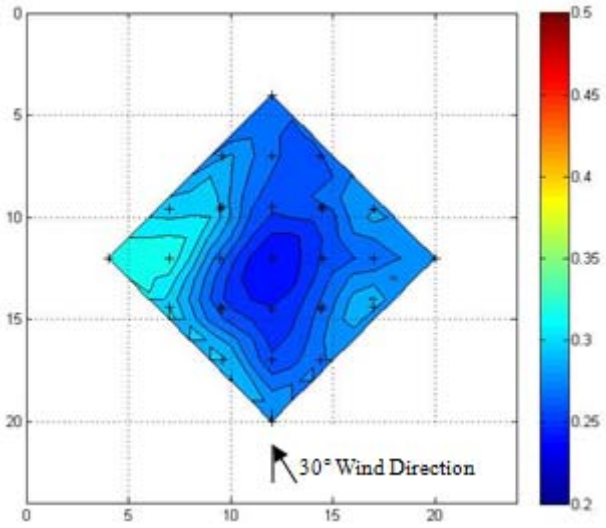


Figure 6.57b - RMS pressure distribution for θ = 30°
(Flat cross vault, 'smooth' BL)

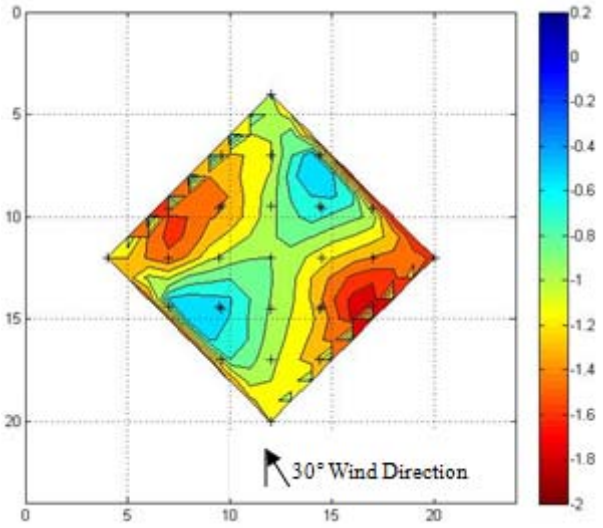


Figure 6.58a - Mean pressure distribution for θ = 30°
(Flat cross vault, 'rough' BL)

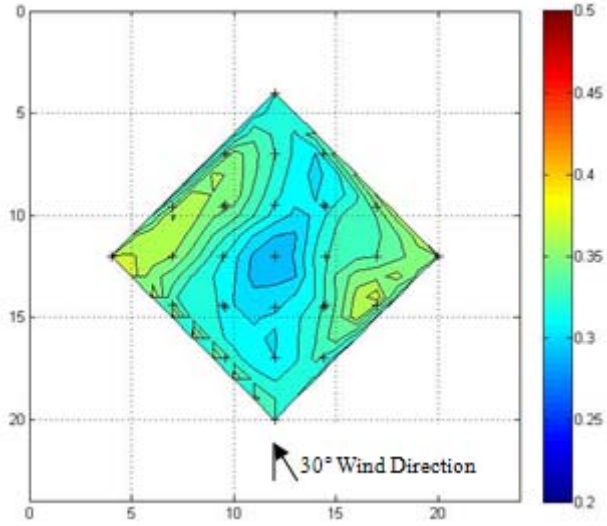


Figure 6.58b - RMS pressure distribution for θ = 30°
(Flat cross vault, 'rough' BL)

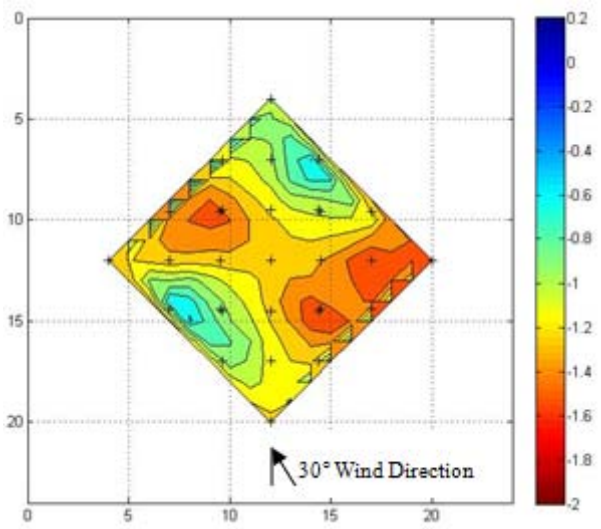


Figure 6.59a- Mean pressure distribution for θ = 30°

(Convex cross vault, 'smooth' BL)

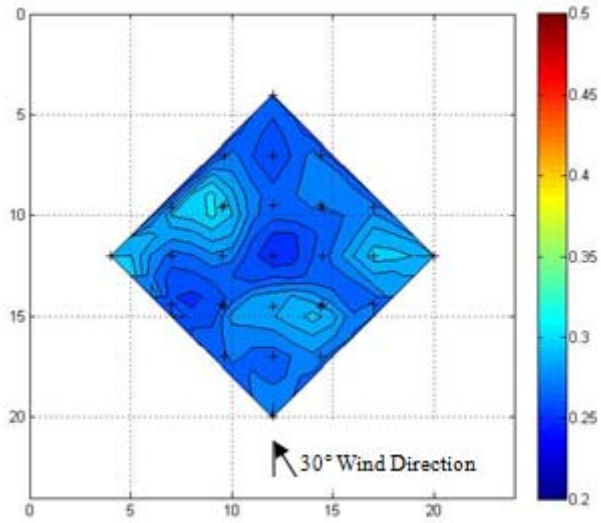


Figure 6.59b - RMS pressure distribution for θ = 30°

(Convex cross vault, 'rough' BL)

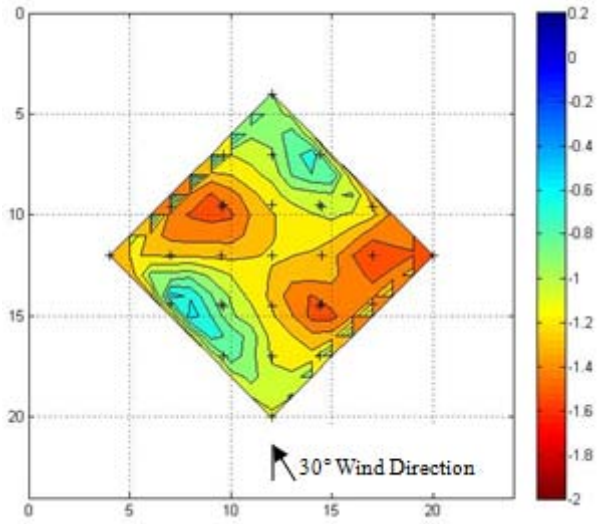


Figure 6.60a - Mean pressure distribution for θ = 30°

(Convex cross vault, 'rough' BL)

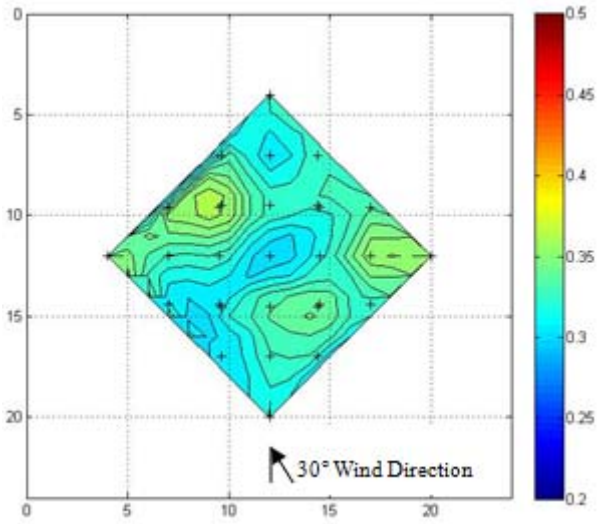


Figure 6.60b - RMS pressure distribution for θ = 30°

(Convex cross vault, 'rough' BL)

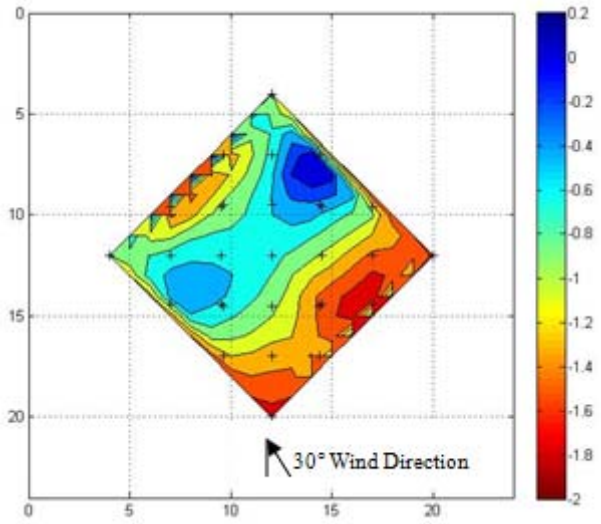


Figure 6.61a - Mean pressure distribution for θ = 30°

(Concave cross vault, 'smooth' BL)

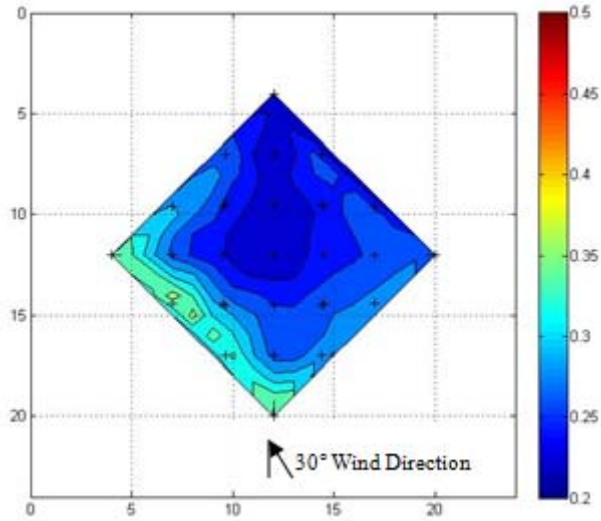


Figure 6.61b - RMS pressure distribution for θ = 30°

(Concave cross vault, 'smooth' BL)

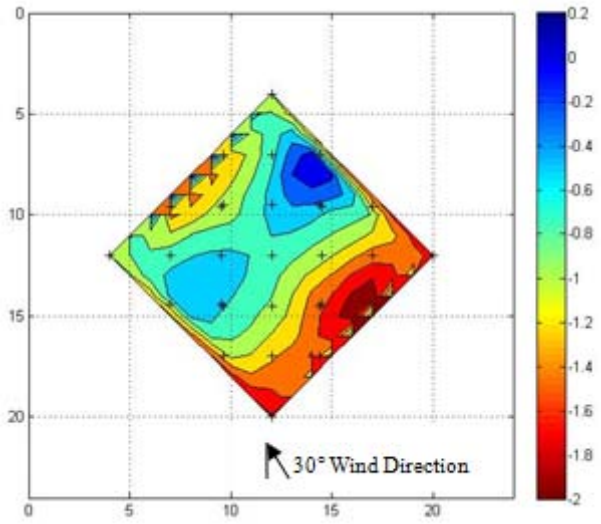


Figure 6.62a - Mean pressure distribution for θ = 30°

(Concave cross vault, 'rough' BL)

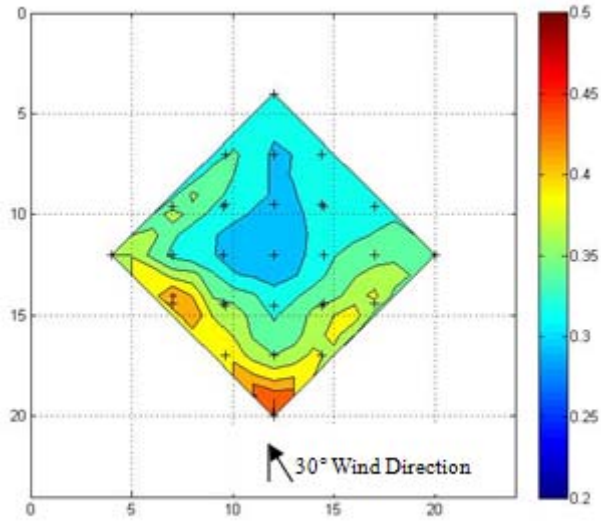


Figure 6.62b - RMS pressure distribution for θ = 30°

(Concave cross vault, 'rough' BL)

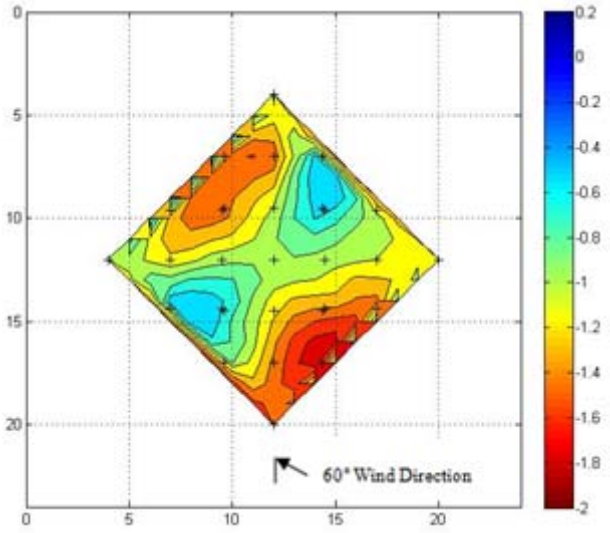


Figure 6.63a - Mean pressure distribution for θ = 60°

(Flat cross vault, 'smooth' BL)

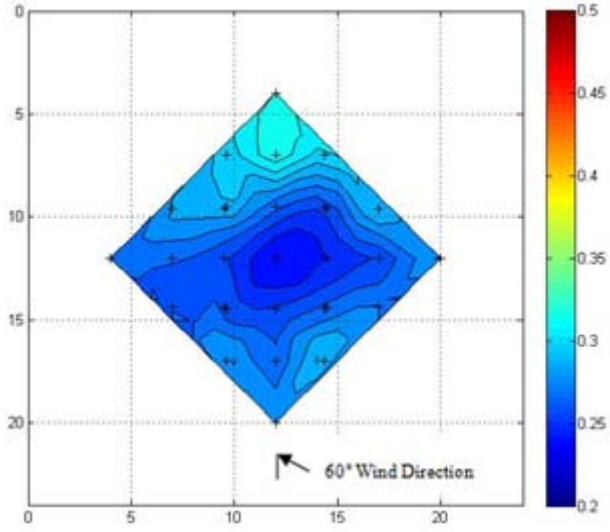


Figure 6.63b - RMS pressure distribution for θ = 60°

(Flat cross vault, 'smooth' BL)

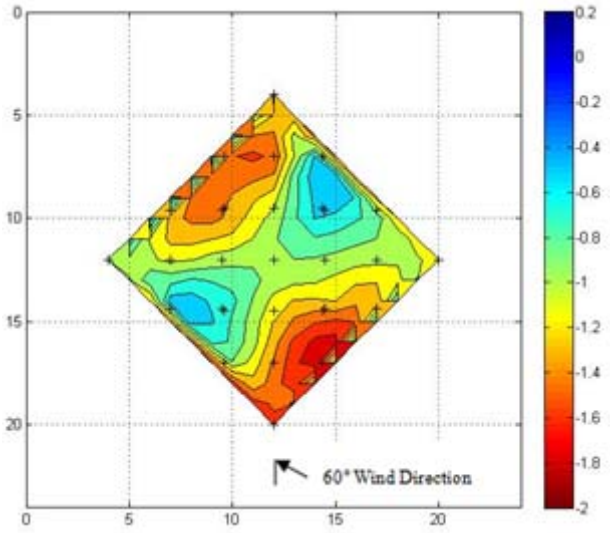


Figure 6.64a - Mean pressure distribution for θ = 60°

(Flat cross vault, 'rough' BL)

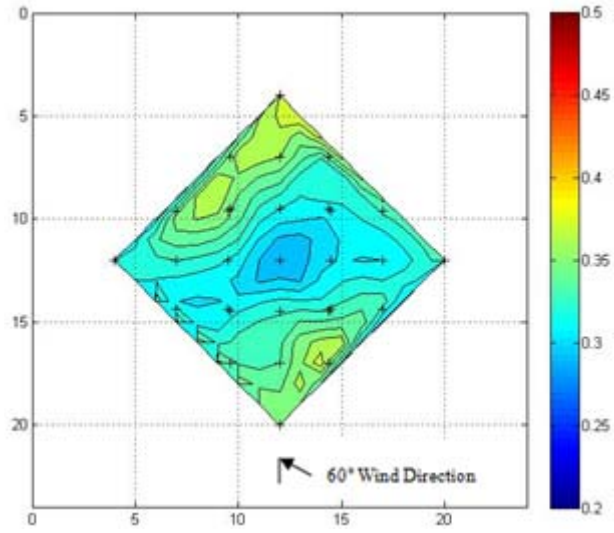


Figure 6.64b - RMS pressure distribution for θ = 60°

(Flat cross vault, 'rough' BL)

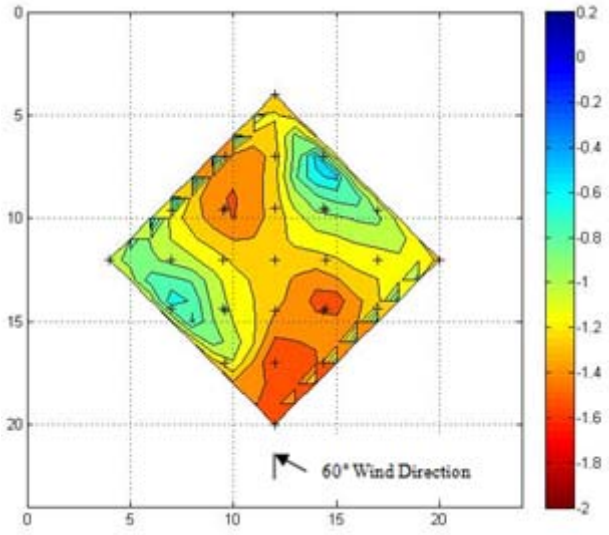


Figure 6.65a - Mean pressure distribution for θ = 60°

(Convex cross vault, 'smooth' BL)

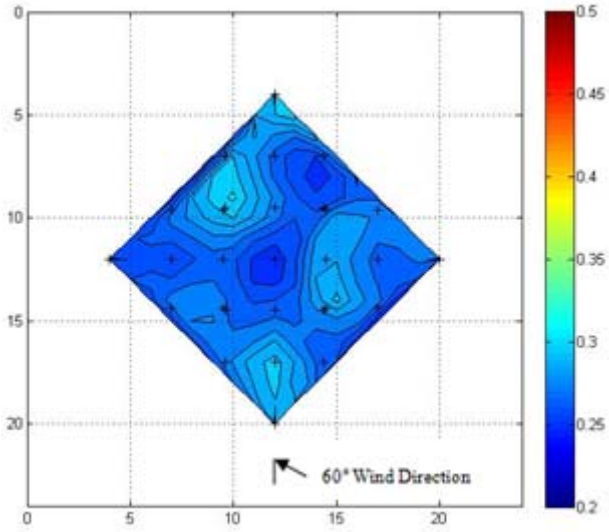


Figure 6.65b - RMS pressure distribution for θ = 60°

(Convex cross vault, 'rough' BL)

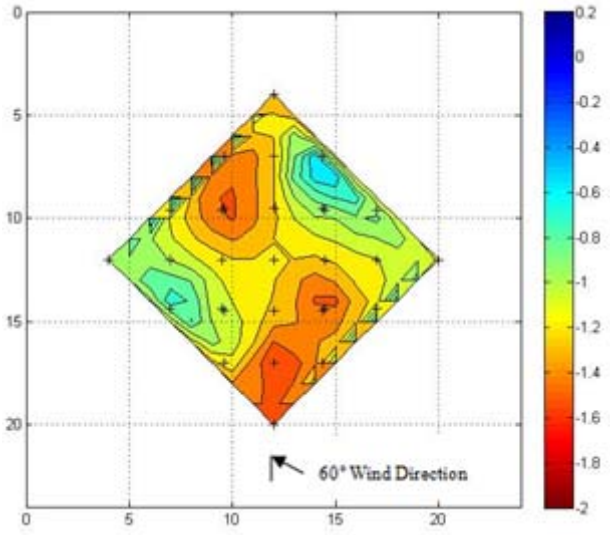


Figure 6.66a - Mean pressure distribution for θ = 60°
(Convex cross vault, 'rough' BL)

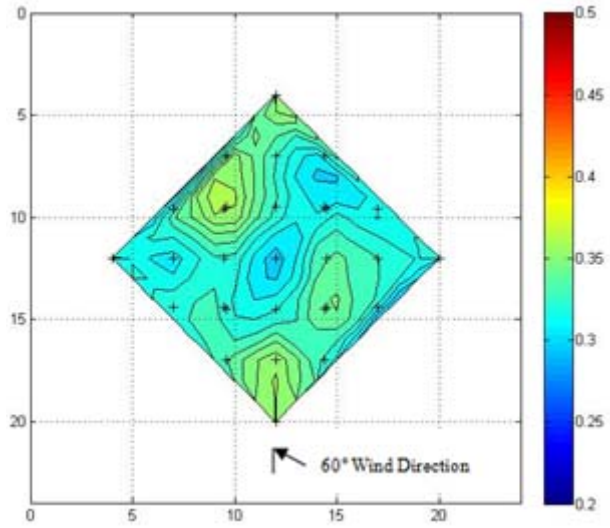


Figure 6.66b - RMS pressure distribution for θ = 60°
(Convex cross vault, 'rough' BL)

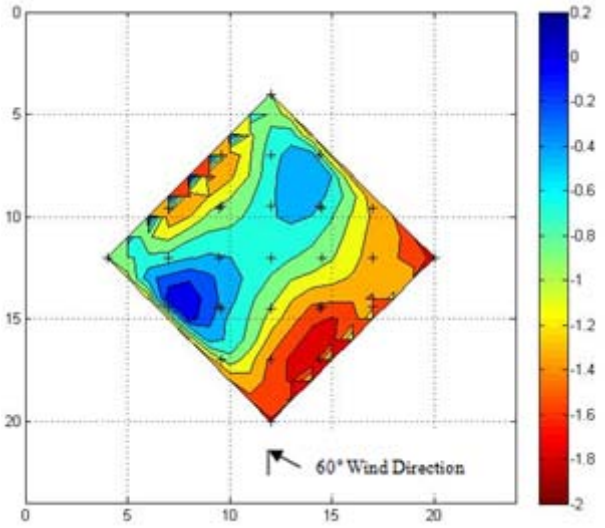


Figure 6.67a - Mean pressure distribution for θ = 60°
(Concave cross vault, 'smooth' BL)

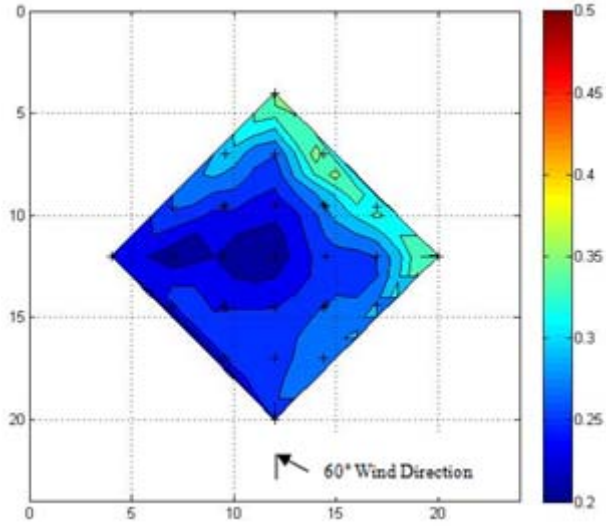


Figure 6.67b - RMS pressure distribution for θ = 60°
(Concave cross vault, 'smooth' BL)

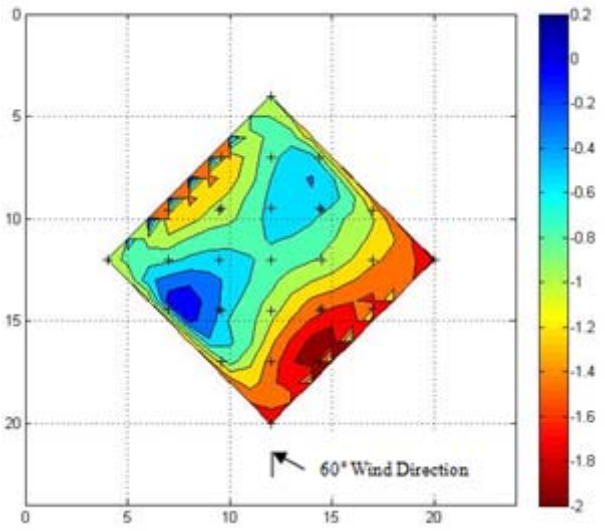


Figure 6.68a - Mean pressure distribution for θ = 60°
(Concave cross vault, 'rough' BL)

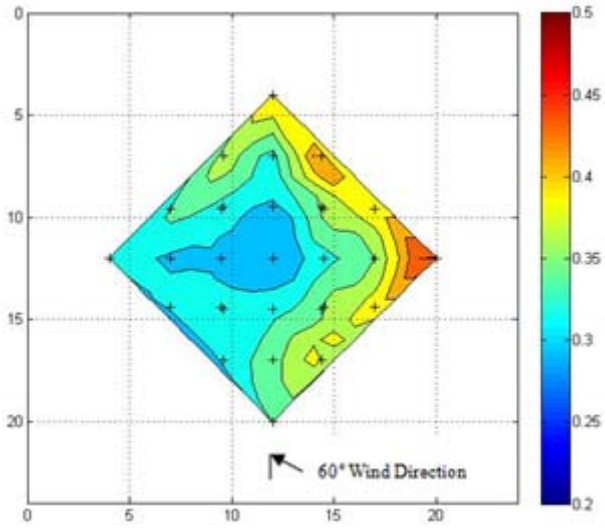


Figure 6.68b - RMS pressure distribution for θ = 60°
(Concave cross vault, 'rough' BL)

6.5 Flow Visualisation

The wind pressure distribution for the 0°, 90° and 180° wind directions are controlled by a strong flow separation at the roof wall interface, as shown in Figure 6.69. Figure 6.69 also indentifies that the flow attempted to re-attach. However, the relatively uniform distribution of the RMS centreline pressure coefficient, shown in Figure 6.70, indicates that the separated shear layer did not reattach over the central region. It is to be noted that re-attachment is believed to have occurred at some position on the vault (with the curvature normal to the flow), as discussed in section 6.2.7.

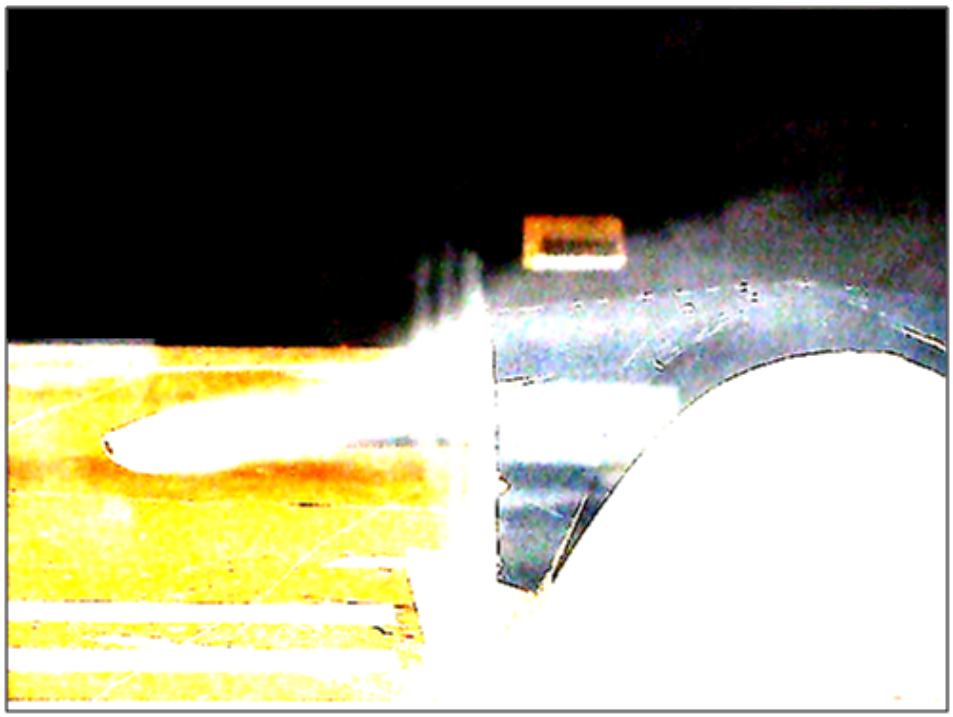


Figure 6.69 - Smoke visualization at roof edge

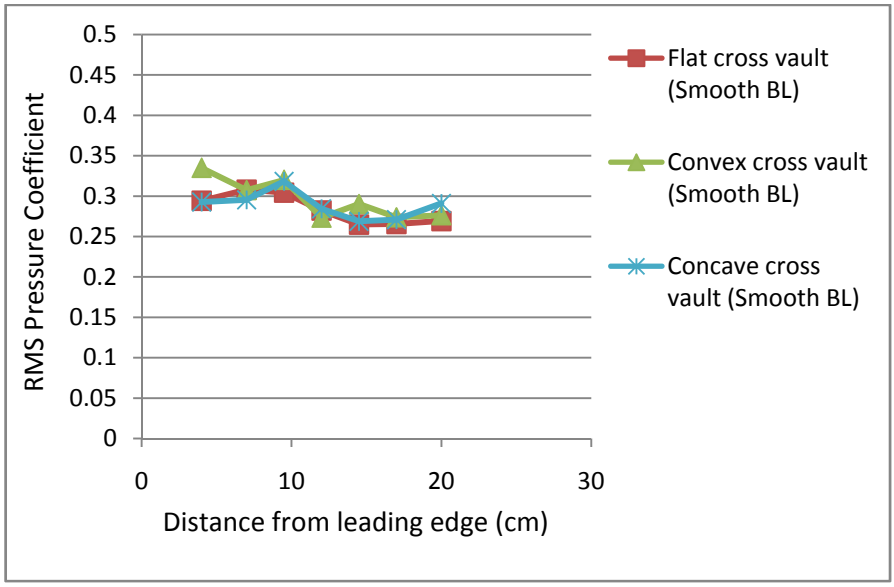


Figure 6.70 - Centreline RMS pressure coefficient distribution for θ = 0° and 180°

Figures 6.71 through 6.73 show the flow directions in front, over and behind the cross vault for the 0° wind direction. The distribution of flow directions observed is similar to that of rectangular bluff bodies. Arrows have been added to Figures 6.71 through 6.73 to clearly illustrate the flow lines and directions.

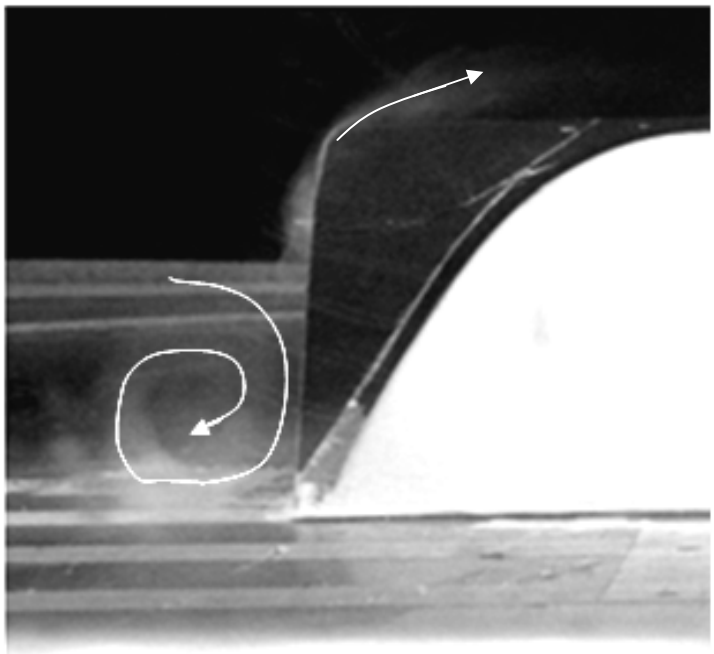


Figure 6.71 - Smoke visualization in front of the flat cross vault

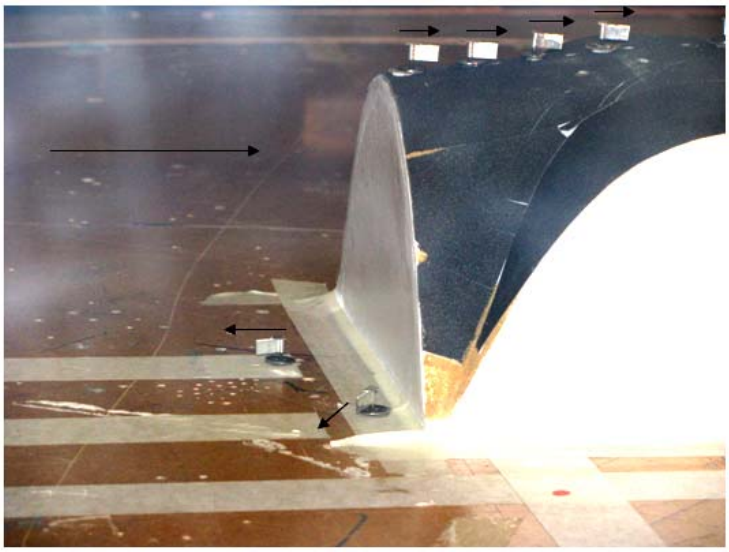


Figure 6.72 - Flow direction devices in front and attached to a model for the 0° wind direction

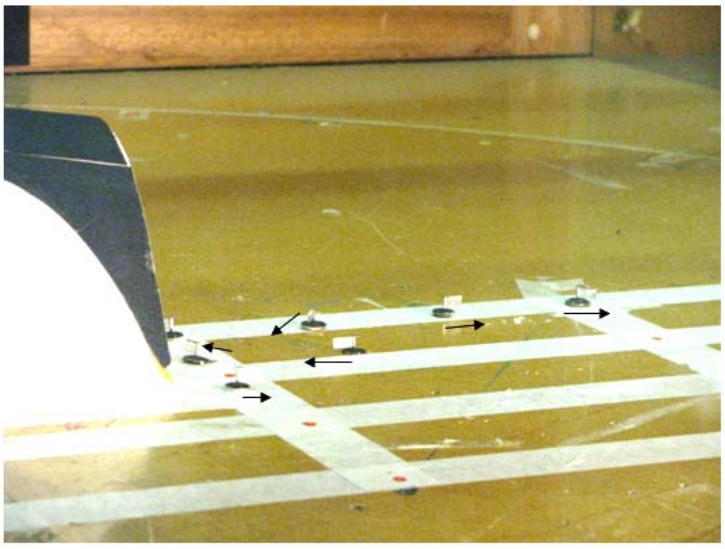


Figure 6.73 - Flow direction devices behind a model for the 0° wind direction

6.6 Conclusions

Three roof geometries were investigated, and the least significant mean and negative peak pressure variations were evident for flow normal to the cross vault wall (i.e. $\theta = 0°$, 90° and 180°). This result is somewhat expected, given that the flow separation was controlled by the wall-roof edge, which is identical for all cross vault types. It is also to be noted that pressure distribution patterns were, generally, similar for all vault types between 30° and 75°; however, the pressure coefficient magnitudes showed visible variation at some tap positions, for certain wind directions.

The most notable trend was that the mean and negative peak pressures closest to the apex (i.e. taps 1 to 4) for the convex cross vault were generally more negative than those over the flat and concave cross vaults. These results reveal increased flow velocity over the convex apex, when compared with the apex pressures (and local wind velocities) for the flat and concave cross vaults.

Substantial mean, RMS and negative pressure coefficient discrepancy, between all vault types, was evident at taps 5 through 8 for the 15° wind direction. At this wind direction, the mean and negative peak pressures were lowest for the concave cross vault and largest for the convex cross vault. This trend is also apparent at the 30° wind direction, but to a lesser extent. These differences are believed to be due to the effects of the roof pitch on the wake.

Mean and negative peak pressure coefficients also showed considerable variation at the 120° and 150° wind directions, which is believed to be due to roof pitch and apex geometry (i.e. flat, convex and concave). Generally, mean and peak pressures were lowest for the convex cross vault, and largest for the concave cross vault. These large mean and peak pressure coefficient variations identify a clear effect of vault geometry on surface pressures at certain wind directions.

7 EFFECTS OF ROOF GEOMETRY: AVERAGED PRESSURES

7.1 General

It was noted in the previous chapter that point pressure coefficients are typically applicable to the design of cladding and fixing of external elements. The measurement of area-averaged pressures is generally undertaken for the design of secondary supporting elements.

Various areas, consisting of 4 pressure taps, were selected to assess the variation of the surface averaged pressure coefficients with wind direction for the flat, convex and concave cross vault forms. Mean and RMS pressure coefficients were also pneumatically averaged, for a selected area comprising taps 2, 3, 5 and 6, to validate those averaged numerically. The manifold used in these investigations was attached to the model in the manner shown in Figure 7.1. The testing was conducted within the 'rough' boundary-layer profile, for the flat cross vault and at selected wind directions ranging from 0° to 180°.

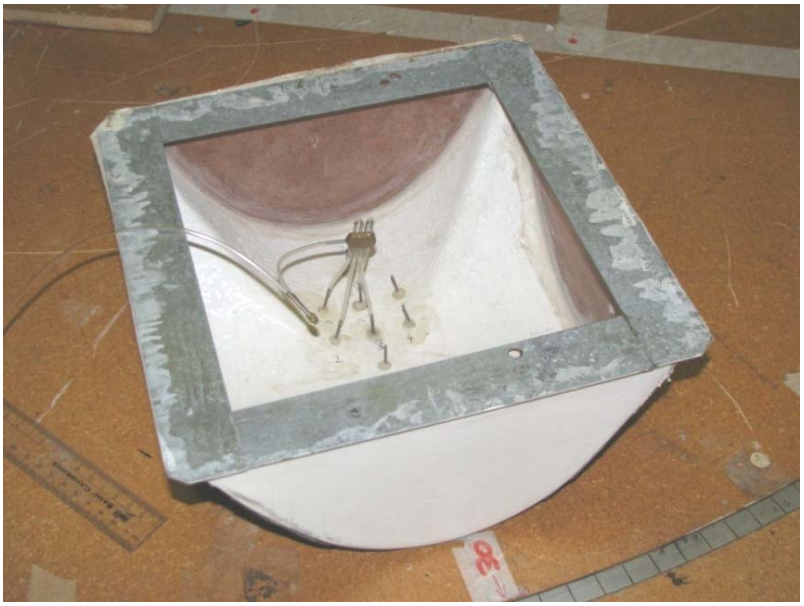


Figure 7.1 - Manifold attached to the flat cross vault

Mean and peak pressures coefficients were averaged by means of the following procedure:

$$Cp_{mean/peak(numerical)} = \sum_{i=1}^{N}(Cp_{mean/peak,i}.A_i)\Big/A_{Total} \quad (6.1)$$

where $Cp_{mean/peak,i}$ is the individual mean/peak pressure coefficient corresponding to tap i, A_i is the area defined for tap i, A_{total} is the total area, i = 1 to 4 and N = 4. This form of numerical averaging is dependent on the assumed influence area assigned to each tap, and variations in these areas may lead to differences in the averaged mean pressure coefficients.

The pneumatically averaged RMS pressure coefficients were evaluated against the numerical pressure coefficients, which were calculated from the square root of the sum of squares of the individual RMS pressure coefficients, as indicated below:

$$Cp_{RMS(numerical)} = \left(\sqrt{\sum_{i=1}^{N} Cp_{RMS,i}^2}\right)/N \quad (6.2)$$

where $Cp_{RMS,i}$ is the individual RMS pressure coefficient corresponding to tap i, for i = 1 to 4 and N = 4. It should be noted that this form of averaging does not account for any correlation of the fluctuating pressures.

The comparison of the numerically and pneumatically averaged mean pressure coefficients is shown in Figure 7.2. The resultant averages are consistent, although the numerically averaged mean pressure coefficients are more negative than those obtained from pneumatic averaging. A large maximum percent difference of approximately 30 % is noted at the 75° wind direction.

Goliger and Milford (1990) compared numerically and pneumatically averaged surface pressures over a hangar, at specific areas and wind directions, within separated turbulent flow. The authors noted very good mean pressure consistency, even though pressures measured at the individual taps varied significantly. It should also be noted that the area assigned to each tap influences the resultant numerical pressure. Goliger and Milford (1990) assigned an equivalent tributary

area to each tap. In the present investigation, the influence area assigned to each tap was identical for taps 3, 5 and 6, whereas tap 2 was assigned a smaller area because of its proximity to the vault intersection. However, when assigning all taps an equivalent area, there is practically no change. The reasoning for the discrepancy observed in Figure 7.2 may, in some part, be due to the area assigned to each tap.

Szepessy and Bearman (1993) analysed a pneumatic pressure averaging device for measuring aerodynamic forces on a circular cylinder. In their investigation, they recorded large mean pressure gradients on the model surface, as well as large gradients of fluctuating pressure, and noted that these can induce internal flow in the tubing and manifold. They also report that once internal flow has been established, within the averaging system, it is evident that the angle between the approaching flow and the surface is essential for achieving accuracy, because it affects the pressure losses at the pressure tap surface connections. The authors believed that using pressure tappings with different angles to the oncoming flow (i.e. on curved elements) causes, in conjunction with large pressure gradients, a misreading in the average pressure. The above mentioned reason may contribute to the observed discrepancy, but more experimental work would be required to draw any conclusions.

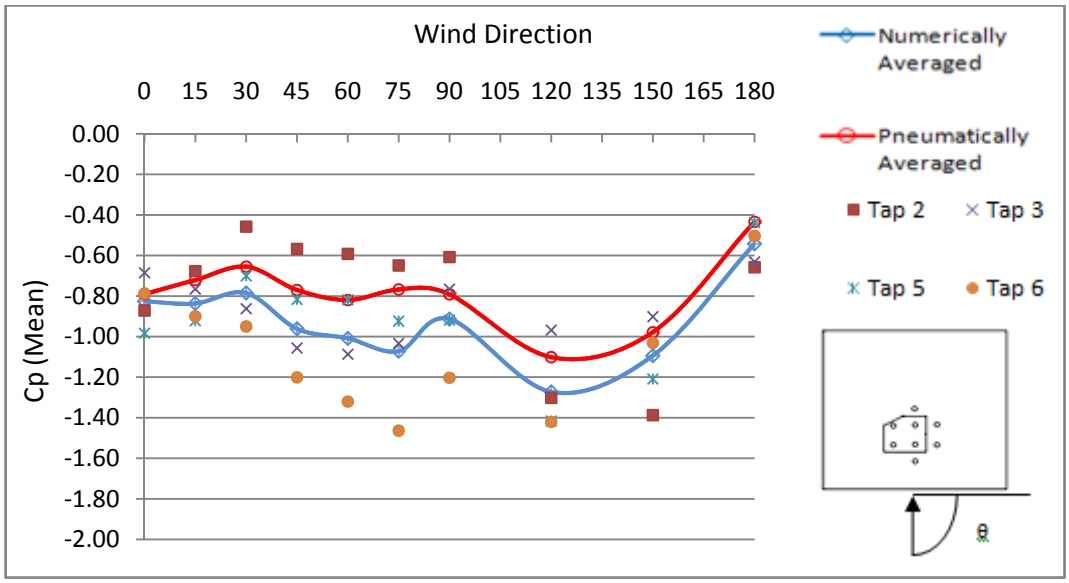


Figure 7.2 - Comparison of mean pressure coefficients (Taps 2, 3, 5 and 6)

The numerically averaged RMS pressure coefficients are lower than the corresponding pneumatically averaged pressure coefficients, as shown in Figure 7.3. Goliger and Milford (1990) note that numerically averaged pressure coefficients are typically lower than the corresponding pneumatically averaged pressure coefficients, because numerical averaging neglects any correlation of the individual pressures. In their study, a maximum difference, between the numerically and pneumatically results, of approximately 55% was observed. For the current investigation, a fairly constant percent difference of around 50%, noted at all wind directions, was measured. However, there is still a reasonable degree of consistency between the numerically and pneumatically averaged results.

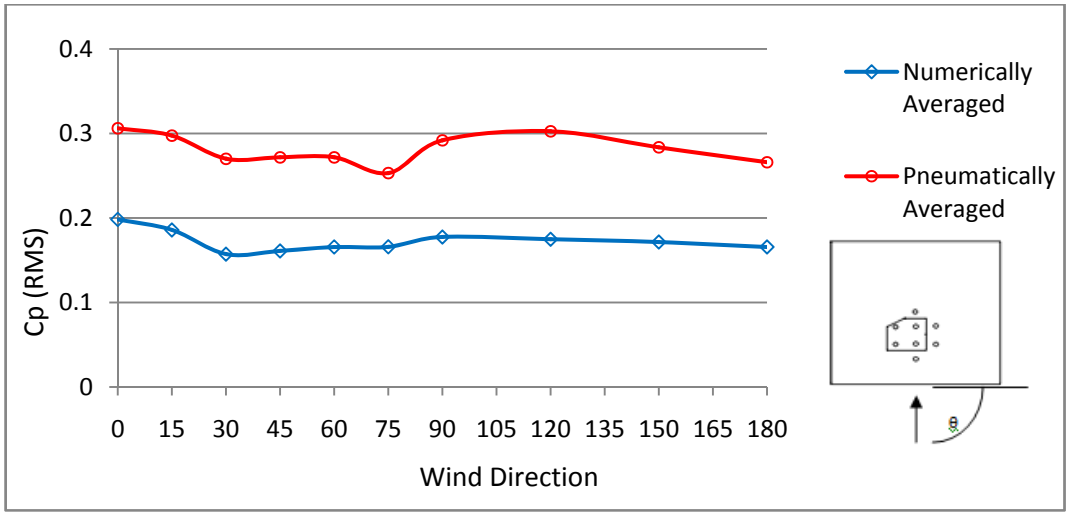


Figure 7.3 - Comparison of RMS pressure coefficients (Area 2)

7.2 Results, Discussion and Conclusions

Four areas, each consisting of four pressure taps, were selected for numerical averaging. These areas, referred to as 'Area 1' (taps: 2, 3, 5 and 6), 'Area 2' (taps: 1, 2, 3 and 4), 'Area 3' (taps: 5, 6, 7 and 8) and 'Area 4' (taps: 3, 4, 6 and 7), are shown in Figure 7.4.

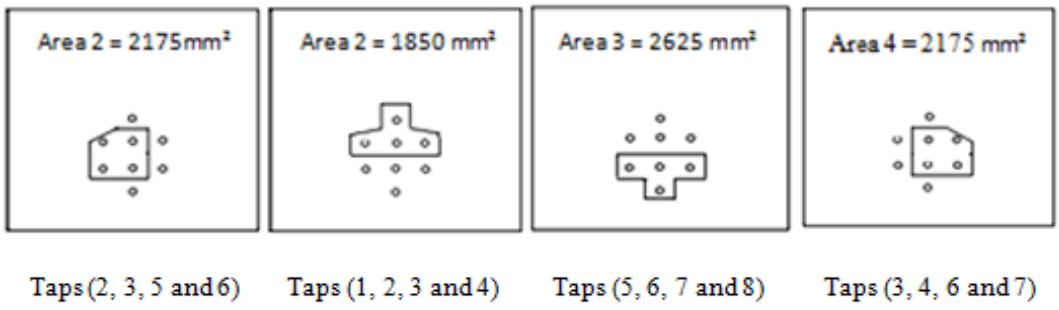


Figure 7.4 - Simple representations of the numerically averaged areas

The pressure coefficients averaged numerically are shown in Figures 7.5a through 7.12c. These results confirm trends corresponding to those noted for the point pressure distributions. The most significant variations are noted below:

1) At the 15° wind direction, the mean, RMS and negative peak averaged pressures, for all vault types, show notable dissimilarity from trends evident at the other wind directions, as shown in Figures 7.5a to 7.12c. These results show significant effects of roof pitch on the wake.
2) As can be seen from Figures 7.9a to 7.10c, the mean, RMS and negative peak area-averaged pressures corresponding to 'Area 3', over the concave cross vault and at the 30° direction, show noticeable variation with trends evident at other wind directions. Generally, RMS pressures are again larger over the concave vault, clearly indicating geometric effects.
3) Mean and negative peak area-averaged pressures over the concave cross vault, at the 120° and 150° wind directions, and within both boundary layer profiles, show considerable variation form pressures over the flat and convex cross vaults. (Refer to Figures 7.5a, 7.5c, 7.6a, 7.6c, 7.7a, 7.7c, 7.8a, 7.8c, 7.9a, 7.9c, 7.10a, 7.10c, 7.11a, 7.11c, 7.12a and 7.12c). This result is believed to be due apex geometry, as discussed in Chapter 6.
4) The mean and negative peak averaged pressures corresponding to 'Area 1' are shown in Figure 7.5a, 7.5c, 7.6a and 7.7c. The flat and convex cross vault pressures illustrate good consistency from 75° through to the 180° wind direction, whereas variations are evident at the 15°, 30°, 45° and 60° wind directions. The reasons for the discrepancies at the 30°, 45° and 60° wind

directions are due to the significantly lower negative pressures at taps 2 and 3 over the convex cross vault. These lower pressures near the apex are believed to be due to the apex shape (i.e. flat, convex and concave), as discussed in Chapter 6.

5) The surface averaged mean and negative peak pressures corresponding to 'Area 2' are shown in Figures 7.7a, 7.7c, 7.8a and 7.8c. The figures show a clear trend, in which the convex and concave cross vaults experience the lowest and largest pressures, respectively. This trend has been discussed in Chapter 6 and is believed to be due to apex geometry.
6) Surface averaged mean and negative peak pressure coefficients corresponding to 'Area 3' are shown in Figure 7.9a, 7.9c, 7.10a and 7.10c. The flat and convex vaults show noticeable variations at the 15° and 75° wind directions. However, similarity is evident at all other wind directions investigated. The disparity at the 15° wind direction has been noted previously, but the discrepancy at the 75° wind direction may be accounted for by the significantly larger pressure recorded at tap 7 on the convex cross vault. Pressure coefficients measured at this tap were visibly larger than those over the flat and concave cross vaults between the 30° and 75° wind orientations.
7) Surface averaged mean and negative peak pressure coefficients corresponding to 'Area 4' are shown in Figure 7.11a, 7.11c, 7.12a, and 7.12c. The concave cross vault shows noticeable variation with the flat and convex cross vaults at the 15°, 30°, 120° and 150° wind directions. Disparity between the convex and flat vaults is also evident at the 75° wind direction, as noted for 'Area 3'. The reasons for the inconsistencies, noted at these wind directions, were discussed in Chapter 6.
8) Generally, the RMS pressures at the 15°, 30° and 90° wind directions, for all areas and over the concave cross vault show visible variation from the other cross vault types (refer to Figures 7.5b, 7.6b, 7.7b, 7.8b, 7.9b, 7.10b, 7.11b and 7.12b). The RMS pressures for the flat and convex cross vaults are practically identical, apart from the 15° wind direction, which was discussed in Chapter 6.

9) Numerically averaged negative peak pressures demonstrate similar distribution patterns to those for the mean pressures. Inconsistencies are evident at some areas and wind directions. Reasons for these inconsistencies have been discussed in Chapter 6.

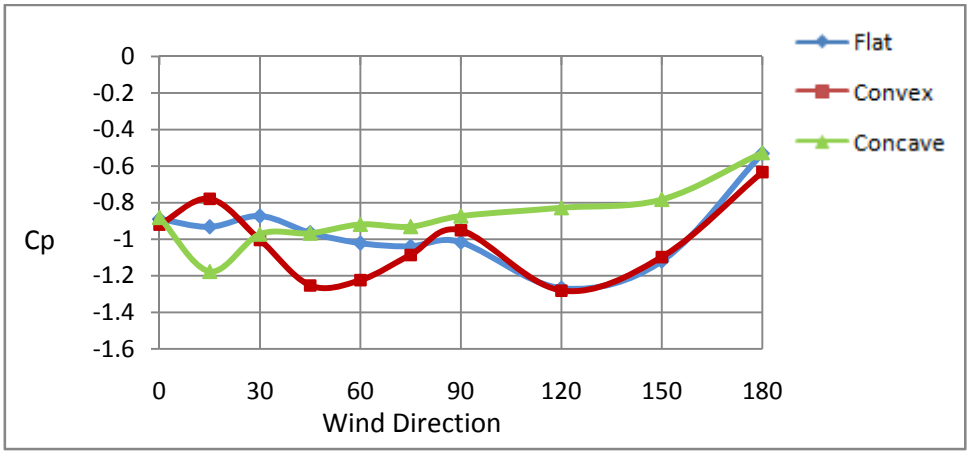


Figure 7.5a - Mean pressure coefficient variation with wind direction [Area 1 (Taps 2, 3, 5 and 6) and ('smooth' BL)]

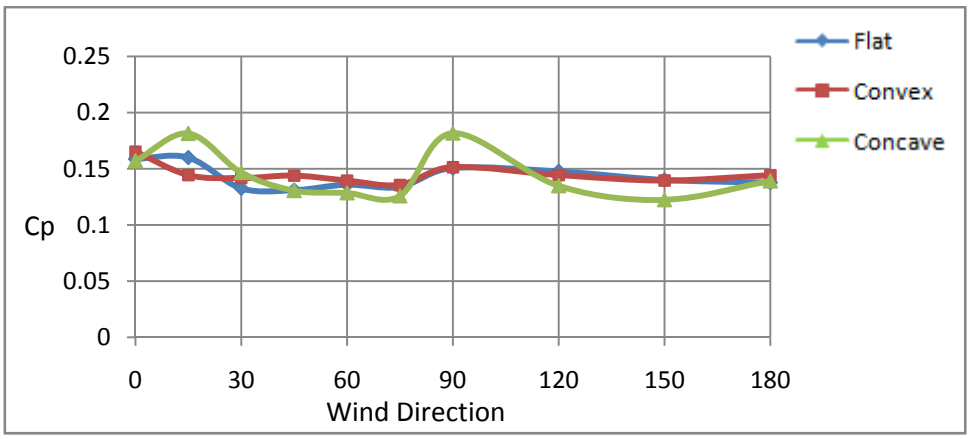


Figure 7.5b - RMS pressure coefficient variation with wind direction [Area 1 (Taps 2, 3, 5 and 6) and ('smooth' BL)]

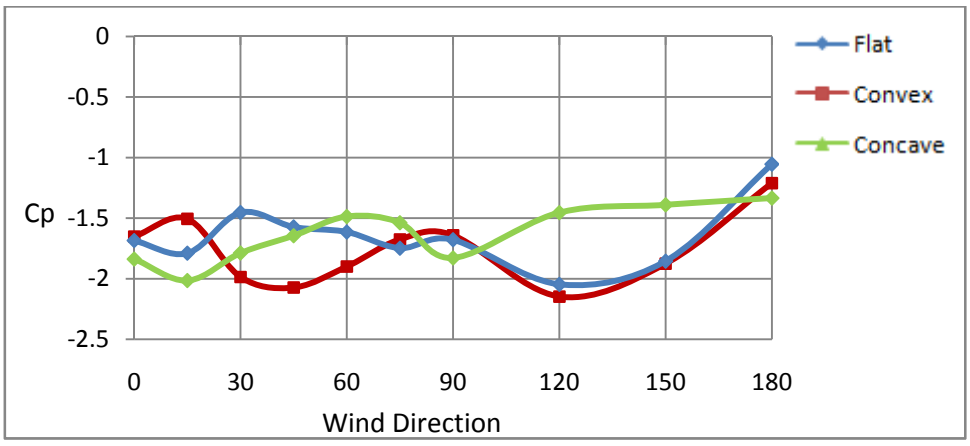


Figure 7.5c - Negative 3s peak pressure coefficient variation with wind direction [Area 1 (Taps 2, 3, 5 and 6) and ('smooth' BL)]

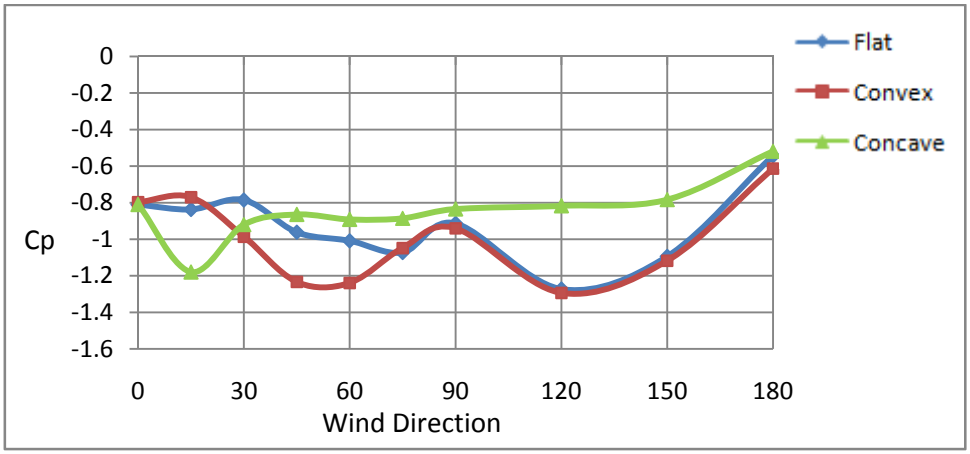


Figure 7.6a - Mean pressure coefficient variation with wind direction [Area 1 (Taps 2, 3, 5 and 6) and ('rough' BL)]

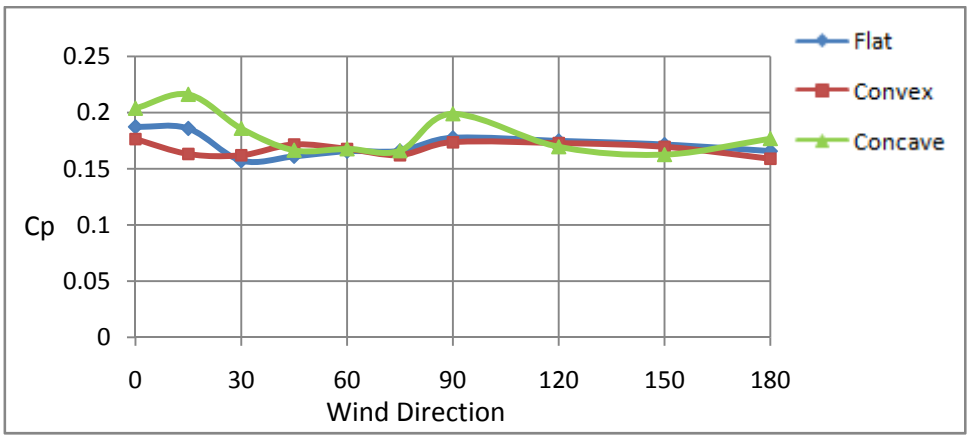


Figure 7.6b - RMS pressure coefficient variation with wind direction [Area 1 (Taps 2, 3, 5 and 6)] and ('rough' BL)]

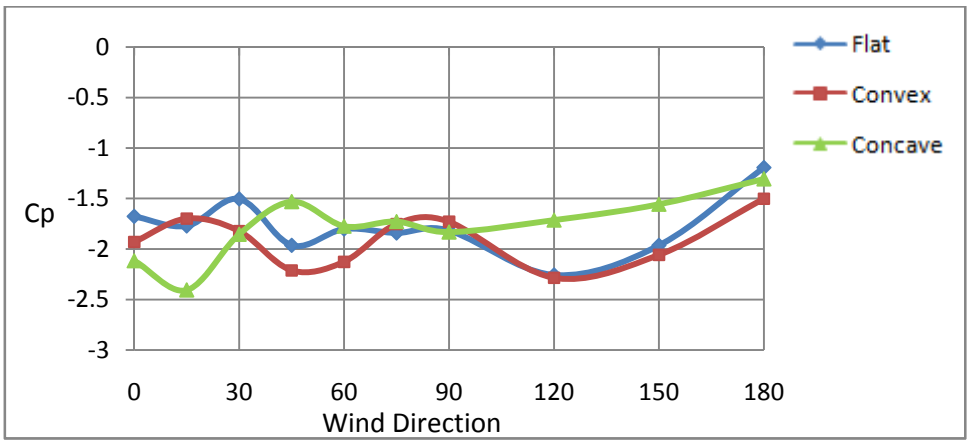


Figure 7.6c - Negative 3s peak pressure coefficient variation with wind direction [Area 1 (Taps 2, 3, 5 and 6) and ('rough' BL)]

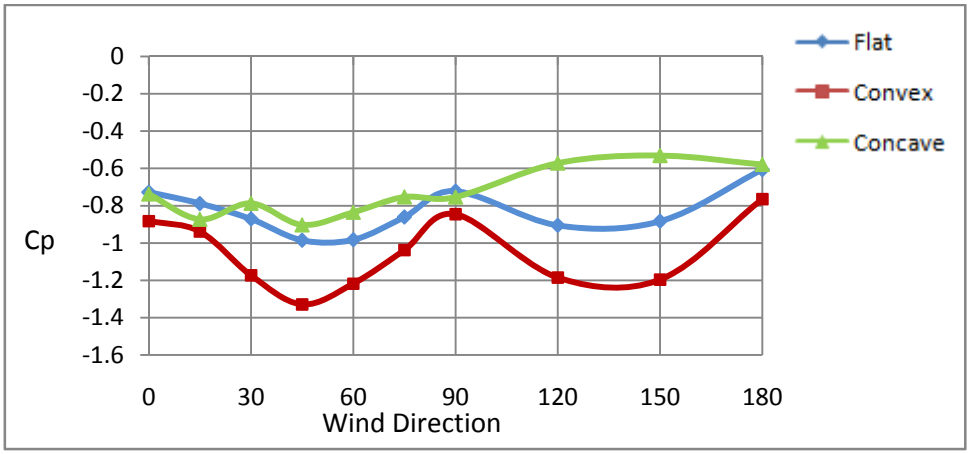


Figure 7.7a - Mean pressure coefficient variation with wind direction [Area 2 (Taps 1, 2, 3 and 4) and ('smooth' BL)]

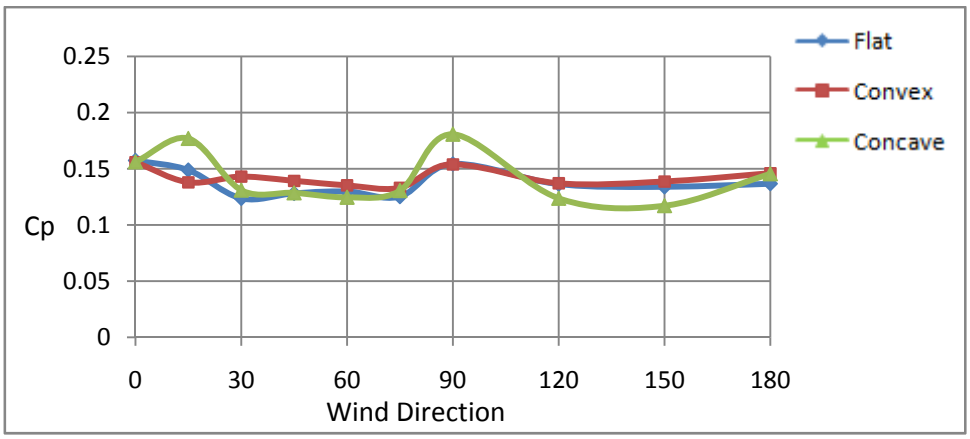


Figure 7.7b - RMS pressure coefficient variation with wind direction [Area 2 (Taps 1, 2, 3 and 4) and ('smooth' BL)]

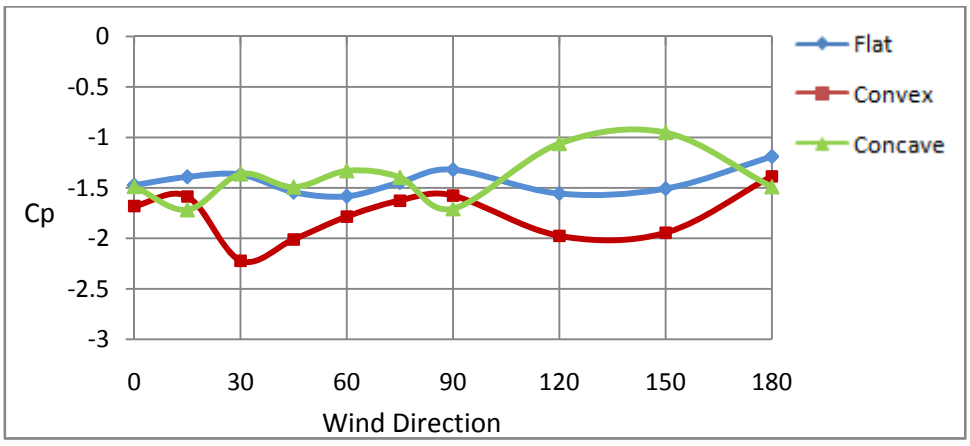


Figure 7.7c - Negative 3s peak pressure coefficient variation with wind direction [Area 2 (Taps 1, 2, 3 and 4) and ('smooth' BL)]

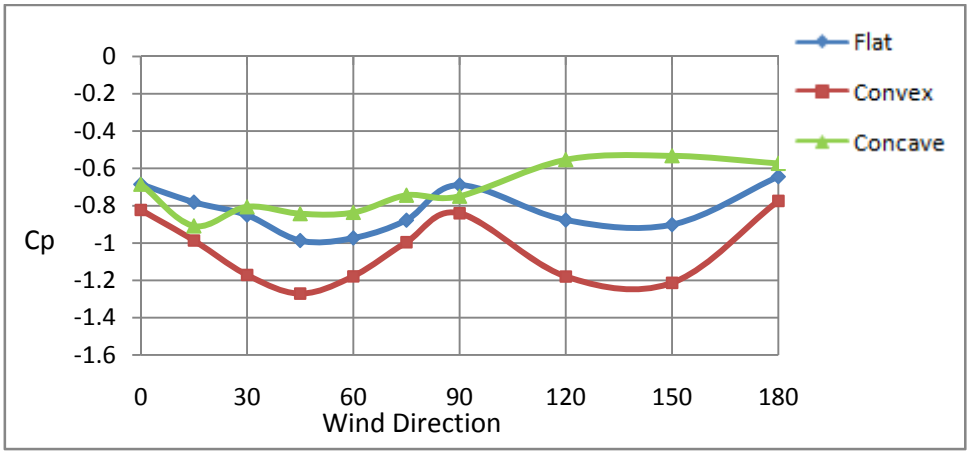


Figure 7.8a - Mean pressure coefficient variation with wind direction [Area 2 (Taps 1, 2, 3 and 4) and ('rough' BL)]

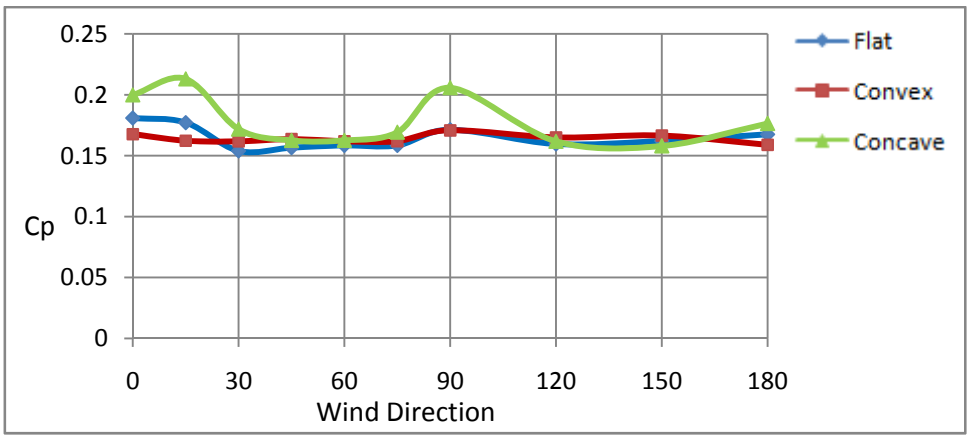


Figure 7.8b - RMS pressure coefficient variation with wind direction [Area 2 (Taps 1, 2, 3 and 4) and ('rough' BL)]

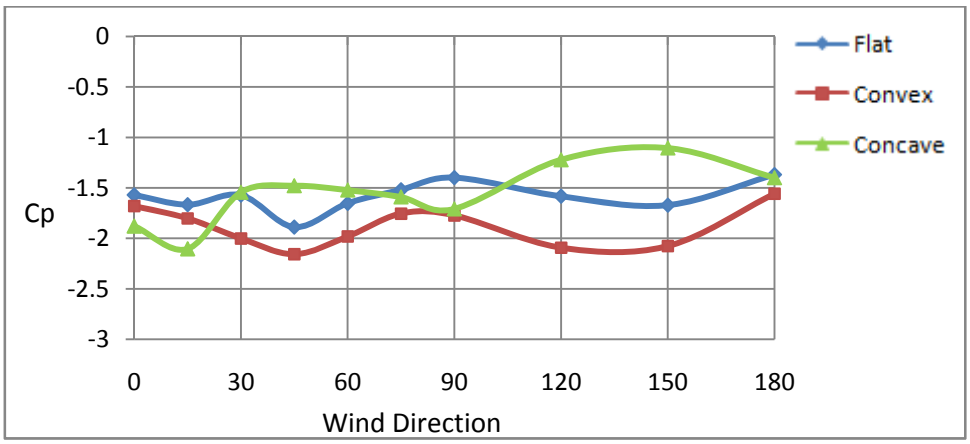


Figure 7.8c - Negative 3s peak pressure coefficient variation with wind direction [Area 2 (Taps 1, 2, 3 and 4) and ('rough' BL)]

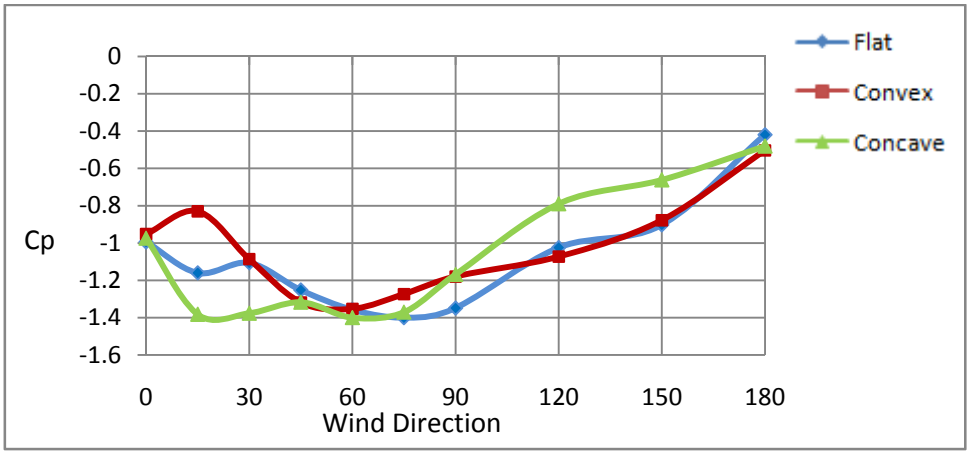


Figure 7.9a - Mean pressure coefficient variation with wind direction [Area 3 (Taps 5, 6, 7 and 8) and ('smooth' BL)]

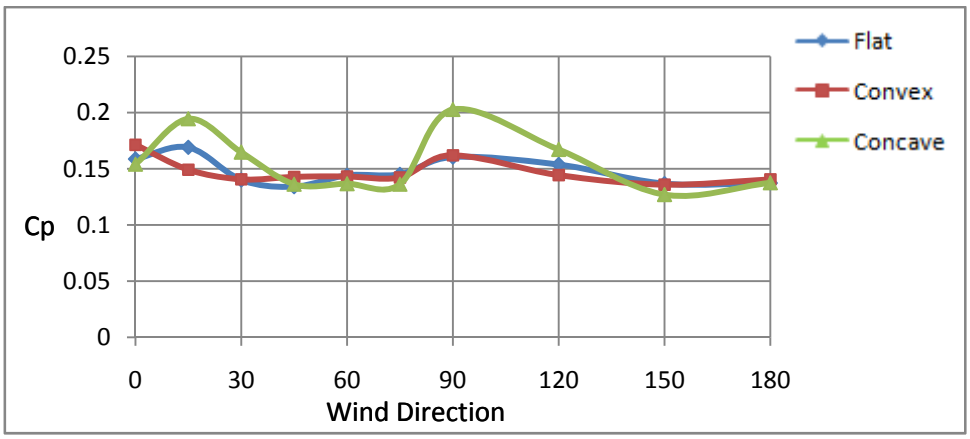


Figure 7.9b - RMS pressure coefficient variation with wind direction [Area 3 (Taps 5, 6, 7 and 8) and ('smooth' BL)]

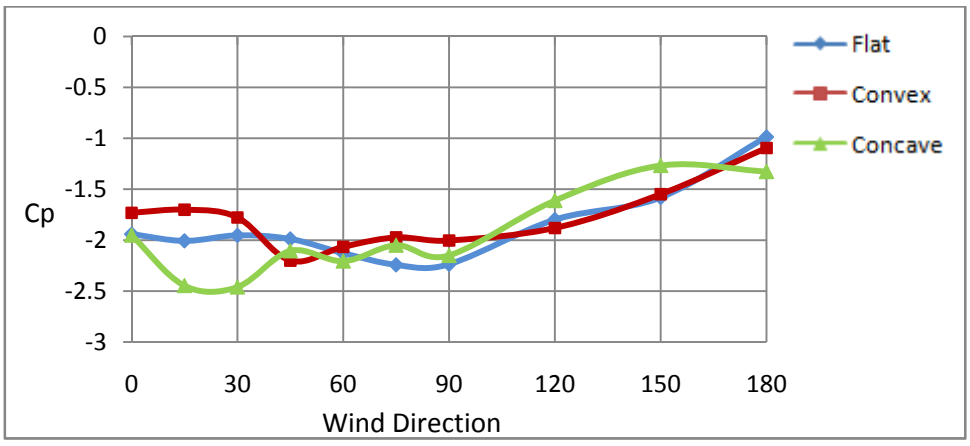


Figure 7.9c - Negative 3s peak pressure coefficient variation with wind direction [Area 3 (Taps 5, 6, 7 and 8) and ('smooth' BL)]

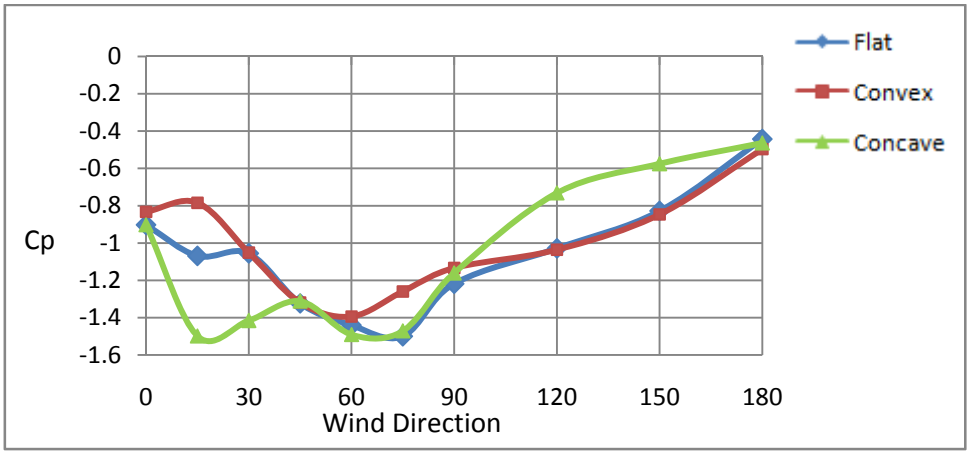


Figure 7.10a - Mean pressure coefficient variation with wind direction [Area 3 (Taps 5, 6, 7 and 8) and ('rough' BL)]

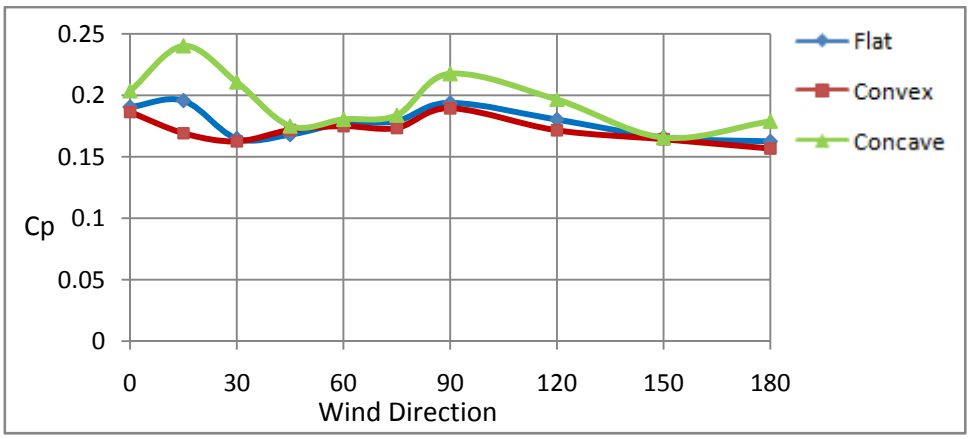


Figure 7.10b - RMS pressure coefficient variation with wind direction [Area 3 (Taps 5, 6, 7 and 8) and ('rough' BL)]

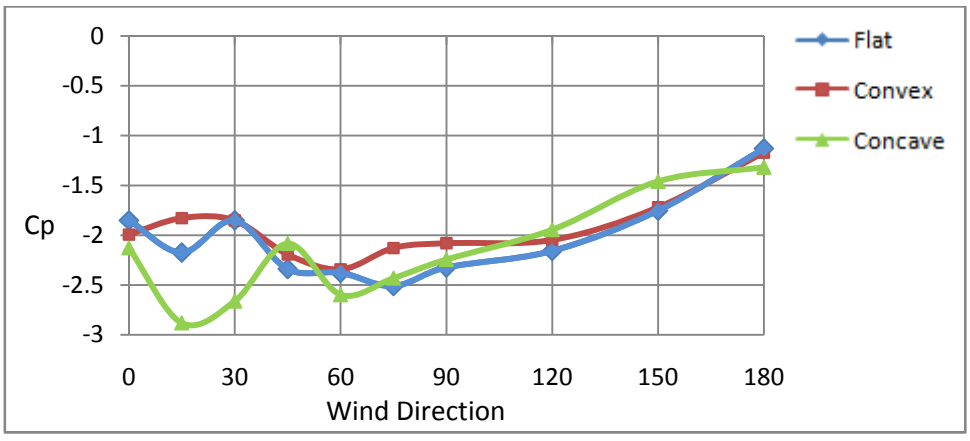


Figure 7.10c - Negative 3s peak pressure coefficient variation with wind direction [Area 3 (Taps 5, 6, 7 and 8) and 'rough' BL)]

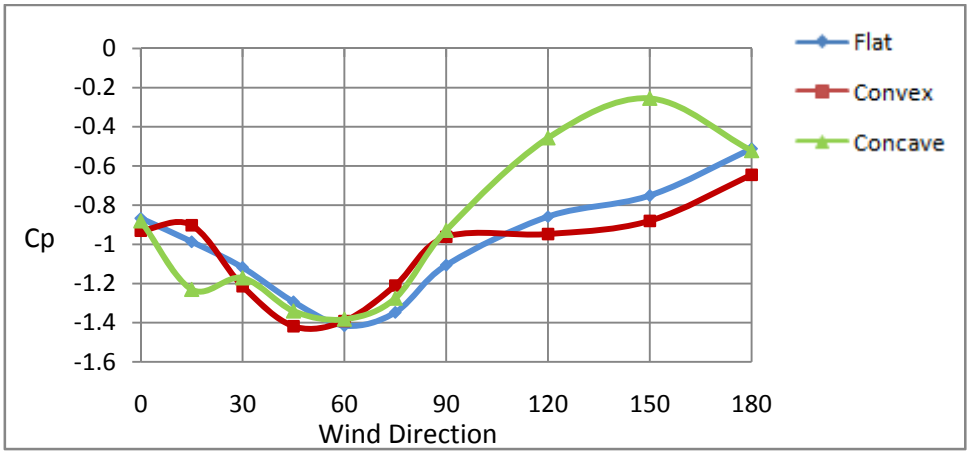


Figure 7.11a - Mean pressure coefficient variation with wind direction [Area 4 (Taps 3, 4, 6 and 7) and ('smooth' BL)]

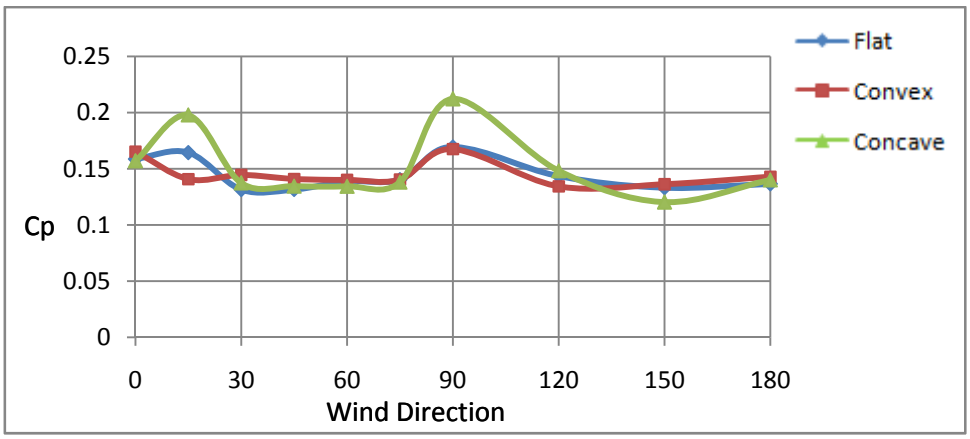


Figure 7.11b - RMS pressure coefficient variation with wind direction [Area 4 (Taps 3, 4, 6 and 7) and ('smooth' BL)]

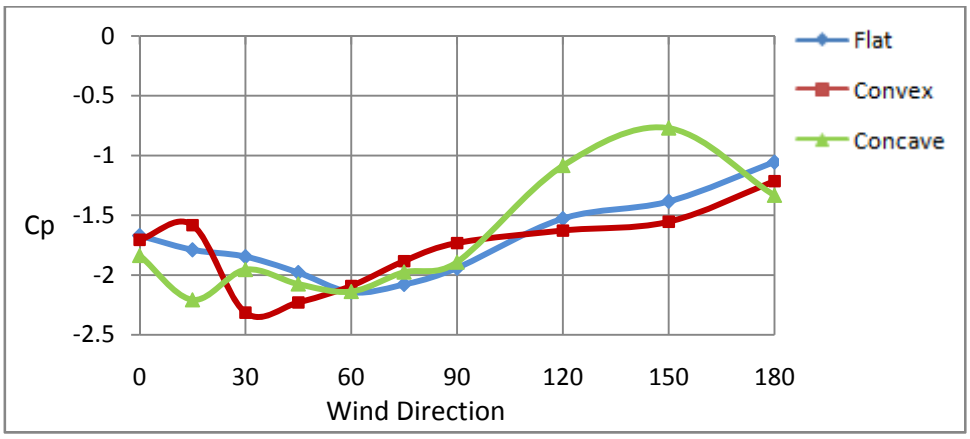


Figure 7.11c - Negative 3s peak pressure coefficient variation with wind direction [Area 4 (Taps 3, 4, 6 and 7) and ('smooth' BL)]

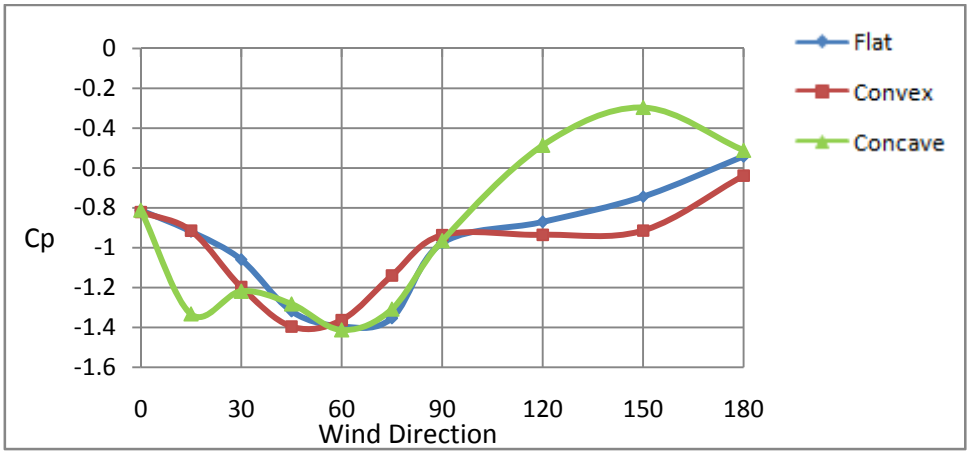


Figure 7.12a - Mean pressure coefficient variation with wind direction [Area 4 (Taps 3, 4, 6 and 7) and ('rough' BL)]

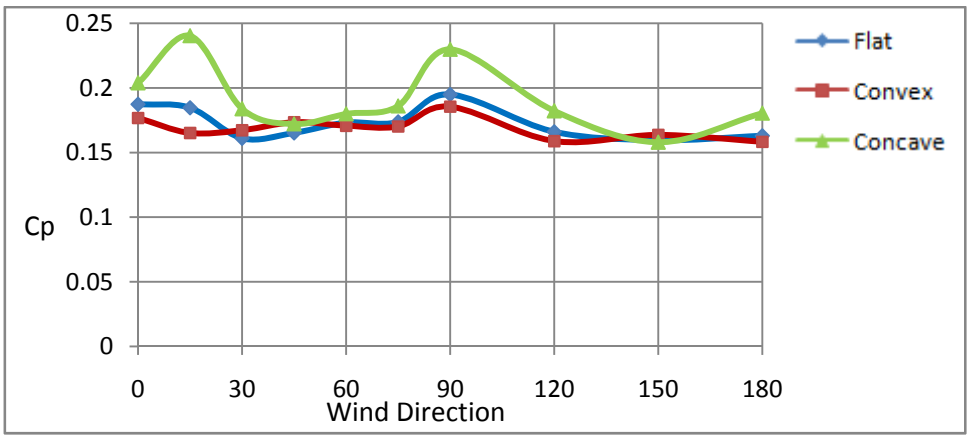


Figure 7.12b - RMS pressure coefficient variation with wind direction [Area 4 (Taps 3, 4, 6 and 7) and ('rough' BL)]

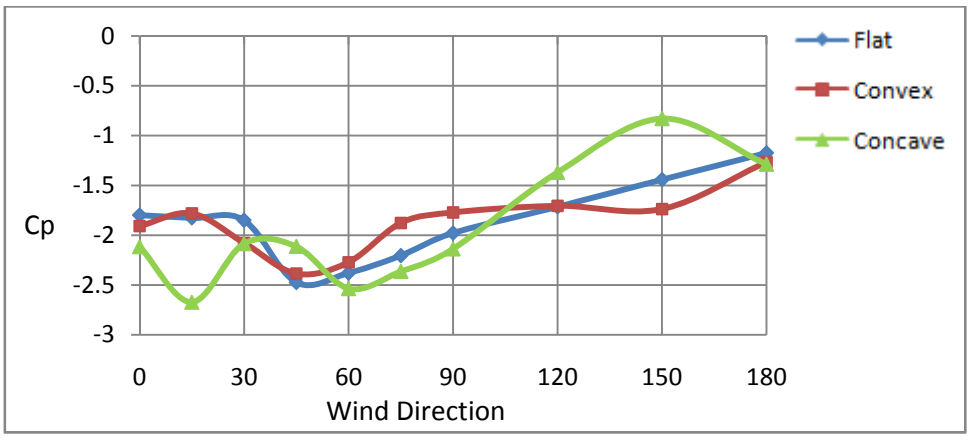


Figure 7.12c - Negative 3s peak pressure coefficient variation with wind direction [Area 4 (Taps 3, 4, 6 and 7) and 'rough' BL)]

8 COMPARASION OF EXPERIMENTAL RESULTS WITH CODIFIED DATA USED FOR THE DESIGN OF SINGLE VAULT STRUCTURES

8.1 Introduction

Wind loading generated on large roofs can be significant in terms of the overall uplift for the design of the support structure, as well as the local peak pressures affecting the design of cladding and its fixing. Design data obtained from wind-tunnel testing is generally incorporated into structural loading codes by means of the mean pressure coefficients combined with peak wind speed profiles stipulated in the respective code. In this chapter, mean and negative peak pressures at central locations are identified for design purposes, and mean pressure coefficients for the flat cross vault are compared with the design information referring to single vault structures.

The design of roof elements and cladding which are susceptible to local wind actions is vital for both economic and safety issues. Scanlan and Simiu (1978) note that roof components, such as fasteners and cladding, are susceptible to local wind action. However, these components are usually rigid, so the dynamic effects are negligible, and are ignored. Of major concern for large low pitched roofs are local suctions, which cause cladding to fail at fasteners. Various cases of cladding damage have been observed and Cook (1985) indicates that cladding is often peeled away from the supporting structure, leaving the roof structure intact. Cladding damage observed on a large cross vault structure is shown in Figure 8.1. The damage is near the roof-wall interface, which generally experiences the most severe loading conditions.



Figure 8.1- Local cladding damage observed on the Good Hope Centre

8.2 Minimum Pressure Coefficients at Central Locations over Cross Vault Structures

It must be noted that generally 2° to 3° wind direction increments are investigated to determine maximum pressures and critical wind directions. However, 15° to 30° increments were used in these investigations. For the above mentioned reason, peaks may occur at directions not investigated, but trends indicate wind direction ranges where peaks are expected (Refer to appendix C).

The lowest (most negative) mean, negative 3s and 10s peak pressure coefficients for each tap and vault type, between θ = 0° and θ = 180°, are shown in Tables 8.1 and 8.2. It should also be noted that minimum pressure coefficients occur at varied wind directions for the three cross vault types. Minimum point and averaged mean pressure coefficients, for all vault types and boundary-layer profiles, are also presented in Figures 8.2 to 8.4, and Table 8.3, respectively. Negative 3s peak pressure coefficients, appropriate to the design of cladding and their fixings, are included in Figures 8.2 to 8.4.

The critical minimum mean pressure coefficients for the convex, flat and concave cross vaults were Cp_{mean} = -1.6, Cp_{mean} = -1.8, Cp_{mean} = -2.0 , respectively. A clear trend is evident in Figures 8.2 and 8.3, in which mean pressures decrease, as the

distance for the centre of the cross vault increases. For this reason, lower mean pressures than those acquired in this investigation could be expected further from the apex, most notably near the edge. The minimum area-averaged pressures over large areas of the roof, shown in Table 8.3, are by and large similar in magnitude for all vault types, with minimum Cp_{av} between -1.4 and -1.5.

The lowest negative peak pressure coefficients were experienced over the concave cross vault. Negative peak pressures coefficients of the order of Cp_{peak} = -3.1 and Cp_{peak} = -3.6 for the respective profiles of increasing turbulence intensity were acquired. As shown in Figures 8.2 and 8.3, the negative peak pressures for the other cross vaults, for both boundary-layer profiles, are somewhat smaller than those corresponding to the concave cross vault.

Table 8.1 - Lowest measured mean, 10s and 3s peak pressure coefficients ('smooth' boundary-layer)

	Flat Cross Vault		**Convex Cross Vault**		**Concave Cross Vault**	
Tap	Direction	Mean C*p*	Direction	Mean C*p*	Direction	Mean C*p*
1	45	-0.95	45	-1.30	45	-0.76
2	150	-1.41	120	-1.45	15	-0.94
3	60	-1.12	45	-1.37	45	-0.97
4	60	-1.39	45	-1.60	45	-1.55
5	120	-1.41	120	-1.33	120	-1.43
6	75	-1.43	60	-1.52	15	-1.51
7	60	-1.80	45	-1.42	60	-1.82
8	90	-1.63	90	-1.60	30	-1.64

	Flat Cross Vault		**Convex Cross Vault**		**Concave Cross Vault**	
Tap	Direction	10s Peak	Direction	10s Peak	Direction	10s Peak
1	120	-1.37	120	-1.77	90	-1.38
2	120	-2.00	120	-2.25	15	-1.55
3	60	-1.61	120	-1.82	15	-1.83
4	60	-1.94	30	-2.23	60	-2.23
5	150	-2.04	120	-2.14	120	-2.16
6	90	-2.04	60	-2.35	0	-2.28
7	60	-2.76	45	-1.99	60	-2.66
8	60	-2.36	90	-2.57	30	-2.78

	Flat Cross Vault		**Convex Cross Vault**		**Concave Cross Vault**	
Tap	Direction	3s Peak	Direction	3s Peak	Direction	3s Peak
1	60	-1.52	45	-2.00	90	-1.73
2	120	-2.28	150	-2.49	15	-1.87
3	60	-1.69	120	-2.14	90	-1.74
4	60	-2.00	30	-2.59	60	-2.31
5	120	-2.25	120	-2.31	120	-2.38
6	90	-2.31	45	-2.55	15	-2.53
7	60	-2.87	45	-2.09	60	-2.90
8	60	-2.59	90	-2.55	30	-3.06

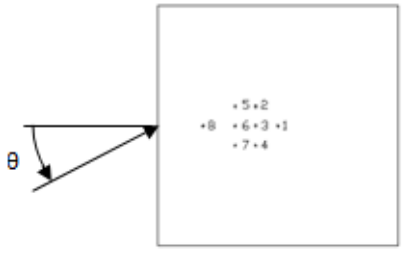
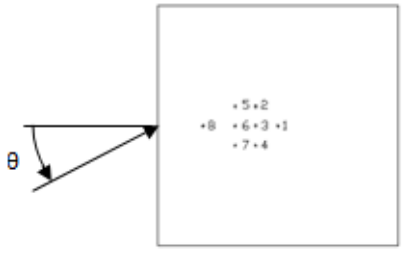


Table 8.2 - Lowest measured mean, 10s and 3s peak pressure coefficients ('rough' boundary-layer)

	Flat Cross Vault		**Convex Cross Vault**		**Concave Cross Vault**	
Tap	Direction	Mean C*p*	Direction	Mean C*p*	Direction	Mean C*p*
1	45	-0.94	150	-1.22	45	-0.70
2	150	-1.39	120	-1.49	15	-1.03
3	60	-1.09	45	-1.33	15	-0.96
4	45	-1.36	45	-1.63	45	-1.47
5	120	-1.42	120	-1.38	120	-1.33
6	75	-1.47	60	-1.55	15	-1.51
7	60	-1.80	45	-1.31	60	-2.00
8	75	-1.63	90	-1.56	30	-1.71

	Flat Cross Vault		**Convex Cross Vault**		**Concave Cross Vault**	
Tap	Direction	10s Peak	Direction	10s Peak	Direction	10s Peak
1	15	-1.80	120	-1.91	15	-1.59
2	150	-2.13	120	-2.68	15	-1.88
3	60	-1.68	45	-2.11	15	-2.10
4	30	-2.07	15	-2.54	15	-2.46
5	120	-2.26	120	-2.30	120	-2.27
6	120	-2.36	120	-2.41	15	-2.54
7	60	-2.79	45	-2.00	60	-3.10
8	75	-2.78	90	-2.55	30	-3.13

	Flat Cross Vault		**Convex Cross Vault**		**Concave Cross Vault**	
Tap	Direction	3s Peak	Direction	3s Peak	Direction	3s Peak
1	15	-1.67	120	-2.00	15	-1.57
2	150	-2.37	120	-2.84	15	-2.33
3	60	-1.78	45	-2.47	15	-2.38
4	60	-2.39	15	-2.70	60	-2.49
5	120	-2.61	120	-2.37	120	-2.62
6	120	-2.53	120	-2.69	60	-2.76
7	45	-3.01	60	-2.16	60	-3.29
8	75	-3.03	90	-2.76	30	-3.57



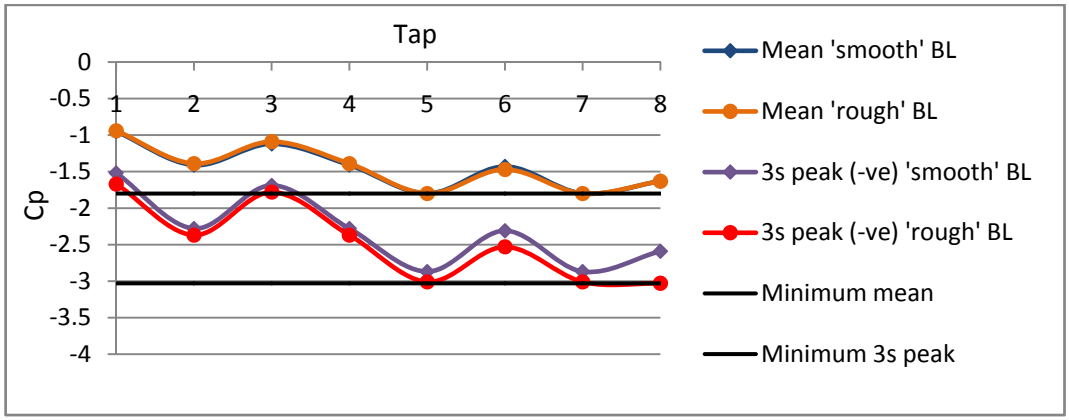


Figure 8.2 - Design coefficients at central locations for the flat roof for any wind direction

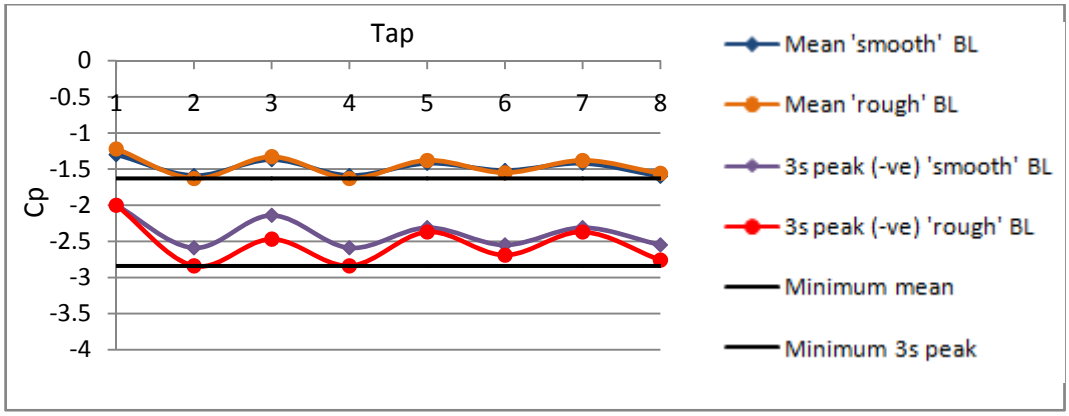


Figure 8.3 - Design coefficients at central locations for the convex roof for any wind direction

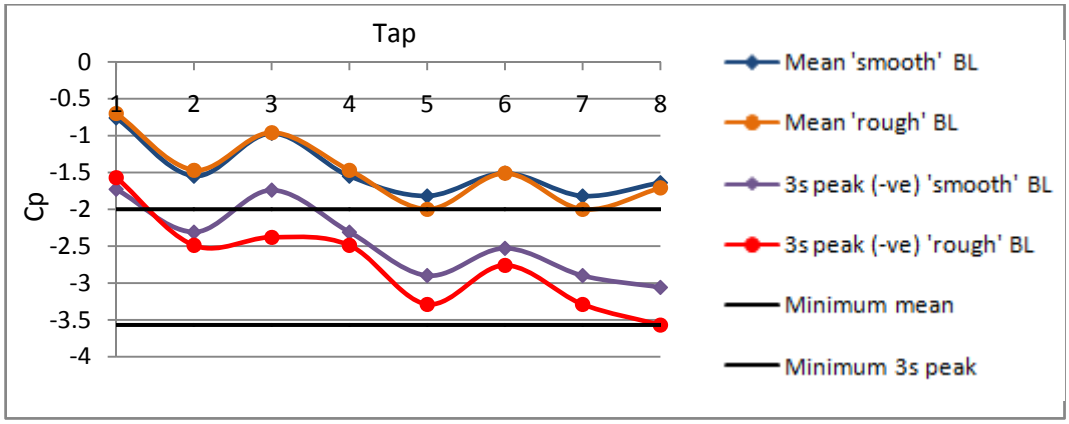


Figure 8.4 - Design coefficients at central locations for the concave roof for any wind direction

Table 8.3 - Area-averaged design coefficients for any wind direction

Boundary-layer profile	Model type	Cp_{av}			
		area 1	area 2	area 3	area 4
'smooth' boundary-layer	flat	-1.3	-1.0	-1.4	-1.4
	convex	-1.3	-1.3	-1.4	-1.4
	concave	-1.2	-0.9	-1.4	-1.4
'rough' boundary-layer	flat	-1.3	-1.0	-1.5	-1.4
	convex	-1.3	-1.3	-1.4	-1.4
	concave	-1.2	-0.9	-1.5	-1.4

* area 1 - taps 2, 3,5 and , area 2 - taps 1, 2,3 and 4, area 3 - taps 5, 6, 7 and 8, area 4 - taps 3, 4, 6 and 7

8.3 Design Data for Arched Roof Structures

In this section, the EN 1991-1-4 codified data and experimental results provided by Toy and Tahouri (1988), Blackmore and Tsokri (2006) and Paluch et al (2003) are compared with selected results from the current experimental point and area-averaged pressures, for winds normal and parallel to the roof eaves. These wind directions are identified as the critical orientations for single vaults.

8.3.1 Wind normal to curvature

It must be noted, that for the θ = 90° wind direction (as shown in Figure 8.5), the position of separation for a single vault is controlled entirely by Reynolds number, surface roughness and turbulence characteristics, whereas separation for the cross vault is heavily influenced by the roof - wall edge. However, it is apparent that flow re-attached at some positions on the vault, with curvature normal to the flow, as discussed in Chapter 6. This re-attached flow was identified by the low pressure coefficient measured at tap 8, which is furthest from the apex, as shown in Tables 8.1 and 8.2.

Figure 8.5 shows the EN 1991-1-4 Cpe_{10} pressure coefficient distribution for single vaults with f/d = 0.5, where f is the height and d is the diameter of the vault.

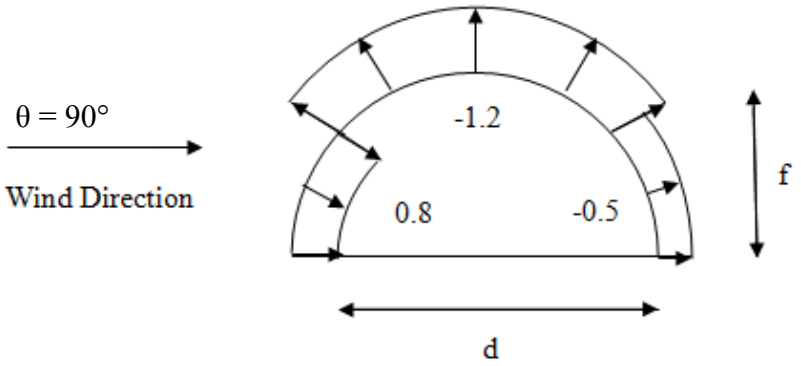
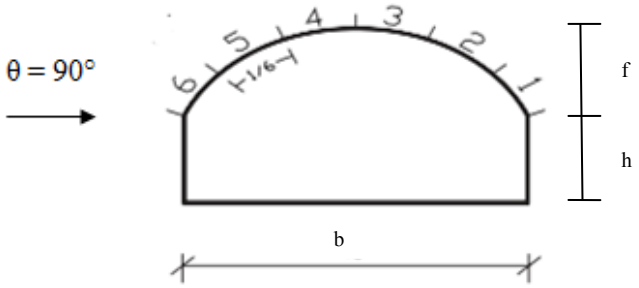


Figure 8.5 - EN 1991-1-4 Cpe_{10} distribution

Area-averaged design coefficient distributions were produced by Paluch et al. (2003) for various arched-roofs situated on a rectangular base within a simulated sub-urban boundary-layer. Design values for one model, with f/b =0.3 and h/b = 0.12, are shown in Figure 8.6



Area	1	2	3	4	5	6
Cp_{av}	-0.6	-0.3	-0.5	-1.0	-0.6	0.3

Figure 8.6 - Mean design pressure coefficients for arch-roof building
(Reproduced from Paluch et al (2003))

Toy and Tahouri (1988) conducted tests on 3-dimesional semi-cylindrical models with different shapes, length/height (L/f) and height/diameter (f/d) ratios. Figure 8.7 is reproduced from their research, for a semi-cylinder with L/f = 2 and f/d = 0.5, and reveals near constant mean pressure coefficient contours along lines parallel to the major axis.

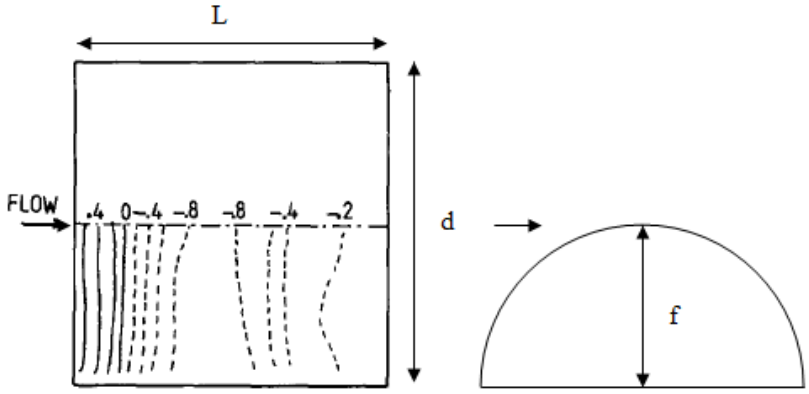


Figure 8.7 - Surface point pressure distribution for a single circular vault (Reproduced from Toy and Tahouri (1988))

Figure 8.8 compares the point pressure coefficients located near the barrel apex, at a wind direction of 90°, for the current experiment and literature noted previously. Figure 8.8 reveals that mean pressures vary considerably along lines parallel to the major axis for the cross vault, whereas a constant pressure coefficient is given for a single vault, which emphasizes the effect of the intersecting vault on the pressure coefficients. In fact, flow over a single vault is attached in this region, whereas near the vault apex, the flow is separated. However, it is believed that flow at tap 8 is attached. These comparisons show that simple curved roof design data, for the 90° wind direction, is not applicable for the design of cross vault structures.

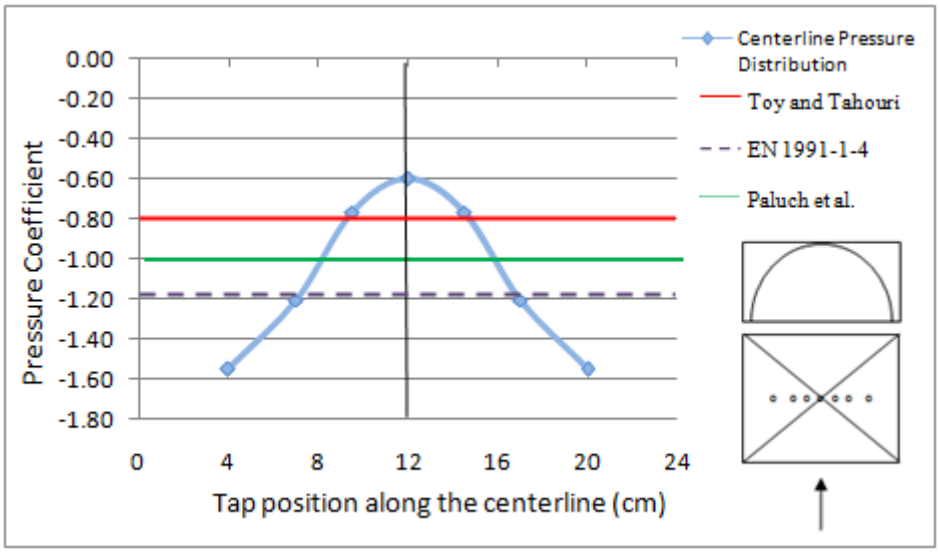
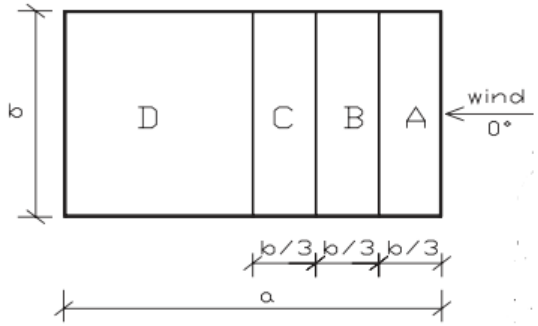


Figure 8.8 - Mean point pressures coefficients for θ=90°

8.3.2 Wind normal to the arch

The design coefficients for the wind direction normal to the arch are not included in many codes of practice. However, experimental work is applicable. Figure 8.9, reproduced from Paluch et al (2003), shows the design data applicable to a single vault. Figure 8.10, reproduced from Toy and Tahouri (1988), shows a mean pressure coefficient contour plot for a circular vault with side-walls normal to the flow.



Area	A	B	C	D
$Cp_{,av}$	-0.9	-0.3	-0.2	-0.1

Figure 8.9 - Mean design pressure coefficients for arch-roof building (f/b =0.3, h/b =0.12) (Data from Paluch et al (2003))

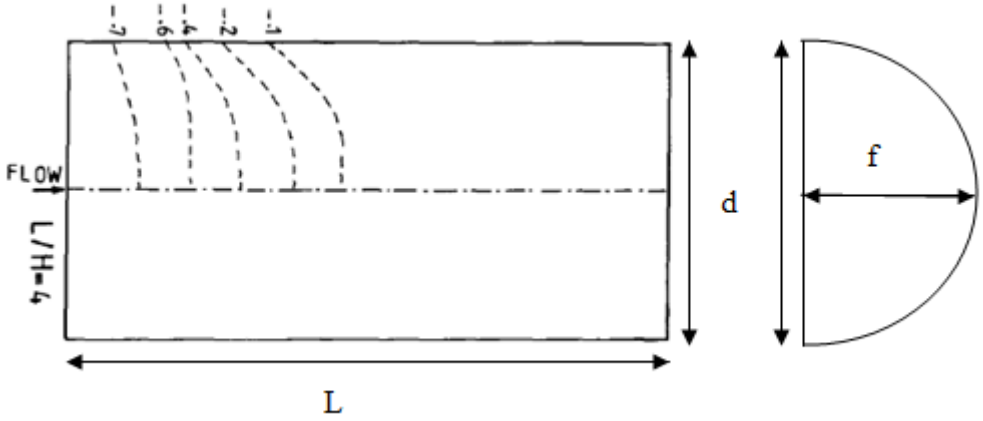


Figure 8.10 - Surface pressure distribution for a single circular vault (L/f=2 and f/d=0.5) (Reproduced from Toy and Tahouri (1988))

Blackmore and Tsokri (2006) proposed a procedure using EN 1991-1-4 duo-pitch roof design pressure coefficients for wind normal to the eaves. The authors compared experimental pressure coefficients measured for arch-roof structures

with duo-pitch codified pressure coefficients, and found an acceptable degree of similarity for design purposes. The specified areas and results for f/d = 0.5 and h/d = 0 are shown, for both the experimental and duo-pitch pressure coefficients, in Figures 8.11 and Table 8.4, respectively.

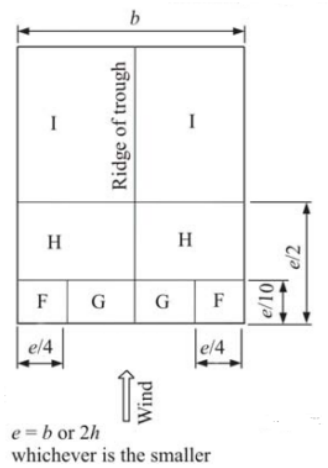


Figure 8.11 - Specified duo-pitch areas (Reproduced from EN 1991 -1-4)

Table 8.4 - Area-averaged pressure coefficients (Data from Blackmore and Tsokri (2006))

h=0, f/d =0.5, θ = 90°, α = 45°	Zone F	Zone G	Zone H	Zone I
Cpe_{10} - duo-pitch roof (EN 1991-1-4)	-1.2	-1.4	-0.9	-0.5
Cpe_{10} - arch (Blackmore and Tsokri)	-1.1	-0.95	-1.0	-0.5

The surface averaged pressure coefficients which coincide with zones specified by Blackmore and Tsokri (2006), for the flat cross vault, are compared in Table 8.5. As shown in Table 8.5, the flat cross vault pressure coefficients show comparable magnitudes with that of Blackmore and Tsokri (2006). However, point pressures show visible variation at some tap positions. For the above-mentioned reason, the use of design data for this wind direction is only applicable to the foremost areas over the vault.

Table 8.5 - Flat cross vault surface averaged pressure coefficients

		Zone H	Zone I
Blackmore and Tsokri	Cpe_{10}	-1.0	-0.5
Current	Cp_{av} Area 1 (Taps 2, 3, 5 and 6) - Pneumatic	-0.75	-0.40
	Cp_{av} Area 1 (Taps 2, 3, 5 and 6) - Numerical	-0.83	-0.55
	Cp_{av} Area 3 (Taps 5, 6, 7 and 8) - Numerical	-0.91	-0.45
	Cp_{av} Area 4 (Taps 3, 4, 6 and 7) - Numerical	-0.81	-0.55

8.4 Predicted Design Coefficients over Cross Vault Structures

Pressure coefficients were measured at central areas over the cross vault structure; however, the entire pressure distribution is required for design purposes. In this section, pressures have been predicted for areas not investigated in this study. These predicted results may not be entirely valid; however, they can give a suitable guide to pressure coefficients for design.

8.4.1 0° wind direction

Roof

In this section pressures have been extrapolated away from the centre of the cross vault utilizing three aspects, namely: pressures increase linearly from the leading edge along the vault with wind normal to the walls, pressures appear to be lowest near the apex of the vault with walls parallel to the flow, and that there is a degree of similitude between pressures over single vault and cross vault structures for certain areas of the roof.

For wind blowing normal to the walls, the cross vault has been divided into nine sections, as shown in Figure 8.12. The pressure coefficient values corresponding to these areas are given in Table 8.6. Large local suctions may occur near the leading edge for normal and oblique wind directions. A pressure coefficient corresponding to the region for an arched roof has been taken from Newberry and Eaton (1974). Newberry and Eaton (1974) give a value of -1.8 for the hatched region, as illustrated in Figure 8.12.

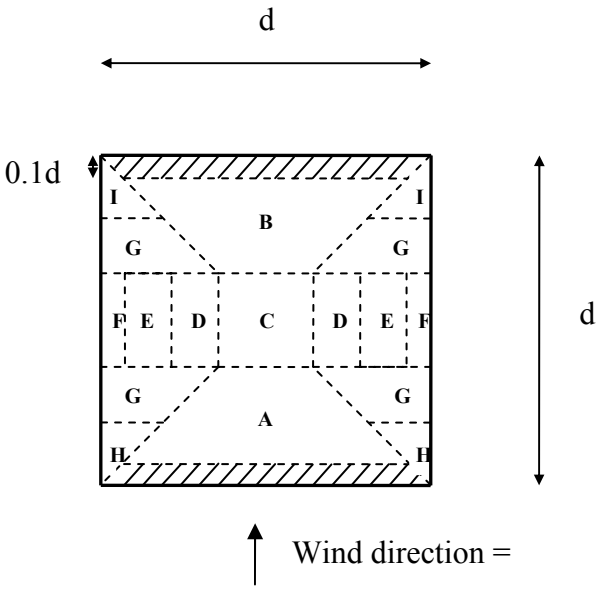


Figure 8.12 - Plan view: pressure coefficient segments for the 0° direction

Table 8.6 - Pressure coefficient values corresponding to the areas defined in Figure 8.12

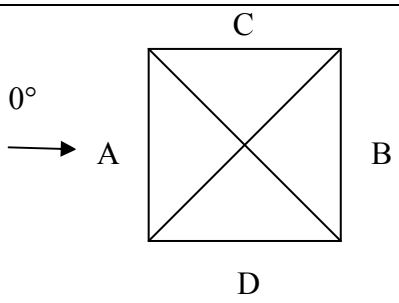
	Flat	**Convex**	**Concave**
Section	***Cp***	***Cp***	***Cp***
A	-1.0	-1.0	-1.0
B	-0.5	-0.5	-0.5
C	-0.8	-1.0	-0.8
D	-1.2	-1.2	-1.2
E	-1.6	-1.6	-1.6
F	-2.0	-2.0	-2.0
G	-1.2	-1.2	-1.2
H	+0.5	+0.5	+0.5
I	-0.5	-0.5	-0.5

Local C_p in the hatched area of figure 8.12 is -1.8

Walls

External wind pressure coefficients corresponding to the cross vault walls have been defined from design information for rectangular clad buildings as given by SABS 0160-1989.

Table 8.7 - Wall pressures

			Average Cp for surface			
Building height ratio	Building plan ratio	Plan	A	B	C	D
h/w= 0.5	b/w= 1		+0.7	- 0.2	-0.5	-0.5

*Where h is the height, w is the width and b is the breadth.

8.4.2 30°- 60° wind directions

Roof

Pressure zones have been identified for the 30°, 45° and 60° wind directions in a single form, as shown in Figure 8.13, noting that the pressure patterns are very similar for these orientations. For these directions, pressures have been defined for large regions, as shown in Figure 8.13, since there is insufficient experimental information to perform more precise predictions. The pressure coefficient values corresponding to these regions are given in Table 8.8. The local pressure coefficient near the cross vault edges is the same as that given in Table 8.6.

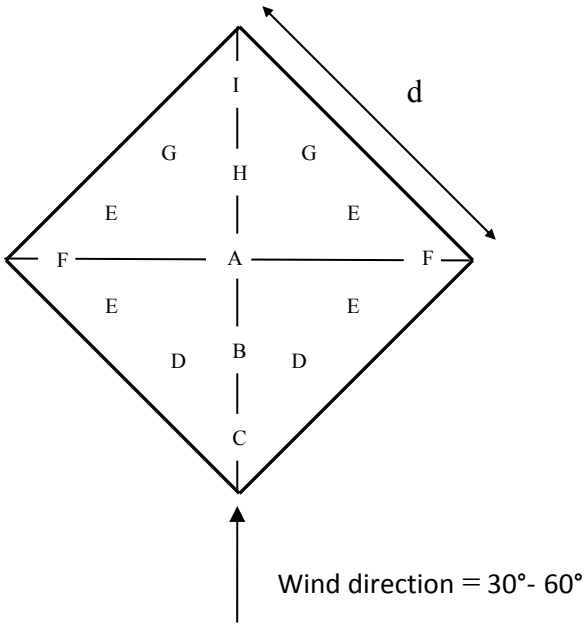


Figure 8.13 - Plan view: pressure coefficient segments for the 30°- 60° directions

Table 8.8 – Pressure coefficient values corresponding to the areas defined in Figure 8.13

	Flat	**Convex**	**Concave**
Section	***Cp***	***Cp***	***Cp***
A	-1.0	-1.2	-0.9
B	-2.0	-2.0	-2.0
C	-0.5	-0.5	-0.5
D	-2.0	-2.0	-2.0
E	-0.6	-1.0	-0.6
F	-0.4	-0.4	-0.4
G	-0.9	-1.3	-0.9
H	-1.5	-1.5	-1.5
I	-0.5	-0.5	-0.5

8.5 Conclusions

The design information for single vault structures is given for the most critical wind directions, namely: normal and parallel to curvature. It should also be noted that minimum pressures (both mean and negative peaks) measured in the present

study were generally observed at either the 45° or 60° wind directions. This is opposed to Toy and Tahouri (1988) who showed that, for single vaults, the pressures at the 45° wind direction were more positive than those at both 0° and 90°. Design values were also compared with the current experimental results and revealed the general lack of applicability of this information for the design of cross vault structures, due to the significant influence of cross vault geometry. However, certain areas ahead of the vault intersection do show consistency with data found in the literature.

9 CONCLUSIONS AND RECOMMENDATIONS

9.1 Summary and Conclusions of the Present Study

A series of wind-tunnel tests was conducted to examine the effects of surface roughness (Reynolds number sensitivity), turbulence intensity, wind orientation and roof geometry on the external pressure distribution over cross vault structures. Three cross vault models, at a scale of 1 in 500, with different roof slopes (and heights) of the apex were constructed and have been investigated in the wind-tunnel.

Comparisons of mean, RMS and negative peak pressures, measured with different attached roughness magnitudes, have been carried out to verify surface pressure sensitivity to Reynolds number. Generally, mean and negative peak pressure coefficients corresponding to the roughest sandpaper were visibly less negative than those over the smooth fibreglass cross vault. Mean pressures corresponding to the P150 sandpaper were generally larger than those over the smooth, flat cross vault, but no definite negative peak pressure trend were evident. Comparison of the RMS pressure coefficients indicated them to be lower for the rougher surfaces at the 0° wind direction. This result is consistent with studies conducted on roughened rectangular bluff bodies, with flow separation at sharp edges. The RMS pressures at the 30° and 45° directions did not show any apparent trend. Because of mean pressure coefficient differences which were observed, the roughness of $k/d \times 10^3 = 0.63$ (P150 sandpaper), in accordance with the ESDU procedure, was selected for this study.

Experimentation was conducted in two generic boundary-layer profiles to determine the influence of boundary-layer characteristics on surface pressure coefficients. Mean pressure coefficients were not significantly affected by the change in boundary-layer approach flow. However, it should be noted that mean pressures measured in the ‘smooth’ boundary-layer were generally slightly lower than those for the ‘rough’ boundary-layer, and more substantial mean pressure increases would be expected with further boundary-layer growth. It was apparent that the boundary-layer characteristics affected the RMS and negative peak

pressures. RMS pressures increased, whereas negative peak pressures generally decreased with the increased turbulence intensity. This trend is consistent with findings of previous measurements of sharp edged and curved bluff body structures.

Three roof geometries, with relatively small geometrical changes of the apex (rise) of the cross vault roofs, were investigated. Some prominent trends were evident at specific wind directions and roof areas. The most notable trend was that the mean and negative peak pressures closest to the roof apex (taps 1 to 4) for the convex cross vault were generally more negative than those over the flat and concave cross vaults. Marginal mean and negative peak pressure coefficient variations for the three models were evident at the 0°, 90° and 180° wind directions. This result was somewhat expected, given that the flow separation was controlled by the wall-roof edge. Noticeable mean, RMS and negative peak pressure coefficient variation was evident at the 15°, 30°, 120° and 150° wind directions. These results reveal that relatively small changes in roof geometry can noticeably influence the distribution of surface pressures, at certain directions and areas of the roof.

The minimum pressures (both mean and negative peaks) measured in the present study were generally observed at either the 45° or 60° wind directions. The design information for single vault structures was also compared with the current experimental results and revealed that the codified data was generally not applicable for the design of cross vault structures, due to the significant influence of geometry. However, the area-averaged pressures ahead of the vault intersection do show consistency with design data applicable to single vaults.

9.2 Recommendations for Future Wind-Tunnel Studies related to the Cross Vault Structure

The nature of this study was to ascertain the effects of surface roughness (or Reynolds number sensitivity), turbulence intensity, wind orientation and roof geometry on the centrally located surface pressures for cross vault structures. However, numerous situations which include the effects of: grouping, surrounding

obstacles, height to diameter ratio, widely varying terrain categories (i.e. ‘open country’ and ‘city centre’) and openings, are also pertinent to the loading on cross vault structures. These aspects would require further investigation to ascertain their influence on pressure distributions.

Numerically averaged pressure coefficients were assessed in this study. However, comparisons with pneumatically averaged results revealed notable variations. The possible reasons for these discrepancies were discussed, but further testing would be of interest as numerous issues could be responsible.

The effects of wind direction are significant at some tap positions and it would be of interest in a further study to utilise smaller wind direction increments and full tap coverage to completely clarify pressure distributions over these structures. Especially, noting that codified data for the design of single vaults is generally not applicable for the design of cross vault structures.

REFERENCES

Archenbach, E. (1971) "Influence of surface roughness on the cross flow around a circular cylinder" Journal of Fluid Mechanics, 46(2): Pages 321 -335.

Basu, RI. **(**1986) "Aerodynamic forces on structures with circular cross section Part 2: The influence of turbulence and three-dimensional effects" Journal of Wind Engineering and Industrial Aerodynamics, Volume 24: Pages 33-59.

Bienkiewicz, B and Sun, Y. (1992) "Local wind loading on the roof of a low rise building" Journal of Wind Engineering and Industrial Aerodynamics, Volume 45: Pages 11-24.

Blackmore, PA and Tsokri, E**. (**2006) "Wind loads on curved roofs". Journal of Wind Engineering and Industrial Aerodynamics, Volume 94, Issue11: Pages 833-844.

Boggs, D and Lepage, A. (2004) "Wind tunnel methods", ACI SP-240 - Performance Based Design of Concrete Building for Wind Loads, Pages 125 - 142.

Cheung, JCK and Melbourne, WH. (1983) "Turbulence effects on some aerodynamic effects of a circular cylinder at supercritical Reynolds number" Journal of Wind Engineering and Industrial Aerodynamics, Volume 14: Pages 399-410.

Cook, N J. (1985). The designers guide to wind loading of building structures-part 1, Kent: Butterworths.

Davenport, AG. (2007). Wind-tunnel testing: a general outline, INTERNET. *http://www.blwtl.uwo.ca/User/Doc/Wind%20Tunnel%20Outline-Web.pdf*

EN1991-1-4 (2004). Eurocode 1: Actions on structures - Part 1–4: General Actions - wind actions.

Engineering Sciences Data Unit (1980) Mean forces, pressure and flow field velocities for circular cylindrical structures: single cylinders with two-dimensional flow, *Data Item ESDU- 80025*

Goliger, AM and Milford, RV. (1990) "A note on surface pressure averaging-internal report" Building Technology, Council for Scientific and Industrial Research, Pretoria, South Africa.

Guven, O, Patel, VG and Farrel, C. (1975) "Surface roughness effects on the mean flow past circular cylinders" Iowa Institute of Hydraulic Research, University of Iowa, Iowa City, Iowa.

Holmes, JD. (2001) Wind loading of structures, London: Spon Press

Letchford, CW, Sarkar, PP. (2000) "Mean and fluctuating wind loads on rough and smooth parabolic domes" Journal of Wind Engineering and Industrial Aerodynamics, Volume 88: Pages 101-117.

Maruta, E, Kanda, M and Sato, J. (1998) "Effects of surface roughness for wind pressure on glass and cladding of buildings" Journal of Wind Engineering and Industrial Aerodynamics, Volume 74-76: Pages 651-663.

Newberry, CW and Eaton, KJ. (1974). Wind loading handbook,
London: Her Majesty's Stationery Office

Ogawa, T, Nakayama, M, Murayama, S and Sasaki, Y. (1991) "Characteristics of wind pressures on basic structures with curved surfaces and their response in turbulent flow" Journal of Wind Engineering and Industrial Aerodynamics, Volume 38, Issues 2-3: Pages 427-438.

Paluch, MJ, Loredo-Souza, AM and Blessmann, J. (2003). "Wind loads on attached canopies and their effect on the pressure distribution over arch-roof industrial buildings" Journal of Wind Engineering and Industrial Aerodynamics, Volume 91: Pages 975-994.

SABS (1989). The general procedures and loadings to be adopted in the design of buildings, SABS 0160 -1989, The Council for the South African Bureau of Standards, Pretoria,1989.

Sachs, P. (1972) Wind forces in engineering, Oxford: Pergamon Press

Scruton, C. (1981). An Introduction to Wind Effects on Structures, Oxford: Oxford University Press.

Simiu, E and Scanlan, RH. (1978) Wind effects on structures: an introduction to wind engineering, New York: John Wiley and sons

Stathopoulos, T and Zhu, X. (1988) "Wind pressures on building with appurtenances" Journal of Wind Engineering and Industrial Aerodynamics, Volume 31, Issues 2-3: Pages 265-281.

Stathopoulus, T and Baniotopoulos, CC. (2007) Wind Effects on Buildings and Design of Wind Sensitive Structures. New York: Springer Wien.

Surry, D and Stathopoulos, T. (1977) "An experimental approach to the economical measurements of spatially averaged wind loads" Journal of Wind Engineering and Industrial Aerodynamics, Volume 2: Pages 385-397.

Szepessy, S and Bearman, PW. (1993) "Analysis of a pressure averaging device for measuring aerodynamic forces on a circular cylinder" Experiments in Fluids, Volume 16: Pages 120-128.

Toy, N and Tahouri, B. (1988) **"**Pressure distributions on semi-cylindrical structures of different geometrical cross-sections" Journal of Wind Engineering and Industrial Aerodynamics, Volume 29: Pages 263-272.

Taylor, TJ. (1992) "Wind pressures on a hemispherical dome" Journal of Wind Engineering and Industrial Aerodynamics, Volume 40, Issue 2: Pages 199-213.

Tieleman, H.W (1993) "Pressures on surface-mounted prisms: the effects of incident turbulence" Journal of Wind Engineering and Industrial Aerodynamics, Volume 49: Pages 189-300.

Ribeiro, JLD. (1991) "Effects of surface roughness on the two-dimensional flow past circular cylinders I: mean forces and pressures" Journal of Wind Engineering and Industrial Aerodynamics, Volume 37, Issue 3: Pages 299-309.

Ribeiro, JLD. (1991) "Effects of surface roughness on the two-dimensional flow past circular cylinders II: fluctuating forces and pressures" Journal of Wind Engineering and Industrial Aerodynamics, Volume 37, Issue 3: Pages 311-326.

Wang, K. (1998) "Wind pressure coefficients for gable roofs of intermediate slopes" Concordia University, Montreal, Canada, *Engineering Thesis.*

Zdravkovich, MM. (1990) "Conceptual overview of laminar and turbulent flows past smooth and rough circular cylinders" Journal of Wind Engineering and Industrial Aerodynamics, Volume 33, Issue 1: Pages 53-62.

BIBLIOGRAPHY

Amoroso, SD. (2007) "Wind loads for petrochemical structures" Louisiana State University and Agricultural and Mechanical College, United States of America, *Engineering Dissertation (Phd.)*

Barbosa, PA, Cataldi, M and Freire, APS. (2002) "Wind-tunnel simulation of atmospheric boundary-layer flows" Journal of the Brazilian Society of Mechanical Sciences, vol.24, no.3

Chen, WF, Lui, EM (2001). Handbook of structural engineering - second edition. Florida: CRC Press.

Cochran, LS. (2006) "State of the art review of wind-tunnels and physical modelling to obtain structural loads and cladding pressures." Architectural Science Review, Volume 50, Number 1: pages 7-16.

Goliger, AM (2007) "South African wind loading specifications: the euro way?" Journal of Wind Engineering and Industrial Aerodynamics, Volume 95: Pages 1053-1064.

Goliger, AM (2010) "Wind tunnel testing of sports stadia to optimise their use and safety" Journal of the South African Institution of Civil Engineering, Volume 52, Number 1, Paper 690: Pages 28-35.

Goliger, AM and Waldeck, JL. (1996) "Wind tunnel tests of conveyor-belt housing structures" Journal of Wind Engineering and Industrial Aerodynamics, Volume 65: Pages 405-413.

Houghton, EL and Carruthers, NB. (1976) Wind forces on buildings and structures: an introduction, London: Edward Arnold.

Krishna, P. (1995**) "**Wind loads on low rise buildings - a review". Journal of Wind Engineering and Industrial Aerodynamics, Volumes 54-55: Pages 383-396.

Lawson TV. (1982) "The use of roughness to produce high Reynolds number flows around circular cylinders at lower Reynolds numbers" Journal of Wind Engineering and Industrial Aerodynamics, Volume 10, Issue 3: Pages 381-387.

Sabransky, IJ and Melbourne WH (1987) "Design pressure distribution on circular silos with conical roofs" Journal of Wind Engineering and Industrial Aerodynamics, Volume 26: Pages 65-84.

Saathoff, P.J and Melbourne, W.H (1987) Free-stream turbulence and wind-tunnel blockage effects on streamwise surface pressures" Journal of Wind Engineering and Industrial Aerodynamics, Volume 26: Pages 353-370.

Stathopoulos, T and Surry, D**. (**1983**)** "Scale effects in wind-tunnel testing of low buildings" Journal of Wind Engineering and Industrial Aerodynamics, Volume 13: Issues 1-3: Pages 313-326.

Surry, D. (1967) "Turbulence in wind-tunnel and its use in studying the turbulence effects on the aerodynamics of a rigid circular cylinder." Wind effects on buildings and structures, Toronto: University of Toronto press.

Tahouri, B, Toy, N and Savory, E. (1990)**. "**Surface pressures and wake flows associated with highly curved agricultural buildings" Journal of Wind Engineering and Industrial Aerodynamics, Volume 36: Issues 1-3: Pages 319-327.

Taniguchi, A, Sakamoto, H, Kiya, M and Arie , M. (1982) "Time averaged aerodynamic forces acting on a hemisphere immersed in a turbulent boundary". Journal of Wind Engineering and Industrial Aerodynamics, Volume 9: Pages 257-273.

Tieleman, HW, Hajj, MR and Reinhold, TA.(1998) "Importance of turbulence for the prediction of surface pressures on low-rise structures" Journal of Wind Engineering and Industrial Aerodynamics, Volumes 69-71: Pages 519-528.

Tieleman, HW, Hajj, MR and Reinhold, TA. (1998) "Wind tunnel simulation requirements to assess wind loads on low-rise buildings" Journal of Wind Engineering and Industrial Aerodynamics, Volumes 74-76: Pages 675-685.

Uematsu, Y and Isyumov, N. (1999) “Wind pressure acting on low rise buildings” Journal of Wind Engineering and Industrial Aerodynamics, Volume 82: Pages 1-25.

Zasso, A, Giappino, S and Muggiasca, S. (2006) **“**Wind tunnel study of a cone-like shaped roof: Reynolds number effects. Journal of Wind Engineering and Industrial Aerodynamics, Volume 94, Issue 5: Pages 431-444

APPENDIX A C_{DO} AND Cp CALCULATION PROCEDURES OUTLINED IN ESDU- 80025 (1980)

Drag Coefficient (C_{DO}) calculation procedure outlined in ESDU- 80025 (1980)

1) Attain a value for surface roughness ε

2) Calculate Roughness Factor (λ_R)

$\lambda_R = 1 + (\lambda_{R'} - 1)\{ 1 - \exp[-5(R_{e_e} * 10^{-4})^2]\}$ (A1)

$\lambda_{R'} = \lambda_R$ for $R_{e_e} > 10^4$ (A2)

$\lambda_{R'} = 7 - 6*\exp[-0.11E]$ (A3)

$E = (\varepsilon/D) *10^3$ (Relative Roughness) (A4)

3) Calculate Turbulence Factor (λ_T)

$\lambda_T = (\lambda_{Tcrit} - 1)*1.28*\exp[-20(-R_1)^{2.8}] -1,$ for $R_e/R_{ecrit} <= 0.5$ (A5)

$\lambda_T = (\lambda_{Tcrit} - 1)*1.28*\exp[-1.3*R_1^{1.4}\ 0.1 * R_1^4] - 1,$ for $R_e/R_{ecrit} >= 0.5$ (A6)

$R_e\lambda_{Tcrit} = 13 - 12\exp[-11.5*I_u(D * L_u)^{1/5}]$ (A7)

$R_{ecrit} = 4.5 * 10^5/(\lambda_{Tcrit} * \lambda_R)$ (A8)

$R_1 = log_{10}(2*R_e/R_{ecrit})$ (A9)

I_u (Intensity of Turbulence)

L_u (Scale of Turbulence)

4) Calculate the Effective Reynolds Number (R_{e_e})

$R_{e_e} = \lambda_R\lambda_T R_e$ (A10)

5) Calculate the Drag Coefficient (C_{D0})

$log_{10}R_{e_{eA}} = 5.55 + 0.19*\exp[-0.32*E^{0.35}]$ (A11)

$log_{10}R_{e_{eB}} = 5.65 + 0.22*\exp[-0.7*E^{0.5}]$ (A12)

$R = log_{10}(\frac{R_{e_e}}{R_{e_{eB}}})$ (A13)

$f_1 = 1 - \exp[-(R + 2bR^2 - bR * R^2)]$ (A14)

$$b = \frac{4.5}{1+5(log_{10}E-0.15)^2} + 4 \quad \text{(A15)}$$

$$C_M = 1.04 - 0.47\exp[-(0.9E + 0.55E^{1.5})] + 0.11[1 - \exp(-8 * 10^{-4}E^2)] \quad \text{(A16)}$$

$$C_B = 1.1 - 0.83\exp[-(0.01E + 0.34E^{.5})] \quad \text{(A17)}$$

$$n = 0.06*\exp(-0.04E^2) \quad \text{(A18)}$$

For $3 * 10^4 \leq R_{e_e} \leq R_{e_{eA}}$

$$C_{D0} = (1 + 2*\varepsilon/D)\{0.27 + 0.93*\exp[-1.65 * 10^{-7} (R_{e_e} * 10^{-5})^{10}]\} \quad \text{(A19)}$$

For $R_{e_{eA}} \leq R_{e_e} \leq 3 * 10^7$

$$C_{D0} = (1 + 2*\varepsilon/D)*\{f_1(C_M\text{-}C_B) + C_B - n*[1 - \exp(-0.5*R^2*R^2)]\} \quad \text{(A20)}$$

Mean centreline pressure coefficient (C*p*) distribution calculation procedure outlined in ESDU- 80025 (1980)

1) Calculate C_{D0}, as illustrated above.

2) Calculate the base pressure coefficient (Cp_b), the angle at which the base pressure occurs (θ_b), and the angle at which the minimum pressures occurs (θ_m).

$$Cp_b = 0.00796\ (1.3 - C_{D0}^{0.8})^{10} - 0.918C_{D0} - 0.098 \quad \text{(A21)}$$

$$\theta_b = 145.4 + 42.4Cp_b - 7.8Cp_b2 + k/(0.076 + 0.939\ (c^2 + c) \quad \text{(A22)}$$

$$\theta_m = 90 - 23\exp\ [-0.363\ (0.01\ \theta_b)^5] \quad \text{(A23)}$$

$$c = (1.3 + Cp_b)^3 \quad \text{(A24)}$$

$$k = 0 \text{ for } Re_e <= Re_{eA} \quad \text{(A25)}$$

$$k = (Re_e - Re_{eA})/(Re_{eB} - Re_{eA}) \text{ for } Re_{eA} < Re_e < Re_{eB} \quad \text{(A26)}$$

$$k = 1 \text{ for } Re_e >= Re_{eB} \quad \text{(A27)}$$

3) Calculate (θ_b -θ_m) and obtain Cp_b - Cp_m.

$$Cp_b - Cp_m = 4[1.013 - \exp(-6 \text{ x } 10^{-6}\ \Delta\ \theta_{bm}{}^3)] - (1/(4.7 + 0.028(\lceil \Delta\ \theta_{bm} - 28 \rceil)^3) \quad \text{(A28)}$$

$$\Delta\ \theta_{bm} = \theta_b - \theta_m \quad \text{(A29)}$$

4) Calculate the values of Cp at values of θ, for the zones shown in Figure A1.

For $0 <= \theta <= \theta_m$: $Cp = 1 - (1 - Cp_m).\sin^2[(\theta/\theta_m).90°]$ (A30)

For $\theta_m < \theta <= \theta_b$: $Cp = Cp_b - (Cp_b - Cp_m).\cos^2[((\theta - \theta_m)/(\theta_b - \theta_m)).90°]$ (A31)

For $\theta_b <= \theta <= 180°$: $Cp = Cp_b$ (A32)

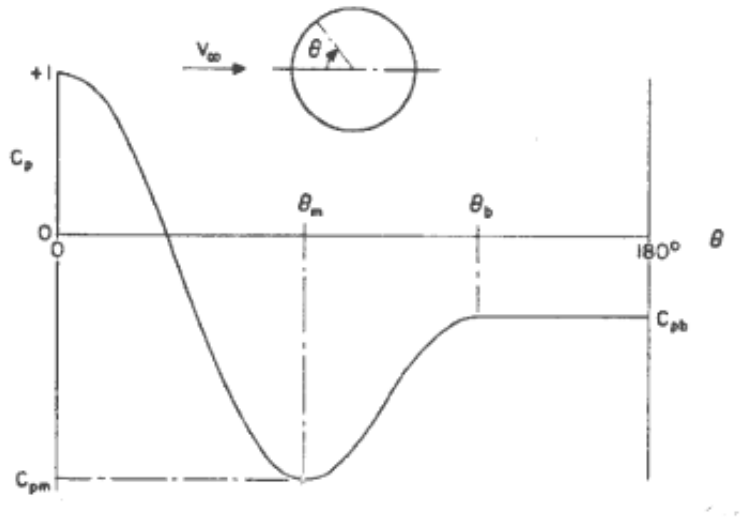


Figure A1 – Pressure distribution parameters

APPENDIX B EXPERIMENTAL SCATTER

Table B1 and B2 below indicate the percentage range for both the mean and RMS pressure coefficients for the tests conducted on the flat cross vault, with a smooth model surface, and for the 'smooth' boundary-layer.

Table B1 - Experimental Range (Mean C*p*)

	Repetition 1	Repetition 2	Repetition 3	Mean	%Range
Tap 6(θ=0)	-1.00	-1.06	-1.07	-1.04	6
Tap 7(θ=0)	-1.16	-1.23	-1.28	-1.22	10
Tap 8(θ=0)	-1.20	-1.29	-1.25	-1.25	7
Tap 6(θ=30)	-1.04	-1.06	-1.11	-1.06	7
Tap 7(θ=30)	-1.49	-1.57	-1.61	-1.56	8
Tap 8(θ=30)	-1.33	-1.44	-1.47	-1.41	10
Tap 6(θ=45)	-1.38	-1.36	-1.34	-1.36	3
Tap 7(θ=45)	-1.82	-1.80	-1.82	-1.82	1
Tap 8(θ=45)	-1.52	-1.59	-1.51	-1.54	5

Table B2 - Experimental Range (RMS C*p*)

	Repetition 1	Repetition 2	Repetition 3	Mean	%Range
Tap 6(θ=0)	0.343	0.341	0.350	0.345	3
Tap 7(θ=0)	0.388	0.389	0.409	0.395	5
Tap 8(θ=0)	0.357	0.357	0.363	0.359	2
Tap 6(θ=30)	0.264	0.272	0.283	0.273	7
Tap 7(θ=30)	0.306	0.310	0.317	0.311	4
Tap 8(θ=30)	0.337	0.353	0.348	0.346	5
Tap 6(θ=45)	0.275	0.271	0.263	0.270	4
Tap 7(θ=45)	0.310	0.305	0.300	0.305	3
Tap 8(θ=45)	0.307	0.320	0.303	0.310	5

Table B3 and B4 show the percentage range for both the 10 second and 3 second pressure coefficients for the tests conducted on the flat cross vault, with a smooth model surface, and for the 'smooth' boundary-layer.

Table B3 - Range (Negative 10s Peak C*p*)

	Repetition 1	Repetition 2	Repetition 3	Mean	%Range
Tap 6(θ=0)	-1.68	-1.91	-1.67	-1.75	13
Tap 7(θ=0)	-1.89	-2.27	-2.14	-2.07	18
Tap 8(θ=0)	-1.85	-2.07	-1.97	-1.96	11
Tap 6(θ=30)	-1.44	-1.52	-1.73	-1.56	18
Tap 7(θ=30)	-2.09	-2.46	-2.33	-2.29	16
Tap 8(θ=30)	-2.00	-2.20	-2.28	-2.16	13
Tap 6(θ=45)	-1.9	-1.97	-1.91	-1.93	4
Tap 7(θ=45)	-2.42	-2.86	-2.39	-2.56	18
Tap 8(θ=45)	-2.22	-2.38	-2.11	-2.24	12

Table B4 - Range (Negative 3s Peak C*p*)

	Repetition 1	Repetition 2	Repetition 3	Mean	%Range
Tap 6(θ=0)	-1.92	-2.33	-1.91	-2.05	20
Tap 7(θ=0)	-2.29	-2.27	-2.43	-2.33	7
Tap 8(θ=0)	-2.06	-2.36	-2.09	-2.17	14
Tap 6(θ=30)	-1.73	-1.70	-1.87	-1.77	10
Tap 7(θ=30)	-2.43	-2.35	-2.43	-2.40	3
Tap 8(θ=30)	-2.20	-2.33	-2.55	-2.36	15
Tap 6(θ=45)	-2.11	-2.10	-2.04	-2.08	3
Tap 7(θ=45)	-2.61	-2.77	-2.53	-2.64	9
Tap 8(θ=45)	-2.44	-2.55	-2.25	-2.41	13

APPENDIX C PRESSURE COEFFICIENT VARIATION WITH WIND DIRECTION

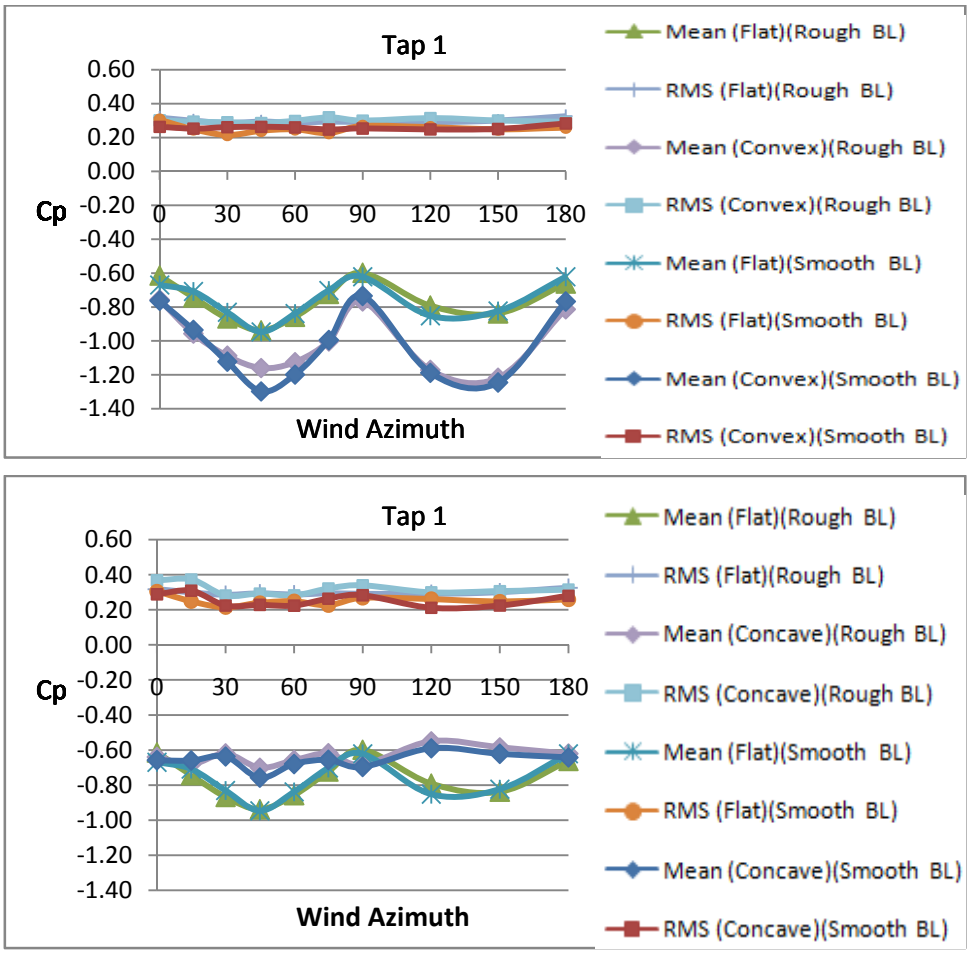


Figure C1 - Pressure coefficient variation with wind direction (Tap 1)

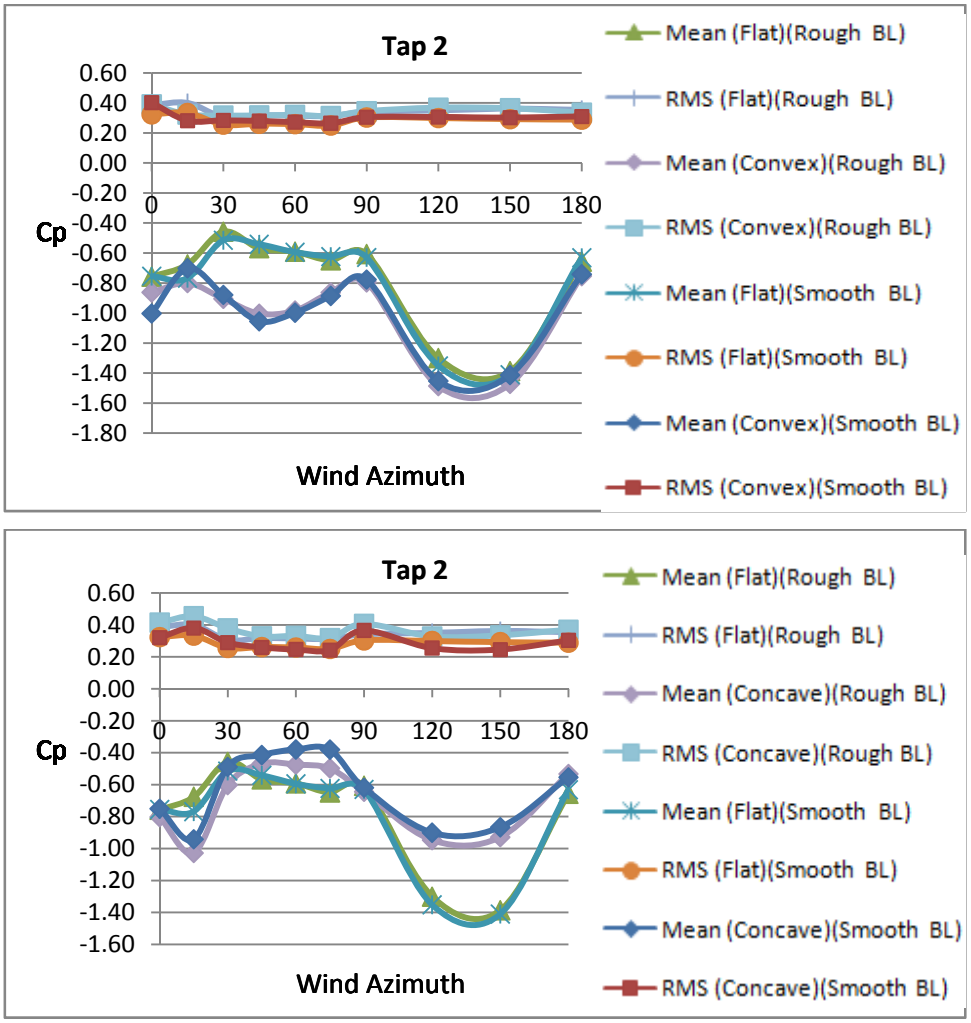


Figure C2 - Pressure coefficient variation with wind direction (Tap 2)

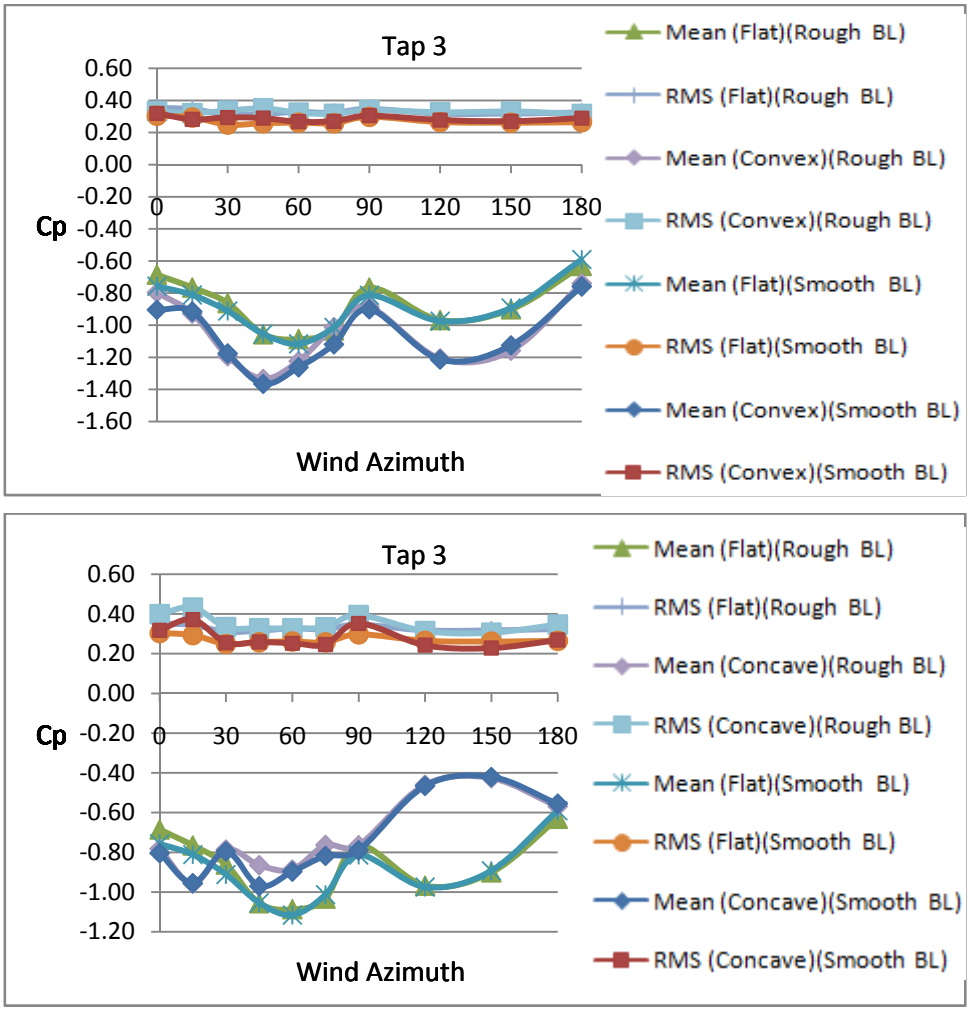


Figure C3 - Pressure coefficient variation with wind direction (Tap 3)

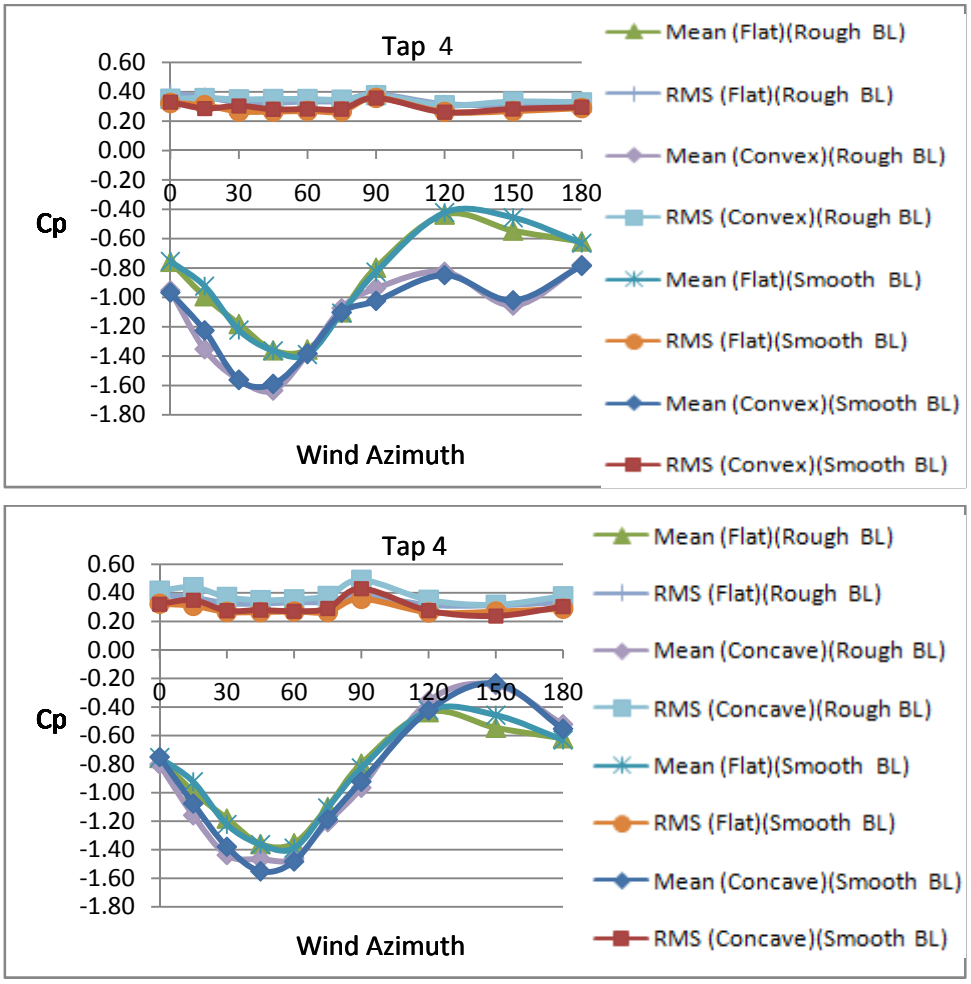


Figure C4 - Pressure coefficient variation with wind direction (Tap 4)

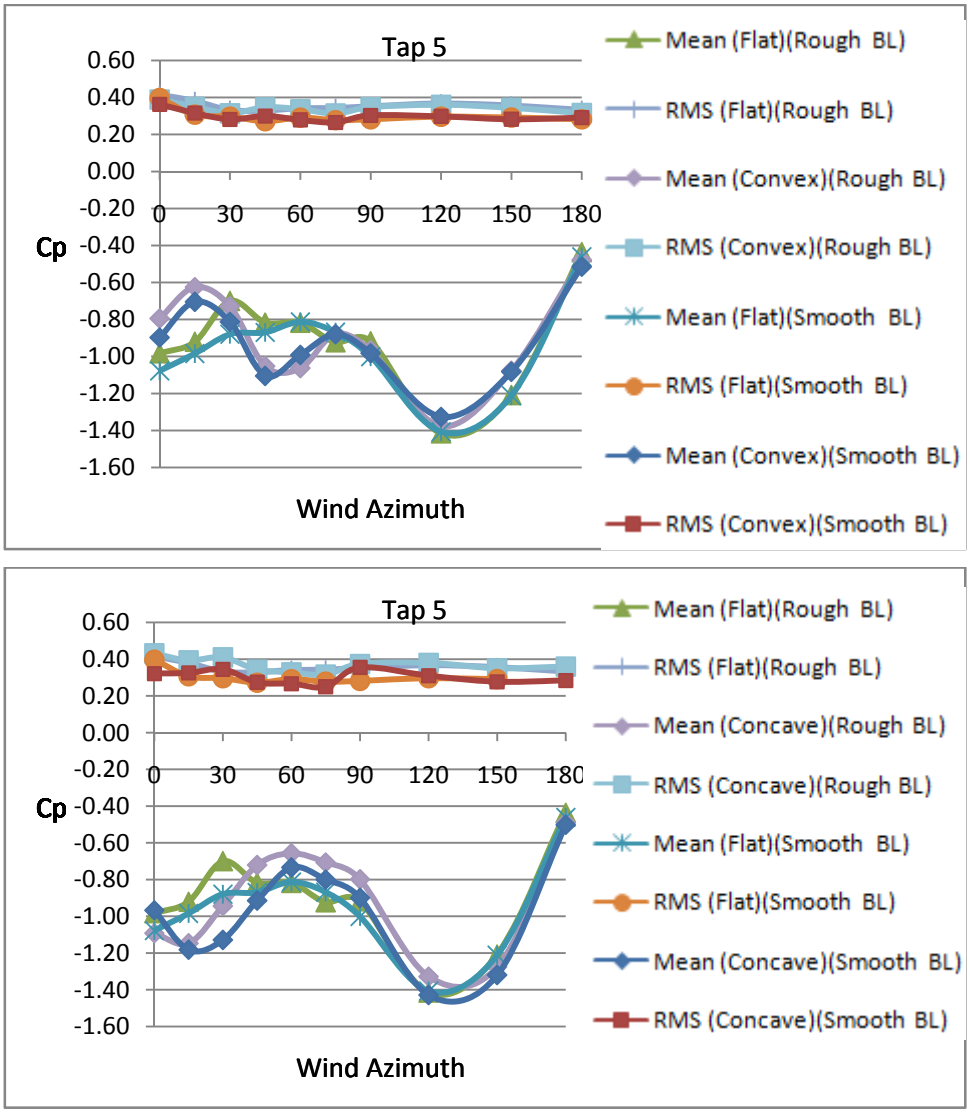


Figure C5 - Pressure coefficient variation with wind direction (Tap 5)

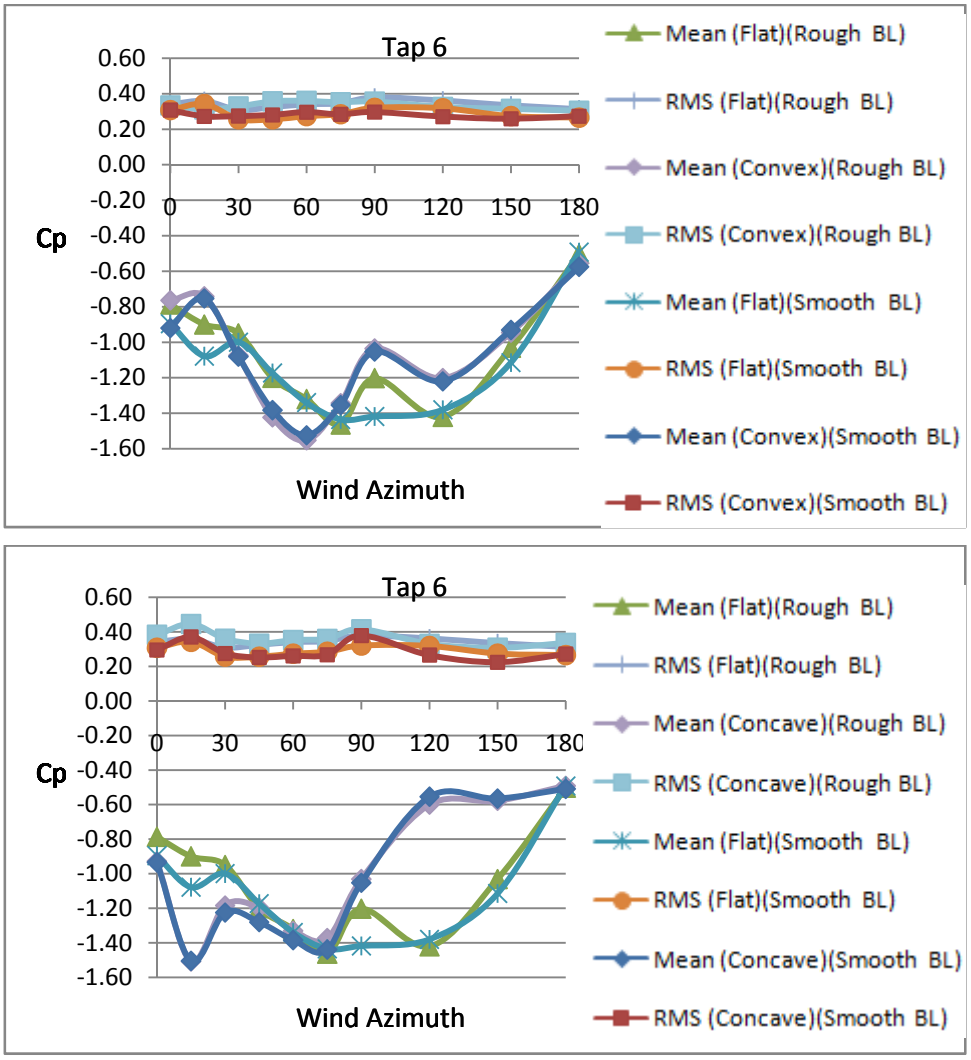


Figure C6 - Pressure coefficient variation with wind direction (Tap 6)

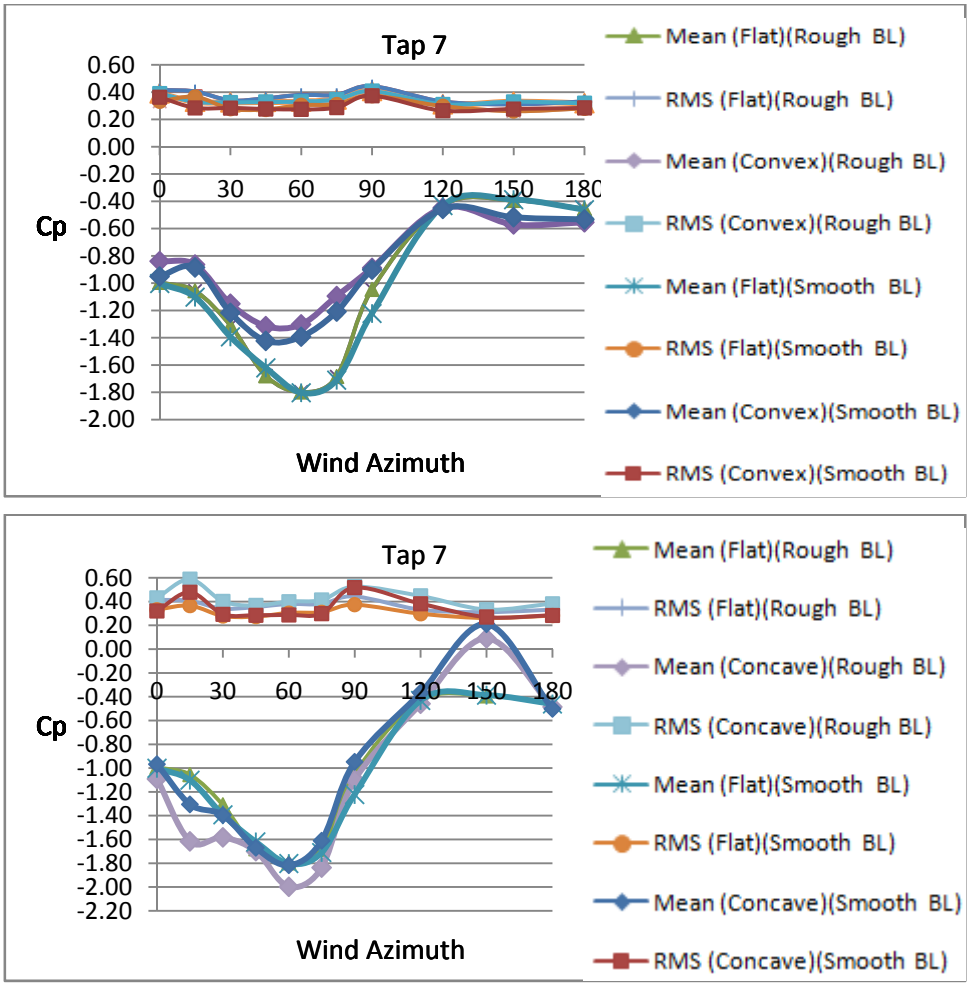


Figure C7 - Pressure coefficient variation with wind direction (Tap 7)

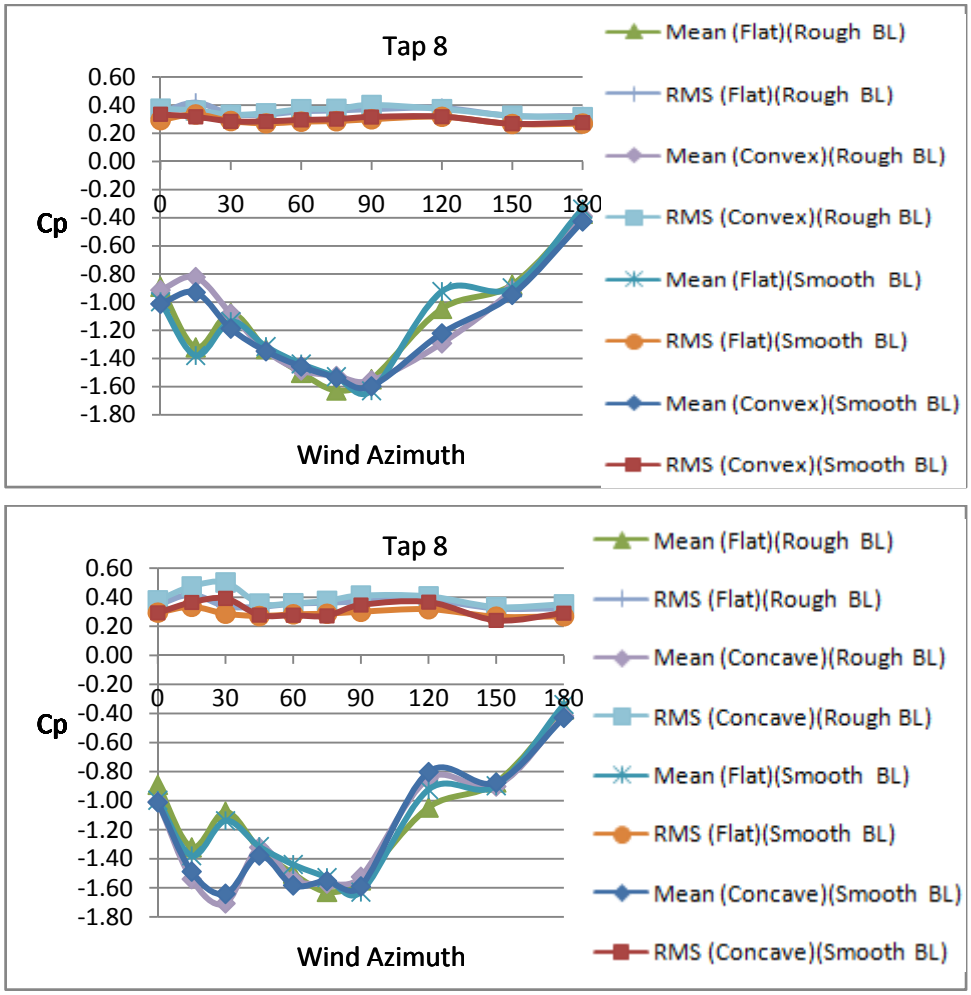


Figure C8 - Pressure coefficient variation with wind direction (Tap 8)